UNIVERSITÀ DEGLI STUDI
DI MODENA E REGGIO EMILIA

Dipartimento di Scienze Fisiche, Informatiche e Matematiche

DOTTORATO DI RICERCA IN PHYSICS AND NANOSCIENCES

Ciclo XXXIV

AUTOMATED ACCURATE DESCRIPTION OF RESPONSE FUNCTIONS IN LOW-DIMENSIONAL MATERIALS BY MANY-BODY PERTURBATION THEORY

Relatore:
Prof. Elisa MOLINARI

Candidato:
Dr. Miki BONACCI

Coordinatore del Corso di Dottorato:
Prof. Marco AFFRONTE

A.A. 2020/2021

The following Thesis was supervised by the main tutor Prof. Elisa Molinari, and co-supervised by Dr. Andrea Ferretti, Dr. Daniele Varsano and Dr. Deborah Prezzi, all Senior Researchers at Consiglio Nazionale delle Ricerche (CNR), Institute of Nanoscience, Modena (Italy).

La seguente Tesi ha come relatore principale la Prof. Elisa Molinari, e ha come correlatori il Dr. Andrea Ferretti, il Dr. Daniele Varsano e la Dr. Deborah Prezzi, Ricercatori Senior presso il Consiglio Nazionale delle Ricerche (CNR), Istituto di Nanoscienze, Modena (Italia).

Abstract in lingua italiana

In questa Tesi, schemi high-throughput (HT) e teoria delle perturbazioni a molti corpi (many-body perturbation theory, MBPT) sono combinati al fine di studiare le proprietà di stato eccitato di sistemi a bassa dimensionalità. In particolare, adottiamo l'approssimazione GW per studiare le strutture a bande elettroniche e l'equazione di Bethe-Salpeter (BSE) per calcolare gli spettri ottici.

La prima parte del lavoro è stata dedicata allo sviluppo di una serie di workflow per eseguire in maniera automatizzata simulazioni MBPT. Questo passaggio è stato essenziale nello sforzo di unire MBPT e schemi HT. I workflow sopra menzionati sono stati utilizzati in tutte le simulazioni mostrate in questo lavoro.

Il dataset GW100 è composto da 100 molecole ed é utilizzato per confrontare l'accuratezza dei principali codici MBPT, in termini di approssimazione G0W0. Per tutte le molecole abbiamo calcolato potenziale di ionizzazione e affinità elettronica, al fine di studiare l'accuratezza dell'approssimazione di plasmon-pole di Godby-Needs (GN-PPA) implementata in Yambo. I risultati di questo studio ci hanno permesso di concludere che la GN-PPA é più accurata di altre approssimazioni usate come il modello PPA di Hybertsen-Louie, e risulta in un accordo molto buono con implementazioni GW più sofisticate.

Il monolayer C_3N è un semiconduttore 2D a gap indiretto con interessanti proprietà meccaniche, termiche ed elettroniche. In questa tesi abbiamo eseguito una descrizione completa delle proprietà elettroniche e dielettriche del C_3N, concentrandoci sulla struttura a bande eccitoniche. Come per altri materiali 2D, troviamo una dispersione eccitonica lineare, che mostra tuttavia una convessità negativa, legata alla natura indiretta del band gap.

I workflow vengono quindi utilizzati per studiare le proprietà dielettriche di diverse configurazioni di grafene altamente idrogenato, corroborando i risultati ottenuti da due gruppi sperimentali, tra cui quello della Prof. Maria Grazia Betti e del Prof. Carlo Mariani dell'Università La Sapienza di Roma, e quello del Prof. Roberto Biagi e Prof. Valentina De Renzi all'interno del nostro Dipartimento di Fisica dell'Università di Modena e Reggio Emilia.

La parte finale di questa tesi è dedicata allo studio delle proprietà elettroniche ed ottiche di un gruppo di sistemi 2D recentemente scoperti, al fine di identificare eventuali materiali candidati che possano realizzare la fase di isolante eccitonico (EI), a lungo ricercata. La fase EI è una fase correlata della materia, proposta più

di 50 anni fa da L. Keldysh, W. Kohn, in cui lo stato fondamentale di un sistema, al di sotto di una temperatura critica, è formato da un condensato di Bose di eccitoni. Per fare previsioni sulle possibili instabilità eccitoniche nello stato fondamentale, sono indispensabili una stima molto accurata del band gap elettronico e delle energie di legame eccitoniche. Workflow in grado di eseguire calcoli automatici basati su MBPT costituiscono uno strumento estremamente efficace per questa ricerca. Un protocollo di screening é stato sviluppato e applicato con successo. In questa tesi verranno mostrati risultati preliminari molto promettenti.

Abstract

In this Thesis, high-throughput (HT) schemes and many-body perturbation theory (MBPT) are combined to study the excited state properties of low-dimensional systems. A set of workflows to automate MBPT calculations are developed and used for all the simulations contained in this work.

The GW100 dataset is composed of 100 molecules and used to benchmark the main MBPT codes by means of G0W0 approximation. For all the molecules we computed converged ionization potential and electron affinity, in order to study the accuracy of the Godby-Needs plasmon-pole approximation (GN-PPA) implemented in the Yambo code. The outcomes of this study allowed us to conclude that the GN-PPA scheme outperforms other commonly used approximations such as the Hybertsen-Louie plasmon pole model, and results in a reasonable agreement with more sophisticated GW implementation.

Monolayer C_3N is an emerging 2D indirect gap semiconductor with interesting mechanical, thermal, and electronic properties. In this Thesis we have performed a complete description of C_3N electronic and dielectric properties, focusing on the momentum-resolved excitonic band structure.

The workflows then are used to study electronic and optical properties a several highly hydrogenated graphene configurations, corroborating experimental results obtained by two experimental groups, including Prof. Maria Grazia Betti and Prof. Carlo Mariani at the Sapienza University in Roma, and Prof. Roberto Biagi and Prof. Valentina De Renzi within our Physics Department at the University of Modena and Reggio Emilia.

The final part of this Thesis is dedicated to the investigation of the electronic and optical properties of a subset of recently discovered 2D systems, in order to possibly identify candidate materials that can realize the long sought excitonic insulator (EI) phase. The EI phase is a correlated phase of matter, proposed more than 50 years ago by L. Keldysh, W. Kohn, in which the ground state of a system, below a critical temperature, is formed by a Bose condensate of excitons. Very accurate estimation of the electronic band gap and excitonic binding energies are crucial. Workflows capable of making automatic calculations based on MBPT constitute an extremely effective tool for this research. An ad-hoc screening protocol is developed and successfully applied: promising preliminary results are shown.

Contents

Introduction

In this Thesis I combine the power of high-throughput (HT) calculations with the accuracy of Many-Body Perturbation Theory (MBPT) to study the electronic and optical properties of low-dimensional systems. The work is focused on two-dimensional (2D) materials, where the electronic screening is reduced and the electronic and excitonic effects are strongly enhanced with respect to three-dimensional systems. Therefore I have adopted MBPT methods, including the GW approximation [1, 2, 3], to study the quasiparticle band structures, and the Bethe-Salpeter Equation (BSE) [4] to compute optical spectra. MBPT methods applied to 2D materials represent a computational challenge per se, typically involving several computationally expensive simulations. Concerning the simulation software, this challenge required a number of technical developments that I have addressed and accomplished during this Thesis work.

Since the rise of graphene [5, 6], two-dimensional (2D) materials attract ever increasing attention in materials science. The reduced dimensionality and high surface-volume ratio affect all the properties of these systems leading to unique features. For example, graphene is well known for its superior mechanical stability [7] and electron mobility [8], relevant for applications in optoelectronics, sensing, mechanical and energy storage technologies [9, 10, 11]. However, graphene is a zero band-gap semimetal, which limits its real application in digital electronic devices that usually require a semiconducting character. Hence we have assisted to a the great effort, from both theoretical and experimental communities, to find post-graphene layered materials with a finite band gap appropriate for selected applications. The list of candidates is very large [12, 13, 14] and includes, among others, transition metal dichalcogenides [15], phosphorene [16], and hexagonal boron nitride [17].

The HT computational screening of predicted properties is nowadays a fundamental resource in materials discovery [18, 19, 20], as a complementary and accelerating tool with respect to experimental approaches. In the last decades, several HT works were performed in various condensed matter and materials science research fields, e.g. for the discovery of novel 2D materials [21, 22, 12, 23, 13, 14, 24], the identification of optimal new lithium-ion battery anodes [25, 26], thermo-

electric [27, 28], photocatalysts [29] and photovoltaic light harvesting [30, 31] materials. The vast majority of the HT works performed up to now are based on Density Functional Theory (DFT), which allows very accurate predictions of total energies, optimized geometries and other ground state properties of materials. The success of these studies relies on the effort from the materials science community in the development of automated and robust workflows able to handle several calculations at the same time, by managing the input generation, submission and analysis of output data with the least possible human intervention [32, 33, 34, 35, 36, 37, 38, 39, 40].

The situation is different for the accurate prediction of excited-state properties of materials, such as quasiparticle band gaps and absorption spectra, which result from the interaction of matter with an external electromagnetic radiation, and are fundamental in order to determine the potential applications of materials in modern technologies, like light-emitting diodes (LEDs), photoelectrochemical [41] (PEC), photodetector [42, 43], laser diode [44](LD) and scintillator devices [45]. In this context, MBPT and Green's function methods represent the state-of-the-art to describe excited state properties of materials. In particular, charged (electronic quasi-particle levels) and neutral excitations (optical properties, EEL spectra) can be obtained by means of the GW approximation and BSE, respectively. Within DFT, basic simulations can be performed easily by non-experts of the field using different software and implementations [46], accuracy is guaranteed thanks to dedicated efforts oriented to encode years of experience of specialists into automated workflows enfording rigorous computational protocols [46, 47]. Conversely, GW-BSE calculations still require strong knowledge of both the theoretical and the computational sides in order to obtain accurate and reliable results.

From the methodological point of view, several flavours of the theory are proposed in many codes [48], concerning for example different approaches to treat the frequency dependence of the involved quantities [49, 50, 51, 52, 53, 54]. Convergence of GW-BSE calculations requires the control over a larger number of parameters with respect the DFT counterpart as for instance the dimension of the dielectric matrix in both GW and BSE, summation over empty bands in the polarizability and self-energy expression [1], frequency integrals, active valence-conduction space in BSE and **k**-point grid integrations. Moreover, some of the parameters to be converged turn out to be interdependent among each other. Often, model functions have to be considered to predict infinite basis extrapolations and converged parameters [60]. Moreover, in non self-consistent calculations, additional uncertainty comes from the well known problem of the starting point dependence (LDA, GGA, hybrid functionals) of the final results. [61, 62].

From the computational point of view, a typical GW-BSE flow is composed of several simulations, including for example the DFT preliminary part, several

[1] We note here that some GW implementations can avoid summation over empty states [55, 56, 57, 58, 59]

convergence steps and final production calculations. Memory requirements are much heavier than in standard DFT simulations, thus requiring, even for moderate system size, massive use of parallel computing resources. Calculations often fail due to memory overflow and have to be restarted with careful choice of parameters. All of these problems make MBPT not easy to automate within robust algorithms and workflows.

The first development described in this Thesis concerns the design and implementation of a set of algorithms and workflows for the automation of all the simulations, i.e. with no need of human supervision. These workflows take care of several procedures, from error detection/handling to convergence evaluation of many-body quantities like, e.g., quasiparticle energy levels. I have implemented such procedures in the YAMBO plugin for the AiiDA platform [35, 39] and they have been validated on a few representative semiconductor and metallic systems. *These workflows are used to run all the simulations performed throughout this Thesis*, and are the subject of a paper that is currently in preparation [63].

Other technical developments are related to the implementation of memory optimization procedures in GW simulations, all oriented towards a massive use of GPU-enabled HPC machines, and critical for the treatment of low-dimensional systems studied in this Thesis. All these GPU-oriented developments are included in the YAMBO code, a large-scale open-source community software implementing GW and BSE [64, 65]. Throughout this work, I have greatly benefited from the insight and collaboration of the YAMBO developer team which has a strong component in Modena. Combining the GPU-oriented developments with the implementation of the above mentioned workflows, we provided the benchmark of the YAMBO code against the GW100 dataset of molecules [66] for what concerns the quasiparticle evaluation the vertical ionization potential (IP) and the vertical electron affinity (EA). This enlarges the different numerical implementations of the GW-codes that run the GW100 set, as we adopt the Godby-Needs plasmon pole approximation (GNPPA) [53] for the first time.

For what concerns the systems studied, I have applied the above methodology to a GW+BSE study of C_3N, a graphene-like 2D system synthesized for the first time in 2016 [67] with interesting mechanical [68, 69] and thermal [70, 71] properties. I focused the study on the so-called momentum-resolved exciton band structure. Excitation energies and oscillator strengths are computed in order to characterize bright and dark states, and discussed also with respect to the crystal symmetry. This work has been the subject of a dedicated publication [72], providing insights into finite-momentum excitonic features in 2D systems.

Next, I have studied a class of highly hydrogenated free-standing graphene-based systems, where unprecedented level of hydrogenation was achieved by two experimental groups including Prof. Maria Grazia Betti and Prof. Carlo Mariani at the Sapienza University in Roma, and Prof. Roberto Biagi and Prof. Valentina De Renzi within our Physics Department at the University of Modena and Reggio Emilia. GW and BSE calculations for the quasiparticle energy bands, the density

of states and the absorption spectra were used to characterize the candidate structures, the band gap opening associated with hydrogenation as well as excitonic effects. This collaboration resulted in a publication [73] and another paper is in preparation [74].

Finally, I focused on a subset of the recently generated Material Cloud 2D materials database (MC2D) [13], developed by the THEOS-MARVEL group at EPFL (Lausanne, CH) [12]. Here, I specifically designed and applied an ad-hoc screening protocol, in order to identify possible candidate materials that can realize the long sought excitonic insulator (EI) phase [75, 76], a macroscopic quantum coherent state made of excitons which spontaneously form and condense at thermodynamic equilibrium. In this phase, excitons are expected to collectively enforce a many-body gap by sharing the same wave function, akin to Cooper pairs in the superconductor [77, 78]. The excitonic insulator phase might thus display new, intriguing forms of macroscopic quantum coherence [79, 80, 81, 82]. The work is performed in strict collaboration with the THEOS-MARVEL group, where I spent a fruitful visiting period of three months under the supervision of Prof. Nicola Marzari and Dr. Giovanni Pizzi. The work is still in progress: in this Thesis I only show preliminary, but very promising, results.

The Thesis is organized as follows. In the first part, the theoretical methodologies used in this work are briefly summarized, namely Density Functional Theory in Chapter 1 and Many-Body Perturbation Theory in Chapter 2. Then, in the second part, the technical developments are presented. Chapter 3 describes the development and implementation of the automated MBPT workflows; then in Chapter 4 additional GPU-oriented optimizations of the YAMBO code are shown and validated by means of the GW100 dataset benchmark.

The final part of the Thesis is devoted to the results obtained using the tools developed in the previous chapters to study different set of systems, in collaboration with several other members of the team in Modena (at the University and at Nanoscience Institute of CNR). The electronic and optical properties of C_3N are shown in Chapter 5, and the results on highly hydrogenated graphene in Chapter 6. Eventually, Chapter 7 concerns the preliminary outcomes of the search for novel 2D excitonic insulators among the ones belonging to the MC2D.

Part I

Theoretical methodologies

Atoms, molecules, clusters, solids are constituted by mutually interacting ions and electrons. Interaction is driven by the Coulomb potential between charged particles. The dynamics of these particles, in general, cannot be considered separately (they interact) and is described by an Hamiltonian of the following type:

$$\begin{aligned} H =& \sum_{i}^{N} \frac{\mathbf{p}_i^2}{2m} + \sum_{I}^{N'} \frac{\mathbf{P}_I^2}{2M} - \sum_{i}^{N} \sum_{I}^{N'} \frac{Z_I e^2}{|\mathbf{r}_i - \mathbf{R}_I|} + \frac{1}{2} \sum_{i \neq j}^{N} \frac{e^2}{|\mathbf{r}_i - \mathbf{r}_j|} \\ &+ \frac{1}{2} \sum_{I \neq J}^{N'} \frac{Z_I Z_J e^2}{|\mathbf{R}_I - \mathbf{R}_J|} \\ =& T_e + T_I + V_{I-e} + V_{e-e} + V_{I-I} \end{aligned} \tag{1}$$

this is the total non-relativistic Hamiltonian of a system of N electrons of coordinates $\mathbf{r}_i$, momenta $\mathbf{p}_i$, charge -e, and N′ ions of coordinates $\mathbf{R}_i$, momenta $\mathbf{P}_i$, charge $Z_I e$. Respectively, T_e, T_I, V_{I-e}, V_{e-e} and V_{I-I} are the electronic, nuclei kinetic energies and the nuclei-electron, electron-electron and nuclei-nuclei interacting terms. Despite the simple structure of Eq. 1, the problem becomes easily prohibitive to be solved as the number of particles increases, and becomes impossible to be treated exactly for solids: approximations have to be applied. The first simplification of the problem is given by the Born-Oppenheimer approximation [83]: it is possible to separate the dynamics of electrons and nuclei. Indeed, nuclei are much heavier than electrons (about three order of magnitude): the nuclei can be then considered frozen and their positions enters in Eq. 1 only in a parametric way, and so the ionic kinetic term T_I can be neglected. In this way, we can study separately the electronic problem, the one which we are interested in during this work. The many-body Hamiltonian for n interacting electrons then becomes:

$$H_e = T_e + V_{I-e} + V_{e-e} \tag{2}$$

where we have further neglected the contribution from the ion-ion interactions, as, for fixed ionic configurations, it is just a constant [2]. Equation 2 embodies the electronic structure problem, where the only system-dependent term is V_{I-e}, the other two being in principle universal for all problems. The many-body problem then reads:

$$H_e \Psi_0(\mathbf{r}_1\sigma_1, \mathbf{r}_2\sigma_2, ..., \mathbf{r}_N\sigma_N) = E\Psi_0(\mathbf{r}_1\sigma_1, \mathbf{r}_2\sigma_2, ..., \mathbf{r}_N\sigma_N) \tag{3}$$

where E is the total energy of the electronic system and $\Psi_0(\mathbf{r}_1\sigma_1, \mathbf{r}_2\sigma_2, ..., \mathbf{r}_N\sigma_N)$ is the many-body N-electron ground-state (GS) wavefunction. The main difficulty

[2] Anyway, the term has to be considered if we want to compute total energies of the systems or its cohesive energies.

of the problem is the calculation of this wavefunction, which does not factorize exactly in the product of single-particle orbitals due to electron-electron interactions V_{e-e}.

The problem can be reformulated in a variational scheme: one searches for the minimum of a certain quantity (typically the total energy) optimizing the GS wavefunction. The pioneering approach to solve Eq.3 is the Hartree theory[84], where the Ψ_0 is represented by the best simple product of n one electron spin-orbitals. The next major improvement, that correctly embodies the Pauli exclusion principle for identical fermions, is the Hartree-Fock theory[85], where the wavefunction is represented by the best antisymmetrized product of n one-electron spin-orbitals (a single *Slater determinant*). Multi-reference Hartree–Fock is a generalization to a sum of a few Slater determinants (or configurations) that are especially important.

In Density Functional Theory (DFT) instead, the emphasis shifts from the GS wavefunction to the much more manageable GS one-body electronic density $n(\mathbf{r})$. DFT shows that the GS energy of a many-particle system can be expressed as a functional of the one-body density; the minimization of this functional allows in principle the determination of the actual GS density and all the other GS properties. The success of the theory stands on its rigorous formulation and on the concomitant possibility to provide reasonably simple and accurate approximation of the functional to be minimized. The peculiarity of the density functional approach to the many-body theory is to attain a one-electron Schrödinger equation with a local effective potential for the study of the GS electronic density of the many-electron system.

Anyway, when one wants to go beyond and study excited states properties, it is necessary to rely on more advanced theories that approach one- and two- particle excitations in a proper way. These methods belong to Many-Body Perturbation Theory.

Chapter 1

Density Functional Theory

Mean Field theories approach the many-body problem by considering an effective one-body interaction that is, in principle, an average over all the possible interactions that can happen in a material or, more generally, in a physical system. For example, in Density Functional Theory (DFT) [86, 87] the interacting system is mapped into a non-interacting one responding to an effective external potential by virtue of the Hohenberg-Kohn (HK) theorems [88].

1.1 Hohenberg-Kohn theorems

Consider a system of N electrons, described by the many-electron Hamiltonian Eq. 3. For simplicity, we can suppose that the Ground-State (GS) of the system Ψ_0 is non-degenerate (but anyway this condition can be relaxed [89, 90, 91]). DFT is based on the HK theorems, relating the GS of a system and its electronic density [1]. The first Hohenberg-Kohn theorem states that *there is a one-to-one correspondence between the GS density of an N-electron system and the external potential* v_{ext} *acting on it*; in this sense, the GS electron density becomes the variable of interest. Here, v_{ext} is given by the electrons-ions interactions (V_{I-e} in Eq. 1), and its knowledge allows (in principle) to solve the associated Schrödinger equation and compute the exact eigenfunctions and eigenvalues of the electronic problem; then, the GS electronic density $n(\mathbf{r})$ can be obtained:

$$v_{ext}(\mathbf{r}) \Longrightarrow \Psi_0[v_{ext}] \Longrightarrow n(\mathbf{r}) \tag{1.1}$$

In practice, there exists a functional F that links $n(\mathbf{r})$ and v_{ext}, and we can write:

$$n(\mathbf{r}) = F[v_{ext}] \tag{1.2}$$

The real novelty of the first HK theorem is the possibility to revert Eq. 1.2:

$$v_{ext} = G[n(\mathbf{r})] \tag{1.3}$$

[1] Their proof can be found in several books [87, 92].

meaning that from the knowledge of $n(\mathbf{r})$ we can determine uniquely v_{ext}, the Hamiltonian and in principle any other property of the system. Thus, due to the first HK theorem, we have that the GS energy E_0 is a functional of the GS density $n(\mathbf{r})$. A most important consequence is the second HK theorem, a reformulation of a variational principle concerning the GS density of a system. We can construct the functional:

$$\begin{aligned} E^{HK}[n(\mathbf{r}), v_{ext}(\mathbf{r})] &= \langle \Psi[n] | \, T_e + V_{e-e} + v_{ext} \, | \Psi[n] \rangle \\ &= T[n(\mathbf{r})] + V_{e-e}[n(\mathbf{r})] + \int v_{ext}(\mathbf{r}) n(\mathbf{r}) d\mathbf{r} \end{aligned} \tag{1.4}$$

the absolute minimum of this energy functional occurs when $\Psi[n]$ is the GS operator of the corresponding Hamiltonian $\Psi_0[n]$, i.e. when $n(\mathbf{r})$ is the exact electron density of the system. Moreover, the functional $F[n] = T[n(\mathbf{r})] + V_{e-e}[n(\mathbf{r})]$ is universal, i.e. it does not depend on v_{ext}: it is the same for all electron systems. However, in general $F[n]$ is not known and must be approximated in some way.

1.2 Kohn-Sham equations

The Kohn-Sham (KS) equations [93] represent a simple and effective method to overcome the problem of the knowledge of the functional $F[n]$ of the interacting electron system. The solution proposed by Kohn and Sham is based on the assumption that, for each non-uniform GS density $n(\mathbf{r})$ of an interacting electron system, there exist a non-interacting electron system with the same non-uniform GS density, i.e. with the same external potential v_{ext}, by virtue of HK theorems. The existence of this auxiliary KS non-interacting system allows to decompose exactly the $n(\mathbf{r})$ of the interacting electron system into the sum of n independent orbital contribution of the form:

$$n(\mathbf{r}) = \sum_i \phi_i^*(\mathbf{r}) \phi_i(\mathbf{r}) \tag{1.5}$$

where $\phi_i(\mathbf{r})$ are orthonormal orbitals. It is possible to rewrite the HK functional of Eq.1.4 as:

$$E^{HK}[n(\mathbf{r}), v_{ext}(\mathbf{r})] = T[n(\mathbf{r})] + V_H[n(\mathbf{r})] + E_{xc}[n(\mathbf{r})] + \int v_{ext}(\mathbf{r}) n(\mathbf{r}) d\mathbf{r} \tag{1.6}$$

where we separated V_{e-e} into the contribution coming from the Hartree energy functional

$$V_H[n(\mathbf{r})] = \frac{1}{2} \int n(\mathbf{r}) \frac{e^2}{|\mathbf{r} - \mathbf{r}'|} n(\mathbf{r}') d\mathbf{r}' \tag{1.7}$$

and the exchange-correlation functional $E_{xc}[n(\mathbf{r})]$, defined as:

$$E_{xc}[n(\mathbf{r})] = F[n(\mathbf{r})] - T[n(\mathbf{r})] - V_H[n(\mathbf{r})] n(\mathbf{r}) d\mathbf{r} \tag{1.8}$$

it includes all the exchange (effects due to the fermionic nature of the electrons) and correlation effects, and is not known a priori. Performing a variational calculation of the functional Eq. 1.6 leads to the Kohn-Sham equations:

$$\left[-\frac{\hbar^2}{2m}\nabla^2 + v_{ext}(\mathbf{r}) + V_H(\mathbf{r}) + V_{xc}(\mathbf{r})\right]\phi_i(\mathbf{r}) = \epsilon_i\phi_i(\mathbf{r}) \tag{1.9}$$

Where $V_{xc} \equiv \delta E_{xc}/\delta n(\mathbf{r})$ is the functional derivative of the exchange-correlation functional with respect to the density. These KS equations are non-linear differential equations with a local effective potential $V_{eff}(\mathbf{r}) = v_{ext}(\mathbf{r}) + V_H(\mathbf{r}) + V_{xc}(\mathbf{r})$. They have to be solved self-consistently since the potential is a functional of the density: starting with a general approximation of the solution $\{n^0, \phi_i^0\}$, the KS effecttive potential is computed, then KS equations are solved the new output solution $\{n^1, \phi_i^1\}$ is constructed. The cycle is repeated until the convergence of the total energy (or the density) of the system is achieved.

1.3 Practical DFT

KS-DFT is an in-principle-exact method for the calculation of the ground-state density and energy. Of course, for practical calculations some approximations and choices have to be done, for example in the determination of the XC functional, the KS-wavefunctions basis-set expansion, and the description of the valence-core interaction. These lead to different implementations of the theory, i.e. different numerical procedures and software that can be used to study the same properties.

1.3.1 Approximated Exchange-Correlation functionals

The only difficulty in solving Eqs. 1.9 is confined in a reasonable guess of E_{xc}. The most popular one was introduced in the original work by Kohn and Sham [93] and is the local density approximation (LDA), which is particularly justified for systems with slowly varying spatial density (for example, the homogeneous electron gas). Within LDA, the exchange correlation functional is approximated in the form:

$$E_{xc}^{LDA}[n(\mathbf{r})] = \int \epsilon_{xc}^{HEG}(n(\mathbf{r}))n(\mathbf{r})d\mathbf{r} \tag{1.10}$$

where $\epsilon_{xc}(n(\mathbf{r})))$ is the many-body exchange-correlation energy per electron of a uniform gas of interacting electrons of density n(r) and its correlation part can be approximated in different ways, for example by Perdew and Zunger [94] was parameterized using Quantum Monte Carlo results [95]. Its exchange part is just the analytic function of the density [96]:

$$\epsilon_c^{HEG}(n(\mathbf{r})) = -\frac{3}{4}\left[\frac{3n}{\pi}\right]^{1/3}. \tag{1.11}$$

The LDA assumes that the density is the same everywhere. Because of this, the LDA has a tendency to underestimate the exchange energy and over-estimate the correlation energy [97]. The errors due to the exchange and correlation parts tend to compensate each other to a certain degree. To correct for this tendency, it is common to expand in terms of the gradient of the density in order to account for the non-homogeneity of the true electron density. This allows corrections based on the changes in density away from the coordinates. These expansions are referred to as generalized gradient approximations (GGA) [98] and have the following form:

$$E_{xc}^{GGA}[n(\mathbf{r})] = \int \epsilon_{xc}(n(\mathbf{r}), \nabla n(\mathbf{r}))n(\mathbf{r})d\mathbf{r} \tag{1.12}$$

The reason KS-DFT is so successful is that even very simple approximate functionals can be remarkably accurate for ground-state properties of many systems. In this work, we used both GGA and LDA approximations for the description of E_{xc} of the system studied.

1.3.2 The pseudopotential approach

The many-electron Schrödinger equation can be very much simplified if electrons are divided in two groups: valence and core electrons. The electrons in the inner shells are strongly bound to the nucleus and so do not participate significantly in the chemical binding of atoms, forming with the nucleus an (almost) inert core. Binding properties are fundamentally addressed to valence electrons. This separation suggests that core electrons can be safely neglected in a large number of cases, thereby simplifying the atom to an ionic core that interacts with the valence electrons. The use of an effective interaction, a *pseudopotential*, that approximates the potential felt by the valence electrons, was first proposed by Fermi in 1934 [99], and then used extensively since the works of Phillips and Kleinman [100, 101]. Consider the exact solution of the Schrödinger equation for core and valence electrons, respectively (E_c, $|\psi_c\rangle$ and (E_v, $|\psi_v\rangle$)). Following Ref. 102, valence orbitals can be written as the sum of a smooth function (called the pseudo-wavefunction), $|\phi_v\rangle$, with an oscillating function that results from the orthogonalization of the valence to the inner core orbitals

$$|\psi_v\rangle = |\phi_v\rangle + \sum_c \alpha_{cv} |\psi_c\rangle \tag{1.13}$$

where $\alpha_{cv} = -\langle\psi_c|\phi_v\rangle$. The Schrödinger equation for the smooth orbital $|\phi_v\rangle$ leads to

$$\hat{H}|\psi_v\rangle = E_v|\phi_v\rangle + \sum_c (E_c - E_v)|\psi_c\rangle\langle\psi_c|\phi_v\rangle \tag{1.14}$$

Then the pseudo-wavefunctions satisfy a Schrödinger equation with an pseudo-Hamiltonian:

$$\hat{H}^{PK}(E) = \hat{H} - \sum_c (E_c - E) \left|\psi_c\right\rangle \left\langle\psi_c\right| . \tag{1.15}$$

It is possible to define the pseudopotential $\hat{v}^{PK}$ as:

$$\hat{v}^{PK} = \hat{v} - \sum_c (E_c - E) \left|\psi_c\right\rangle \left\langle\psi_c\right| \tag{1.16}$$

where $\hat{v}$ is the true potential, as the effective potential in which valence electrons move. This pseudopotential is non-local and depends on the eigenenergies of the electronic states. At a certain distance from the ionic core $\hat{v}^{PK}$ becomes $\hat{v}$ due to the decay of the core orbitals. In the region near the core, the orthogonalization of the valence orbitals to the strongly oscillating core orbitals forces valence electrons to have a high kinetic energy (The kinetic energy density is essentially a measure of the curvature of the wavefunction). The valence electrons feel an effective potential which is the result of the screening of the nuclear potential by the core electrons, the Pauli repulsion and xc effects between the valence and core electrons. The second term of Eq. 1.16 represents then a repulsive potential, making the pseudopotential much weaker than the true potential in the vicinity of the core. All this implies that the pseudo-wavefunctions will be smooth and will not oscillate in the core region, as desired. A consequence of the cancellation between the two terms of Eq. 1.16 is the surprisingly good description of the electronic structure of solids given by the nearly-free electron approximation. The fact that many metal and semiconductor band structures are a small distortion of the free electron gas band structure suggests that the valence electrons do indeed feel a weak potential.

Ab-initio Norm-Conserving pseudopotential

Empirical pseudopotentials, fitted from experimental data, were proposed in the 60's [103, 104, 105]. The main application of these model potentials was the theory of metallic cohesion [106]. A crucial step toward realistic pseudopotentials was given by Topp and Hopfield [107], who suggested that the pseudopotential should be adjusted such that they describe the valence charge density accurately. Based on that idea, modern pseudo-potentials are obtained inverting the free atom Schrödinger equation for a given reference electronic configuration [108], and forcing the pseudo-wavefunctions to coincide with the true valence wavefunctions beyond a certain distance r_l. The pseudo-wavefunctions are also forced to have the same norm as the true valence wavefunctions. These conditions can be written as

$$\begin{aligned} R_l^{PP}(\mathbf{r}) &= R_{nl}^{AE}(\mathbf{r}) && \text{if } r > r_l \\ \int_0^{r_l} dr |R_l^{PP}(\mathbf{r})|^2 r^2 &= \int_0^{r_l} dr |R_{nl}^{AE}(\mathbf{r})|^2 r^2 && \text{if } r < r_l \end{aligned} \tag{1.17}$$

where $R_l(\mathbf{r})$ is the radial part of the wavefunction with angular momentum l, and PP and AE denote, respectively, the pseudo-wavefunction and the true all-electron wave-function. The index n in the true wave-functions denotes the valence level. The distance beyond which the true and the pseudo-wavefunctions are equal, x_l, is also l-dependent. Besides Eq. 1.17, there are still two other conditions imposed on the pseudopotential: the pseudo-wavefunctions should not have nodal surfaces and the pseudo energy-eigenvalues should match the true valence eigenvalues: $\epsilon_l^{PP} = \epsilon_{nl}^{EA}$. The potentials thus constructed are called *norm-conserving* pseudopotentials, and are semi-local potentials that depend on the energies of the reference electronic levels, ϵ_l^{EA}. In summary, to obtain pseudopotentials, the procedure is:

1. Solve the free atom KS radial equations with an AE calculation;
2. determination of the pseudo-wavefunctions using norm-conservation;
3. compute the pseudopotential by inverting the KS equation for the pseudo-wavefunctions and the valence electron density.

One of the most used parameterization for the pseudo-wavefunction is the one proposed in 1979 by Hamann, Schlüter and Chiang [109]. The method proposed consists of using an intermediate pseudopotential:

$$\bar{V}(\mathbf{r}) + V_H[n^{PP}](\mathbf{r}) + V_{xc}[n^{PP}](\mathbf{r}) = V_{KS}^{AE}[n^{AE}](\mathbf{r}) \left[1 - f\left(\frac{r}{r_l}\right)\right] + c_l f\left(\frac{r}{r_l}\right) \quad (1.18)$$

where $f(x) = e^{-r^\lambda}$, λ=4.0 in Ref. 109. The parameters c_l are adjusted by imposing the equality between the logarithmic derivatives:

$$\frac{d}{dr} ln[r R_{nl}^{AE}(r)]|_{r=\tilde{r}_l} = \frac{d}{dr} ln[r \bar{R}_{nl}(r)]|_{r=\tilde{r}_l} \quad (1.19)$$

To impose norm-conservation, the final pseudo wavefunctions, $R^{PP}(r)$ are defined as a correction to the intermediate wave-functions

$$R_l^{PP}(r) = \gamma_l[\bar{R}_l(r) + \delta_l g_l(r)] \quad (1.20)$$

where γ_l is the ratio $R^{AE}(r)/\bar{R}_l(r)$ in the region where $r > \tilde{r}_l$ and $g_l(r) = r^{l+1} f(r/r_l)$. The constants δ_l are adjusted to conserve the norm. Fig. 1.1 shows the Hamann pseudopotential for Al, with $\mathrm{r}_0 = 1.24$, $\mathrm{r}_1 = 1.54$ and $\mathrm{r}_2 = 1.40$ bohr. Note that the true and the pseudo wavefunctions do not coincide at r_l – this only happens at $r > \tilde{r}_l$. In this work, we used optimized norm-conserving pseudopotentials [110], in particular the SG15 [111] and the Pseudo-Dojo [112] families (the latter only for the study of ZnO). The latter one also implements the non-linear core corrections, described in the next section.

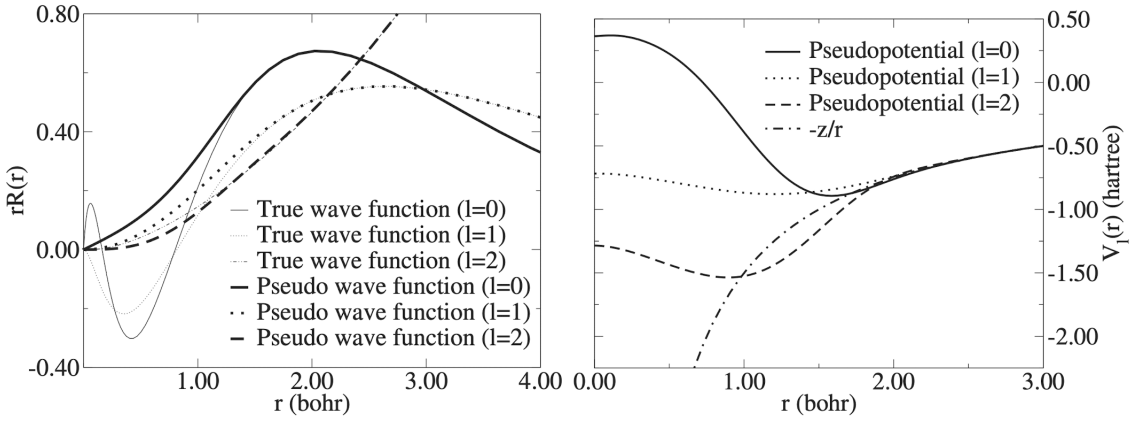

Figure 1.1: Hamann pseudopotential for Al, with $r_0 = 1.24$, $r_1 = 1.54$ and $r_2 = 1.40$ bohr: pseudo wave-functions vs. true wave-functions (left) and pseudopotentials (right). Figure adapted from Ref. 102.

Non-linear core corrections

A fundamental but implicit approximation that we made up to now is the fact that we are considering all the quantities in Eqs. 1.9 without the contribution of the core charge density n^c. This means that we consider all the quantities linearly dependent on the total charge density, factoring out the n^c contribution very straightforwardly. However, the xc term is not linearly dependent on the charge density:

$$V_{xc}[n^{AE}](\mathbf{r}) \equiv V_{xc}[n^{core} + n^{PP}](\mathbf{r}) \neq V_{xc}[n^{core}](\mathbf{r}) + V_{xc}[n^{PP}](\mathbf{r}) \tag{1.21}$$

The problem is that, due to the non linearity of the V_{xc}, the ionic resulting pseudopotential is dependent on the valence configuration, as the real valence contribution is not exactly factored out. These corrections are more important for the alkali metals and other elements with few valence electrons and core orbitals extending into the tail of the valence density (e.g., Zn and Cd). A new method for generating and using ab-initio pseudopotentials treating explicitly the nonlinear xc interaction between the core and the valence electrons was first proposed by Louie, Froyen and Cohen in 1982 [113], leading to significant improvement in the transferability of the potential. In particular, the spin-polarized configurations are well described with a single potential.

1.3.3 DFT in plane-waves basis set

Electronic properties of solids, by solving the KS equations, can be obtained once an appropriate basis set is given to expand the Kohn-Sham wave-functions. Common choice is the usage of plane-wave (PW) basis sets, as easily accounting

for the periodicity of the crystal by means of the Bloch theorem [92, 114]. This means that a Bloch-like electronic wavefunction for the n-th bands and wavevector $\mathbf{k}$ can be expanded in this basis as:

$$\phi_{n\mathbf{k}}(\mathbf{r}) = \frac{1}{\sqrt{\Omega}} e^{i\mathbf{k}\cdot\mathbf{r}} \sum_{\mathbf{G}} C_{n\mathbf{k}}(\mathbf{G}) e^{i\mathbf{G}\cdot\mathbf{r}} = e^{i\mathbf{k}\cdot\mathbf{r}} u_{n\mathbf{k}}(\mathbf{r}) \tag{1.22}$$

where $\mathbf{k}$ is restricted to the First Brillouin Zone (BZ) and $\mathbf{G}$ is a reciprocal lattice vector. The function $u_{n\mathbf{k}}(\mathbf{r})$ expresses the periodicity of the crystal lattice. Ω is the volume of the unit cell describing the system. Moreover, the translational invariance of the potential allows us to express the KS Hamiltonian as:

$$h_{\mathbf{G}\mathbf{G}'} = \frac{1}{2}|\mathbf{k}+\mathbf{G}|^2\delta_{GG'} + v(\mathbf{k}+\mathbf{G}, \mathbf{k}+\mathbf{G}') + v_H[n](\mathbf{G}-\mathbf{G}') + v_{xc}[n](\mathbf{G}-\mathbf{G}') \tag{1.23}$$

where the kinetic term is diagonal, and the Hartree term is analytical (just consider the Poisson's equation $\nabla^2 V(\mathbf{r}) = 4\pi n(\mathbf{r})$ in reciprocal space):

$$v_H[n](\mathbf{G}) = 4\pi \frac{n(\mathbf{G})}{G^2}. \tag{1.24}$$

The KS equations now read:

$$\sum_{\mathbf{G}'} \hat{h}_{\mathbf{G}\mathbf{G}'}(\mathbf{k}) c_{n\mathbf{k}}(\mathbf{G}') = \epsilon_{n\mathbf{k}} c_{n\mathbf{k}}(\mathbf{G}) \tag{1.25}$$

In principle, the plane-wave basis is a complete set, and so the expansion of whatever quantity should be exact. In practice, we have to choose a cutoff up to we stop the expansion, to perform real calculations. This parameter is chosen to be the cutoff in energy to which corresponds the kinetic energy for an electron of momentum $|\mathbf{k}+\mathbf{G}|$:

$$\frac{1}{2}|\mathbf{k}+\mathbf{G}|^2 \leq E_{cutoff} \tag{1.26}$$

The number of plane waves involved in the calculation scales as $\Omega_{cell} \times E_{cutoff}^{3/2}$, where Ω_{cell} is the volume of the unit cell. Fast convergence in PW basis calculations can be obtained using smooth pseudopotentials. Localized Gaussian basis sets, on the contrary, do not provide a clear and systematic way to improve the convergence of the calculations and do not form an orthonormal set. As a result, the calculations often depend on the choice of basis set. For low-dimensional or finite systems, such as atoms, molecules and clusters, plane-waves can also be used in a supercell approach. A large amount of vacuum along non-periodic directions is added to the unit cell (now a supercell), in such a way to avoid spurious interactions among cell replica along non periodic directions, then the system is treated as a 3D one. A truncation of the Coulomb interaction can be applied to reduce the volume of the supercell (i.e. the amount of vacuum required), as described in Appendix C.3 and Ref. 115. In this work, all DFT simulations are performed using the QUANTUM ESPRESSO simulation package [116, 117], implementing PW basis set and pseudopotential approach.

1.3.4 The band gap problem

The band gap of an N electron system is defined as the difference between the ionization potential IP = $E^0_{N-1} - E^0_N = -E_{HOMO}$ the electron affinity EA = $E^0_N - E^0_{N+1}$ = $-E_{LUMO}$:

$$E_{gap} = IP - EA = E_{LUMO} - E_{HOMO} \tag{1.27}$$

where HOMO and LUMO stand, respectively, for highest occupied and lowest unoccupied molecular orbital. So, the gap is just the difference between two single-electron removal/addition energies, so it is immediately addressed by Many-Body Perturbation Theory (MBPT), the main theory applied in this work. The quantity E_{gap} can also be calculated by means of KS-DFT energies ϵ_i^{KS}:

$$E_{gap} = \epsilon^{KS}_{N+1}(N+1) - \epsilon^{KS}_N \tag{1.28}$$

being ϵ^{KS}_{N+1}(N+1) is the energy of the highest occupied KS orbital of the N+1 electron system, and ϵ^{KS}_N(N) the HOMO level of the N electron system. Indeed, the affinity of an N electron system is the opposite of the ionization potential of the N + 1 electrons, and that the Kohn-Sham HOMO level equals the actual one (this is the only KS energy with an explicit physical meaning). For a non-interacting system, the gap can be readily written in terms of its orbital energies. Therefore, for the fictitious N electron KS system we have

$$E^{KS}_{gap} = \epsilon^{KS}_{N+1} - \epsilon^{KS}_N \tag{1.29}$$

which is well-known to be an underestimation of the real band gap of a system [118]. This failure is related to a pathological non-analytical behaviour of the *true* xc energy functional. Namely, the xc potential may be increased by a finite constant of the order of the eV as a result of the addition of an extra electron to an extended system, that is, after an infinitesimal change of the electron density. Indeed, we can relate the real and the KS gap as

$$E_{gap} = (\epsilon^{KS}_{N+1} - \epsilon^{KS}_N) + (\epsilon^{KS}_{N+1}(N+1) - \epsilon^{KS}_{N+1}) = E^{KS}_{gap} + \Delta_{xc} \tag{1.30}$$

relation also depicted in Fig. 1.2. Δ_{xc} is just the difference between the energies of the (N + 1)-th orbitals of the KS systems that correspond to the neutral and ionised electron systems, and it is a finite variation of $V_{xc}(\mathbf{r})$ due to and infinitesimal variation of n($\mathbf{r}$):

$$\Delta_{xc} = \left(\left.\frac{\delta E_{xc}[n]}{\delta n(\mathbf{r})}\right|_{N+1} - \left.\frac{\delta E_{xc}[n]}{\delta n(\mathbf{r})}\right|_{N} \right) + O\left(\frac{1}{N}\right) \tag{1.31}$$

Now it is easy to see the relation between a non-analytical $V_{xc}(\mathbf{r})$ and the band gap problem. If $V_{xc}(\mathbf{r})$ were actually discontinuous, the actual band gap would not be

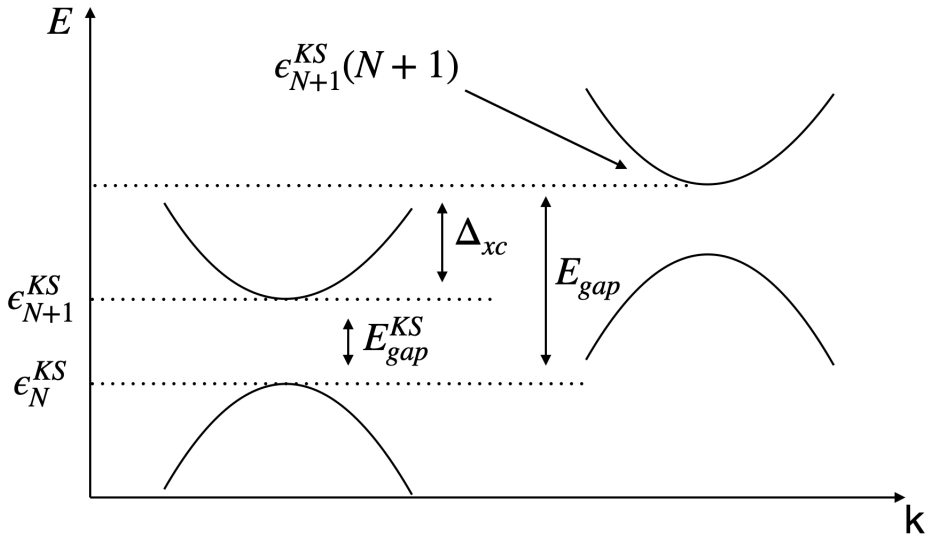

Figure 1.2: Sketch of the KS band structure before and after the addition of the Δ_{xc} term.

given in terms of the KS energies of the N electron system. On the contrary, if Δ_{xc} were zero (or very close to zero), the difference between the actual gap and the KS-DFT one would be just an inherent limitation of the LDA/GGA approximations. Godby showed in 1988 [119] that indeed the main cause of discrepancy between the real and KS band gap has to be addressed to the discontinuity Δ_{xc}, so to intrinsically the KS scheme rather than DFT itself or LDA. The band gap of a system, as well as its full band structure, can be accurately reproduced by means of MBPT, specifically within the GW approximation. This will be the object of the next chapter.

Chapter 2

Many-Body Perturbation Theory

In matter, a moving electron interacts with the surrounding medium (i.e. other electrons, ions etc.) by means of the bare Coulomb interaction $v(|\mathbf{r}-\mathbf{r}'|)$. Following the concept of *quasiparticle* [120, 96, 121], it is possible to consider a new entity composed of the electron plus its surrounding screening cloud. The quasiparticle is then a weakly interacting particle where the interaction is mediated by the screened Coulomb potential $W(\mathbf{r},\mathbf{r}',t-t')$, which allows us to describe the interaction in terms of perturbative expansions, from which the name "Many-Body Perturbation Theory" [96]. A systematic method to solve Schrödinger equation to all order in perturbation theory is possible if we adopt the Green's function approach.

2.1 Response functions

The aim of MBPT is to study how the system behaves under the action of an external perturbation (in general weak). This perturbation can induce a finite polarization, due to charge redistribution, charge/spin density waves, plasmonic excitations. The quantity that describes this response of the system is called *response function*. Considering a generic Hamiltonian $\hat{H} = \hat{H}_0 + \hat{H}_1(t)$, where[1] $\hat{H}_1(t) = \theta(t)\hat{H}_1(t)$ is the perturbed, time- (but also, generally, space-) dependent part of the Hamiltonian, the response functions describe the change in the expectation value of an operator $\hat{O}(t)$[2]. If we limit ourselves to *linear response theory*[3], where we consider only the first-order response function, we obtain the *Kubo formula* [96, 121]:

$$\delta \langle N|\, \hat{O}(t)\, |N\rangle = \int_0^t dt' \, \langle N|\, [\hat{H}_1(t'), \hat{O}(t)]\, |N\rangle \tag{2.1}$$

[1] We define $\theta(t)$ as the Heaviside step function.

[2] We consider the operator in the Heisenberg representation. See Eq. A.3

[3] This is the regime where most of the spectroscopic measurements are performed.

which describes the variation of an observable at time t due to a perturbation switched on at time $t = 0$. We may here explicit a general form of the interacting part of the Hamilatonian as $\hat{H}_1(t) = \int d\mathbf{r}\ \phi(\mathbf{r})\hat{B}(\mathbf{r})$, where $\phi(\mathbf{r}, t)$ is the external perturbation and $\hat{B}(\mathbf{r})$ is an operator acting on the system. In this way we can rewrite Eq. 2.1 as:

$$\delta \langle N| \hat{O}(t) |N\rangle = \int dt' \int d\mathbf{r}\ \chi(\mathbf{r}, \mathbf{r}', t - t')\phi(\mathbf{r}, t') \tag{2.2}$$

where we have defined a (*retarded*) correlation function $\chi(\mathbf{r}, \mathbf{r}', t-t')$, the so called *linear response function*:

$$\chi(\mathbf{r}, \mathbf{r}', t - t') = -i\Theta(t - t') \langle N| [\hat{O}(t)(\mathbf{r}, t), B(\mathbf{r}', t')] |N\rangle \tag{2.3}$$

Now we should consider what happens when our electronic system, where the electrostatic interaction is described via the instantaneous[4] Coulomb potential $v(|\mathbf{r} - \mathbf{r}'|) = \frac{4\pi}{|\mathbf{r}-\mathbf{r}'|}$, is perturbed by longitudinal external potential $\phi(\mathbf{r}, t) = V_{ext}(\mathbf{r}, t)$. This is physically interpreted as the injection of an external charge into the system. Under the action of this field, the system may react with a reorganization of its charge density $\rho(\mathbf{r}, t)$, in the attempt to create an opposing *polarization* field. This results in a variation $\delta\rho(\mathbf{r}, t)$, called *induced* charge density, which generates a modification of the total potential: $V_{tot} = V_{ext} + V_{ind}$, where V_{ind} is the new induced potential, described *classically* as:

$$V_{ind}(\mathbf{r}, t) = \int d\mathbf{r}'\ v(|\mathbf{r} - \mathbf{r}'|)\delta\rho(\mathbf{r}', t) \tag{2.4}$$

In this case, the interacting term of the Hamiltonian is

$$\hat{H}_1(t) = \int d\mathbf{r}\ \rho(\mathbf{r}, t)V_{ext}(\mathbf{r}, t) \tag{2.5}$$

Using Eq.2.1 we obtain the induced charge density as:

$$\delta\rho(\mathbf{r}, t) = \int d\mathbf{r}' \int dt'\chi(\mathbf{r}, \mathbf{r}', t - t')V_{ext}(\mathbf{r}', t') \tag{2.6}$$

Where we defined the *reducible* polarizability as:

$$\begin{aligned} \chi(\mathbf{r}, \mathbf{r}', t - t') &= -i\Theta(t - t') \langle N| [\rho(\mathbf{r}, t), \rho(\mathbf{r}', t')] |N\rangle \\ &= \frac{\delta\rho(\mathbf{r}, t)}{\delta V_{ext}(\mathbf{r}', t')} \end{aligned} \tag{2.7}$$

Let's define the corresponding *time-ordered* reducible polarizability as:

$$\chi(\mathbf{r}, \mathbf{r}', t - t') = -i \langle N| \hat{T}[\rho(\mathbf{r}, t)\rho(\mathbf{r}', t')] |N\rangle \tag{2.8}$$

[4]Here we are neglecting relativistic effects.

To inspect its analytical structure, we can insert the complete basis of N-particle state $|N_i\rangle$ (the corresponding eigenvalue being E_i^N) inside Eq. 2.8 and express the density operator in the interaction picture as $\delta\rho(\mathbf{r},t) = e^{iH_0t}\delta\rho(\mathbf{r},0)e^{-iH_0t}$ (where $H_0|N\rangle = E_0^N|N\rangle$). These two operation lead, in turn, to:

$$\begin{aligned}\chi(\mathbf{r},\mathbf{r}',t-t') &= -i\sum_i \hat{T}\left[\langle N|\rho(\mathbf{r},t)|N_i\rangle\langle N_i|\rho(\mathbf{r}',t')|N\rangle\right] \\ &= -i\sum_i \hat{T}\left[f_i(\mathbf{r})f_i^*(\mathbf{r}')e^{-i(E_0^N-E_i^N)(t-t')}\right]\end{aligned} \tag{2.9}$$

The quantities $f_i(\mathbf{r}) = \langle N|\rho(\mathbf{r},0)|N_i\rangle$ are also defined as the oscillator strenghts of the i-th transition contributing the excited state of the system. Indeed, a final Fourier transform in time makes then explicit the analytic structure of the polarizability in energy space as:

$$\chi(\mathbf{r},\mathbf{r}',\omega) = \sum_i\left[\frac{f_i(\mathbf{r})f_i^*(\mathbf{r}')}{\omega-\Omega_i+i\eta} + \frac{f_i(\mathbf{r}')f_i^*(\mathbf{r})}{\omega+\Omega_i+i\eta}\right] \tag{2.10}$$

The above quantity has poles at $\Omega_i = (E_0^N - E_i^N)$, the *exact* excitation energies of the *interacting* N-particle system. The first (second) term of Eq. 2.10 is defined as the resonant (antiresonant, or a.r.) part. The fictitious parameter η is added in order to regularize the time integral.
If we consider a non-interacting system, and its corresponding ground state, by using Eq. 2.10 in conjunction with Eqs A.1 - A.4 we can easily define the *independent-particle polarizability* as:

$$\chi^0(\mathbf{r},\mathbf{r}',\omega) = \sum_{i,i'}\frac{(f_i-f_{i'})\phi_i^*(\mathbf{r})\phi_{i'}(\mathbf{r})\phi_{i'}^*(\mathbf{r})\phi_i^*(\mathbf{r})}{\omega-\omega_{ii'}+i\eta} + \text{a.r.} \tag{2.11}$$

The quantities f_i and $\omega_{ii'} = \epsilon_i - \epsilon_{i'}$ represent the occupation number and the excitation energies in the independent-particle case. For periodic systems described in a PW basis (see Eq. 1.22), Eq. 2.11 (as well as Eq 2.10) assumes a tensorial form in the reciprocal space (and omitting the regulator factor $i\eta$):

$$\begin{aligned}\chi^0_{\mathbf{GG}'}(\mathbf{q},\omega) =& 2\sum_{nm}\int_{BZ}\frac{d\mathbf{k}}{(2\pi)^3}\,\rho^*_{mn}(\mathbf{k},\mathbf{q},\mathbf{G})\rho_{mn}(\mathbf{k},\mathbf{q},\mathbf{G}')f_{n\mathbf{k}-\mathbf{q}}(1-f_{n'\mathbf{k}}) \\ &\times\left[\frac{1}{\omega+\epsilon_{n\mathbf{k}-\mathbf{q}}-\epsilon_{m\mathbf{k}}} - \frac{1}{+\epsilon_{m\mathbf{k}}-\epsilon_{n\mathbf{k}-\mathbf{q}}}\right]\end{aligned} \tag{2.12}$$

where we defined the matrix element of orbitals pairs as:

$$\begin{aligned}\rho_{nm}(\mathbf{k},\mathbf{q},\mathbf{G}) &= \langle n\mathbf{k}|\,e^{i(\mathbf{q}+\mathbf{G})\cdot\mathbf{r}}\,|m\mathbf{k}-\mathbf{q}\rangle \\ &= \frac{1}{\Omega}\sum_{\mathbf{G}'}C^*_{n\mathbf{k}}(\mathbf{G}')C_{n\mathbf{k}-\mathbf{q}}(\mathbf{G}-\mathbf{G}').\end{aligned} \tag{2.13}$$

To compute practically Eq. 2.12, the integral over the BZ is transformed into a discrete sum:

$$\int_{BZ} \frac{d\mathbf{k}}{(2\pi)^3} \rightarrow \frac{1}{N_{\mathbf{k}}\Omega} \sum_{\mathbf{k}} \tag{2.14}$$

where $N_{\mathbf{k}}$ are the number of $\mathbf{k}$-points in the real sampling of the BZ, Ω is the volume of the primitive cell in real lattice.

2.1.1 Microscopic dielectric function

Using Equations 2.4 and 2.6, the total potential (felt and produced) by the system can be expressed as a response to the external potential as:

$$\begin{aligned} V_{tot}(\mathbf{r},t) &= V_{ext}(\mathbf{r},t) + V_{ind}(\mathbf{r},t) \\ &= V_{ext}(\mathbf{r},t) + \int dt' \int d\mathbf{r}' \int d\mathbf{r}'' \; v(|\mathbf{r}-\mathbf{r}'|)\chi(\mathbf{r}',\mathbf{r}'',t-t')V_{ext}(\mathbf{r}'',t') \\ &= \int dt' \int d\mathbf{r}' \; \epsilon^{-1}(\mathbf{r},\mathbf{r}',t-t')V_{ext}(\mathbf{r}',t') \end{aligned} \tag{2.15}$$

where we have defined the inverse microscopic dielectric function:

$$\epsilon^{-1}(\mathbf{r},\mathbf{r}',t-t') = \delta(\mathbf{r}-\mathbf{r}')\delta(t-t') + \int d\mathbf{r}'' v(\mathbf{r}-\mathbf{r}'')\chi(\mathbf{r}'',\mathbf{r}',t-t') \tag{2.16}$$

Persevering in going towards periodic system and plane-wave basis, the space and time Fourier transform of Eq. 2.16:

$$\epsilon^{-1}_{\mathbf{G}\mathbf{G}'}(\mathbf{q},\omega') = \delta_{\mathbf{G}\mathbf{G}'} + v(\mathbf{q}+\mathbf{G})\chi_{\mathbf{G}\mathbf{G}'}(\mathbf{q},\omega) \tag{2.17}$$

where $v(\mathbf{q}+\mathbf{G}) = \frac{4\pi}{|\mathbf{q}+\mathbf{G}|^2}$ is the Fourier transform in the reciprocal space of the Coulomb potential. The physical meaning of the total field V_{tot} is now evident: it represent the *screened* resulting interaction that the electrons (or generally the particles in the system) feel, generated in part by the external field and in part by the response of all the charges to it. We can then define the *screened Coulomb interaction* as:

$$\begin{aligned} W_{\mathbf{G}\mathbf{G}'}(\mathbf{q},\omega) &= \epsilon^{-1}_{\mathbf{G}\mathbf{G}'}(\mathbf{q},\omega)v(\mathbf{q}+\mathbf{G}') \\ &= v(\mathbf{q}+\mathbf{G}) + v(\mathbf{q}+\mathbf{G})\chi_{\mathbf{G}\mathbf{G}'}(\mathbf{q},\omega)v(\mathbf{q}+\mathbf{G}') \\ &= \epsilon^{-1}_{\mathbf{G}\mathbf{G}'}(\mathbf{q},\omega)\frac{4\pi}{|\mathbf{q}+\mathbf{G}||\mathbf{q}+\mathbf{G}'|} \\ &= v(\mathbf{q}+\mathbf{G}) + W^p_{\mathbf{G}\mathbf{G}'}(\mathbf{q},\omega) \end{aligned} \tag{2.18}$$

where, following the notation of Ref. [121], we defined $W^p_{\mathbf{G}\mathbf{G}'}(\mathbf{q},\omega')$ as the *polarization* contribution. It is worth noting that this contribution is a *dynamical* one, as exploited by its frequency dependence. This represents the momentum-energy (or space-time) response of the system to the external perturbation. Analogously to Eq. 2.7 we now define the *irreducible* polarizability $\tilde{\chi}$ as:

$$\tilde{\chi}(\mathbf{r},\mathbf{r}',t-t') = \frac{\delta\rho(\mathbf{r},t)}{\delta V_{tot}(\mathbf{r}',t')} \tag{2.19}$$

if we expand the functional derivative of Eq. 2.7 in terms of V_{tot} and we use Eq. 2.19, we obtain a Dyson's equation [122] for the reducible polarizability:

$$\chi = \tilde{\chi} + \tilde{\chi} v \chi \tag{2.20}$$

which gives us the solution, written in a plane wave basis:

$$\chi_{\mathbf{G}\mathbf{G}'}(\mathbf{q},\omega) = [\delta_{\mathbf{G}\mathbf{G}''} - v(\mathbf{q}+\mathbf{G}'')\tilde{\chi}_{\mathbf{G}\mathbf{G}''}(\mathbf{q},\omega)]^{-1}\tilde{\chi}_{\mathbf{G}''\mathbf{G}}(\mathbf{q},\omega) \tag{2.21}$$

a fundamental result that will be used in the next sections. Indeed, the common Random Phase Approximation (RPA) [2], puts the $\tilde{\chi}$ equal to the independent-particle one χ^0, allowing us to solve (at least partially) the many-body problem of charged excitations.
Finally, we further proceed with definition, and we write here another particular response function:

$$\bar{\chi} = \tilde{\chi} + \tilde{\chi}\bar{v}\bar{\chi} \tag{2.22}$$

where $\bar{v}$ is the bare Coulomb interacting without it long-range term:

$$\bar{v}(\mathbf{q}) = \begin{cases} 0 & \text{if } \mathbf{q} = 0 \\ v(\mathbf{q}) & \text{if } \mathbf{q} \neq 0 \end{cases} \tag{2.23}$$

In this way only the short-wavelength limit of the Coulomb potential is explicitly considered. The long range term is hidden in the definition of the perturbation. Eq. 2.22 will be of fundamental importance in the next sections.

2.1.2 Macroscopic dielectric function and Local Field Effects

We can infer about the tensorial nature of Eq. 2.17. What does it mean physically? We may answer this question by observing the connection between the microscopic-macroscopic worlds, the first concerning band structures, density of states etc., the second one obeying Maxwell's equations (see Appendix B). Here we want to underline that microscopic quantities are in general local both in space and time, like $\epsilon^{-1}(\mathbf{r},\mathbf{r}',t-t')$. Instead, the analogous macroscopic counterpart has

to be represented by taking an average of a microscopic quantity. This allows us to access from the microscopic world to macroscopic quantities like absorption or energy loss spectra. In the case of dielectric function, following the works of Adler [123] and Wiser [124], we can define the *macroscopic dielectric function* as:

$$\epsilon_M(\omega) = \lim_{\mathbf{q}\to 0} \frac{1}{[\epsilon^{-1}(\mathbf{q},\omega)]_{\mathbf{G}=\mathbf{G}'=0}} \tag{2.24}$$

which is not simply the reciprocal of the *head* of the matrix $\epsilon(\mathbf{q},\omega)$, but is the reciprocal of the first element of its inverse. This means that we are effectively mixing all the $\mathbf{G},\mathbf{G}'$ components in doing the inverse. The physical reason to do this is that an external perturbation induces charge fluctuations and potentials at both macroscopic (described by the long-range part $\mathbf{G}$=0) and microscopic (short-range, $\mathbf{G} \neq 0$) levels. By including also short-range effects, also known as *Local Field Effects* (LFE), we are taking into account the inhomogeneity of the system, and appropriately describing experiments where shorter distances are probed (with increasing momentum transfer).

2.1.3 Connection with experiments

We have already shown in the previous section the connection between microscopic and macroscopic dielectric functions. In the long-wavelength limit (vertical transitions), this allows us to compute the photo-absorption spectrum as:

$$\text{Abs}(\omega) = \text{Im}\ \epsilon_M(\omega). \tag{2.25}$$

If we escape the optical limit for a while, and we consider possible indirect transition where initial and final state have different momentum $\mathbf{k}$ and $\mathbf{k}$' we can define [121]:

$$\begin{aligned}\epsilon_M(\mathbf{q},\omega) &= \frac{1}{\epsilon^{-1}_{\mathbf{G}=\mathbf{G}'}(\mathbf{q},\omega)} \\ &= \frac{1}{1+v(\mathbf{q}+\mathbf{G})\chi_{\mathbf{GG}}(\mathbf{q},\omega)} \\ &= 1 - \frac{v(\mathbf{q}+\mathbf{G})}{1+v(\mathbf{q}+\mathbf{G})\chi_{\mathbf{GG}}(\mathbf{q},\omega)}\end{aligned} \tag{2.26}$$

where $\mathbf{k}-\mathbf{k}'=\mathbf{q}$. This relation can be further rewritten using Eq. 2.22:

$$\epsilon_M(\mathbf{q},\omega) = 1 - v(\mathbf{q}+\mathbf{G})\bar{\chi}_{\mathbf{GG}}(\mathbf{q},\omega) \tag{2.27}$$

The *generalized* absorption spectra, i.e. still $\mathbf{q}$-dependent, is then defined as:

$$\text{Abs}(\mathbf{q},\omega) = -v(\mathbf{q}+\mathbf{G})\ \text{Im}\ \bar{\chi}_{\mathbf{GG}}(\mathbf{q},\omega) = \text{Im}\ \epsilon_M(\mathbf{q},\omega). \tag{2.28}$$

If we now consider the Loss function, which can be experimentally accessed by electron energy loss spectroscopy (EELS) and non-resonant inelastic X-ray scattering (NRIXS), we have [5] (see Appendix B):

$$\mathrm{L}(\mathbf{q},\omega) = -v(\mathbf{q}+\mathbf{G})\ \mathrm{Im}\ \chi_{\mathbf{GG}}(\mathbf{q},\omega) = -\mathrm{Im}\left(\frac{1}{\epsilon_M(\mathbf{q},\omega)}\right). \tag{2.29}$$

We notice similarities between Eq. 2.28 and Eq. 2.29: they only differ in the definition of the polarizability (with or without the long-range component of the Coulomb interaction).
In EELS and NRIXS experiments, the measured quantity is the intensity of the scattered particles resolved with respect to the scattering angle and to the energy of the outgoing particles (either electrons or photons). This quantity, that is the differential cross-section $\frac{d^2\sigma}{d\Omega dE}$ of the process, can be related to the loss function by the relation [125, 126]:

$$\frac{d^2\sigma}{d\Omega dE} \sim \begin{cases} q^{-2}L(\mathbf{q},\omega) & \text{EELS,} \\ \\ q^{2}L(\mathbf{q},\omega) & \text{NRIXS.} \end{cases} \tag{2.30}$$

2.2 Green's function formalism

We now define another correlation function, the (*time-ordered*) single-particle Green's function (GF) as [127, 121]:

$$\begin{aligned} G(\mathbf{r}t,\mathbf{r}'t') &= -i\,\langle N|\,\hat{T}[\Psi(\mathbf{r},t)\Psi^\dagger(\mathbf{r}',t')]\,|N\rangle \\ &= \begin{cases} -i\,\langle N|\,\Psi(\mathbf{r},t)\Psi^\dagger(\mathbf{r}',t')\,|N\rangle & \text{if } t>t' \\ \\ i\,\langle N|\,\Psi^\dagger(\mathbf{r}',t')\Psi(\mathbf{r},t)\,|N\rangle & \text{if } t<t' \end{cases} \end{aligned} \tag{2.31}$$

where $\hat{T}$ is the time-ordering operator. For simplicity, we don't consider here the dependence on the spin coordinate σ_i. We observe that this form of GF is non-local both in space and time, and has the physical meaning of a particle propagator. Indeed, for $t > t'$, it expresses the probability amplitude that a particle generated at $(\mathbf{r}', t')$ will be annihilated at $(\mathbf{r}, t)$: this represents the life/propagation of a conduction electron. The second term of Eq. 2.31, non-vanishing for $t < t'$, instead has the same meaning but regarding the propagation of a hole (seen in other terms as a particle going backward in time).
The single-particle GF contains a considerable amount of information about the

[5] $\mathrm{L}(\mathbf{q},\omega) = -\mathrm{Im}\ \epsilon_M^{-1}(\mathbf{q},\omega)$

system which belongs[6]. It is straightforward to show [96] that the ground-state expectation value of any single-particle operator[7] $\hat{O} = \int d\mathbf{r}\Psi^\dagger(\mathbf{r})O(\mathbf{r})\Psi(\mathbf{r})$ can be expressed as:

$$\langle \hat{O}(\mathbf{r}) \rangle = -i \lim_{t' \to t^+} \lim_{\mathbf{r}' \to \mathbf{r}} O(\mathbf{r}) G(\mathbf{r}t, \mathbf{r}'t') \tag{2.32}$$

Where the time t^+ is an infinitesimal time greater than t in order to ensure the correct time ordering. In particular, we can express the ground state expectation value of the density operator $\hat{\rho}(\mathbf{r}) = \Psi^\dagger(\mathbf{r})\Psi(\mathbf{r})$ as:

$$\langle \hat{\rho}(\mathbf{r}) \rangle = -iG(\mathbf{r}t, \mathbf{r}t^+). \tag{2.33}$$

Another quantity that can be expressed in terms of GF is the total energy of the system[8], through the very general Migdal–Galitzki formula [127]:

$$E_0 = \pm \frac{1}{2} i \lim_{t' \to t^+} \lim_{\mathbf{r}' \to \mathbf{r}} \int d\mathbf{r} \left[i\frac{\partial}{\partial t} + T(\mathbf{r}) \right] G(\mathbf{r}t, \mathbf{r}'t'). \tag{2.34}$$

Moreover, it is worth to rewrite here the independent irreducible polarization of Eq. 2.7 in terms of Green's functions as:

$$\chi^0(\mathbf{r}, \mathbf{r}', t - t') = -iG^0(\mathbf{r}, t')G^0(\mathbf{r}', t') \tag{2.35}$$

that describes the uncorrelated propagation of two particles, meaning that they do not mutually interact. We recognise immediately that such a picture is adequate to describe the processes of direct and inverse photoemission, i.e. charged excitations, where the excited electron/hole and the corresponding counterpart propagate independently. Neutral excitations like exciton formations are not included in this description, but are correctly captured by a 2-particles Green's Function, which will be described in the following sections.

2.2.1 Diagrammatic expansion of GF: Dyson's equations

The explicit calculation of the exact GF as described in Eq. 2.31 is not possible for the system of interest (real solids). How can we solve the problem? The answer relies in the Wick's theorem [128] and Feynman diagrams [129], that allows us to compute at all orders of perturbation theory an approximate expression of

[6] For an extended list of these properties see Ref. [121]

[7] As we will see later, the two-particle GF is related to two-particle operators, and so on.

[8] Indeed, also the 2-body operator potential $V(\mathbf{r}, \mathbf{r}')$ can be expressed in terms of single-particle GF [96].

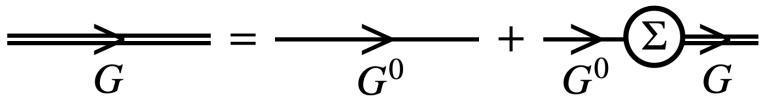

Figure 2.1: Dyson equation for G in terms of Feynman diagrams. We can interpret this expansion in terms of a bare propagation G^0 and an effective interaction Σ

$G(\mathbf{r}t, \mathbf{r}'t')$. This eventually [96] leads to a Dyson-like equation for our Green's function:

$$G(12) = G^0(12) + \int d3d4\ G^0(13)\Sigma(34)G(42) \tag{2.36}$$

where we condensed space and time coordinates $(\mathbf{r}_1 t_1, \mathbf{r}_2 t_2) \rightarrow (12)$ and $\Sigma(34)$ is the *proper/irreducible self-energy*, containing implicitly all the many-body interacting terms of the problem. Eq. 2.36, depicted also in Fig. 2.1 in terms of Feynman diagrams [96], is of fundamental relevance, as implies the possibility to describe $G(12)$ in terms of perturbative expansions, where the lowest order is represented by the non-interacting $G^0(12)$. The advantage of perturbative expansions is that we can stop at a certain order to include only the desired physics, i.e. we do not need to solve the full problem to obtain the properties that we are interested in. We observe that Eq. 2.36 is an integral equation where the kernel is the self-energy Σ, containing the effective coupling (the Coulomb interaction $v(|\mathbf{r} - \mathbf{r}'|)$. It is possible to consider in perturbation expansion also the self-energy Σ [96].
The first orders of the self-energy expansion leads us to the direct-Hartree Σ^H (usually already contained in G^0) and exchange-Fock Σ^x results [96]:

$$\begin{aligned} \Sigma^H(\mathbf{r}\mathbf{r}') &= -iv(|\mathbf{r} - \mathbf{r}'|) \lim_{t' \rightarrow t^+} G^0(\mathbf{r}'\mathbf{r}', t - t') \\ \Sigma^x(\mathbf{r}\mathbf{r}') &= iv(|\mathbf{r} - \mathbf{r}'|) \lim_{t' \rightarrow t^+} G^0(\mathbf{r}\mathbf{r}', t - t') \end{aligned} \tag{2.37}$$

We observe that the Hartree-Fock interaction $\Sigma^{HF} = \Sigma^H + \Sigma^x$ is *static* and *unscreened*, i.e. does not consider dynamical effects like charge oscillations and retarded response to the potential (the system is "frozen"). This is why usually the HF picture fails for materials: the system has no time to produce an appropriate response to the excitation (charge and spin oscillations etc.). We need the dynamically screened potential W defined in Eq. 2.18 to correctly describe correlation effects in solids. Usually, even DFT performs better for solids, as KS equations already contain an attempt to describe all the correlations effects happening in the materials, through the exchange-correlation potential v_{xc}.
Dyson equations are not restricted to single particle Green's functions and self-energy, but are valid also for any N-particles Green's function and the corresponding derived quantities.

2.2.2 The Lehmann representation

Moreover, the single-particle GF gives us access to the true single-particle excitation spectrum (i.e., the energy level of the electronic states). Indeed, by inserting in Eq. 2.31 the complete set of many-body $|N \pm 1, i\rangle$ excited states[9], and taking a Fourier transform in time, we obtain the so-called *Lehmann representation* of the GF:

$$G(\mathbf{r}\mathbf{r}', \omega) = \sum_n \frac{\psi_n(\mathbf{r})\psi_n^*(\mathbf{r}')}{\omega - (E_n - E_0) + i\eta \; sgn(E_n - E_0 - \mu)} \tag{2.38}$$

Where $E_n = E_n(N \pm 1)$ and $\psi_n(\mathbf{r}) = \langle N| \Psi(\mathbf{r}) |N+1; n, \mathbf{k}\rangle \langle N \pm 1; n, \mathbf{k}|$. Let's analyse he energy difference in the first denominator of Eq. 2.38:

$$\begin{aligned} E_n(N+1) - E_0(N) &= [E_n(N+1) - E_0(N+1)] + \\ &+ [E_0(N+1) - E_0(N)] \\ &= \epsilon_n + \mu \end{aligned} \tag{2.39}$$

where ϵ_n and μ are respectively the *excitation energy* of the N+1 particle system and the chemical potential[10]. By doing the same analysis for the second denominator in Eq. 2.38 and then Fourier transforming in space, we obtain the final form of the GF which explicitly shows as poles the excitation energies of the system:

$$\begin{aligned} G(\mathbf{k}, \omega) &= \sum_n \frac{\psi_{n\mathbf{k}}\psi_{n\mathbf{k}}^*}{\omega - \epsilon_{n\mathbf{k}} + i\eta \; sgn(\epsilon_{n\mathbf{k}} - \mu)} \\ &= \sum_{n\mathbf{k}} G_{n\mathbf{k}}(\omega) \end{aligned} \tag{2.40}$$

Analogously, the *non-interacting* Green's function G^0 is obtained considering the $\psi_{n\mathbf{k}}$ as the single particle orbitals. In this basis, $G^0(\mathbf{k}, \omega)$ is diagonal, and so it is possible to write:

$$G^0_{n\mathbf{k}}(\omega) = \frac{f_{n\mathbf{k}}}{\omega - \epsilon_{n\mathbf{k}} - i\eta} + \frac{1 - f_{n\mathbf{k}}}{\omega - \epsilon_{n\mathbf{k}} + i\eta} \tag{2.41}$$

where $f_{n\mathbf{k}}$ are then the occupation number of the state $|n\mathbf{k}\rangle$. This quantity is fundamental for a practical solution of the many-body problem, as we will see in the next sections.

2.2.3 The spectral function

From the equation of motion of the annihilation operator

$$i\frac{\partial}{\partial t_1}\Psi = \left[\Psi, \hat{H}\right]_- \tag{2.42}$$

[9] solution of the fully interacting Hamiltonian $\hat{H} |N \pm 1, n\rangle = E_n |N \pm 1, n\rangle$.

[10] which equals the Fermi level at zero temperature [114].

it is possible to derive the equation of motion for the full GF:

$$\left[i\frac{\partial}{\partial t_1} - H_0(1)\right] G(12) - \int d3\ \Sigma(13)G(32) = \delta(12) \tag{2.43}$$

with $H_0(1)$ being the non-interacting part of the Hamiltonian:

$$H_0(1) = -\frac{1}{2}\nabla_1^2 + V_{ext}(1) + V_{Hartree}(1) \tag{2.44}$$

It is easy to obtain the equation of motion for the non-interacting G, namely G^0:

$$\left[i\frac{\partial}{\partial t_1} - H_0(1)\right] G^0(12) = \delta(12) \tag{2.45}$$

Combining the Eq. 2.43 and Eq. 2.45 we obtain the very same Eq. 2.36. Inserting Eq. 2.43 in Eq. 2.42, we obtain the so-called quasi-particle equation[11] [121]:

$$H_0(\mathbf{r})\Psi_i(\mathbf{r},\omega) + \int d\mathbf{r}'\ \Sigma(\mathbf{r},\mathbf{r}',\omega)\Psi_i(\mathbf{r}',\omega) = E_i(\omega)\Psi_i(\mathrm{x},\omega) \tag{2.46}$$

Which shows a frequency dependence, meaning that the interaction described by the self-energy is a dynamical one. Indeed, a particle suffering of a screened potential responds to it with a certain delay in time.
The analogy between Eqs. 2.43 and 2.46 sheds a light also on the mathematical meaning of the single-particle GF: it is actually the *solvent*, i.e. the mathematical operator called Green's function [130] of Eq. 2.46, being verified the relation:

$$G(\mathbf{r},\mathbf{r}',\omega) = [\omega - \epsilon_0 - \Sigma(\mathbf{r},\mathbf{r}',\omega)]^{-1} \tag{2.47}$$

This allows us to write the GF in terms of a spectral representation:

$$G(\mathbf{r},\mathbf{r}',\omega) = \sum_i \frac{\Psi^\dagger(\mathbf{r})\Psi(\mathbf{r}')}{\omega - E_i} \tag{2.48}$$

which actually corresponds to Eq. 2.38. If we go to reciprocal space, we can define the *spectral function* [12] as:

$$A(\mathbf{r},\mathbf{r}',\omega) = \frac{1}{\pi}\mathrm{Im}G(\mathbf{r},\mathbf{r}',\omega) \tag{2.49}$$

which, for a general diagonal element in reciprocal space, is written as:

$$A_{\mathbf{k}}(\omega) = \frac{1}{\pi}\frac{|\mathrm{Im}\Sigma(\omega)|}{[\omega - \epsilon^0_{\mathbf{k}} - \mathrm{Re}\Sigma(\omega)]^2 + [\mathrm{Im}\Sigma(\omega)]^2} \tag{2.50}$$

[11] We notice here that we can recover the KS equations 1.9 just by letting $\Sigma(\mathbf{r},\mathbf{r}',\omega) = V_{xc}[n](\mathbf{r})\delta(\mathbf{r}-\mathbf{r}')$, which express the locality of the V_{xc}.
[12] For a general discussion on spectral functions, we redirect the reader to Ref. [121]

If we start by considering the non-interacting picture, we have a vanishing Σ, the spectral function has a series of δ-peak centered at the non-interacting single-particle energies $\epsilon^0_{\mathbf{k}}$; when we turn on the interaction, the self-energy shifts the peaks of $\epsilon^0_{n\mathbf{k}} \rightarrow \epsilon^0_{n\mathbf{k}} + \mathrm{Re}[\Sigma_{n\mathbf{k}}(\omega)]$ and applies a broadening $\Gamma_{n\mathbf{k}} = \mathrm{Im}\Sigma_{n\mathbf{k}}(\omega)$. Because of the one-to-one correspondence with the non-interacting peaks, this structure is called quasi-particle peak [121]. The quantity $\Gamma_{n\mathbf{k}}$ is also known as quasiparticle lifetime. A schematic representation is provided in Fig. 2.2. However, in the interacting case we see other peaks, called *satellites* and coming from the imaginary part of the self-energy. These are due to excitations that can be created when a particle is added/removed in/from the system, e.g. plasmons and atomic-like excitations. If these peaks have too much weight in the spectrum, the single-particle like picture is no more valid and we talk about *strong correlation*[13].

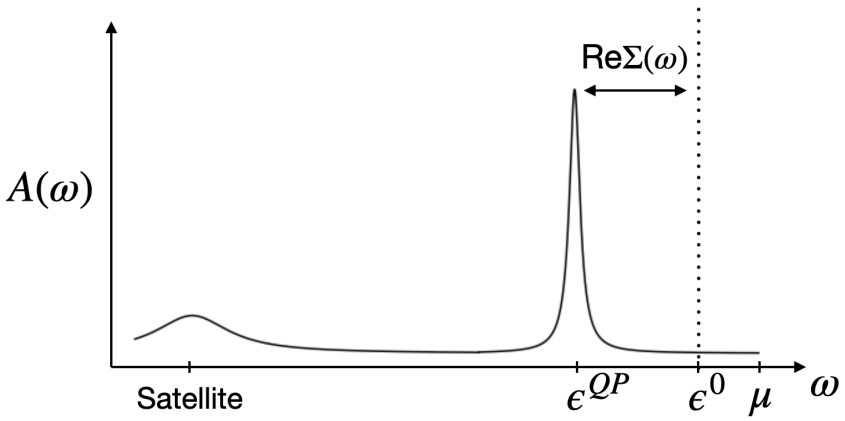

Figure 2.2: Effects of the many-body self-energy: the delta-like independent-particle peak (ϵ^0) is shifted $\epsilon^0 \rightarrow \epsilon^0 + \mathrm{Re}[\Sigma(\omega)]$ and its weight is redistributed between the quasiparticle peak ϵ^{QP} and satellites.

The experimental analogous that allows to measure such spectral functions (and hence the quasiparticle levels of the system) are *direct* and *inverse* photoemission, shown in Fig. 2.3. Experimental measures of the full band structure of a system can be carried out within Angle-Resolved Photoemission Spectroscopy (ARPES) [131, 132].

[13]The total weight of the spectral function is conserved and governed by its own sum-rule.

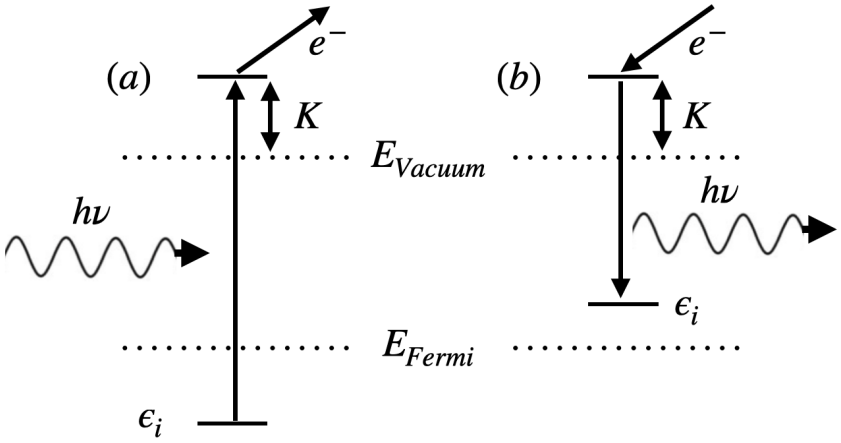

Figure 2.3: (a) Direct photoemission: an incident photon $h\nu$ excites an electron in the system, occupying a state ϵ_i, which is emitted with kinetic energy K. (b) Inversion photoemission: an impinging electron loses energy and is captured by the system, emitting a photon $h\nu$. In both cases, the conservation of energy requires $K = h\nu + \epsilon_i$.

2.3 Hedin's equations

In the last part of the previous section we showed the connection between the Green's function of a system, the associated quasiparticle energy levels $\epsilon_{n\mathbf{k}}$ of a system, and their experimental counterpart. We have not yet proposed a scheme to practically obtain such quantities. This could be a very difficult task, as we need the knowledge of the exact Self-energy $\Sigma(\mathbf{x}, \mathbf{x}', \omega)$, to be inserted in Eq. 2.46. Moreover, an additional degree of complexity is that, as shown in Eq. 2.46, the Self-energy is dynamical, i.e. presents a frequency dependence.
An iterative procedure was proposed by Lars Hedin more than 50 years ago, and starts from a closed (self-consistent) set of Dyson's equations, the Hedin's equations [1]:

$$\begin{aligned}
\Sigma(12) &= i \int d(34) G(14) W(1^+3) \tilde{\Gamma}(42,3) \\
G(12) &= G^0(12) + \int d(34) G^0(13) \Sigma(34) G(42) \\
\tilde{\Gamma}(12,3) &= \delta(12)\delta(13) + \int d(4567) \frac{\partial \Sigma(12)}{\partial G(45)} G(46) G(75) \tilde{\Gamma}(67,3) \\
P(12) &= -i \int d(34) G(13) (G(41^+) \tilde{\Gamma}(34,2) \\
W(12) &= V(12) + \int d(34) W(13) P(34) V(42)
\end{aligned} \tag{2.51}$$

where we condensed space and time variables using the compact notation $(\mathbf{x}_i, \mathrm{t}_i) \rightarrow (i)$. We introduced here the irreducible *vertex* function $\tilde{\Gamma}(12,3)$:

$$\tilde{\Gamma}(12,3) = -\frac{\delta G^{-1}(12)}{\delta V_{tot}(3)} \tag{2.52}$$

responsible of the introduction of two-particle effects in the irreducible polarizability P[14]. $W = \epsilon^{-1} V$ is the screened interaction, containing the response to the external and the classical induced (Hartree) fields. G^0 is the independent-particle (or *Hartree*) Green's function.
Hedin's equations are exact, but not practically solvable exactly. This means that approximations are needed, in particular starting from the functional form of the self-energy Σ in terms of Green's functions G. If one starts from an approximate form of Σ, for example, it is possible then to *iterate* along the so-called *Hedin's pentagon*, shown in Fig. 2.4 and solve the equations 2.51 self-consistently. The last step of the cyclic iterative procedure is dictated by the physics that we want to describe.

[14] also mentioned throughout this thesis as $\tilde{\chi}$, response to the total potential V_{tot} as expressed in Eq. 2.19.

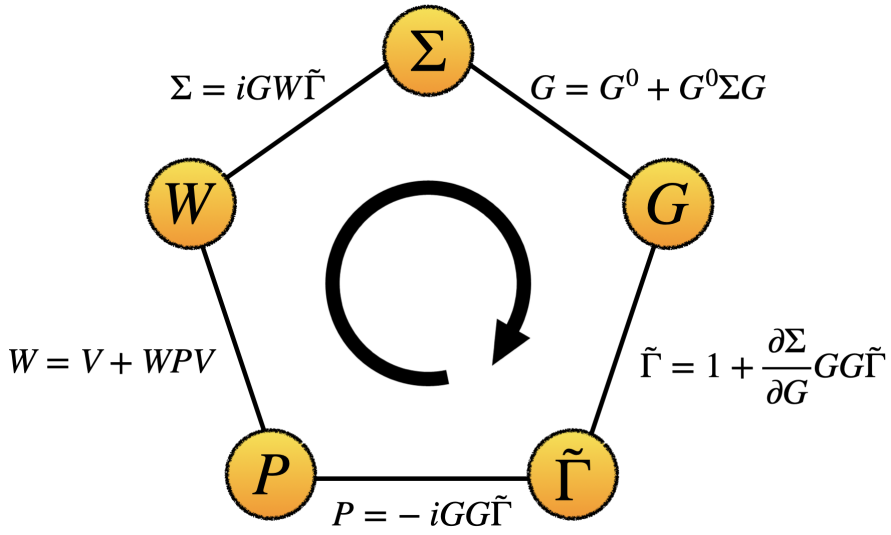

Figure 2.4: Hedin's pentagon, corresponding to the iterative solution of Equations 2.51. If a starting value of the self-energy Σ is guessed, then the iteration can start and give as result a new approximated value of Σ.

2.4 GW approximation

The simplest starting point to solve the problem was suggested by the same Hedin in its seminal work [1], and consists in a single iteration over the Hedin's pentagon, starting from $\Sigma = 0$ and neglecting vertex corrections, i.e. $\tilde{\Gamma}(12,3) = \delta(12)\delta(13)$. This is practically done by skipping the vertex part in the Hedin's pentagon and going directly from G to P. Following the loop of Fig. 2.4, we obtain the first order expression of the self-energy:

$$\begin{aligned}
\Sigma(12) &= 0 \\
\tilde{\Gamma}(12,3)) &= \delta(12)\delta(13) \\
G(12) &= G^0(12) \\
P(12) &= -iG^0(12)G^0(21^+) = P^0(12) \\
W(12) &= V(12) + \int d(34)W^0(13)P^0(34)V(42) = W^0(12) \\
\Sigma(12) &= iG^0(12)W^0(1^+2)
\end{aligned} \tag{2.53}$$

The effect of starting from $\Sigma = 0$ makes the Green's function to be the independent particle one. This in turn leads to the RPA for the polarizability $P^0 = \tilde{\chi}^0 = \chi^0$ (Eq. 2.12) and the screening W^0. Finally, we complete the first iteration of the loop and now the new approximated Self-energy, the last of Equations 2.53, is expressed as the product between G^0 and W^0. Due to this concise form, this approximation is called GW *approximation*. In particular, a single iteration on

the Hedin's pentagon is properly called (single-shot) G_0W_0. More advanced self-consistent GW calculation can be performed, but usually the G_0W_0 is good enough to describe the quasiparticle band structure of a material within the accuracy of tens of meV [133]. In this work we only considered single-shot non self-consistent G_0W_0 calculations.
In frequency space, the GW self-energy reads:

$$\Sigma^{GW}(\omega) = -\int \frac{d\omega'}{2\pi i} e^{i\omega' 0^+} \; G(\omega+\omega')W(\omega'). \tag{2.54}$$

The non-interacting Green's function G^0 used in the approximation is not the Hartree one, but the one built on the non-interacting Kohn-Sham single-particle orbitals $\phi^{KS}_{n\mathbf{k}}$ ($|n\mathbf{k}\rangle$ in abstract vector space). This is a better choice as in $\phi^{KS}_{n\mathbf{k}}$ there is already an attempt to include exchange and correlation effects, encoded in v_{xc}. The self-energy can be further split into the (Fock) exchange, Σ^x, and in the frequency dependent correlation parts Σ^c. The diagonal elements read:

$$\begin{aligned}\Sigma_{n\mathbf{k}} &= \langle n\mathbf{k}|\, \Sigma^x \,|n\mathbf{k}\rangle + \langle n\mathbf{k}|\, \Sigma^c \,|n\mathbf{k}\rangle \\ &= \Sigma^x_{n\mathbf{k}} + \Sigma^c_{n\mathbf{k}}\end{aligned} \tag{2.55}$$

that can be expanded in plane waves as:

$$\Sigma^x_{n\mathbf{k}} = -\sum_m^{\text{occ}} \int \frac{d\mathbf{q}}{(2\pi)^3} \sum_{\mathbf{G}} v(\mathbf{q}+\mathbf{G})|\rho_{nm}(\mathbf{k},\mathbf{q},\mathbf{G})|^2 f_{m,\mathbf{k}-\mathbf{q}} \tag{2.56}$$

$$\begin{aligned}\Sigma^c_{n\mathbf{k}}(\omega) = &-i\sum_m^{N_b} \int \frac{d\mathbf{q}}{(2\pi)^3} \sum_{\mathbf{G}\mathbf{G}'}^{G_{\text{cut}}} \rho_{nm}(\mathbf{k},\mathbf{q},\mathbf{G})\rho^*_{n'm}(\mathbf{k},\mathbf{q},\mathbf{G}')\times \\ &\int d\omega W_{\mathbf{G}\mathbf{G}'}(\mathbf{q},\omega')\times \\ &\left[\frac{f_{m,\mathbf{k}-\mathbf{q}}}{\omega-\omega'-\epsilon_{m,\mathbf{k}-\mathbf{q}}-i\eta} + \frac{(1-f_{m,\mathbf{k}-\mathbf{q}})}{\omega-\omega'-\epsilon_{m,\mathbf{k}-\mathbf{q}}+i\eta}\right].\end{aligned} \tag{2.57}$$

where the quantity $W^{\delta}_{\mathbf{G}\mathbf{G}'}(\mathbf{q},\omega)$ is the δ-like part[15] of the screened interaction $W_{\mathbf{G}\mathbf{G}'}(\mathbf{q},\omega)$ already shown in Eq. 2.18.
It is clear that the screened potential can be computed once known the dynamical screening matrix $\epsilon^{-1}_{\mathbf{G}\mathbf{G}'}(\mathbf{q},\omega)$ (Eq. 2.17). This can be eventually computed using the Dyson's equation for the reducible polarizability χ, which in the RPA becomes:

$$\chi_{\mathbf{G}\mathbf{G}'}(\mathbf{q},\omega) = [\delta_{\mathbf{G}\mathbf{G}''} - v(\mathbf{q}+\mathbf{G}'')\chi^0_{\mathbf{G}\mathbf{G}''}(\mathbf{q},\omega)]^{-1}\chi^0_{\mathbf{G}''\mathbf{G}}(\mathbf{q},\omega) \tag{2.58}$$

[15] Its full expression is shown in Ref. 65.

where the expression of $\chi^0_{\mathbf{GG''}}(\mathbf{q},\omega)$ is given in Eq. 2.12. Usually, the integral involved in Eq. 2.57 is computationally demanding, due to the high number of frequencies needed in the numerical integration. This integral can be performed analytically, within the so-called *plasmon-pole approximation* (PPA) [52]. The approximation considers a modellic single-pole function for $\epsilon^{-1}_{\mathbf{GG'}}(\mathbf{q},\omega)$:

$$\begin{aligned}\text{Im }\epsilon^{-1}_{\mathbf{GG'}}(\mathbf{q},\omega) =& A_{\mathbf{GG'}}(\mathbf{q})\times \\ & [\delta(\omega-\tilde{\omega}_{\mathbf{GG'}}(\mathbf{q}))-\delta(\omega+\tilde{\omega}_{\mathbf{GG'}}(\mathbf{q}))] \\ \text{Re }\epsilon^{-1}_{\mathbf{GG'}}(\mathbf{q},\omega) =& 1-\frac{A_{\mathbf{GG'}}(\mathbf{q})\tilde{\omega}^2_{\mathbf{GG'}}(\mathbf{q})}{\omega^2-\tilde{\omega}^2_{\mathbf{GG'}}(\mathbf{q})}\end{aligned} \tag{2.59}$$

This corresponds to assigning all the spectral weight of the dielectric function at a plasmon excitation pole. The parameters[16] of the model $A_{\mathbf{GG'}}(\mathbf{q})$ and $\tilde{\omega}^2_{\mathbf{GG'}}(\mathbf{q})$ can be obtained by imposing different constraints [134], that distinguish different flavors of PPA. Details on the PPA implemented in the YAMBO code, the Godby-Needs PPA [53], together with other technicalities of the code are provided in Appendix C.

The solution of the quasiparticle equation will be:

$$\epsilon_{n\mathbf{k}} = \epsilon^{\text{KS}}_{n\mathbf{k}} + \langle n\mathbf{k}|\,\Sigma(\epsilon^{\text{KS}}_{n\mathbf{k}}) - v^{\text{KS}}_{xc}\,|n\mathbf{k}\rangle \tag{2.60}$$

self-consistent in the quasiparticle energies. Since this involves only diagonal elements of the self-energy, solutions of this equation are cheaper to determine than poles of the fully interacting Green's function. This is a good approximation if the self-energy is diagonally dominant in the basis of the DFT orbitals. This is in general the case, a part some special case [135, 136]. This is particularly the case of isolated atoms or molecules, since the KS orbitals do not decay properly at large distances. We observe that we have to subtract to the self-energy the exchange-correlation potential v_{xc} used in the KS solution, to avoid double counting of these effects. Near the QP solution, the self-energy is approximately linear in frequency: we can Taylor expand it around $\omega = \epsilon^{KS}_{n\mathbf{k}}$ and stop at the first order (Newton's approximation). We eventually obtain:

$$\epsilon_{n\mathbf{k}} = \epsilon^{\text{KS}}_{n\mathbf{k}} + Z_{n\mathbf{k}}\,\langle n\mathbf{k}|\,\Sigma(\epsilon^{\text{KS}}_{n\mathbf{k}}) - v^{\text{KS}}_{xc}\,|n\mathbf{k}\rangle \tag{2.61}$$

where the *renormalization factor* $Z_{n\mathbf{k}} = [1-\langle n\mathbf{k}|\,\partial\Sigma_{xc}/\partial\omega\,|n\mathbf{k}\rangle\,|_{\epsilon^{KS}_{n\mathbf{k}}}]^{-1}$ represents the weight of the quasiparticle peak in the full spectral function, Eq. 2.49, which in the linearized case becomes:

$$A_{n\mathbf{k}}(\omega) \approx Z_{n\mathbf{k}}\frac{Z_{n\mathbf{k}}|\text{Im}\Sigma(\omega)|}{[\omega-\epsilon^0_{\mathbf{k}}-\text{Re}\Sigma(\omega)]^2+[Z_{n\mathbf{k}}\text{Im}\Sigma(\omega)]^2}. \tag{2.62}$$

The QP solution (main peak) is characterized by large $Z_{n\mathbf{k}}$ values, which lie around 0.7 to 0.8 for simple insulators, semiconductors and metals and around 0.9 for molecules [137]. Small $Z_{n\mathbf{k}}$ values indicate satellite features.

[16] which, for instance, are matrices.

2.5 Bethe-Salpeter equation

We are now interested in the theoretical counterparts of experiments that concern neutral excitations. These are, for example, absorption, electron energy loss spectroscopy (EELS), or non-resonant inelastic x-ray scattering (NRIXS), and are fundamental in order to describe optical properties of materials. These effects are not effectively captured by the RPA-GW approximation: the piece of theory still missing is the interaction between two particles, like the electron and the hole couples created by the absorption of a photon, and propagating together in the system interacting with each other. The envelope of couples of such electrons and holes contributes to the formation of a quasiparticle called *exciton*.

2.5.1 2-particle Green's function and 4-point polarizabilities

In terms of Green's function, we now use the *two-particle* Green's function, defined as:

$$G_2(1234) = (-i)^2 \langle N| \hat{T}[\Psi(1)\Psi(2)\Psi^\dagger(3)\Psi^\dagger(4)] |N\rangle \tag{2.63}$$

Which allows us to define a *reducible two-particle correlation function* L, or reducible 4-point polarization, subtracting from G_2 the uncorrelated contribution:

$$L(1234) = -G_2(1234) + G(13)G(24). \tag{2.64}$$

This equation describes the propagation of two interacting particles, and contains information that can be accessible from a series of experiments: optical spectra, EELS spectra, dynamic structure factor (from NRIXS). By choosing appropriate time orderings, we can describe different processes: for example, the choice of equal time limits $t_3 = t_1^+$ and $t_4 = t_2^+$ corresponds to the propagation of an electron-hole pair. Moreover, setting $x_1 = x_3$ and $x_2 = x_4$ allows us to recover the density-density response function of Eq. 2.7:

$$\chi(12) = -iL(121^+2^+) = -i\theta(t_1 - t_2) < [\rho(1)\rho(2)] > \tag{2.65}$$

It is possible to show [4, 2] that Eq. 2.64 can be rewritten as a Dyson's equation, the so-called *Bethe-Salpeter equation* (BSE) [138]:

$$L(1234) = L_0(1234) + L_0(1536)\Xi(5678)L(7284) \tag{2.66}$$

where L_0 is the non-interacting electron-hole contribution and $\Xi(1234)$ is the interaction kernel of the equations, i.e. the effective two-particle interaction:

$$\Xi(1234) = -i\delta(12)\delta(34)v(12) + \frac{\delta\Sigma_{xc}(13)}{\delta G(42)} \tag{2.67}$$

In the $\Sigma_{xc}(12) = iG(12)W(12)$ approximation it reads [17]:

$$\Xi(1234) = -i\delta(12)\delta(34)v(12) + i\delta(13)\delta(24)W(12) \tag{2.68}$$

where the first term is called *exchange term*, the second one is the *direct term*[18], and contains the screened interaction W. It is possible to obtain this expression as a second iteration of Hedin's equations Eq. 2.51, where we recalculate the vertex correction Γ.
Moreover, we further define [2] a new polarization function $\bar{L}$ as:

$$\bar{L}(1234) = L_0(1234) + L_0(1536)\bar{\Xi}(5678)\bar{L}(7284) \tag{2.69}$$

where, as we may guess with the analogy with respect to Eq. 2.22, the new kernel $\bar{\Xi}$ contains only the short-range part $\bar{v}$ of the bare Coulomb potential (defined in Eq. 2.23):

$$\bar{\Xi}(1234) = -i\delta(12)\delta(34)\bar{v}(12) + i\delta(13)\delta(24)W(12). \tag{2.70}$$

The contraction of Eq. 2.69 from a 4- to a 2-point polarization gives us Eq. 2.22:

$$\bar{\chi}(12) = -i\bar{L}(121^+2^+) \tag{2.71}$$

which, together with Eq. 2.65, connects directly $\bar{L}$ and L with experiments, as explained in Sec. 2.1.3. Indeed, we can rewrite Eq. 2.27:

$$\epsilon_M(\mathbf{q},\omega) = 1 - v(\mathbf{q}) \int d\mathbf{r}_1 d\mathbf{r}_2 e^{i\mathbf{q}\cdot(\mathbf{r}_1-\mathbf{r}_2)} \bar{L}(\mathbf{r}_1,\mathbf{r}_1,\mathbf{r}_2,\mathbf{r}_2,\omega). \tag{2.72}$$

The same equation can be written for L.

2.5.2 Effective two-particle Schrödinger equation

The solution of the Dyson's equations of Eq. 2.64 and 2.69 can be done through inversion. The problem can be mapped into an effective two-particle Hamiltonian, whose eigenvalue-eigenvector problem can be solved by a single diagonalization [141]. Let's consider $\bar{L}$ for the explanation of such a procedure. The first step is to neglect all the dynamical effects that may be contained in the Kernel Ξ through the frequency dependence of the screening W. This corresponds to consider the propagation of the particle simultaneous and their interaction instantaneous, i.e. $W(12) = W(\mathbf{r}_1,\mathbf{r}_2)\delta(t_1 - t_2)$: excitons do not interact with each other. Eventually, this assumption leads to a single frequency coordinate in the Fourier transform of $\bar{L}$:

$$\bar{L}(1234) \to \bar{L}(1234|\omega) \tag{2.73}$$

[17] We omitted the derivative of the screening potential, as it can be safely neglected. [139, 140]
[18] If we neglect this term, Eq. 2.66 defines the irreducible response function $\tilde{L}$.

The basis set of the problem is the *transition basis*, i.e. the basis composed by pairs of single particle orbitals $\phi_i(\mathbf{r})$. In such transition space, the polarizability reads:

$$\bar{L}_{(n_1n_2)(n_3n_4)} = \int d\mathbf{r}_1 d\mathbf{r}_2 d\mathbf{r}_3 d\mathbf{r}_4 \bar{L}(1234)\phi_{n_1}(\mathbf{r}_1)\phi^*_{n_2}(\mathbf{r}_2)\phi^*_{n_3}(\mathbf{r}_3)\phi_{n_4}(\mathbf{r}_4) \quad (2.74)$$

where n_i implicitly considers both the band index n and wave vector index $\mathbf{k}$. The non-interacting polarizability L_0 is expressed as:

$$L^0_{(n_1n_2)(n_3n_4)} = \frac{(f_{n_2} - f_{n_1})\delta_{n_1,n_3}\delta_{n_2,n_4}}{\epsilon_{n_2} - \epsilon_{n_1} - \omega - i\eta} \quad (2.75)$$

Solving Eq. 2.69 by inversion, it is possible to show [2] that the polarizability $\bar{L}$ can be rewritten as[19]

$$\bar{L}_{(n_1n_2)(n_3n_4)} = [H^{exc} - I\omega]^{-1}_{(n_1n_2)(n_3n_4)}(f_{n_3} - f_{n_4}) = \bar{l}_{(n_1n_2)(n_3n_4)}(f_{n_3} - f_{n_4}) \quad (2.76)$$

where H^{exc} is the desired *excitonic Hamiltonian*:

$$H^{exc}_{(n_1n_2)(n_3n_4)} = (\epsilon_{n_2} - \epsilon_{n_1})\delta_{n_1,n_3}\delta_{n_2,n_4} + i(f_{n_2} - f_{n_1})\bar{\Xi}_{(n_1n_2)(n_3n_4)}. \quad (2.77)$$

the first term consists in the difference of the quasiparticle energies, i.e. the independent particle transition. The kernel in transition space is:

$$\bar{\Xi}_{(n_1n_2)(n_3n_4)} = -i(\bar{\Xi}^x_{(n_1n_2)(n_3n_4)} - \bar{\Xi}^d_{(n_1n_2)(n_3n_4)}) \quad (2.78)$$

where we define the exchange and direct terms in transitions space as:

$$\begin{aligned} \bar{\Xi}^x_{(n_1n_2)(n_3n_4)} &= 2\gamma \int d\mathbf{r}d\mathbf{r}'\phi^*_{n_1}(\mathbf{r})\phi_{n_2}(\mathbf{r})\bar{v}(|\mathbf{r} - \mathbf{r}'|)\phi^*_{n_3}(\mathbf{r}')\phi_{n_4}(\mathbf{r}') \\ \bar{\Xi}^d_{(n_1n_2)(n_3n_4)} &= \int d\mathbf{r}d\mathbf{r}'\phi^*_{n_2}(\mathbf{r})\phi_{n_4}(\mathbf{r})W(\mathbf{r},\mathbf{r}')\phi^*_{n_3}(\mathbf{r}')\phi_{n_1}(\mathbf{r}') \end{aligned} \quad (2.79)$$

where γ=0 in the case of singlet excitons (electron and hole with opposite spins), γ=1 if the excitons are triplets (same spin)[20]. The kernel $\bar{\Xi}$ represents the electron-hole mutual interaction, and gives rise to the so called *Excitonic Binding Energy* (EBE), the difference between the quasiparticle energy of the transition and the excitation energy solution of the BSE. The EBE discriminates the strength of an electron-hole couple and determines how much energy it is needed to separate them.

[19] The same can be done for the independent particle polarizability as well, that in the case of RPA-GW it can be written as: $L^0_{(n_1n_2)(n_3n_4)} = [H^{QP} - I\omega]^{-1}_{(n_1n_2)(n_3n_4)}(f_{n_3} - f_{n_4})$.

[20] The singlet excitons are the ones that can be accessed experimentally with linearly polarized light, due to selection rules. If the spin-orbit coupling is not negligible, the spin structure of the excitonic Hamiltonian is different [121]

In analogy with Eq. 2.47, we can say that the term $\bar{l}_{(n_1n_2)(n_3n_4)}$ of Eq. 2.76, coincides with the mathematical Green's function of Eq. 2.77. This allows us to rewrite $\bar{l}_{(n_1n_2)(n_3n_4)}$ in its spectral representation:

$$\bar{l} = \sum_{\lambda\lambda'} \frac{|\lambda\rangle\, S^{-1}_{\lambda\lambda'}\, \langle\lambda|}{E_\lambda - \omega} \tag{2.80}$$

valid for a general non-hermitian matrix. E_λ and $|\lambda\rangle$ are the excitonic energies and eigenvectors, solution of:

$$\begin{aligned} H^{exc}\,|\lambda\rangle &= E_\lambda\,|\lambda\rangle \\ |\lambda\rangle &= \sum_{n_1n_2} A^\lambda_{n_1n_2} |n_1n_2\rangle \end{aligned} \tag{2.81}$$

where $|n_1n_2\rangle \equiv |n_2\rangle \otimes |n_1\rangle$, $|n_1\rangle$ and $|n_2\rangle$ being valence and conduction wavefunctions, respectively. $S_{\lambda\lambda'} = \langle\lambda|\lambda\rangle$ is called overlap matrix. In our transition basis, the excitonic wavefunction is expressed as:

$$\Psi_\lambda(\mathbf{r}_1, \mathbf{r}_2) = \langle \mathbf{r}_1, \mathbf{r}_2 | \lambda\rangle = \sum_{n_1n_2} A^\lambda_{n_1n_2} \phi_{n_1}(\mathbf{r}_1)\phi_{n_2}(\mathbf{r}_2) \tag{2.82}$$

in this way we define the *effective two-particle Schrödinger equation* as:

$$H^{exc}_{(n_1n_2)(n_3n_4)} A^{(n_3n_4)}_\lambda = E_\lambda A^\lambda_{n_1n_2} \tag{2.83}$$

This problem can be solved simply diagonalizing the excitonic Hamiltonian, and at the end allow us to evaluate $\bar{L}$ through Equations 2.76 and 2.80:

$$\bar{L}_{(n_1n_2)(n_3n_4)} = \sum_{\lambda\lambda'} \frac{A^\lambda_{n_1n_2} S^{-1}_{\lambda\lambda'} A^{\lambda'*}_{n_3n_4}}{E_\lambda - \omega} \tag{2.84}$$

The overlap matrix is now given by $S_{\lambda\lambda'} = \sum_{(n_1n_2)} A^{\lambda*}_{n_1n_2} A^{\lambda'}_{n_1n_2}$, and for a general non-hermitian matrix differs from the identity: the eigenstates are not orthogonal. The macroscopic dielectric function of Eq. 2.72 then becomes, for a general transferred momentum $\mathbf{q} = \mathbf{k} - \mathbf{k}'$:

$$\begin{aligned} \epsilon_M(\mathbf{q},\omega) = 1 - v(\mathbf{q}) \sum_{\lambda\lambda'} \Bigg[& \sum_{(n_1n_2)} \langle n_1|\, e^{-i\mathbf{q}\cdot\mathbf{r}_1}\, |n_2\rangle \, \frac{A^\lambda_{n_1n_2}}{E_\lambda(\mathbf{q}) - \omega - i\eta} \\ & \times S^{-1}_{\lambda\lambda'} \sum_{(n_3n_4)} \langle n_4|\, e^{i\mathbf{q}\cdot\mathbf{r}_2}\, |n_3\rangle \, A^{*\lambda'}_{(n_3n_4)} (f_{n_4} - f_{n_3}) \Bigg] \end{aligned} \tag{2.85}$$

2.5.3 Structure of the Excitonic Hamiltonian

To understand the structure of Eq. 2.77, we need to assign a precise character to each n_i, which then corresponds to a valence v or conduction c at a given $\mathbf{k}$ [21]. Moreover, we do not take into account the spin structure of the problem, whose exhaustive description is done in Ref. [121]. Considering the occupations factors in Eq. 2.77, it is easy to write the excitonic matrix in a triangular block form:

$$H^{exc} = \begin{pmatrix} A & B \\ 0 & D \end{pmatrix} \tag{2.86}$$

or, explicitly:

$$H^{exc}_{(n_1n_2)(n_3n_4)} = \begin{pmatrix} H^{exc}_{(v,c)(v',c')} & \bar{\Xi}_{(v,c)(c',v')} & \bar{\Xi}_{(c,v)(v',\tilde{v}')} & \bar{\Xi}_{(v,c)(c',\tilde{c}')} \\ -[\bar{\Xi}_{(v,c)(v',c')}]^* & -[H^{exc,res}_{(v,c)(v',c')}]^* & \bar{\Xi}_{(c,v)(v',\tilde{v}')} & -\bar{\Xi}_{(c,v)(c',\tilde{c}')} \\ 0 & 0 & (\epsilon_{\tilde{v}} - \epsilon_v)\delta_{v,v'}\delta_{\tilde{v},\tilde{v}'} & 0 \\ 0 & 0 & 0 & (\epsilon_{\tilde{c}} - \epsilon_c)\delta_{c,c'}\delta_{\tilde{c},\tilde{c}'} \end{pmatrix} \tag{2.87}$$

which is still rather complex to manage. Furthermore, to simplify this matrix structure we take the hint of the occupation factors explicitly written in Eq. 2.76, which tells us that only the first block column of the $\bar{l}$ matrix will contribute to our description. This means that, as H^{exc} is an upper triangular matrix, we can safely reduce the full matrix to the block A of Eq. 2.87:

$$H^{exc} = \begin{pmatrix} H^{exc,res}_{(v,c)(v',c')} & K^{coupling}_{(v,c)(v',c')} \\ -[K^{coupling}_{(v,c)(v',c')}]^* & -[H^{exc,res}_{(v,c)(v',c')}]^* \end{pmatrix} \tag{2.88}$$

where we $H^{exc,res}_{(v,c)(v',c')}$ is the *resonant* term, which considers only positive frequency transitions ($v \to c$):

$$H^{exc,res}_{(v,c)(v',c')} = (\epsilon_c - \epsilon_v)\delta_{vv'}\delta_{cc'} + i\bar{\Xi}_{(v,c)(v',c')} \tag{2.89}$$

The off-diagonal terms $\mathrm{K}^{coupling}_{(v,c)(v',c')}$ are the coupling terms, as they mix positive and negative frequency transitions (excitations and de-excitations). The last term is the anti-resonant one, concerning only negative energy transitions (important for photo-luminescence). In most of the cases, we can safely neglect the coupling terms, as often these matrix elements are small with respect to the energy range of transitions. This approximation is called *Tamn-Dancoff approximation* (TDA) [142, 143], and allows one to work with hermitian matrices and reduce the matrix size of a factor 2.

[21] For the moment we are considering only vertical transitions.

In plane wave basis set, we have the following resonant excitonic Hamiltonian:

$$\begin{aligned} H^{exc,res}_{(vc,\mathbf{k})(v'c',\mathbf{k}')} &= (\epsilon_{c\mathbf{k}} - \epsilon_{v\mathbf{k}})\delta_{vv'}\delta_{cc'}\delta_{\mathbf{k}\mathbf{k}'} \\ &+ 2\gamma\bar{\Xi}^{x}_{(vc,\mathbf{k})(v'c',\mathbf{k}')} \\ &- \bar{\Xi}^{d}_{(vc,\mathbf{k})(v'c',\mathbf{k}')} \end{aligned} \tag{2.90}$$

where the exchange and direct term are, respectively:

$$\begin{aligned} \bar{\Xi}^{x,res}_{(vc,\mathbf{k})(v'c',\mathbf{k}')} =& \frac{2\gamma}{\Omega}\sum_{\mathbf{G}\mathbf{G}'}\bar{v}(\mathbf{G})\left\langle c,\mathbf{k}\right| e^{i\mathbf{G}\cdot\mathbf{r}}\left|v,\mathbf{k}\right\rangle \times \\ & \left\langle v',\mathbf{k}'\right| e^{-i\mathbf{G}'\cdot\mathbf{r}}\left|c',\mathbf{k}'\right\rangle, \end{aligned} \tag{2.91}$$

and

$$\begin{aligned} \bar{\Xi}^{d,res}_{(vc,\mathbf{k})(v'c',\mathbf{k}')} =& -\frac{1}{\Omega}\sum_{\mathbf{G}\mathbf{G}'}\bar{v}(\mathbf{q}'+\mathbf{G})\epsilon^{-1}_{\mathbf{G}\mathbf{G}'}(\mathbf{q}')\left\langle c,\mathbf{k}\right| e^{i(\mathbf{q}'+\mathbf{G})\cdot\mathbf{r}}\left|c',\mathbf{k}'\right\rangle \times \\ & \left\langle v',\mathbf{k}'\right| e^{-i(\mathbf{q}'+\mathbf{G}')\cdot\mathbf{r}}\left|v,\mathbf{k}\right\rangle \delta_{\mathbf{k}-\mathbf{k}',\mathbf{q}'}. \end{aligned} \tag{2.92}$$

The formulation of the BSE contemplates excitons with a general transferred momentum $\mathbf{q}$ between the valence v and conduction c states: both direct and indirect excitons are considered and will be studied throughout this work. The long-wavelength limit can be easily recovered just by letting $\mathbf{q}\to 0$.

The eigenvalue eigenvector problem Eq. 2.83 can be rewritten as:

$$H^{exc}_{(vc,\mathbf{k})(v'c',\mathbf{k}')}(\mathbf{q})A^{\lambda}_{v'c'\mathbf{k}'}(\mathbf{q}) = E_{\lambda}(\mathbf{q})A^{\lambda}_{vc\mathbf{k}}(\mathbf{q}) \tag{2.93}$$

where the eigenvectors are

$$\left|\lambda,\mathbf{q}\right\rangle = \sum_{vc,\mathbf{k}} A^{\lambda}_{vc\mathbf{k}}(\mathbf{q})\left|vc\mathbf{k},\mathbf{q}\right\rangle \tag{2.94}$$

and $\left|vc\mathbf{k},\mathbf{q}\right\rangle \equiv \left|c,\mathbf{k}\right\rangle \otimes \left|v,\mathbf{k}-\mathbf{q}\right\rangle$, $\left|v,\mathbf{k}-\mathbf{q}\right\rangle$ and $\left|c,\mathbf{k}\right\rangle$ being valence and conduction wave-functions, respectively. The eigenvalues $E_{\lambda}(\mathbf{q})$ constitutes the *excitonic band structure* or *exciton dispersion*. So, the finite-momentum resonant excitonic Hamiltonian reads:

$$\begin{aligned} H^{exc,res}_{(vc,\mathbf{k})(v'c',\mathbf{k}')}(\mathbf{q}) &= (\epsilon_{c\mathbf{k}} - \epsilon_{v\mathbf{k}-\mathbf{q}})\delta_{vv'}\delta_{cc'}\delta_{\mathbf{k}\mathbf{k}'} \\ &+ 2\gamma\bar{\Xi}^{x}_{(vc,\mathbf{k})(v'c',\mathbf{k}')}(\mathbf{q}) \\ &- \bar{\Xi}^{d}_{(vc,\mathbf{k})(v'c',\mathbf{k}')}(\mathbf{q}) \end{aligned} \tag{2.95}$$

where the exchange and direct term are, respectively:

$$\begin{aligned} \bar{\Xi}^{x,res}_{(vc,\mathbf{k})(v'c',\mathbf{k}')}(\mathbf{q}) =& \frac{2\gamma}{\Omega}\sum_{\mathbf{G}\mathbf{G}'}\bar{v}(\mathbf{q}+\mathbf{G})\left\langle c,\mathbf{k}\right| e^{i(\mathbf{q}+\mathbf{G})\cdot\mathbf{r}}\left|v,\mathbf{k}-\mathbf{q}\right\rangle \times \\ & \left\langle v',\mathbf{k}'-\mathbf{q}\right| e^{-i(\mathbf{q}+\mathbf{G}')\cdot\mathbf{r}}\left|c',\mathbf{k}'\right\rangle, \end{aligned} \tag{2.96}$$

and

$$\bar{\Xi}^{d,res}_{(vc,\mathbf{k})(v'c',\mathbf{k}')}(\mathbf{q}) = -\frac{1}{\Omega}\sum_{\mathbf{G}\mathbf{G}'}\bar{v}(\mathbf{q}'+\mathbf{G})\epsilon^{-1}_{\mathbf{G}\mathbf{G}'}(\mathbf{q}')\,\langle c,\mathbf{k}|\,e^{i(\mathbf{q}'+\mathbf{G})\cdot\mathbf{r}}\,|c',\mathbf{k}'\rangle \times \langle v',\mathbf{k}'-\mathbf{q}|\,e^{-i(\mathbf{q}'+\mathbf{G}')\cdot\mathbf{r}}\,|v,\mathbf{k}-\mathbf{q}\rangle\,\delta_{\mathbf{k}-\mathbf{k}',\mathbf{q}'} \tag{2.97}$$

We observe that the excitonic Hamiltonian is an $(N_v \times N_c \times N_{\mathbf{k}})^2$ square matrix, and it has to be inverted for each value of the transferred momentum $\mathbf{q}$ that we want to compute.
Within the TDA, the exciton Hamiltonian matrix is hermitian and the excitonic eigenstates are ortogonal, i.e. $S_{\lambda,\lambda'} = \delta_{\lambda,\lambda'}$. This simplify Eq. 2.85 as the very intuitive form, which for the resonant part becomes:

$$\begin{aligned}\epsilon_M(\mathbf{q},\omega) &= 1 - \frac{2}{\Omega N_{\mathbf{q}}}v(\mathbf{q})\sum_{\lambda}\frac{|\sum_{(vc,\mathbf{k})}\langle v\mathbf{k}-\mathbf{q}|\,e^{-i\mathbf{q}\cdot\mathbf{r}}\,|c\mathbf{k}\rangle\,A^{\lambda}_{vc\mathbf{k}}(\mathbf{q})|^2}{E_\lambda(\mathbf{q})-\omega-i\eta} \\ &= 1 - \frac{2}{\Omega N_{\mathbf{q}}}v(\mathbf{q})\sum_{\lambda}\frac{\Phi_\lambda(\mathbf{q})}{E_\lambda(\mathbf{q})-\omega-i\eta}\end{aligned} \tag{2.98}$$

where we defined $\Phi_\lambda(\mathbf{q})$ as the oscillator strengths of the exciton λ that occur between transitions where valence states and conduction states are separated in $\mathbf{k}$-space by a momentum $\mathbf{q}$. Ω is the volume of the unit cell and $N_{\mathbf{q}}$ is the number of points in the BZ sampling. Within this expression, the Absorption spectrum (Eq. 2.28) can be interpreted as a sum of Lorentzian peaks where the broadening can be tuned by changing the parameters η. Oscillator strengths are used to distinguish between active and inactive excitons (in the $\mathbf{q} = 0$ limit, in particular, to identify those that are dipole active/forbidden, i.e. bright/dark). A very similar equation can be used to describe the inverse macroscopic dielectric function, if Eq. 2.66 is used to solve the BSE:

$$\epsilon^{-1}_M(\mathbf{q},\omega) = 1 + \frac{2}{\Omega N_{\mathbf{q}}}v(\mathbf{q})\sum_{\lambda}\frac{\Phi_\lambda(\mathbf{q})}{E_\lambda(\mathbf{q})-\omega-i\eta} \tag{2.99}$$

In this way we can describe the Loss function Eq. 5.7. Indeed, EELS experiments are able to capture long-range interactions, e.g. plasmons.

Part II

Technical developments

Chapter 3

Towards high-throughput MBPT: efficient algorithms and automated workflows

A first step towards HT GW calculations was made by M. J. van Setten and co-workers [144]. They proposed a scheme to perform automated GW simulations, analyzing also the interdependence between different involved parameters to be converged for ∼80 solids. They showed different levels of correlation between GW gaps with respect to experimental and Kohn-Sham ones, and the need of an improved starting point or self-consistency to obtain more accurate results. Another relevant advancement was presented by Rasmussen et al. [145], where more than 60.000 G_0W_0 self-energy evaluations of 370 2D semiconductors, taken from the Computational 2D Materials Database [14] (C2DB), were analyzed in order to draw useful conclusions for future HT studies. Their results concern the validity of the basis set extrapolation limit, the acceptability of a scissor operation to correct bands and in general the accuracy of GW calculations with respect to experiments.

In this work, I propose algorithms to automate the most common tasks of a MBPT study: GW–BSE convergences and GW band interpolations (by means of Wannierization [146]). Convergence of involved parameters is crucial to obtain accurate GW and BSE results and often its cumbersome resolution has been a limiting factor for the application of MBPT. Besides automation, the algorithm is meant to reach converged results in a limited number of steps, thus minimizing the number of calculations to be performed and related computational effort, which represents one the main bottleneck characterizing GW and BSE studies. I implemented the workflows in the AiiDA framework [39, 40], a platform that is routinely used for HT studies [12, 147, 148, 149] and that incorporates the ADES model for Automation, Data, Environment and Sharing [35]. The implementation is a clear demonstration of software interoperability between different codes/software projects, i.e. Yambo [64, 65], Wannier90 [150] and Quantum

ESPRESSO [116, 117]. Efficient error handling and logic flows are encoded within the workflows. Algorithms are validated for a selection of systems, mainly semiconductors, for G_0W_0 convergences and band interpolations. The following Chapter is contained in the following work: "**Automated Many-Body Perturbation Theory**", by **Miki Bonacci**, Junfeng Qiao, Nicola Spallanzani, Giovanni Pizzi, Antimo Marrazzo, Deborah Prezzi, Elisa Molinari, Daniele Varsano, and Andrea Ferretti (2022, *preprint*).

3.1 Convergence parameters...

In the following, we summarize the main equations of the GW–BSE theory considering a plane wave expansion, as implemented in the YAMBO code [64, 65], the software used to perform the simulations of this work. More details can be found in Chapter 2.

3.1.1 ...in GW

The independent particle polarizability, Eq. 2.12, is defined as:

$$\chi^0_{\mathbf{GG'}}(\mathbf{q},\omega) = 2\sum_{nm}^{N_b}\int_{BZ}\frac{d\mathbf{k}}{(2\pi)^3}\,\rho^*_{mn}(\mathbf{k},\mathbf{q},\mathbf{G})\rho_{mn}(\mathbf{k},\mathbf{q},\mathbf{G'})f_{n\mathbf{k-q}}(1-f_{n'\mathbf{k}}) \times\left[\frac{1}{\omega+\epsilon_{n\mathbf{k-q}}-\epsilon_{m\mathbf{k}}}-\frac{1}{+\epsilon_{m\mathbf{k}}-\epsilon_{n\mathbf{k-q}}}\right] \tag{3.1}$$

where

$$\rho_{nm}(\mathbf{k},\mathbf{q},\mathbf{G}) = \langle n\mathbf{k}|\, e^{i(\mathbf{q}+\mathbf{G})\cdot\mathbf{r}}\,|m\mathbf{k}-\mathbf{q}\rangle\,. \tag{3.2}$$

The parameter N_b ("BndsRnXp" in YAMBO) represents a cutoff over the summation of empty states (usually, all the valence states are included), and the integral in reciprocal space samples the **k**-points belonging to the Brillouin Zone (BZ). Both N_b and the size of the **k**-points grid need to be increased until the convergence is reached. The reducible polarizability χ, Eq. 2.21, defines the response of the system to an external electromagnetic field. It can be expressed through a Dyson's equation which involves the independent particle irreducible polarizabilty $\tilde{\chi} = \chi^0$ (RPA [2]):

$$\chi_{\mathbf{GG'}}(\mathbf{q},\omega) = \left[\delta_{\mathbf{G},\mathbf{G''}} - v(\mathbf{q}+\mathbf{G''})\chi^{\mathbf{0}}_{\mathbf{GG''}}(\mathbf{q},\omega)\right]^{-1}\chi^0_{\mathbf{G''G'}}(\mathbf{q},\omega) \tag{3.3}$$

In practice, Eq. 3.3 is solved including a finite number of **G** vectors determined by a cutoff parameter G_{cut} ("NGsBlkXp" in YAMBO), which defines the size of the response matrix thus having an impact on the accuracy and on the computational effort needed to store and perform the inversion and matrix multiplication.

In the GW approximation the self-energy can be split into the Fock exchange, Σ^x, and in the (frequency dependent) correlation part Σ^c. The diagonal elements read:

$$\begin{aligned}\Sigma_{n\mathbf{k}} &= \langle n\mathbf{k}|\,\Sigma^x\,|n\mathbf{k}\rangle + \langle n\mathbf{k}|\,\Sigma^c\,|n\mathbf{k}\rangle \\ &= \Sigma^x_{n\mathbf{k}} + \Sigma^c_{n\mathbf{k}}\end{aligned} \tag{3.4}$$

that can be expanded in plane waves as (see also Eqs. 2.56 and 2.57):

$$\Sigma^x_{n\mathbf{k}} = -\sum_m^{\text{occ}} \int \frac{d\mathbf{q}}{(2\pi)^3} \sum_{\mathbf{G}}^{G^x_{\text{cut}}} v(\mathbf{q}+\mathbf{G})|\rho_{nm}(\mathbf{k},\mathbf{q},\mathbf{G})|^2 f_{m,\mathbf{k}-\mathbf{q}} \tag{3.5}$$

$$\begin{aligned}\Sigma^c_{n\mathbf{k}}(\omega) = &-i\sum_m^{N_b} \int \frac{d\mathbf{q}}{(2\pi)^3} \sum_{\mathbf{G}\mathbf{G}'}^{G_{\text{cut}}} \rho_{nm}(\mathbf{k},\mathbf{q},\mathbf{G})\rho^*_{nm}(\mathbf{k},\mathbf{q},\mathbf{G}')\times \\ &\int d\omega W_{\mathbf{G}\mathbf{G}'}(\mathbf{q},\omega')\times \\ &\left[\frac{f_{m,\mathbf{k}-\mathbf{q}}}{\omega-\omega'-\epsilon_{m,\mathbf{k}-\mathbf{q}}-i\eta} + \frac{1-f_{m,\mathbf{k}-\mathbf{q}}}{\omega-\omega'-\epsilon_{m,\mathbf{k}-\mathbf{q}}+i\eta}\right].\end{aligned} \tag{3.6}$$

where here N_b, in YAMBO, is indicated as is "GbndRnge". In the following we always consider the same value for "GbndRnge" and "BndsRnXp" (Eq. 3.1). So, a typical GW calculation needs to be converged with respect to the following parameters:

1. N_b: empty states summation for both response $\chi^0_{\mathbf{G}\mathbf{G}'}$, Eq. 3.1, and self-energy Σ^c, Eq. 3.6;

2. G_{cut}: PW Kinetic energy cutoff for $\chi_{\mathbf{G}\mathbf{G}'}$ (or $\epsilon^{-1}_{\mathbf{G}\mathbf{G}'}$), in the calculation of Σ^c;

3. BZ **k**-points sampling, i.e. the **k**-point mesh, to perform integrals in the reciprocal space.

It has been shown in several previous works [134, 151, 144] that the first two parameters, N_b and G_{cut}, are often interdependent. Indeed, we can observe that in Eq. 3.6 we have a summation over both empty states m and reciprocal lattice vectors **G**. The latter determines the size of the screening matrix $\epsilon^{-1}_{\mathbf{G}\mathbf{G}'}$, which through $\chi^0_{\mathbf{G}\mathbf{G}'}$ contains the summation over empty states. The convergence procedure is non-trivial: at fixed G_{cut}, it is possible to converge each element of $\chi^0_{\mathbf{G}\mathbf{G}'}$ with respect to N_b; then, further convergence is required for the $\chi^0_{\mathbf{G}\mathbf{G}'}$ matrix size, i.e. for the parameter G_{cut}, at fixed N_b. Results have then once more to be converged with respect to N_b, and so on up to the overall convergence. Indeed, as Eq. 3.2

is a convolution in **G**-space between the periodic parts of the Bloch states associated in the dipole, screening matrix elements with large **G** should be governed by higher energy KS states, as pointed out by M. J. van Setten and co-workers [144].

The above described interdependence enters in a non-trivial way in the subsequent evaluation of the correlation self-energy, as we have to solve a Dyson's Equation (Eq. 3.3), which requires an inversion. We then have a further summation over empty states in Eq. 3.6, which concerns the generalized dipole matrix elements in the numerator and the relative eigenvalues in the denominator. In the following the same cutoff N_b for summations appearing in the Eqs. 3.6 and 3.1 is considered.

It is clear that N_b and G_{cut} are strictly interdependent, and their convergence has to be performed *jointly*.

At variance, the **k**-mesh convergence can be done separately, as it has been shown [144] that the final converged value of the coupled parameters N_b and G_{cut} is almost independent on the value of the used **k**-mesh (and viceversa).

As final comment, an additional convergence parameter can be the number of **G** vectors for expanding wavefunctions (Eq. 1.22) in transition matrix elements, expressed in Eq. 3.2, and Fast-Fourier-Transform (FFT) operations. This ("FFT-Gvecs" in YAMBO) can be much less than the kinetic energy cutoff used in the corresponding DFT simulation and helps in memory savings.

3.1.2 ...in BSE

Neutral excitation energies are computed by solving the Bethe-Salpeter equation [4]. This allows to compute the macroscopic dielectric function (considering only resonant and anti-resonant parts of the H^{exc}) as:

$$\epsilon_M^{-1}(\omega,\mathbf{q}) = 1 - \frac{2}{VN_{\mathbf{q}}} v(\mathbf{q}) \sum_{\lambda} \Phi_\lambda(\mathbf{q}) \times \left[\frac{1}{E^\lambda(\mathbf{q}) - (\omega + i\eta)} + \frac{1}{E^\lambda(\mathbf{q}) + (\omega + i\eta)} \right], \tag{3.7}$$

where V is the volume of the unit cell and N_q is the number of points in the BZ sampling. We defined $\Phi_\lambda(\mathbf{q})$ as the oscillator strengths of the exciton λ that occur between transitions where valence states and conduction states are separated in **k**-space by $\mathbf{q} = \mathbf{k} - \mathbf{k}'$:

$$\Phi_\lambda(\mathbf{q}) = \left| \sum_{(vc,\mathbf{k})} \langle v\mathbf{k} - \mathbf{q}| \, e^{-i\mathbf{q}\cdot\mathbf{r}} \, |c\mathbf{k}\rangle \, A^\lambda_{vc\mathbf{k}}(\mathbf{q}) \right|^2 \tag{3.8}$$

Summations over valence, conduction bands and **k**-points in Eq. 3.8 indicate that in a practical BSE calculation we have to converge these three parameters. Usually, the summation over bands allows us to choose what bands are included in

the BSE solution, and the range of energy we want to investigate. Instead, the **k**-points are more crucial as an exciton can be composed of transitions from region of the BZ that are extended or not, depending often on how conduction and valence bands are parallel each other. Excitons that are composed of transition from a wide region of the BZ are often very localized in real space, and at variance a very delocalized exciton in real space corresponds to a small region of the BZ for what concerns single particle transitions [1].

Usually, the BSE k-meshes are larger than the one needed to converge the GW band structure.

3.2 Automation of GW and BSE convergences

These non-trivial convergences, combined with computationally expensive calculations, call for efficient procedures to describe and explore the convergence space to minimize the number of runs needed to achieve converged results and save computational resources. A possible strategy is to describe the convergence space as function of the parameters. Different functional forms, such as inverse power laws, have been considered in previous studies [60, 152, 144, 48, 145], and in some cases, the analytical forms were derived from non trivial models [153]. For a general (N+1) dimensional space, a model convergence surface $f(\mathbf{x})$, which represents the value of a given observable (i.e. quasiparticle energies or excitonic eigenvalues) as a function of the values of the N parameters $\mathbf{x} = [x_1, ..., x_N]$, can be expressed as:

$$f(\mathbf{x}) = \prod_i^N \left(\frac{A_i}{x_i^{\alpha_i}} + b_i \right). \tag{3.9}$$

Here, A_i, b_i and α_i are free parameters and $\mathrm{b} = \prod_i^N \mathrm{b}_i$ is the exact theoretical converged value. The accuracy of the latter anyway, depends on the value of the **x** parameters used to evaluate the convergence behaviour, i.e. on how close the estimated values is from the converged one, as noticed by Rasmussen et al. in Ref. 145.

From Eq. 3.9 the interdependence of different parameters can be addressed by looking at the mixed partial derivatives. Not taking this interdependence directly into account can result in a very tedious convergence procedure, as it would require multiple univariate convergences(further details are provided in Appendix G and Ref. 65). The advantage of having an analytical form for the description of the convergence space is the possibility to compute all-order derivatives, once the

[1] Summations over **G** vectors for the calculation of the BSE kernel like in Eq. 2.91 and 2.92, are usually easy to converge and are often borrowed from the GW convergence step (the parameters G_{cut} mentioned in Section 3.1.1).

fitting parameters are known. The gradient components are:

$$f'_{x_i}(\mathbf{x}) = -\alpha_i \frac{A_i}{x_i^{\alpha_i+1}} \prod_{j\neq i}^{N} \left(\frac{A_j}{x_j^{\alpha_j}} + b_j \right) \tag{3.10}$$

while second derivatives are:

$$f''_{x_i}(\mathbf{x}) = \alpha_i(\alpha_i+1) \frac{A_i}{x_i^{\alpha_i+2}} \prod_{j\neq i}^{N} \left(\frac{A_j}{x_j^{\alpha_j}} + b_j \right) \tag{3.11}$$

$$f''_{x_i,x_j}(\mathbf{x}) = \alpha_i\alpha_j \frac{A_iA_j}{x_i^{\alpha_i+1}x_j^{\alpha_j+1}} \prod_{k\neq i,j}^{N} \left(\frac{A_k}{x_k^{\alpha_k}} + b_k \right) \tag{3.12}$$

In order to perform a fit using the functional form of Eq. 3.9, we need at least 3N calculations, where N is the dimensionality of the parameter space and 3 is the minimum number of of calculations for each direction needed to estimate the fitting parameters. A further reduction of the number of needed calculations can be done by performing different fits keeping the α_i parameters to a fixed value in a specified range as done in Ref. 144: in this way the lowest number of needed calculations is reduced to 2N.

The convergence surface will approach the exact result for all the N parameters going to infinite at the same time. For sufficiently high values of the parameters, $f(\mathbf{x})$ can be considered to describe accurately this asymptotic region of the convergence surface. The asymptotic region can be determined by imposing two precise conditions:

$$\begin{cases} |f'_{x_i}(\mathbf{x})| < \Delta_i \\ \\ |f''_{x_i,x_j}(\mathbf{x})| < \Delta_{ij} \end{cases} \tag{3.13}$$

for each parameters x_i, x_j with $i, j = 1, ..., N$. The first condition is used to determine the region in which the convergence surface becomes flat (and so approaches convergence), whereas the condition on second partial derivatives is used to ensure that the different parameters are no longer interdependent [2]. Once this asymptotic region has been determined, a guess for the converged value E_{guess} is made, defined as the value of $f(\mathbf{x})$ with the lowest value of the parameters at convergence with the region satisfying the conditions of Eq. 3.13, in terms of a convergence threshold Δ.

The accuracy of the guess for the converged results is then checked and validated according to the automated algorithm described below.

[2] These threshold values can be tuned according to the desired accuracy, and we found that the values $\Delta_i = 5 \cdot 10^{-5} \frac{eV}{[x_i]}$ and $\Delta_{ij} = 1 \cdot 10^{-8} \frac{eV}{[x_i][x_j]}$ are good thresholds to identify the asymptotic region.

3.2.1 Algorithm

The algorithm is specifically designed to handle the coupled convergence between N_b and G_{cut}, but it can be used also to accelerate convergence tests with respect to other parameters, like the **k**-point mesh in the Brillouin Zone (BZ) and the fast Fourier transforms grids.

The workflow is designed to obtain accurate converged results with the minimum possible number of calculations and is schematically depicted in Fig. 3.1. The first step (i) consists in the construction of the N-dimensional space of parameters as a grid of equally spaced points, with a given spacing and ranges provided as input. Then, M calculations are performed on a subset of the points in the parameter grid, to cover efficiently the space.

Next (ii), the results are fitted using the expression Eq. 3.9 keeping the power laws fixed $\alpha_i \in \{1,2\}\ \forall$ i=1, ...N and choosing the one resulting with the lowest mean squared error.

The asymptotic region is then identified by computing the first and second order derivatives (Eqs. 3.10-3.12) and imposing the conditions Eq. 3.13. If such a region cannot be found, new calculations are performed on a shifted parameter grid, increasing the values of the parameters. Once the asymptotic region has been identified, (iii) a guess converged value is selected $E_{guess}= E(N_b^0, G_{cut}^0)$ where (N_b^0, G_{cut}^0) is the cheapest point at convergence with the asymptotic region.

If not already included in previous calculations, (iv) $E(N_b^0, G_{cut}^0)$ is evaluated and the fit is performed again, considering also this new point.

To establish the accuracy of E_{guess}, the calculated value $E(N_b^0, G_{cut}^0)$ is compared with the outcome of the old fit $E^{fit}(N_b^0, G_{cut}^0)$ with a given convergence threshold Δ and new parameters N_b^1, G_{cut}^1 coming from the fit according to (iii) are evaluated and compared with the previous ones. Steps (ii)-(iv) are repeated until convergence is reached i.e. the two conditions:

$$|E(N_b^i, G_{cut}^i) - E^{fit}(N_b^i, G_{cut}^i)| < \Delta \tag{3.14a}$$

$$(N_b^{i+1}, G_{cut}^{i+1}) = (N_b^i, G_{cut}^i), \tag{3.14b}$$

are simultaneously satisfied.

3.3 The `aiida-yambo` plugin and automated workflows

The above convergence algorithm has been implemented in the new version of the `aiida-yambo` plugin [65] by means of high-level workflows devoted to fully automate YAMBO calculations within the AiiDA informatics infrastructure and workflow management system [39, 40]. In AiiDA, each calculation is a *process* and, together with inputs and outputs, it is stored in the AiiDA relational database. The

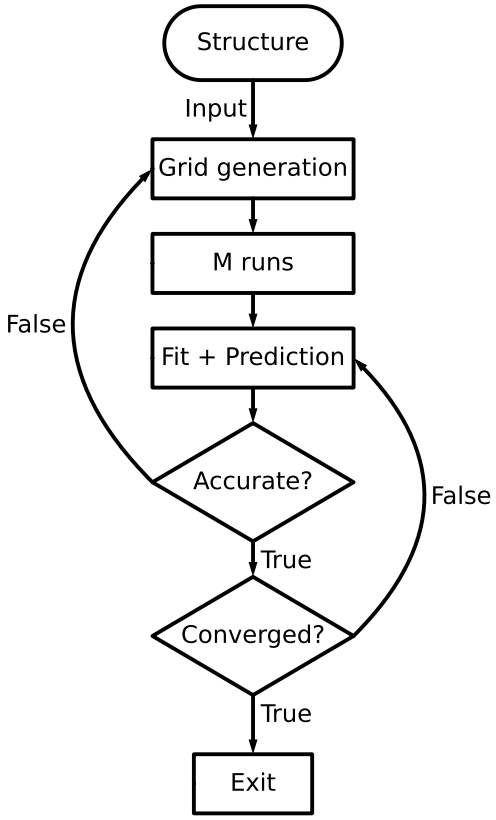

Figure 3.1: Flowchart of the convergence algorithm. After generating the grid for the N-dimensional parameter space, a subset of M simulations are performed. The results are then fitted to predict the converged parameters. Finally, the accuracy (Eq. 3.14a) and the convergence (Eq. 3.14b) of the prediction are verified, and the procedure iterated, if needed.

`aiida-yambo` plugin implements the `YamboCalculation` and `YppCalculation` classes to manage individual simulations that can be performed by using the YAMBO code through the `p2y`, `yambo` and the `ypp` (YAMBO pre/post processing) executables, i.e., Independent-Particle RPA (IP-RPA), GW, BSE calculations, as well as general data interface with different codes (e.g., QUANTUM ESPRESSO and WANNIER90). The automation concerns input generation, scheduler submission, and output parsing phases. Here, the output parsing is partially done by using YAMBOPY functions [65]. Links between single calculations, fundamental for data provenance, are stored as well and usually managed by ad-hoc workflows (the so-called *workchains* in the AiiDA jargon). This ensures data provenance and full reproducibility of results. Workflows are *dynamic*, i.e. their execution path is not fixed, but can depend on the results of completed calculations. This allows for the implementation of complex logics, such as those characterizing the

convergence algorithm that we propose in this work.

Part of the AiiDA philosophy (ADES model [35]) is to organize the workflows in a modular way, in order to automate tasks of increasing complexity, from handling a single calculation to managing thousands of them. These workflows encode the knowledge of expert scientists, where the final goal is the development of complete, turn-key solutions enabling both accuracy and reproducibility of results, as well as the possibility to perform high-throughput screening studies. Within the `aiida-yambo` plugin, three main workflows are provided, each of them targeting a precise task:

- `YamboRestart`: automation of error handling and restart for each `YamboCalculation`;
- `YamboWorkflow`: automation of the single GW/BSE flow (composed of several interlinked steps, explained in the following);
- `YamboConvergence`: automation of the convergence (multiple `YamboWorkflow` runs);

Their nested organization is shown in Fig. 3.2. The highest level workflow is represented by the `YamboConvergence` workchain, which implements the convergence algorithm of Sec. 3.2, in order to fully automate it and reduce the human time needed for input creation and submission steps. All the YAMBO simulations are organized automatically on the fly, without any external user intervention. The fundamental input to provide to `YamboConvergence` is the python list containing the information on the parameter space to be explored. An example of such input reads:

```
[
    {
        'var': [
            'BndsRnXp',
            'GbndRnge',
            'NGsBlkXp',
            ],
        'start': [50, 50, 2],
        'stop': [400, 400, 10],
        'delta': [50, 50, 2],
        'max': [1000, 1000, 36],
        'what': ['gap_GG'],
        'conv_thr': 0.1,
        'conv_thr_units': 'eV',
        },
]
```

The list contains a python dictionary with all the information needed to run the convergence on the empty states N_b ("BndsRnXp" and "GbndRnge") jointly with

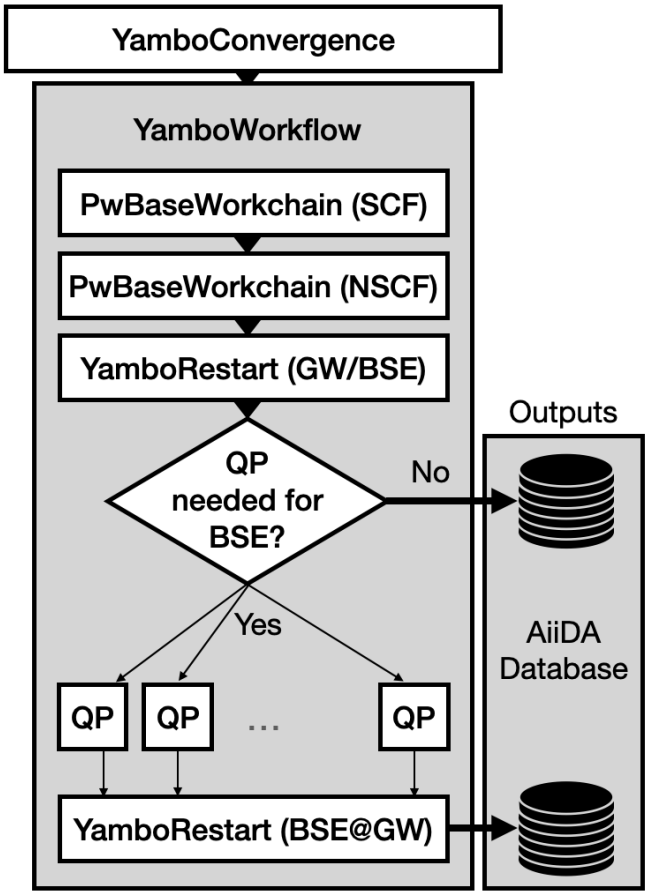

Figure 3.2: Hierarchical structure of aiida-yambo workchains. The highest level one is `YamboConvergence`, which calls multiple `YamboWorkflow` workchains. A single `YamboWorkflow` contains all the possible steps needed to perform a MBPT calculation from scratch. The outputs are stored in the AiiDA database, in a human readable fashion and easily accessible and shareable from the user.

the G_{cut} ("NGsBlkXp"), from the edges of the starting parameter grid ("start" and "stop") to its spacing ("delta"). The key "what" indicates the quantity to be converged: here as an example, we focus on the direct $\Gamma - \Gamma$ band gap of the material under scrutiny, up to 0.1 eV ("conv_thr"). The "max" keyword is needed in order to set an upper limit to computationally affordable values of the parameters. The output summarizes the convergence history and allows the user to easily parse the converged simulation. `YamboConvergence` allows one to converge several many-body quantities like quasiparticle levels, band-gaps, as well as excitation energies. Notably, the convergence block in Fig. 3.2 can be skipped if converged parameters are already known.

A single GW (BSE) flow is automated within the `YamboWorkflow`. This is

the core workchain of the plugin, to be used each time a YAMBO calculation has to be performed within the AIIDA-YAMBO plugin. Indeed, the `YamboWorkflow` takes care of performing all the steps needed in a typical MBPT simulation: self-consistent (SCF) and non-self-consistent (NSCF) QUANTUM ESPRESSO DFT calculations, and actual YAMBO calculations. The workflow ensures robust interoperability between codes (YAMBO and QUANTUM ESPRESSO) and links subsequent calculations, interfacing data automatically. In this way, it is possible to skip the steps already done, in the case a parent calculation is provided at the `YamboWorkflow` input level. For example, the workflow is able to reuse the desired NSCF calculation if already stored in the database. Furthermore, quasiparticle eigenvalues are often needed in order to build the BSE Hamiltonian. If required, `YamboWorkflow` is able to run this intermediate GW step by computing the quasiparticle bands. The precise states to be computed can also be decided automatically by means of an energy range provided in input (default is set to be 120% of the DFT computed band gap). The states belonging to this energy window (centered at the Fermi level) are explicitly computed. Often, the number of requested quasiparticle is large and because of limited wall-time reason,the simulation have to be split in several runs calculating a fraction of quasiparticle corrections. Here, the procedure is again automated, and –taking advantage of functionalities provided within the yambopy package– a final database collecting all the quasiparticle corrections is provided as output, ready to be used in the final BSE calculation. Finally, `YamboWorkflow` can parse ad-hoc quantities, like energy levels, gaps and excitation energies. This is particularly useful in the `YamboConvergence` workflow, used to converge these specific quantities.

`YamboWorkflow` performs DFT calculations by calling the `PwBaseWorkchain`, provided in the `aiida-quantumespresso` plugin. This workchain contains automatic error handlers (inherithed from the `BaseRestartWorkchain` class, implemented within the AiiDA software). An analogous automatic error handling is used for the YAMBO part by means of the `YamboRestart` workchain, called as a sub-workflow by the `YamboWorkflow`. The restart run is then dependent on the encountered error. In presence of out-of-memory errors, `YamboRestart` submits a new calculation by changing appropriately the requested memory resources, concerning specifically the number of processors involved and the balance between distributed and shared memory. Parallelization errors, due to wrong distribution of quantities among involved processors, are managed by setting the default parallelism decided on the fly by yambo, overriding all the parallelism instructions of the input parameters. Instead, for errors due to exceeding the requested walltime, the new run is submitted increasing the walltime by a factor of 1.5*N, where N is the number of the restarting iteration, up to a maximum walltime provided in input (the default value is 24 hours). In all these cases, the workchain understands if we already have some useful outputs computed in the remote directory of the failed calculation and, if any, these are copied in the remote directory of the new calculation and then reused. In this way, it is possible to provide an efficient,

CPU-time-saving restart mechanism that avoids to recompute quantities that are already available. The workchain resubmits a failed calculation up to a maximum number of iterations, fixed to 5 as default value.

For an easier development of automated workflows, AiiDA allows one to create inputs with pre-populated default values for several parameters, which are defined by the so-called protocols. Most of DFT-based AiiDA plugins provide the same protocols, corresponding to an increasing level of accuracy: *fast*, *moderate* and *precise* [154]. Such code-agnostic protocols are robust due to the well-known high level of reproducibility of DFT with different quantum engines [46], and their reliability is guaranteed by means of large scale studies on several systems with different characteristics (i.e. metals, semiconductors, dimensionality and so on) and represent a valid alternative with respect to heuristic approaches only guided by the user's knowledge. However, defining protocols for GW and BSE calculations is still an open issue [144], as the high computational cost limited the number of systems to be studied extensively in such a way to define safe convergence parameters. Moreover, code-agnostic parameters are not easy to be determined as for DFT based codes, as GW (BSE) implementations can differ in several aspects, starting from different considered parameters to be converged [134, 48]. Here, in the `aiida-yambo` plugin, we provide heuristic protocols based on previous experience on limited subset of systems, for both GW and BSE simulations. Such protocols, namely "fast", "moderate" and "accurate", concern several parameters (YAMBO input variables): FFT grid ("FFTGvecs"), empty states summations ("BndsRnXp" and "GbndRnge"), plane-wave expansion for the polarizability ("NGsBlkXp") and the **k**-point sampling of the BZ. The `aiida-yambo` plugin is fully available online with an open MIT license [155] and a detailed documentation is also provided [156]. Example of provenance graph can be found in Appendix E.

3.4 Validation of the convergence workflow

The `YamboConvergence` workchain has been validated by performing convergence studies for the quasiparticle G_0W_0 gap of a small set of well-known semiconductors: Silicon, ZnO, rutile TiO_2, monolayer MoS_2, bulk and monolayer hBN. We used symmetrized geometries in such a way to reduce the computational cost of simulations: we do not expect relevant differences in the results obtained with fully-relaxed structures. The KS-DFT exchange-correlation functional was approximated using GGA-PBE [98], through the optimized norm-conserving Vanderbilt (ONCV) SG15 [110, 111] pseudopotentials. In the case of ZnO, we adopted Local Density Approximation (LDA), to compare the results with the existing literature [134, 48], and PseudoDojo pseudopotentials [112]. The Bruneval-Gonze technique [157] was used to reduce the number of empty states N_b needed in the construction of the correlation self-energy Σ_c (Eq. 2.57). For low-dimensional

System	$E_{gap}^{G_0W_0}$ (eV)	Refs. (eV)	N_b	G_{cut} (Ry)	$\rho_{\mathbf{k}}$(Å^{-1})	$\Delta^{\Gamma-\Gamma}$(meV)	$\Delta_{\%}^{\Gamma-\Gamma}$
Si	1.18	1.16 [48]	400	16	0.33	10	0.3
Diamond	5.42	5.42 [160]	300	20	1	70	0.1
ZnO	2.36	2.35 [134]	800	28	0.25	10	0.4
TiO_2	3.2	3.2 [48]	600	12	0.2	10	0.3
MoS_2	2.54	2.49 [161]	400	8	0.25	10	0.3
hBN bulk	6.27	6.30 [162]	800	20	0.25	82	1.0
hBN 2D	6.84	6.58 [162]	1200	28	0.2	42	0.5

Table 3.1: Results for the G_0W_0 convergence tests. We observe good agreement between our results and ones taken from existing literature (shown in the third column). For completeness, the other columns report the converged number of empty states N_b, PW cutoff G_{cut} and irreducible Brillouin Zone (iBZ) **k**-points density $\rho_{\mathbf{k}}$, expressed as the maximum distance between adjacent points along a reciprocal axis. The last two columns refer to the convergence thresholds imposed on the $\Gamma - \Gamma$ G_0W_0 band gap, both in absolute ($\Delta^{\Gamma-\Gamma}$) and relative ($\Delta_{\%}^{\Gamma-\Gamma}$) terms. Deviations with respect to reference results may be due to different GW implementations and different KS-DFT starting points.

systems, spurious interactions between supercell replica are avoided using a slab truncation of the Coulomb potential [115] along the non-periodic direction, and its divergences are cured by means of the Random Integration Method [158] (RIM), which also accelerates convergence with respect to the BZ sampling. For 2D systems, specifically, we adopted a recently developed accelerating technique based on stochastic integration of the screened potential [159], which allows to have a GW-converged results using Monkhorst-Pack **k**-points grid just slightly denser than the DFT one.

We converged the $\Gamma - \Gamma$ band gap with respect to the two coupled parameters N_b and G_{cut} and the **k**-point grid as well, except for TiO_2 and ZnO. For these two systems, we considered fixed **k**-meshes of 8×8×12 and 8×8×6 respectively, already at convergence according to previous tests. Once was achieved convergence for a given system, we computed the minimum band gap. The results are summarized in Table 3.1, and they are found to be in good agreement with previous works (for each system, references are indicated in the table, and additional details are contained in Appendix F). Deviations with respect to reference results may be due to different GW implementations and different KS-DFT starting points used in the relative works [48].

The choice of the convergence settings, like the initial value of the parameters and the boundaries of the convergence space, is an important aspect to be tackled during the development of an optimization algorithm. We tested the efficiency

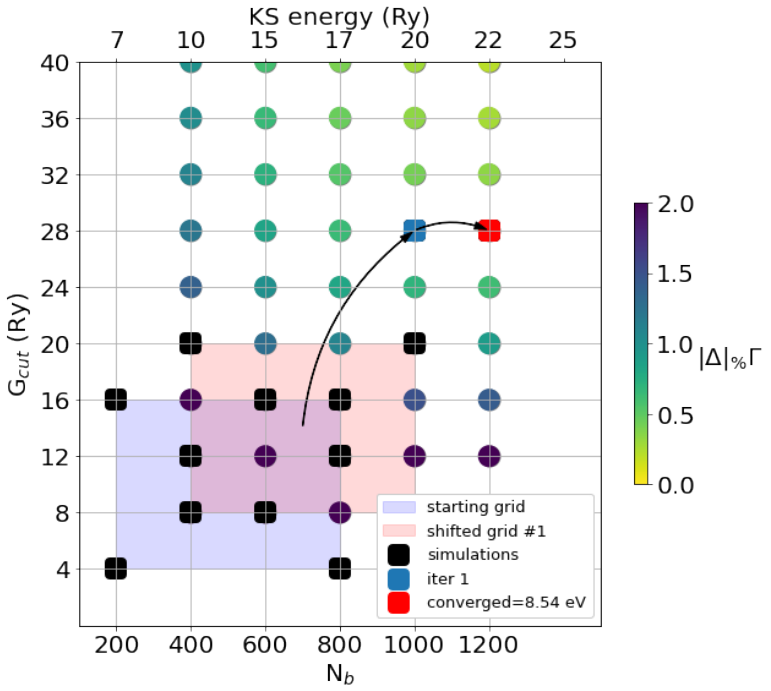

Figure 3.3: Coupled convergence of N_b and G_{cut} for the direct $\Gamma - \Gamma$ quasiparticle band gap of monolayer hBN. The colormap specifies the relative error with respect to the converged point with the highest value of the parameters. A maximum absolute error of $\Delta = 42$ meV is achieved for (N_b, G_{cut}) = (1200,28 Ry), corresponding to a maximum relative error of $\Delta_{\%} = 0.5$ %. Points not showed in the plot are either out of convergence or outside the boundaries imposed by input for what concerns maximum value of the parameters.

with respect to the starting parameter grid for the monolayer MoS_2, by using two different parameter grids: $N_b \in$ [200,800], $G_{cut} \in$ [4,20] Ry and $N_b \in$ [200,1200], $G_{cut} \in$ [8,24] Ry. The same converged couple (N_b,G_{cut}) = (400,8) is obtained, meaning that there is no change in the description of the space (i.e. we have the same fitting parameters) by changing the grid. For the other systems, we adopted the following parameter grid: $N_b \in$ [200,800], $G_{cut} \in$ [4,16] Ry. We found that in general (except for Silicon) this grid is not a sufficient starting guess, as a new shifted grid is always generated from the workflow to determine the converged point: $N_b \in$ [400,1000], $G_{cut} \in$ [8,20] Ry. Fig. 3.3 shows the convergence path for the monolayer hBN, where indeed a new grid (the red one) is created and then the converged result is found and verified to be consistent with the prediction. Anyway, in all cases, the workflow is able to achieve convergence after a limited number of calculations (<20). Figure 3.4 shows the convergence plot of the **k**-mesh in the 2D-hBN case. The workflow, as in the previous case, performed a limited number calculations on the parameter grid (in this case four calcula-

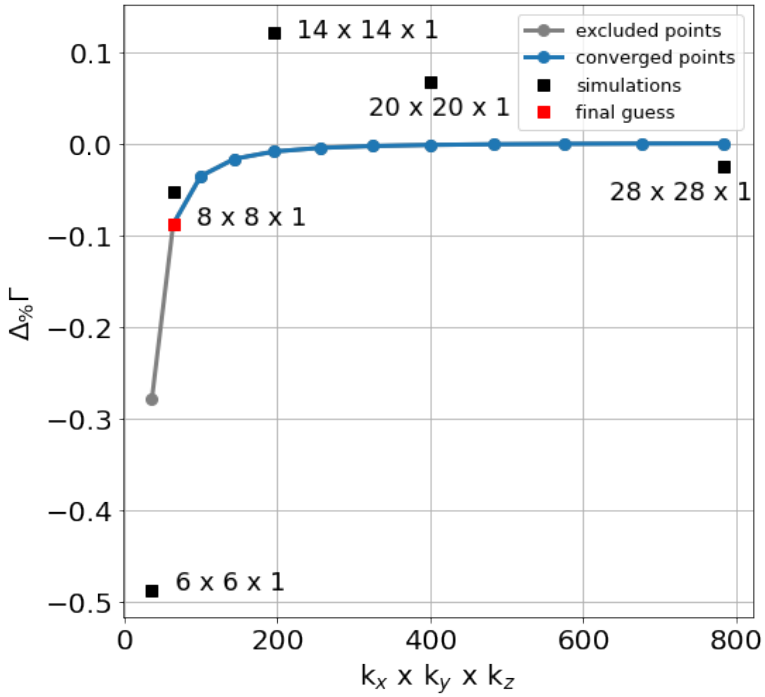

Figure 3.4: Convergence of the **k**-mesh for 2D hBN. The black points represent the actual calculations performed by the workflow on the parameter grid, whereas the blue points are the ones obtained within the fitting procedure and used to predict the convergence. After 5 simulations, the final mesh of 8×8×1 is predicted (and verified) to be converged.

tions, corresponding to the black squares of Fig. 3.4), and then a fit is performed, resulting in the prediction curve (blue curve). Despite the results of the simulations seem to have an oscillating behavior with respect to the fitted curve, it is important to note that the error bar considered in the plot is $\sim 0.13\%$ of the $\Gamma - \Gamma$ gap, i.e. $\sim$ 10 meV, similar to the accuracy of state-of-the-art GW. In the end, the **k**-mesh corresponding to the 8×8×1 is found to be the smallest parameter grid achieving converged gap. The parameter grids used in this work are guided by previous experience and heuristics, as there are no large scale studies devoted to define protocols as for DFT simulations, even if some attempts were done in the last years [144, 145]. Anyway, parameters can be efficiently expressed in terms of energy cutoffs (for the PW expansion), number of electrons (for the KS empty states) and inverse distances between points (for the **k**-point meshes). The `YamboConvergence` may be used in the future to capture default parameters also for MBPT simulations, both for convergence studies and single calculations with a certain level of desired accuracy, guided by statistical inference performed on a larger set of systems.

3.5 Automatic GW interpolation within `aiida-yambo-wannier90`

GW band interpolation from Wannierization is a crucial task in order to obtain the most accurate quasiparticle band structure with low computational cost. The `aiida-yambo-wannier90` plugin [163, 164] is a tool to perform this task. Essentially, the plugin provides a meta workflow, called `YamboWannier90WorkChain`, which utilizes the automation and error handling of the underlying `aiida-yambo` and `aiida-wannier90-workflows` plugins for GW convergence and Wannierization, respectively. The flowchart of the workflow is summarized in Fig. 3.5. Firstly, the workflow accepts a crystal structure as input, then launches a full `YamboConvergence` workflow for automatic convergence. Secondly, it finds the minimal commensurate mesh between GW and WANNIER90 (the exact procedure will be discussed in the next paragraph). If the commensurate mesh is different from the GW converged mesh, it launches an additional `YamboWorkflow` on the new mesh; otherwise this step is skipped. Thirdly, it runs a `YamboWorkflow` to compute the corresponding quasiparticle corrections needed for the Wannierization, and a subsequent `ypp` calculation to extract the GW correction in a WANNIER90 `eig` file format. Fourthly, the workflow Wannierizes the structure at DFT level, saves the unitary transformation matrices of maximal localization, and interpolates the band structure. Finally, the workflow launches the Wannierization at G0W0 level, which comprises the step of incorporating the GW corrections for eigenenergies, and the step of Wannier interpolation of the band structure.

During the workflow, one crucial step is finding a commensurate mesh for both the GW quasiparticle calculation and Wannierization. Specifically, the workflow utilizes `YamboConvergence` to converge the GW parameters. However, since Wannier interpolation requires a sufficiently dense **k**-point mesh to maintain interpolation accuracy, the automatically chosen GW mesh is not always compatible with WANNIER90 mesh. The Wannierization requires quasiparticle energies on a Monkhorst-Pack (MP) grid, therefore the GW mesh must be integer multiples of the MP grid.

We propose a recipe to find the commensurate meshes for both GW and WANNIER90, as depicted in Fig. 3.6. Suppose n_d is the number of **k**-points chosen by the YamboConvergence workflow, and n_c is the number of **k**-points chosen by the Wannierization protocol (**k**-point spacing = 0.2 Å^{-1} [149]), the target is to find a new (n'_d, n'_c) such that the dense mesh $n'_d = k \cdot n'_c$ where $k \in \mathbb{N}$, i.e. a natural number. The given input (n_d, n_c) restricts the search space to a sector bounded by k_{low} and k_{high} (see Fig. 3.6), where $k_{\text{low}} = 1$ since $n'_d = n'_c = \max(n_d, n_c)$ is always a good solution, and $k_{\text{high}} = \lceil \frac{n_d}{n_c} \rceil$ where $\lceil \cdot \rceil$ means the ceiling integer. Then we check each grid point between the two bounds and collect all the valid solutions. The search always succeeds since $s_{\text{low}} = (\max(n_d, n_c), \max(n_d, n_c))$ and $s_{\text{high}} = (k_{\text{high}} \cdot n_c, n_c)$ are already two good solutions. However, we want to look for

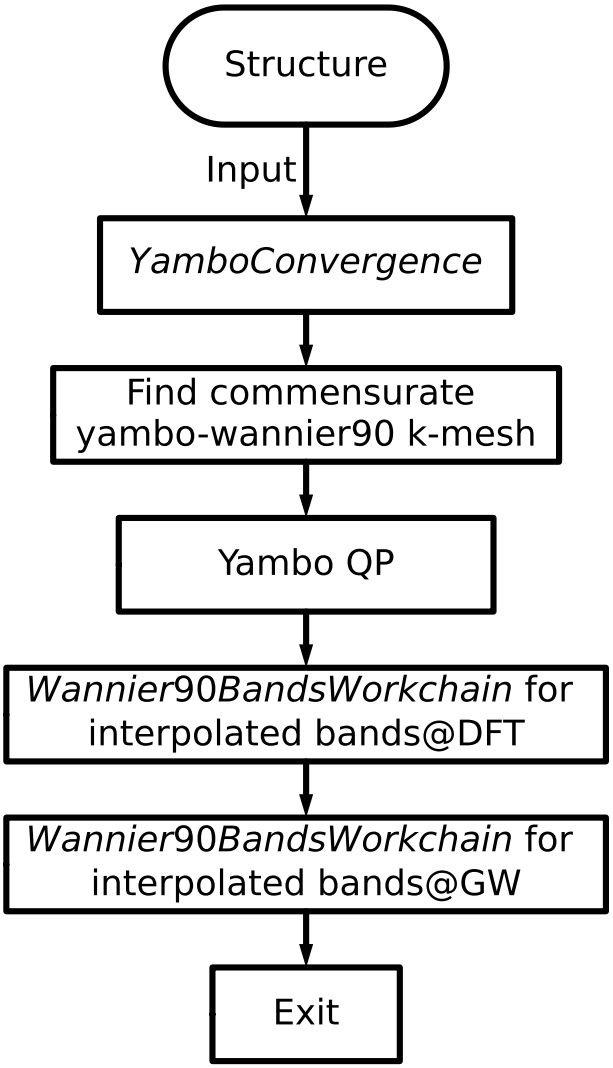

Figure 3.5: Flowchart of the `YamboWannier90WorkChain` for automated GW convergence and Wannier-interpolated GW band structure. The workflow performs the YAMBO convergence, searching of commensurate **k**-point mesh between YAMBO and WANNIER90, and running the Yambo quasiparticle calculation. The quasiparticle correction is provided and the final steps of the flow comprise the Wannierizations and the band interpolations at DFT level and GW level.

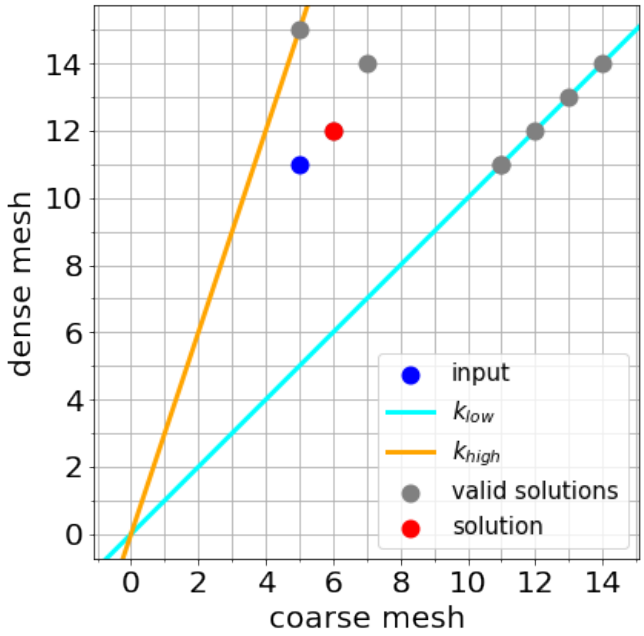

Figure 3.6: Recipe to find commensurate meshes for GW and WANNIER90, using an input meshes (11, 5) as an example. Final commensurate meshes (12,6) are found. The orange and cyan lines are the upper and lower bounds for searching the commensurate meshes, respectively. the grey dots are valid solutions, the red dot is the chosen solution which is the closest to the input, in the metric of ℓ^1 norm.

a computationally effective solution. In fact, often the optimal solution is inside the triangular region determined by the input (n_d, n_c), s_{low}, and s_{high}. The final solution is chosen according to the ℓ^1 distance to the input, therefore minimal increase of computational cost. It is also possible to change the metric, e.g., pushing the solution towards increasing the Wannier mesh or GW mesh, depending on which calculation is cheaper. The aforementioned recipe is repeated for each of the three dimensions of the MP grid, to find the commensurate meshes for arbitrary input.

3.6 Bands interpolation for Silicon and Copper

For Silicon, we tested also the `YamboWannier90` workchain, to validate the automatic W90@GW band interpolation workflow. Results are plotted in Fig. 3.7, where we compared the QUANTUM ESPRESSO bands, the interpolated W90@DFT and W90@GW bands. Comparison between the DFT bands shows that the results are almost identical, meaning that the Wannierization of the KS wavefunctions was precise enough. The typical quasiparticle band gap opening

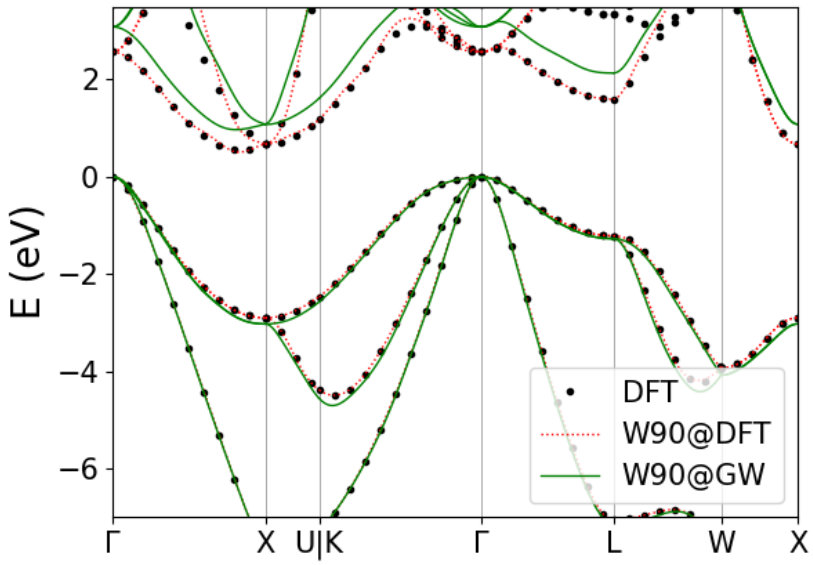

Figure 3.7: Interpolated band structure of Silicon for both DFT (red dashed) and GW (green solid) solutions, compared with the DFT bands (black dots). W90@DFT and DFT bands show very good agreement, as they are almost overlapping. The GW effect results in a larger final band gap. The top of the valence band is set to zero for both DFT and GW results.

is shown in the GW band structure. In the following we show the results obtained applying the automated band interpolation of Copper. Results are shown in Fig. 3.8, and the comparison between QE bands and W90@DFT shows a discrepancy of ~ 10 meV around the Fermi energy (here set to zero). Better accuracy can be achieved imposing more stringent values of the involved parameters. We observe that here the GW correction is very small around the Fermi level (~ 37 meV), but still not negligible. Moreover, here the GW convergence is more strict than Silicon, especially for the **k**-point mesh. Indeed, we need denser parameter grids to have a better approximation of the $\mathbf{q}\to 0$ intraband transition contribution, not explicitly included within the plasmon pole approximation. Converged parameters are (N_b, G_{cut}, $\rho_{\mathbf{k}}$) = (400, 18 Ry, 0.2 Å^{-1}). We needed 2900 quasiparticle evaluations (as we have 20 bands and 145 **k**-points in the iBZ) in order to interpolate the bands for the minimum converged Wannier90 **k**-point mesh (16×16×16). This quite large number of quasiparticle can be easily computed using the `YamboWorkflow` workchain.

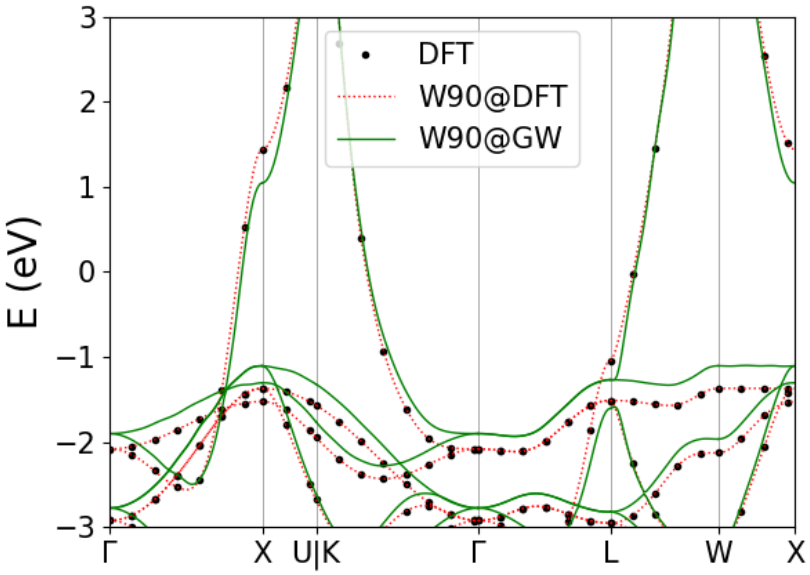

Figure 3.8: Bands interpolation for Copper. The GW correction around the (DFT) Fermi energy is not large, but must be considered for a correct description of properties like the Fermi surface.

3.7 Conclusions

In this Chapter we showed the successful design and implementation of advanced algorithms, to achieve complex tasks in a typical GW (BSE) flow: convergence between interdependent parameters, error handling and automatic band interpolation by means of Wannierization. We validated the tools on a few selected cases among semiconductors and metallic systems.

Chapter 4

Benchmarking the GW100 dataset with the Yambo code by means of G0W0 approximation

In the field of electronic structure and materials science, first principles computational methods are well established as techniques complementary to experimental science. Indeed, the predictive power of computational methods nowadays allows us to compare with experiments and drive them towards the discovery of novel properties and materials. Once the mathematical framework is defined (as is the case for DFT or MBPT), different numerical approaches should ideally yield the same results. However, this is not granted a priori and needs to be checked. When discrepancies are present, those are typically due to the fact that numerical implementations introduce several parameters, used to approximate exact equations and requiring careful, time-consuming and non-trivial convergence. In this respect, a validation of different computational approaches tackling the same problem is crucial in order to define their accuracy and reliability.

During the last decade, several assessments on the accuracy of Density Functional Theory (DFT) calculations for solids [165, 46] have been worked out, showing that most of the commonly used electronic structure codes can now predict essentially very similar results. These works are crucial both to support the reliability of existing methods, as well as for newly developed methodologies, that can be tested e.g. against these benchmarks for cross validation.

Similar studies concerning the quasiparticle energy levels of solids, relevant for the theoretical prediction of direct and inverse photoemission experiments [2], has been done in the past mainly concerning the comparison between theoretical and experimental results [166, 167, 168, 169]. A recent work by Rangel et al. [48] compared the G_0W_0 [1] quasiparticle properties of four solids (Si, Au, TiO_2, and ZnO), obtained within three different plane-wave (PW) codes: Yambo [64, 65], BerkeleyGW [170] (BGW) and Abinit [171]. These code differ in several aspects of their GW implementation, from the treatment of the Coulomb diver-

gences to the frequency integration schemes. On average, results agreed within 100 meV, addressing long-standing controversies on the GW results for difficult systems, such as ZnO.

Concerning molecules, early studies [172, 173, 174, 175] have focused on multiple small datasets mostly driven by specific scientific targets (e.g. molecules for photovoltaic applications) and not for benchmark purposes. More recently, a large scale community effort defining and making use of the GW100 dataset [66, 176] has focused (mostly but not exclusively [177]) on the single-shot G_0W_0 method [66, 152, 178], aiming at the evaluation of vertical ionization potential (IP) and electron affinity (EA). The chosen set was the GW100 dataset [176], a set of 100 closed-shell molecules[1], and results, published in the original GW100 paper [66], showed a discrepancy of around 200 meV of PW based codes with respect to localized basis set codes (which all agree within few meV).

In this work we provide the results for IP and EA of all the 100 molecules of the set as computed within the YAMBO code. In this way, we enlarge the GW100 benchmark considering the largely used Godby-Need Plasmon Pole Approximation [53] (GNPPA), used in YAMBO to describe the frequency dependence of the screening potential and not yet included in previous GW100 studies.

4.1 The GW100 dataset

The GW100 dataset is composed of 100 closed-shell molecules [66], in such a way to cover a wide IP energy range (4–25 eV) and a certain variety of chemical bonding configurations. For example, the set includes carbon-based covalent bonded compounds like C_2H_2, C_2H_4, C_2H_6, as well as ionic bonded molecules like the alkaline metal halide LiF. Moreover, some molecules in the set contain metal atoms (among them Ag_2, Li_2, K_2), and Na_4, Na_6 are included as representative of small metallic clusters. Common molecules such as water and carbon mono- and dioxide are also included. The structures of all molecules considered in this study are the ones from the official GW100 github repository [176], taken from experimental data (for a complete reference, we redirect the reader to Ref. 66) and sometimes optimised using PBE-based relaxation (within the def2-QZVP basis set). The geometries of two molecules of the set, CH_2CHBr and C_6H_5OH, were re-optimized in Ref. 152, and their final structures are taken from there.

For the sake of computing single shot G_0W_0 corrections, a DFT-PBE starting point is usually considered [98]. In this way, in principle, all codes should avoid the critical problem of the GW starting point [180, 181, 182] and give the same G0W0@PBE results. Of course, this is not the case, as different implementations may differ in several aspects. A partial discussion on similarities and differences

[1] They specifically decided to include only closed-shell molecules, to avoid well-known issues of open-shell systems [179].

of some of the approaches used by GW100 codes is reported in Refs. 66, 178, and we summarized the ones considered in this work in Table 4.1.

One of the most critical numerical aspect when comparing different codes is the choice of the basis set. A common choice, particular suitable for the description of extended systems, is the use of plane waves (PWs), which expand the eigenstates of the KS problem by means of Fourier coefficients. Convergence to the infinite basis set limit can be approached by just tuning a parameter, the kinetic energy cutoff used in the wavefunction expansion. On the other side, PWs require the use of pseudo-potentials, and, when dealing with isolated systems such as molecules or clusters, one drawback is that periodic boundary conditions (PBC) must be imposed anyway, resulting in the use of very large supercells to avoid spurious interaction between cell replica along non-periodic directions. In particular for GW simulations the long-range nature of the screened Coulomb interaction usually requires a larger extension of the vacuum region with respect to DFT requirements.

Other basis set used for GW100 studies are: projector augmented waves [183, 184] (PAW), linear augmented plane waves [185] (LAPW), linearized muffin tin orbitals [186] (LMTO), and local orbital (LO) basis sets. LO basis set, like def2-QZVP (contracted Gaussian orbitals [187] GTO, optimized for HF total energies), in particular, are more adapt for the description of isolated systems, and are significantly more compact (i.e. smaller) than the analogous PW sets. There, the main issue is that there is no unique way to increase the basis set expansion; hence in LO schemes it is much more difficult to control accuracy, especially in the description of higher energy states, with respect to other approaches.

An additional level of approximation is in the description of core and valence electrons and their interaction. As already mentioned, when using PWs, the pseudopotential approach [188, 189, 190, 191, 110] is mandatory and shown to be very successful in separating the two different contributions, considering explicitly only the valence electrons. Pseudopotentials may lead to sizable inaccuracies in GW calculations, e.g. because of the neglect of core effects and in particular of core-valence interactions [192, 181, 160], and need to be tested with care. The pseudopotentials used in this work to compute the Kohn-Sham (KS) single-particle energies and electronic density are the optimized norm-conserving Vanderbilt (ONCV) pseudopotentials SG15 [110, 111], and the KS-DFT exchange-correlation functional was approximated using GGA-PBE [98], as for all the other GW100 studies. Non-linear core corrections [113] (NLCC) are not included in the chosen pseudopotentials.

Another important aspect to consider when comparing different GW datasets is the treatment of the dynamical dependence of the screened interaction W. Indeed, the dynamical nature of W plays a key role both in terms of theoretical framework, since it distinguishes the GW approximation from other static theories like Hartree-Fock, as well as because it introduces additional computational challenges when evaluating GW corrections.

A number of different strategies to address this issue have been devised, ranging from fully-analytic [49] (FA) to full-frequency real-axis integration [51] (FF), analytic continuation [50] (AC), contour deformation (CD) [193] and multi-pole [54] (MP) approaches. The earliest and simplest approach to describe the frequency dependence of $W(\omega)$ in the context of GW, is the so called plasmon-pole approximation [52, 53] (PPA), based on a simplified description of the screening matrix. In this respect, PPA models represent a computationally-cheaper alternative to more sophisticated approaches. The basic idea behind PPA, also explained in Appendix C, consists in attributing, for each $\mathbf{q}, \mathbf{G}, \mathbf{G}'$ matrix element, all the spectral weight of the dynamical screening to a single pole:

$$\text{Re } \epsilon^{-1}_{\mathbf{G}\mathbf{G}'}(\mathbf{q},\omega) = 1 - \frac{A_{\mathbf{G}\mathbf{G}'}(\mathbf{q})\tilde{\omega}^2_{\mathbf{G}\mathbf{G}'}(\mathbf{q})}{\omega^2 - \tilde{\omega}^2_{\mathbf{G}\mathbf{G}'}(\mathbf{q})} \tag{4.1}$$

$$\begin{aligned}\text{Im } \epsilon^{-1}_{\mathbf{G}\mathbf{G}'}(\mathbf{q},\omega) &= A_{\mathbf{G}\mathbf{G}'}(\mathbf{q}) \times \\ &\times \left[\delta(\omega - \tilde{\omega}_{\mathbf{G}\mathbf{G}'}(\mathbf{q})) - \delta(\omega + \tilde{\omega}_{\mathbf{G}\mathbf{G}'}(\mathbf{q})\right],\end{aligned} \tag{4.2}$$

where the matrices $A_{\mathbf{G}\mathbf{G}'}(\mathbf{q})$ and $\tilde{\omega}^2_{\mathbf{G}\mathbf{G}'}(\mathbf{q})$ are the parameters of the model. Among the flavours of PPA [134], in this work we will adopt the Godby-Needs PPA (GNPPA) [53], which imposes the condition that the model should exactly fit the ϵ^{-1} function at zero frequency, i.e. $\omega = 0$, and at an imaginary frequency $\omega = iE_{\text{PPA}}$. Here, we set E_{PPA}= 30 eV. The Hybertsen-Louie generalized plasmon-pole model [52] (HLPPM), follows a different approach and, besides the evaluation of the screening at zero frequency, imposes a constraint on the fulfilling of the Johnson's frequency sum-rule (f-sum rule) [194]. For a detailed comparison of the two approaches see e.g. Refs. 134, 54. Importantly, numerical results obtained using GNPPA and HLPPM may differ significantly, as reported in the existing literature [134].

As an additional relevant point, considerable discrepancy between different GW approaches may be carried by the way to solve the quasiparticle equation:

$$E^{\text{qp}}_n = \epsilon^{\text{DFT}}_n + \langle\psi_n|\Sigma^{\text{GW}}(E^{\text{qp}}_n) - v^{\text{KS}}_{\text{xc}}|\psi_n\rangle. \tag{4.3}$$

This is a non-linear equation, also including the possibility to have multiple physical solutions. In this respect, approaches at different level of sophistication exist [66, 178], either addressing the full or a linearized version of the equation. In this work we solved the linearized quasiparticle equation (Newton's method) as implemented in the YAMBO code, which relies on assumption that the PPA self-energy is smooth near the quasiparticle energy. Alternative approaches, such as the secant method, can be used within the YAMBO implementation only in the FF case, which is not the subject of the current work.

Code	basis set	core-valence	empty states	χ-basis	Σ_c-integration	QP solutions	Refs.
TM [195]	def2-QZVP	AE	all	LO	FA [49]	largest weight	66
FHI-aims [196]	def2-QZVP*	AE	all	LO	AC [197, 196]	iterative method	66
BGW [170]	PW	NC	truncated [198]	PW	HLPPM [52]/FF [51]	linearized/graphical	66
VASP [199]	PAW*	PAW	all**	PW*	AC [200]	linearized	152
WEST [59]	PW	ONCV	avoided [58, 59]	PDEP* [201]	CD [193]	secant/linearized	178
Yambo [64, 65]	PW	ONCV	truncated [157]	PW	GNPPA [53]	linearized	this work

Table 4.1: Main approximations of the GW100 codes considered in this work. The * superscript means extrapolated. TM and FHI-aims make use of the resolution-of-identity (RI) technique to compute the four-center Coulomb integrals [66]. The ** superscript means all the states given the number of basis functions. The acronyms FA, AC and CD mean respectively fully-analytic, analytic continuation and contour deformation.

4.2 Technical details

4.2.1 Computational aspects

The accurate simulation of G_0W_0 quasiparticle corrections for isolated systems (like molecules) still represents a computational challenge when using plane-wave implementations and we had to resort to the use of high performance computing (HPC). As a general trend, current HPC architectures are extensively taking advantage of hardware accelerators based on graphical processing units (GPUs), significantly reducing the time-to-solution (and the energy-to-solution) with respect to CPU-only machines. In this respect, a profitable exploitation of GPU acceleration is a pre-requisite of our calculations. As an example, the timing for a typical G_0W_0 flow performed in this study is shown in the right panel of Fig. 4.1. Increasing the number of PWs used to describe the screening matrix (Eq. 2.17) clearly results in a longer time-to-solution, but still within a wall-time of 10 minutes. The cheapest calculation plotted in Fig. 4.1, which takes about 1 minute on GPUs, can take up to 20 minutes on a CPU-only machine using the same MPI/OpenMP (distributed/shared memory) parallel setup.

Anyway, the speedup granted by the GPU acceleration is often capped by a combination of several hardware (RAM amounts and bandwidth) and software (availability of GPU-aware distributed linear algebra (LA) libraries) limitations. In particular, our implementation does not support distributed LA, so large matrices requiring diagonalization have to be stored without memory distribution on each single GPU, quickly exceeding the RAM available on the cards (generally between 16 and 40 GB for current generation harware). For example, in computing the dynamical screening matrix ϵ, we need to compute the irreducible

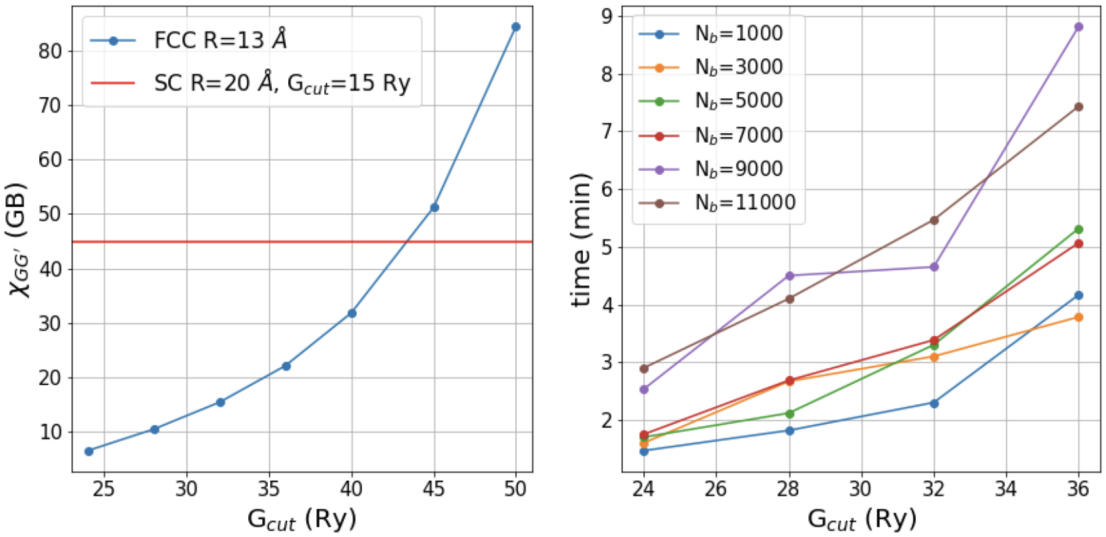

Figure 4.1: GPUs scalings. Left: cubic scaling of the memory needed to store the polarizability matrix $\chi_{GG'}$ with respect to the PW cutoff G_{cut}. We easily reach the maximum GPUs storage value of 40 GB around 40-45 Ry for the FCC reduced cell for the SC cell with 20 $\mathring{A}$ side, we observe that already at 15 Ry we need 45 GB, exceeding the GPUs memory. Right: time-to-solution with respect to N_b and G_{cut} using GPU acceleration. We observe that even for the largest matrices we usually need not more than 10 minutes, a very short time. Calculations are performed using 20-64 nodes of Juwels-Booster (Julich), each of them equipped with 4 A100 GPUs (40 GB of memory).The calculation with N_b=1000 and G_{cut}=24 Ry done with the same number of MPI tasks on a CPU-only machine takes $\sim$ 20 minutes instead of $\sim$1 minute. On average, all 24 calculations will take $\sim$ 1.5 hours per molecule on A100 GPUs the above mentioned memory resources.

polarizability matrix χ (Eq. 3.3)

$$(1 - v\chi_0)\chi = \chi_0. \tag{4.4}$$

To solve this problem on GPUs, we are currently forced to use serial routines and so the whole matrix has to be stored on a single GPU.

The specific problem of treating low-dimensional systems within PW codes lies almost entirely on the fact that we need a very large supercell to avoid spurious interactions among replicas along non-periodic directions. The consequence of large supercells are very short reciprocal lattice vectors, and a large number of PW needed for our expansions. This study is conducted using two PW codes, YAMBO and QUANTUM ESPRESSO, so that an optimized choice of the supercell is very beneficial. Other codes running the GW100 set used a simple-cubic (SC) supercell with different lattice parameters, up to a = 25 Å. In this work, for all molecules, we decided to use a face-centered-cubic (FCC) supercell of a = 13 $\mathring{A}$.

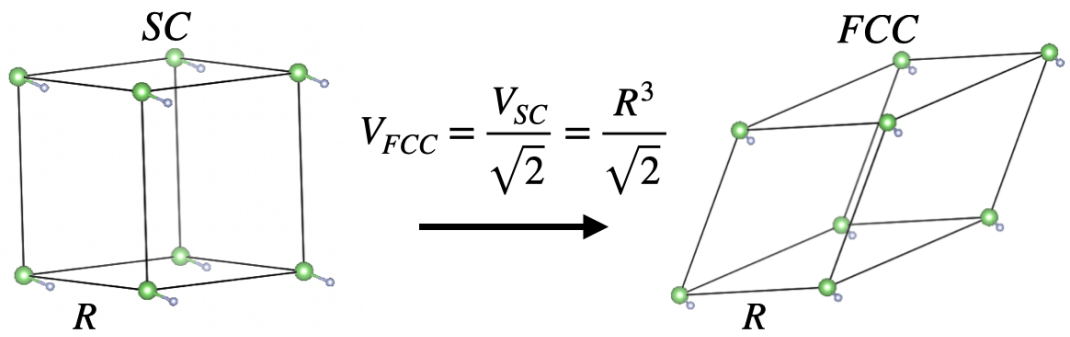

Figure 4.2: From SC to FCC. At the same NN distance a =13 $\mathring{A}$, the volume is reduced by a factor $\sqrt{2}$.

The use of FCC supercells reduces the required volume by a factor $\sqrt{2}$ with respect to cubic ones at fixed nearest neighbor (NN) distances, as shown in Fig. 4.2. This approach helps in reducing the memory needed to store the screening matrix, Eq. 2.17, which scales quadratically with the number of PW used, or cubic when considering the PW energy cutoff (here indicated as G_{cut}). For the sake of completeness, in the left panel of Fig. 4.1 we show the scaling of the $\chi_{\mathbf{GG'}}$ matrix size with respect to the imposed PW cutoff G_{cut}, for an FCC supercell of 13 $\mathring{A}$ side: The cubic scaling of the memory reaches the maximum size of 40 GB (considering NVIDIA A100 GPUs) for a PW cutoff of 43 Ry, while the memory required for G_{cut} = 15 Ry when using the SC cell with 20 $\mathring{A}$ side is already 45 GB (exceeding the GPU capability).

We should also consider that this memory limitation is further increased by the fact that we have to store additional quantities such as wavefunctions or temporary workspace for linear algebra.

We decided to use this small FCC cell in such a way to allow the other convergence parameters (detailed in what follows) to be large, as they are critical to evaluate convergence results, and to provide an estimation of the maximum error bar associated with our reduced volume. We performed the vacuum convergence test for two molecules: LiF and $C_5H_5N_5O$. The first one is very small, and is composed of only 10 electrons, whereas the latter has 56 electrons and is the most elongated molecule, with a maximum distance between two atoms of 7.5 $\mathring{A}$. Convergence data are shown in Fig. 4.3. We performed the calculations considering our FCC cell and three cubic cells of side 13, 20, and 24 $\mathring{A}$. We kept fixed N_b and G_{cut}, both given in terms of energy cutoff, at very low values, in such a way to also perform the calculations for very large supercells.

We observe a good convergence of ∼25 meV for LiF, and a larger discrepancy of ∼180 meV for $C_5H_5N_5O$. Increasing the other convergence parameters, the absolute value of the discrepancy seems to lower. As a result, the maximum error bar can be estimated to be about 180 meV for all the results shown here, but

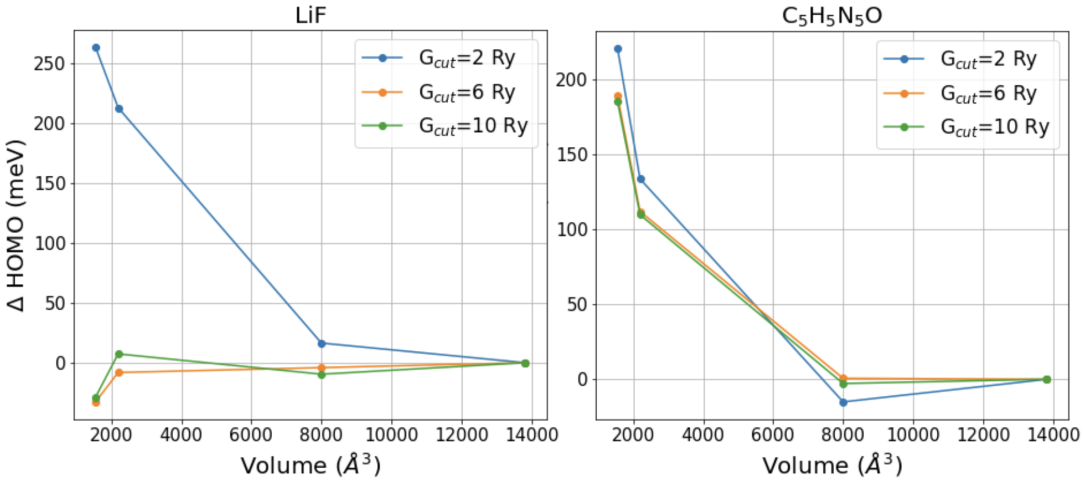

Figure 4.3: Convergence evaluation of the HOMO level for two molecules, LiF and $C_5H_5N_5O$, keeping fixed N_b=0.75 Ry and varying G_{cut} and the cell volume, corresponding to our FCC cell (the lowest volume) and SC cells of lattice vector **R**=13, 20 and 24 $\AA$. For LiF, we have a good convergence of ∼25 meV, whereas the $C_5H_5N_5O$, more elongated in real space than LiF, shows a worse convergence, of only ∼180 meV. Anyway, we can see that increasing the value of G_{cut} results in a better convergence agreement, meaning that an error bar of 180 meV is probably overestimated.

we expect that for the value of the parameters used in the simulations, as well as taking into account the smaller size of many of the GW100 molecules, the actual error bar is smaller. Finally, the usage of such a small cell is possible within YAMBO because we are using a spherical truncation of the Coulomb interaction [115], as implemented in YAMBO, combined with the Martyna-Tuckerman method [202] to correct both total energy and self-consistent-field potential at the DFT level. Moreover, the spherical truncation method cures analytically (i.e. exactly) the divergence of long-range part of the Coulomb interaction $v(\mathbf{q} \to 0)$.

The study is performed entirely on GPU-enabled machines and software, and resulted in a series of technical developments and optimizations to tackle the above-mentioned issues of graphical cards. Indeed, a strong cleanup of the YAMBO code was done in order to avoid memory duplication (i.e. storing data not strictly necessary) and complete the GPU porting of the routines involved in the GW flow. One of the most relevant software developments done during this work is the introduction of a new level of parallelization in the routine responsible of the calculation of the correlation self-energy Σ_c, concerning the block-distribution of the previous computed screening matrix $\epsilon_{\mathbf{GG'}}$. In this way, memory occupation for each single GPU is further reduced.

4.2.2 Interdependence of parameters and extrapolation

To obtain an accurate estimation of the quasiparticle GW corrections to the IP and EA, results need to be converged with respect to the number of empty states N_b and the number of reciprocal lattice vectors G_{cut} used in the evaluation of the screening matrix $\chi_{\mathbf{GG'}}$ and of the correlation Self-energy Σ_c. The parameter G_{cut} expresses the highest kinetic energy of the plane-waves included in the χ basis set, analogously to the kinetic cutoff used to represent wavefunctions, but usually lower. The two parameters N_b and G_{cut} are often found interdependent, so that we have to study their convergence simultaneously. Moreover, for single QP levels, this convergence is non-trivial and often not possible to be achieved for reasonable times-to-solution and computational resources. This is why, for standard studies, the gap is the quantity that is converged. Moreover, in the present study we use rather large supercells which imply a very large density of empty states and a huge number of reciprocal lattice vectors even for a small value of energy cutoff G_{cut}.

Due to the above-mentioned difficulties, the first approximation that we introduce is the usage of an extrapolation procedure to estimate the IP and EA of each molecule.

In this way, we compute quasiparticle corrections on a uniform 2D grid in the parameter space, and then a fit is performed. Except for the case of He and H_2, where we used a reduced grid for memory reasons, for each molecule we performed calculation on a rectangular grid for $(N_b, G_{cut}) \in [1000, 11000] \otimes [24, 36]$ (Ry), with spacing $(\Delta N_b, \Delta G_{cut}) = (2000, 4)$, for a total of 24 calculations per molecule.

The fit is then performed using the functional form:

$$f(N_b, G_{cut}) = \left(\frac{A}{N_b^{\alpha}} + b\right) \times \left(\frac{C}{G_{cut}^{\beta}} + d\right) \tag{4.5}$$

where the exponents α and β are chosen among [1,2,3] in such a way to minimize the mean absolute error (MAE) of the fit. A similar analytic form was already in use in the GW community [153, 60, 203, 144, 145] and captures the interdependence of the parameters (i.e. the Hessian of the convergence surface $f(N_b, G_{cut})$ is not diagonal). The extrapolated value then is

$$E_{extra}^{QP} = f(N_b \to \infty, G_{cut} \to \infty) = b \times d. \tag{4.6}$$

The parameters on which we decided to extrapolate are (N_b,G_{cut}), both expressed in terms of energy cutoff.

Further acceleration on N_b is obtained by using the Bruneval-Gonze (BG) terminator [157] procedure for the correlation part of the self-energy. This approximately accounts for all empty states non included explicitly in the sum-over-poles by adding an extra energy pole contribution. Such auxiliary pole is usually located at an energy E_{GT}=1 Ha higher than the last conduction state explicitly included. Here we performed an optimization of such pole energy and we found that the best value, i.e. the one for which we can achieve convergence faster, is E_{GT}=0.25 Ha. This is shown in the right panel of Fig.4.4. The need of such a small value with respect to the default one (mostly tested on solids) is due to the fact that in molecules, due to the large volume of the supercell, we have a high density of KS empty states, all very close to each other and contributing with small weight to the construction of the correlation self-energy. These contributions can be effectively captured by using an E_{GT} slightly higher than the last explicitly empty state used.

Moreover, during this work, the routine responsible of the BG was entirely ported on GPU (before it was only available for non-accelerated machines), where we have also optimized the search of reciprocal lattice $\mathbf{G}$ vectors involved in the remapping $\mathbf{G}''=\mathbf{G}'-\mathbf{G}$. This in particular is very useful when large supercells are used, due to the large number of G-vectors involved.

4.2.3 Validation of AiiDA workflows

This work is entirely performed using a workflow based on the `aiida-yambo` plugin [39, 40, 155, 63], which takes care of running all the calculations in an organised, reproducible, robust (in terms of error handling) and automatic way. As we are considering 100 molecules for a 2D parameters grid of 24 points, we computed in an automated way about 2400 calculations. The timing of a typical full molecule study is shown in the right panel of Fig. 4.1, showing that all calculations, even the largest ones, take less than 10 minutes to be completed,

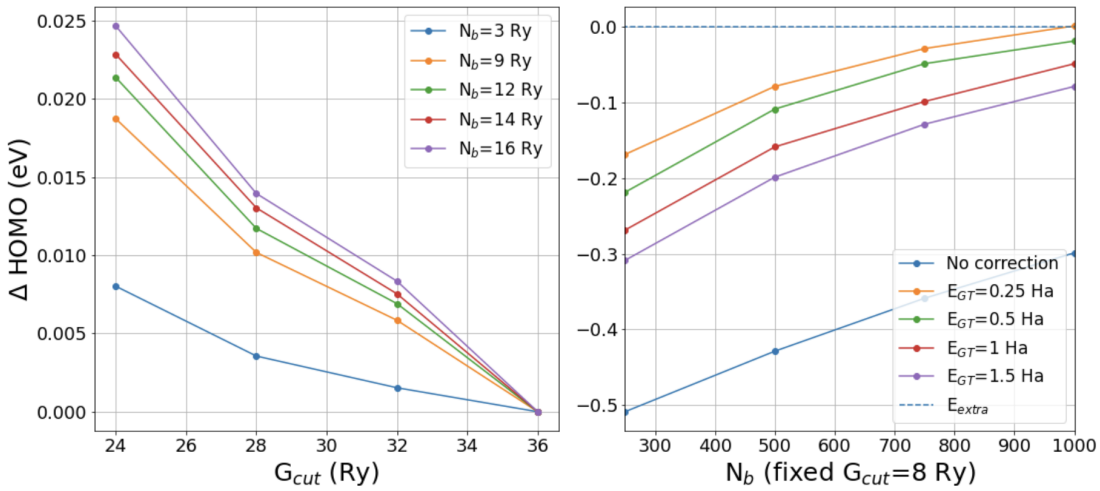

Figure 4.4: Convergence studies for the LiF molecule. On the left, we plotted the convergence the HOMO level with respect to the PW cutoff G_{cut} in the screening matrix, for different values of the number of empty states included N_b and setting to zero the results with the highest G_{cut} (used as reference). We can observe that increasing N_b puts G_{cut} more out of convergence. The values N_b = 3, 9, 12, 14, 16 Ry correspond to 1000, 5000, 7000, 9000 and 11000 bands. Right: optimization of the Bruneval-Gonze terminator energy E_{GT}, corresponding to the parameter *GTermEn* in the YAMBO code. We plotted the discrepancy with respect to the extrapolated value E_{extra} = 10.06 eV (set to zero in the plot). We observe that among the studied values, the one which allows us to approach faster the extrapolated value is E_{GT}=0.25 Ha. For this optimization, the parameter G_{cut} is fixed to 8 Ry.

for a total of 1.5 hours per molecule (including all 24 simulations). This is possible because of the computational speedup provided by GPU-accelerated machines and codes. The predicted wallclock time required to run the whole GW100 set was then estimated in about 150 hours. Calculations are performed using 20-64 nodes of Juwels-Booster (Julich), each of them equipped with 4 A100 GPUs (40 GB of memory). The actual average human time was actually $\sim 150/8 = 18.75$ hours, as most of the time 8 calculations are running at the same time and continuously (i.e. without human intervention to submit new calculations), thanks to the AiiDA scheduling system.

All results are contained in the AiiDA database and are fully reproducible, as all the parent calculations and inputs are stored as well. For each molecule of the set, we used the `YamboConvergence` workchain as implemented in the latest version of the `aiida-yambo` plugin. In this case, we do not want to reach convergence, but only to compute all the points belonging to the user-defined parameter grid, and then run the extrapolation with an ad-hoc python script. This work represents also a validation of the workflows implemented in the plugin, and the first HT-fashioned work done within this code.

4.3 Results

To compare with the other codes running the GW100 set, we computed for all 100 molecules the IP and EA. These are evaluated as:

$$\begin{aligned} IP &= E^{vac} - E^{HOMO} \\ EA &= E^{vac} - E^{LUMO} \end{aligned} \tag{4.7}$$

Where the vacuum energy level E^{vac} is evaluated at the DFT level and is determined by the electrostatics of the system. Results are provided in Tabs. 4.2 and 4.3 for what concerns IPs, and Tab. 4.5 for EAs.

We begin by discussing the verification and validation of IP and EA data computed using the DFT starting point (here PBE). Results are shown in the first column of the Tables (DFT label). These data are compared to results shown in the SI of Ref. 178, obtained with the same code (Quantum ESPRESSO) and the same SG15 pseudopotentials. The only difference here is represented by the unit cell. In Ref. 178, a SC supercell of 25 $\mathring{A}$ side is used, very large with respect to our FCC cell with a lattice vector of 13 $\mathring{A}$. We found a very good agreement of few meV for the majority of the cases. This is not surprising as DFT calculations present a faster convergence with respect to the vacuum introduced in the supercell. Considering the PBE-HOMO results reported for GTO (de2-QZVP) calculations in the SI of Ref. 66, the agreement shows a smaller discrepancy with respect to non-extrapolated basis. This is shown and justified also for VASP results in Ref. 152.

The situation is different when we consider QP HOMO and LUMO corrections, where we have the long-range Coulomb interaction and several additional parameters and approximations to be taken into account during the comparison. We first analyze the convergence of our IP and EA computed at the highest value of the parameters with respect to the extrapolated value, to understand how far we are from the true convergence of HOMO and LUMO QP corrections. In Fig. 4.5 we show an histogram of frequency distribution for the deviation of both IP and EA with respect to extrapolation, for all the 100 molecules. On average, results converge within a mean absolute error (MAE) of 64 and 39 meV, for IP and EA, respectively. We decided to consider as final results the extrapolated ones. Extrapolation can be considered robust in particular when we are solving the linearized QP equation, as its solution is unique in the range of interest. This suggests to focus our analysis to the comparison with other codes taking linearized solutions: $\text{West}^{extra}_{lin}$, VASP, and $\text{BGW}_{\text{HLPPM}}$. Indeed, Tabs. 4.2 and 4.3 show the

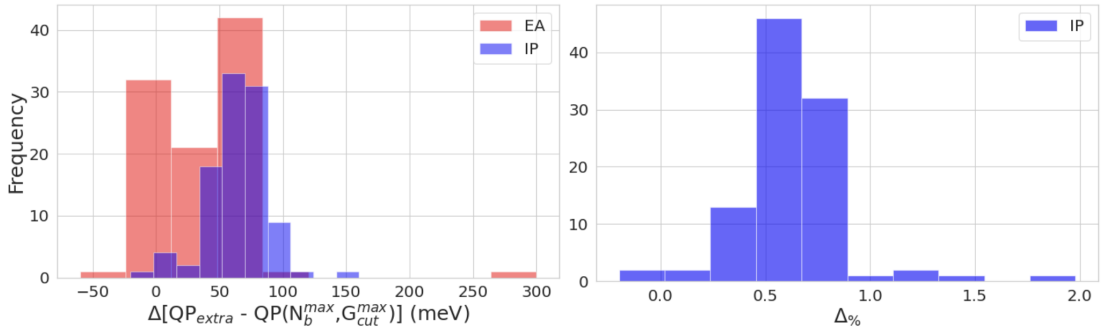

Figure 4.5: Convergence evaluation of Yambo results. Left panel: evaluation of the convergence of IP and EA with respect to the extrapolated value. We observe a MAE of 64 and 39 meV for IP and EA, indicating that part of the molecules are still out of convergence. For this reason we retain as final results the extrapolated ones. Right: evaluation of the relative error with respect to extrapolation for the QP-IP. On the right panel we show the frequency of relative convergence deviation. We can see that in general a good relative convergence threshold lower than 2% is achieved for all molecules.

results for the IP obtained in this work, together with the previous results from other GW codes, CCSD [204] (quantum chemistry methods) and experimental data. These last ones are taken from the NIST database [205].

As expected, different implementations of the G_0W_0 theory agree only within a few to hundreds meV. This is presented in Table 4.4, where the mean error (ME), the MAE, and the mean absolute relative error (MARE) of Yambo results with respect to other codes are shown. We found the best agreement (i.e. the lowest errors) with $\text{West}^{extra}_{sol}$, and a very good agreement with VASP and $\text{West}^{extra}_{lin}$ results. The last two are cases in which, as in our work, the QP equation is linearized. The linearized QP solution is computed also in the $\text{BGW}_{\text{HLPPM}}$ case but,

index	Formula	DFT	Yambo$_{extra}$	West$^{extra}_{lin}$	West$^{extra}_{sol}$	VASP	TM	FHI-aims	BGW$_{HLPPM}$	BGW$_{FF}$	CCSD	EXP
1	He	15.76	23.43	23.65	23.42	23.62	23.48	23.48	24.1	-	24.51	24.59
2	Ne	13.33	20.05	20.52	20.33	20.36	20.38	20.38	21.35	-	21.32	21.56
3	Ar	10.26	15.32	15.5	15.37	15.42	15.13	15.13	15.94	-	15.54	15.76
4	Kr	9.25	13.83	13.87	13.76	14.03	13.57	13.57	14.0	-	13.94	14.0
5	Xe	8.23	13.48	13.38	13.22	12.22	12.0	12.02	12.08	-	-	12.13
6	H_2	10.39	16.03	16.03	15.84	16.06	15.81	15.82	16.23	-	16.4	15.43
7	Li_2	3.23	5.24	5.19	5.04	5.32	5.0	4.99	5.43	-	5.27	4.73
8	Na_2	3.12	5.11	5.07	4.98	5.06	4.84	4.83	5.03	-	4.95	4.89
9	Na_4	2.33	4.13	4.28	4.24	4.23	4.12	4.1	4.34	-	4.22	4.27
10	Na_6	2.4	4.04	4.42	4.37	4.4	4.24	4.24	4.47	-	4.35	4.12
11	K_2	2.51	4.3	4.21	4.14	4.24	3.99	3.98	4.02	-	4.06	4.06
12	Rb_2	2.37	4.14	4.08	4.01	4.14	3.79	3.8	3.92	-	3.92	3.9
13	N_2	10.29	14.84	15.08	14.94	15.06	14.89	14.89	15.43	14.72	15.57	15.58
14	P_2	7.11	10.57	10.48	10.43	10.4	10.2	10.21	10.66	-	10.47	10.62
15	As_2	6.49	9.7	9.58	9.55	9.62	9.47	9.47	9.67	-	9.78	10.0
16	F_2	9.42	14.6	15.16	15.0	15.08	14.96	14.96	15.59	14.73	15.71	15.7
17	Cl_2	7.28	11.43	11.5	11.41	11.4	11.1	11.1	11.85	-	11.41	11.49
18	Br_2	6.8	10.5	10.52	10.44	10.65	10.22	10.22	10.64	-	10.54	10.51
19	I_2	6.26	10.59	10.56	10.41	9.59	9.24	9.28	9.58	-	9.51	9.36
20	CH_4	9.46	14.01	14.1	13.99	14.14	13.93	13.93	14.28	13.8	14.37	13.6
21	C_2H_6	8.16	12.42	12.53	12.44	12.58	12.36	12.36	12.63	12.22	13.04	11.99
22	C_3H_8	7.76	11.84	11.92	11.84	11.98	11.8	11.79	12.05	-	12.05	11.51
23	C_4H_{10}	7.57	11.51	11.48	11.41	11.69	11.49	11.49	11.73	-	11.57	11.09
24	C_2H_4	6.77	10.47	10.46	10.39	10.5	10.32	10.32	10.68	10.3	10.67	10.68
25	C_2H_2	7.19	11.16	11.18	11.09	11.24	11.02	11.02	11.35	10.97	11.42	11.49
26	C_4	7.26	10.96	10.97	10.9	10.97	10.78	10.78	11.49	-	11.26	12.54
27	C_3H_6	7.06	10.62	10.73	10.67	10.78	10.55	10.56	10.93	-	10.86	10.54
28	C_6H_6	6.33	9.09	9.13	9.08	9.16	8.99	8.99	9.21	-	9.29	9.23
29	C_8H_8	5.28	8.09	8.2	8.16	8.24	8.06	8.06	8.47	-	8.35	8.43
30	C_5H_6	5.4	8.47	8.49	8.44	8.51	8.35	8.35	8.77	-	8.68	8.53
31	C_2H_3F	6.55	10.28	10.36	10.29	10.36	10.2	10.2	10.8	10.14	10.55	10.63
32	C_2H_3Cl	6.43	9.96	10.0	9.94	10.0	9.76	9.76	10.32	-	10.09	10.2
33	C_2H_3Br	5.83	9.16	9.71	9.64	9.83	8.99	8.99	9.42	-	9.27	9.9
34	C_2H_3I	6.04	9.9	9.94	9.81	9.36	9.02	9.04	9.48	-	9.33	9.35
35	CF_4	10.44	15.13	15.65	15.51	15.53	15.37	15.36	15.96	-	16.3	16.2
36	CCl_4	7.66	11.33	11.41	11.29	11.31	10.98	10.98	11.77	-	11.56	11.69
37	CBr_4	6.92	10.15	10.22	10.11	10.38	9.9	9.9	10.4	-	10.46	10.54
38	CI_4	6.13	10.01	-	-	9.23	8.75	8.82	9.23	-	9.27	9.1
39	SiH_4	8.51	12.59	12.55	12.42	12.53	12.31	12.31	12.77	-	12.8	12.3
40	GeH_4	8.36	12.53	12.44	12.32	12.24	12.02	12.02	12.28	-	12.5	11.34
41	Si_2H_6	7.27	10.6	10.58	10.52	10.52	10.31	10.31	10.8	-	10.64	10.53
42	Si_5H_{12}	6.1	8.7	9.25	9.19	9.19	8.94	8.94	9.45	-	9.27	9.36
43	LiH	4.36	7.55	7.2	6.62	7.2	6.55	6.54	7.85	6.67	7.96	7.9
44	KH	3.48	5.99	5.39	4.97	5.37	4.86	4.86	5.76	-	6.13	8.0
45	BH_3	8.5	13.06	13.08	12.95	13.09	12.87	12.87	13.28	-	13.28	12.03
46	B_2H_6	7.88	12.01	12.03	11.92	12.04	11.84	11.84	12.17	-	12.26	11.9
47	NH_3	6.16	10.29	10.4	10.18	10.44	10.32	10.32	10.93	-	10.81	10.82
48	HN_3	6.82	10.32	10.54	10.48	10.56	10.4	10.4	10.96	-	10.68	10.72
49	PH_3	6.72	10.61	10.51	10.43	10.45	10.27	10.27	10.79	-	10.52	10.59
50	AsH_3	6.78	10.44	10.4	10.33	10.36	10.12	10.12	10.45	-	10.4	10.58

Table 4.2: Quasiparticle Ionization Potentials of the first 50 molecules of the GW100 dataset as obtained within this work (the last 50 molecules are presented in Table 4.3). Both DFT and QP values are indicated, and for all of the other considered codes the QP-IP values are shown. For almost all molecules, codes agree with a discrepancy of few hundreds of meV.

index	Formula	DFT	Yambo$_{extra}$	West$^{extra}_{lin}$	West$^{extra}_{sol}$	VASP	TM	FHI-aims	BGW$_{HLPPM}$	BGW$_{FF}$	CCSD	EXP
51	SH_2	6.29	10.37	10.36	10.23	10.3	10.03	10.03	10.64	-	10.31	10.5
52	FH	9.65	15.03	15.47	15.23	15.38	15.3	15.3	16.24	-	16.03	16.12
53	ClH	8.03	12.57	12.6	12.48	12.51	12.24	12.25	12.97	-	12.59	12.79
54	LiF	6.13	10.34	10.54	10.11	10.45	9.95	9.95	11.84	-	11.32	11.3
55	F_2Mg	8.31	12.59	12.84	12.46	12.77	12.32	12.32	13.73	12.44	13.71	13.3
56	TiF_4	10.45	13.95	14.31	-	14.22	13.9	13.89	14.88	-	15.48	13.3
57	AlF_3	9.72	14.22	14.63	14.4	14.53	14.25	14.25	15.11	-	15.46	15.45
58	BF	6.78	11.08	10.71	10.56	10.67	10.56	10.56	11.49	-	11.09	11.0
59	SF_4	8.37	12.4	12.41	12.32	12.29	12.12	12.12	12.79	-	12.59	11.69
60	BrK	4.72	8.1	7.96	-	8.04	7.3	7.3	7.99	-	8.13	8.82
61	GaCl	6.58	10.28	10.27	10.19	9.99	9.56	9.55	10.24	-	9.77	10.07
62	NaCl	5.29	9.01	-	-	8.76	8.07	8.1	9.6	-	9.03	9.8
63	$MgCl_2$	7.61	11.44	11.47	11.25	11.41	10.99	10.99	11.98	-	11.66	11.8
64	AlI_3	6.48	10.3	10.59	10.31	9.69	9.28	9.32	9.67	-	9.82	9.66
65	BN	7.47	11.31	-	-	10.61	11.0	11.03	12.19	9.68	11.89	11.5
66	NCH	9.04	13.28	13.41	13.22	13.43	13.21	13.21	13.87	-	13.87	13.61
67	PN	7.74	11.26	11.43	11.26	11.41	11.14	11.14	12.13	-	11.74	11.88
68	H_2NNH_2	5.28	9.23	9.42	9.27	9.45	9.28	9.28	9.78	9.1	9.72	8.98
69	H_2CO	6.27	10.24	10.56	10.41	10.57	10.33	10.33	11.02	-	10.84	10.88
70	CH_4O	6.35	10.36	10.74	10.6	10.72	10.56	10.56	11.14	-	11.04	10.96
71	C_2H_6O	6.16	9.97	10.36	10.21	10.33	10.16	10.16	10.57	-	10.68	10.64
72	C_2H_4O	5.97	9.49	9.81	9.61	9.8	9.55	9.55	10.16	9.43	10.21	10.24
73	$C_4H_{10}O$	5.77	9.09	9.52	9.4	9.52	9.32	9.32	9.7	-	9.82	9.61
74	CH_2O_2	6.95	10.72	11.01	10.82	10.98	10.73	10.73	11.39	-	11.42	11.5
75	HOOH	6.45	10.79	11.16	11.0	11.12	10.99	10.99	11.58	10.82	11.59	11.7
76	H_2O	7.25	11.81	12.09	11.87	12.05	11.97	11.97	12.75	11.68	12.56	12.62
77	CO_2	9.1	13.1	13.46	13.37	13.44	13.25	13.25	13.81	13.17	13.71	13.77
78	CS_2	6.79	10.09	10.1	10.05	10.01	9.75	9.75	10.37	-	9.98	10.09
79	OCS	7.48	11.14	-	-	11.13	10.91	10.91	11.49	11.02	11.17	11.19
80	OCSe	6.94	10.45	10.43	10.37	10.5	10.2	10.2	10.55	-	10.78	10.37
81	CO	9.35	13.77	13.79	13.66	13.76	13.57	13.57	14.33	-	14.21	14.01
82	O_3	7.95	11.86	-	-	12.07	11.4	11.39	13.05	12.0	12.55	12.73
83	SO_2	8.04	11.81	12.08	11.96	12.04	11.82	11.82	12.55	-	13.49	12.5
84	BeO	6.17	9.57	-	-	9.5	8.51	8.58	10.66	8.45	9.94	10.1
85	MgO	4.8	7.32	-	-	7.1	6.68	6.68	8.51	7.08	7.49	8.76
86	C_7H_8	5.97	8.64	8.75	8.71	8.79	8.61	8.61	8.97	-	8.9	8.82
87	C_8H_{10}	5.92	8.51	8.7	8.66	8.73	8.55	8.55	8.92	-	8.85	8.77
88	C_6F_6	6.64	9.46	9.7	9.65	9.69	9.49	9.49	10.04	-	9.93	10.2
89	C_6H_5OH	5.62	8.34	8.42	8.37	8.43	8.37	8.37	8.72	-	8.7	8.75
90	$C_6H_5NH_2$	5.0	7.62	7.8	7.73	7.84	7.64	7.64	7.98	-	7.99	8.05
91	C_5H_5N	5.92	9.07	9.28	9.13	9.31	9.04	9.04	9.5	-	9.66	9.66
92	$C_5H_5N_5O$	5.21	7.52	7.86	7.82	8.18	7.69	7.69	7.92	-	8.03	8.24
93	$C_5H_5N_5O$	5.5	7.88	8.14	8.09	8.18	7.98	7.98	8.35	-	8.33	8.48
94	$C_4H_5N_3O$	5.71	8.23	8.49	8.4	8.5	8.29	8.29	8.77	-	9.51	8.94
95	$C_5H_6N_2O_2$	6.0	8.62	8.88	8.82	8.89	8.71	8.71	9.19	-	9.08	9.2
96	$C_4H_4N_2O_2$	6.27	9.22	9.26	9.19	9.55	9.22	9.22	9.94	-	10.12	9.68
97	CH_4N_2O	5.93	9.33	9.6	9.4	9.59	9.32	9.32	9.94	-	10.05	9.8
98	Ag_2	5.19	8.27	8.12	8.04	7.95	7.67	7.07	8.57	-	7.49	7.66
99	Cu_2	4.75	7.6	-	-	7.4	6.68	7.54	8.6	-	7.57	7.46
100	NCCu	6.78	10.09	-	-	9.99	9.42	9.42	10.91	-	10.85	-

Table 4.3: Continuation of Table 4.2, representing the second half of the IP comparison.

Code	ME (meV)	MAE (meV)	MARE (%)	σ (meV)
BGW_{HLPPM}	-406	515	5	332
BGW_{FF}	269	308	3	424
$\mathrm{West}^{extra}_{sol}$	5.7	157	1.8	166
$\mathrm{West}^{extra}_{lin}$	-122	178	1.8	1359
VASP	-49	234	2.4	213
TM	226	301	3.2	320
AIMS	220	295	3.1	319
CCSD	-343	450	4.2	372
EXP	-259	535	5.2	398

Table 4.4: Mean error (ME), mean absolute error (MAE), mean absolute relative error (MARE) and standard deviation (σ) for the quasiparticle ionization potential between Yambo and other past results, coming from different codes and approximations. We also included experimental (EXP) results. The best agreement is found to be with $\mathrm{West}^{extra}_{sol}$. The largest MAE is found to be with experiments.

as already pointed out in the past [134, 48], the GNPPA and the HLPPM can in general give sensibly different results due to the different constraints imposed during the approximation. The largest MAE concerns the comparison with experimental values, probably due to the neglect of finite temperature effects and coupling with ionic degrees of freedom, but also GW self-consistency, vertex corrections [66]. In this case, the $\mathrm{BGW}_{\mathrm{HLPPM}}$ is shown [66] to have better agreement with experiments [206, 66].

Comparisons with other codes can be further analyzed by means of the violin plot (a box plot combined with a density plot) shown in Fig. 4.6. In general, we observe that the IPs computed within Yambo agree well with the results of other PW codes like West (both linearized and full versions) and VASP. Slightly larger discrepancy is found with respect to LO basis set codes like Turbomole and FHI-aims, as well as with full-frequency BGW_{FF}, anyway with a MAE around 350 meV. This discrepancy is probably due to the usage of a Plasmon-pole approximation for Yambo calculations, and partially due to the fact that we are not considering multiple solutions of QP equation, but only the linearized case. For all these plots, we observe an asymmetric distribution of the results where, depending on the reference code, Yambo overestimates or underestimated the IP-QP correction. The width of each main peak is related to the standard deviation

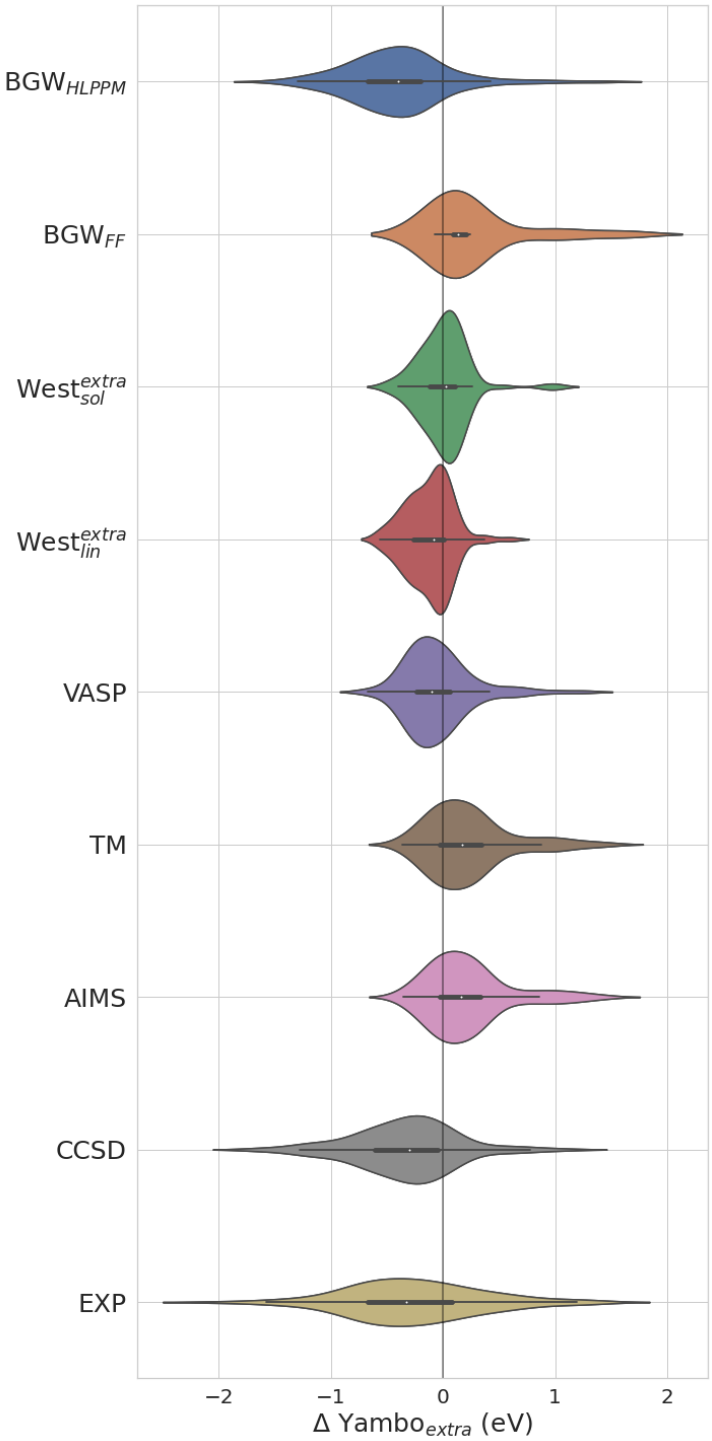

Figure 4.6: Violin plot representing the distribution of the deviation between Yambo and other codes IP. We observe good agreement between Yambo and almost all other results within a few hundreds of meV. The best agreement is found to be with the WEST code. For West$^{extra}_{lin}$ we found that 40% of the results deviate from Yambo results by less than 100 meV. The West$^{extra}_{sol}$ instead presents a peak around 100 meV, due to 38% of the molecules. Outliers, where the absolute deviation is larger than 1 eV, are only a small part of the dataset.

σ, shown in Table 4.4.

In particular, when comparing with $\text{West}_{lin}^{extra}$ data, we observe a systematic deviation peaked around ~ 0 meV for ~ 40 % of the molecules (i.e. 40 molecules), with a σ of only ~ 50 meV. Moreover, an additional shoulder is found at $\sim$ -120 meV. We observe the presence of some outliers for almost all distributions. Specifically the largest deviation with respect to VASP results is due to the Xe molecule, with a deviation of 1.39 eV. Instead, we found that comparing with $\text{West}_{lin}^{extra}$ (with experimental results) the KH molecule presents the largest discrepancy of 600 meV (2 eV), and that significant absolute deviations around 400-500 meV are mainly composed of molecules containing fluorine (F_2, AlF_3, CF_4). This is probably due to the fact the 3d and 2p electrons are strongly localized and challenging to be described within PW approaches.

We can safely assert that our results, carried out within the GNPPA, outperforms in terms of verification the ones obtained with HLPPM as ours better agree with all other codes, except for the CCSD datasets and experimental results. For example, $\text{BGW}_{\text{HLPPM}}$ presents a ME of 254 meV and a MAE of 354 meV with respect to $\text{West}_{lin}^{extra}$. Almost all plots in Fig. 4.6 show an asymmetric distribution towards the overestimation of the IP of Yambo with respect to the other results. The only exceptions are $\text{BGW}_{\text{HLPPM}}$, CCSD and experiments.

As an additional source of discrepancy we identify the reduced amount of vacuum due to the FCC supercells used in this work, as compared to other calculations (like the SC of 25 $\mathring{A}$ side of West [178]). According to our tests, the use of a smaller amount of vacuum results in an underestimation of the quasiparticle IP. In particular with respect to the other linearized solutions ($\text{West}_{lin}^{extra}$, VASP and $\text{BGW}_{\text{HLPPM}}$), we found that indeed our results indicate an underestimation of the IP up to a maximum of 150 meV. This is the region where the VASP peak (more or less represented by 30% of the molecules) in Fig. 4.6 is positioned (in the negative part of the x-axis, so $\sim$-150 meV), and also corresponds to a significant portion (the second highest peak, at $\sim$ -150 meV) of the $\text{West}_{lin}^{extra}$ area (around 30% of the molecules). Moreover, if we consider as an example the two molecules used in our vacuum convergence tests (LiF and $C_5H_5N_5O$, see Fig. 4.3), the discrepancy with respect to $\text{West}_{lin}^{extra}$ and VASP is 340 and 160 meV, respectively. Such an error is compatible with the error bar associated to the volume, estimated here to be ~ 180 meV.

As a final comment, we cannot find a correlation between the error due to the result extrapolation (as compared with our best converged results) and discrepancies with respect to other codes, as shown in Fig. 4.7. This means that the most critical aspects responsible for the discrepancies with the other codes are mainly the following:

- Different numerical implementations;
- reduced FCC volume.

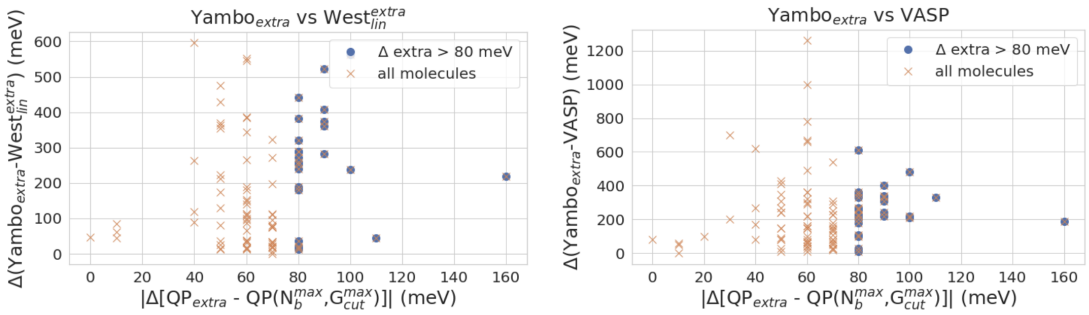

Figure 4.7: Comparison between the error given by the extrapolation procedure (x-axis) and the discrepancies with other codes (y-axis). We cannot find correlation between the two quantities, meaning that difference in results can be only addressed in a minor part to the extrapolation of YAMBO results.

For the analysis of EA data, we just compared our results with the WEST ones, obtained in the linearized version of the QP solution. A summary of the results is shown in Table 4.5, and a distribution of the deviation between Yambo and WEST is shown in Fig. 4.8. The EA results seem to have an accuracy similar to the IP ones, with a ME and a MAE of respectively -15 and 221 meV. As for the IP case, larger deviations >100 meV are observed mainly for molecules with fluorine: F_2, AlF_3, SF_4, TiF_4. The largest deviation of the series, due to the SF_4 molecules, is also justified by the fact that even at the DFT level the LUMO shows a considerable discrepancy of $\sim$ 600 meV with other existing results (see e.g. SI of Ref. [178]).

4.4 Conclusions

In this work we have performed benchmark analysis of IP and EA of 100 molecules in the GW100 set computed with G_0W_0 method as implemented in the Yambo code. We have compared our data against previous results presented in the literature and coming from different approximations and methodologies (GW implemented using PW and LO basis sets, other methods such as CCSD, and also experimental data). In particular, for the first time we provided G_0W_0 results for the GW100 set using the GNPPA approximation for the dynamical dielectric matrix. We successfully performed the study entirely on GPU-accelerated machines and using automated workflows as implemented in the `aiida-yambo` plugin. As additional outcomes of the work, further GPU-oriented optimization of the YAMBO code has been achieved.

We observe that, in general, results present small deviations with respect to other codes, and that the main sources of discrepancy are probably coming from the different approaches to solve the quasiparticle equation, here only linearized,

index	Formula	DFT	Yambo$_{extra}$	West$^{extra}_{lin}$
7	Li_2	1.75	0.76	0.58
8	Na_2	1.7	0.79	0.58
9	Na_4	1.8	1.04	1.04
10	Na_6	1.43	0.93	1.0
11	K_2	1.33	0.79	0.72
12	Rb_2	1.17	0.65	0.71
14	P_2	3.42	1.08	1.08
15	As_2	3.39	1.08	1.08
16	F_2	5.94	0.3	1.05
17	Cl_2	4.22	1.25	1.37
18	Br_2	4.49	1.79	1.87
19	I_2	4.44	3.17	3.21
26	C_4	6.05	2.93	3.11
29	C_8H_8	2.29	-0.04	0.05
35	CCl_4	2.69	0.31	0.39
36	CBr_4	3.48	1.42	1.44
37	CI_4	4.11	3.05	3.03
41	Si_5H_{12}	1.22	-0.17	0.05
42	LiH	1.59	0.1	0.05
43	KH	1.6	0.3	0.22
54	F_2Mg	2.64	0.25	0.32
55	TiF_4	4.08	0.22	0.82
56	AlF_3	2.61	0.03	0.14
58	SF_4	3.57	3.35	0.05
59	BrK	1.82	0.42	0.39
60	GaCl	2.39	0.45	0.42
61	NaCl	2.22	0.46	0.45
62	$MgCl_2$	2.57	0.72	0.68
63	AlI_3	2.58	1.54	1.65
66	PN	3.41	0.34	0.49
77	CS_2	2.79	0.33	0.48
81	O_3	6.17	1.87	2.6
82	SO_2	4.4	1.02	1.36
83	BeO	4.84	2.28	2.23
84	MgO	4.29	1.71	2.03
93	$C_5H_6N_2O_2$	2.24	-0.11	0.08
94	$C_4H_4N_2O_2$	2.44	-0.05	0.13
96	Ag_2	3.08	1.53	1.47
97	Cu_2	3.09	1.3	1.29
98	NCCu	4.12	1.85	1.92

Table 4.5: Quasiparticle electron Affinity for some molecule of the GW100 dataset as obtained within this work, compared with the available results of West$^{extra}_{lin}$. Both DFT and QP values are indicated.

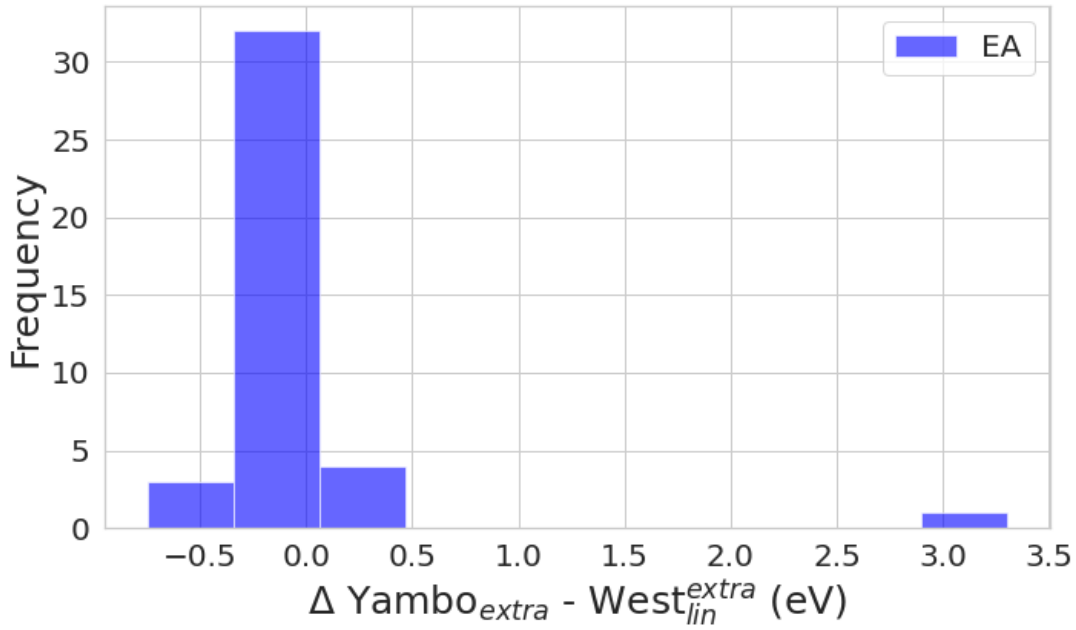

Figure 4.8: Deviation of the quasiparticle electron affinity between the Yambo and the West linearized extrapolated results. On average, results agree well within a ME and a MAE of respectively -15 and 221 meV.

and from the treatment of the frequency dependence of the self-energy, done here within the GNPPA. Additional sources of error can be attributed to the reduced supercell used in this work. Only a small part of the discrepancy can be addressed to the extrapolation procedure of the results, as we did not find a correlation between extrapolation error and discrepancies with respect to previous results obtained with other codes like West and VASP.

In particular, we observe a very good agreement with respect to the West$^{extra}_{lin}$ data, where the few significant deviations (400-500 meV) are due to molecules containing fluorine. Results are in good agreement also with data obtained using local orbital basis set (FHI-aims and Turbomole) and with respect to the full-frequency treatment implemented within the BGW code. The largest discrepancies are due to comparison with CCSD and experimental results, both in better agreement with BGW$_{\text{HLPPM}}$. In general, we show that the GNPPA performs better in terms of verification than the HLPPM as compared with other GW implementations using PWs, and even LO basis sets. As future perspectives, it would be important to provide YAMBO results also using more sophisticated approaches such as the multi-pole approximation [54] or a full-frequency treatment of the GW self-energy.

Part III

Results

Chapter 5

Excited state properties of graphene-like C_3N

Carbon-nitrides C_xN_y (*e.g.* CN, C_2N, C_3N, or C_3N_4) are gaining significant attention in recent years [207]. These are metal-free carbon-based layered materials with comparable (or even superior) structural, chemical, and electronic properties with respect to graphene. While preserving structural affinities with graphene, they generally display a semiconducting behavior. One of the most studied materials in this class is graphitic-C_3N_4 [208], as its strong optical absorption in the visible makes it suitable for solar energy conversion and photocatalysis applications [209]. Recently, a new carbon nitride, C_3N (structurally analogous to graphene and also known as 2D-polyaniline; see Fig. 5.1), an indirect gap semiconductor, has been experimentally synthesized using different methods [67, 210]. Since then, several studies were undertaken to characterize it. Theoretical investigations have shown that monolayer C_3N displays interesting features: remarkable mechanical properties, similar to graphene [68, 69], high stability at room temperature and high thermal conductivity [70, 71]. Moreover, it seems a promising material for acting as anode for Li-, Na-, and K-ion batteries [211, 212, 213, 214]. It was also studied in heterostructures with graphene [69], C_3B [215], and g-C_3N_4 [216], showing interesting properties for optoelectronic and electrochemical energy storage devices.

Despite these interesting features, an extended characterization of excitations, including excitonic effects, in monolayer C_3N is still lacking. This knowledge would be relevant when considering C_3N for optoelectronic applications like photocatalysis, photodetection, solar cells, or light emitting diodes. Since the system is a 2D monolayer, the electronic screening is strongly reduced, implying that the enhanced electron-hole interaction typically leads to large excitonic binding energies (EBE) for all the relevant excitons. In a complementary direction, as discussed by Qiu *et al.* [217] and Cudazzo *et al.* [218], the study of the excitonic dispersion with respect to the transferred momentum $\mathbf{q}$ can give more information on the excitonic features, in particular for low-dimensional systems. Moreover, it

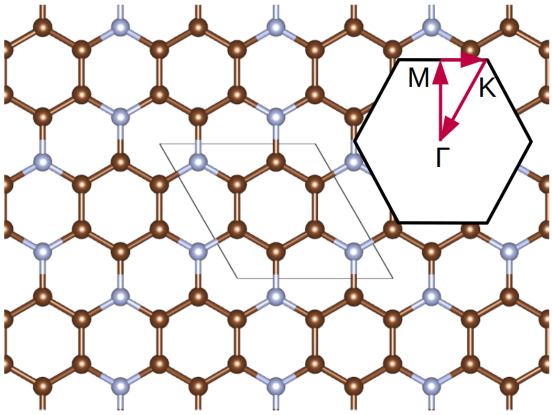

Figure 5.1: Lattice structure of C_3N, with the corresponding unit cell. Brown and grey spheres represent the C and N atoms respectively. Inset: Brillouin zone with the **k**-path considered in this work.

may have implications in plasmon/phonon - exciton coupling phenomena and can help in the determination of the exciton propagation along the crystal, relevant for excitation energy transport in the material [219]. In this work we employ Many-Body Perturbation Theory methods in the GW approximation [1, 2] and the Bethe Salpeter equation (BSE) [4] to study C_3N. In addition to a full characterization of the electronic and optical properties of this system, the excitonic band structure is computed in order to understand the exciton dispersion beyond the long wavelength limit. Specifically, momentum-dependent excitonic wavefunctions are also computed and discussed.

This chapter is extracted from a dedicated publication: "**Excitonic effects in graphene-like C_3N**" from **Miki Bonacci**, Matteo Zanfrognini, Elisa Molinari, Alice Ruini, Marilia J. Caldas, Andrea Ferretti, and Daniele Varsano. The work was published in Physical Review Materials (2022) [72], my first publication as first author.

5.1 Electronic properties

C_3N has a honeycomb lattice, with a unit cell composed of 6 carbon and 2 nitrogen atoms, as shown in Fig. 5.1. Like graphene, it assumes a planar and continuously bonded geometry, due to the character of the sp^2 hybridized orbitals.

We used optimized norm-conserving Vanderbilt (ONCV) pseudopotentials [110] to compute the relaxed structure and the corresponding Kohn-Sham (KS) single-particle energies and electronic density. The KS-DFT exchange-correlation functional was approximated using GGA-PBE [98]. The KS electronic structure was converged using a plane wave kinetic energy cutoff energy of 60 Ry to represent the wavefunctions, and a Monkhorst-Pack **k**-point grid of 8×8×1. We verified that a

gaps	**PBE** (eV)	$\mathbf{G_0W_0}$ (eV)
M $\rightarrow$ Γ	0.42	1.42
Γ $\rightarrow$ Γ	1.86	2.96
M $\rightarrow$ M	1.61	2.67

Table 5.1: Indirect and direct energy gaps at high symmetry points obtained at PBE and G_0W_0 level.

supercell with a vacuum of 15 Å along the vertical direction was enough to treat the system as 2D, avoiding spurious interactions between layers. For monolayer C_3N we find a relaxed lattice constant of 4.857 Å (using GGA-PBE). This result agrees well with previous DFT calculations (4.862 Å) [220] and is slightly larger than the experimental value (4.75 Å) [67]. The KS band structure (Fig. 5.2a) shows a Dirac cone at the K point. Now, since C_3N has two more electrons per unit cell than graphene, the level-filling goes up and the Dirac cone is no longer at the valence-band top. The calculated band gap is indirect ($M \rightarrow \Gamma$) and amounts to 0.42 eV (at the GGA-PBE level). The direct gaps at Γ and M are 1.86 eV and 1.61 eV, respectively. Figure 5.2a highlights also the σ and π character of the bands in the gap region, and we can observe that the top valence bands show π symmetry as well as the two lowest conduction bands, whereas σ-like character is seen in the third and the fourth conduction bands (which start above $\sim$2 eV with respect to the top valence band).

Converged quasiparticle energies were obtained using a kinetic energy cutoff of 10 Ry to represent the screening matrix, including 300 empty states in the sums over transitions and adopting a **k**-point grid of 30×30×1. Convergence on screening matrix cutoff and empty states is reached by means of automated workflows as implemented in the current version of the `aiida-yambo` plugin [65] of the AiiDA software [39], imposing a convergence threshold of 15 meV. More details on the convergence workflow are provided in Section 5.1.1. The inclusion of GW corrections provides a gap opening of $\sim$ 1 eV, resulting in an indirect quasiparticle band gap of 1.42 eV (Fig. 5.2b). The direct gaps at Γ and M are also increased to 2.96 and 2.67 eV, respectively, as summarized in Tab. 5.1. The minimum direct gap is located in the middle of the Γ-M region of the BZ and has a value of 2.62 eV. The GW band gap is consistent with the one obtained in a recent work by Wu *et al.* [221], calculated at the GW level using the Hybertsen-Louie generalized plasmon pole model [52], and as expected is larger than that obtained directly with the HSE06 hybrid functional[222], by $\sim$0.38 eV [220]. The C_3N gap is narrower with respect to the two well-known carbon nitrides g-C_3N_4 ($\sim$4.24 eV for the triazine structure) [223] and C_2N ($\sim$3.75 eV) [224] single layers. This is consistent with the fact that C_3N is continuously bonded, while the two other carbon nitrides have saturated porous structure resulting in electronic confinement.

Along the same BZ path, the C_3N band structure calculated at GW level

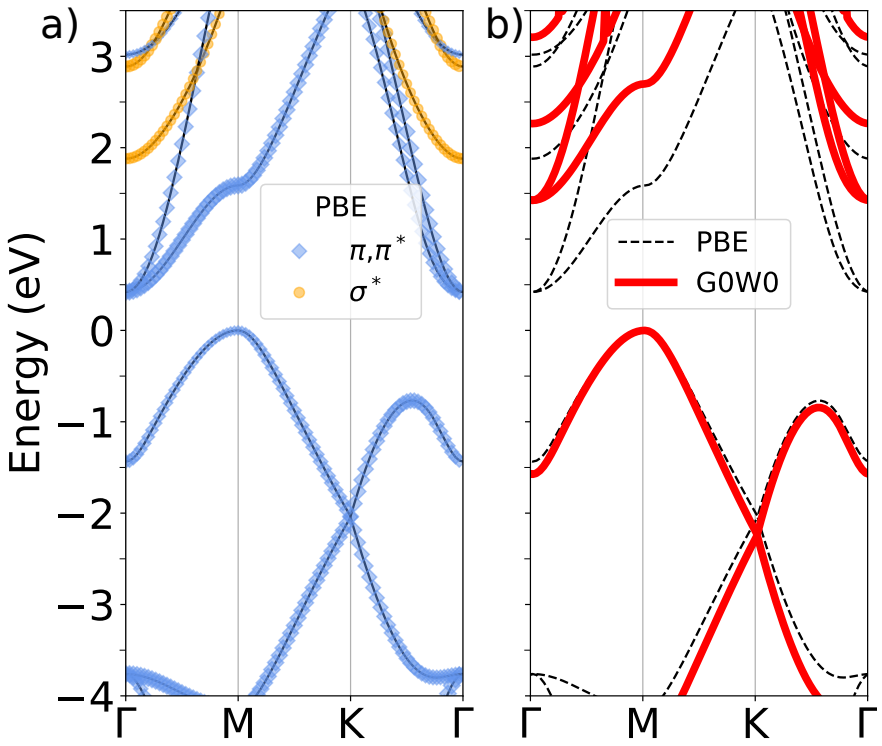

Figure 5.2: a) Orbital projected PBE band structure. π and π^* bands are indicated in blue, σ^* as orange dots. b) G_0W_0 band structure (red); the corresponding PBE bands are reported again as dashed curves for reference. In both panels the zero of the energy scale is set at the top of the valence band for both PBE and G_0W_0 results.

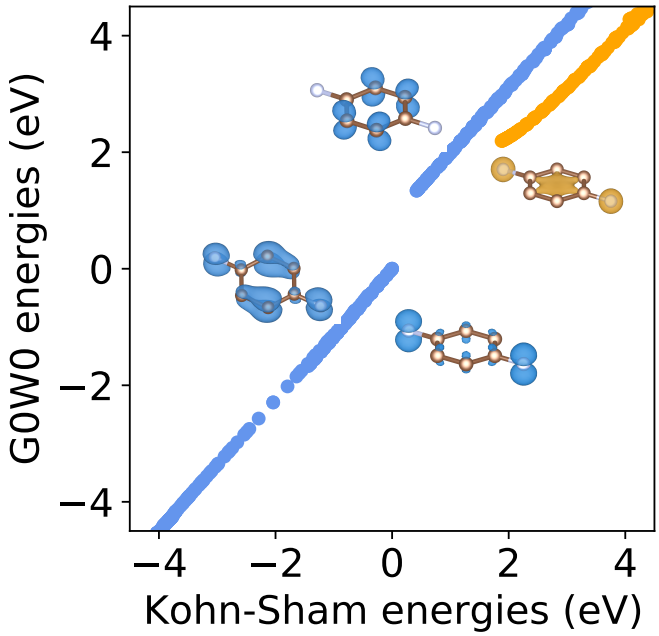

Figure 5.3: Quasiparticle G_0W_0 energies vs. Kohn-Sham PBE eigenvalues. The top of the valence band is chosen as a common zero of the energy. The colors and the corresponding insets indicate the predominant π, π^* (blue) and σ^* (orange) character. In the conduction region, two branches result from the different localization of the π^*- and σ^*-character states leading to different quasiparticle corrections.

is qualitatively similar to the one calculated using PBE, as shown in Fig. 5.2b. In fact, the GW gap is still indirect with the valence band maximum located at M and the conduction band minimum at Γ. We observe, anyhow, that the GW correction is not uniform across the bands, as different corrections apply due to wave functions with different character. Orbital-dependent GW corrections are a well-known feature of GW already discussed in the literature [225, 226]. In particular, the corrections in the low conduction region are distinguished according to the different localization of the KS wavefunctions, as can be observed from Fig. 5.3, where the GW energies are plotted against the respective KS eigenvalues.

A larger correction is observed for the bands with π^* (blue dots) character with respect to bands having σ^* character (orange dots). Since the valence bands considered here only present a π character (σ-states are deeper in energy), their GW correction shows a more common scissor/stretching behavior. We note that this picture allows us to include the GW correction (for instance in the BSE calculations) as a generalized scissor and stretching operator, taking into account different corrections according to the specific localization character of the KS-states.

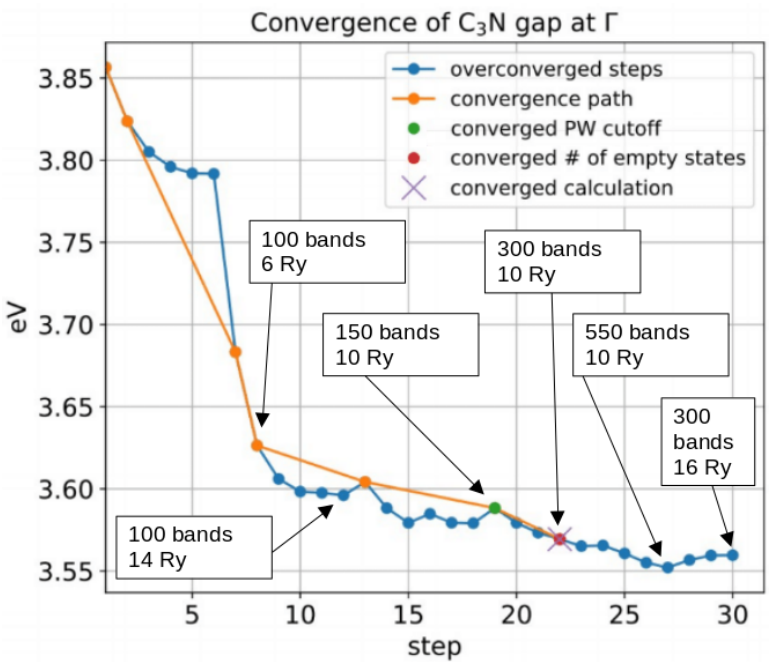

Figure 5.4: Convergence of the direct gap of C_3N at Γ, with respect to empty states and cutoff on the screening matrix. As shown in the plot, 30 GW runs are sufficient to achieve a convergence of about 30 meV. Further convergence on **k**-points mesh has been done without the workflow.

5.1.1 Automatic GW convergences

The convergence of the numerical parameters for the GW calculations, with the exception of the **k**-point grid, was achieved using the automatic workflow implemented in the `aiida-yambo` plugin [65, 155, 156] and as explained in Chapter 3. In particular, the automatic workflow was used to converge the kinetic energy cutoff to represent the screening matrix and the number of empty states needed to converge the polarizability and the GW self-energy. These two parameters are strongly interdependent, and cannot be treated separately [227].

The workflow used here, as shown in Fig. 5.4, performs several convergence tests on each parameter, increasing one value while keeping fixed the other(s). The increment applied in each iteration is provided as input by the user. The convergence threshold is chosen to be ± 15 meV with respect to the last simulation performed by the workflow, meaning that the final error bar is of 30 meV.

All the calculations are performed taking advantage of other sub-workflows of the plugin, mainly concerning automatic error handling.

5.2 Optical properties

The optical absorption, obtained from the $\mathbf{q} \to 0$ limit of the macroscopic dielectric response, according to Eq. 2.25, is shown in Fig. 5.5. Excitonic effects were included by solving the BSE equation. All the excitation energies are plotted, together with the independent-particle onset, at E_{IP-GW}=2.62 eV, indicated by the vertical red line. The absorption spectrum is dominated by a main peak at 1.96 eV, originated by the doubly-degenerate exciton $E_0^{4,5}$. At lower energies, three dark excitons are present, the lowest ones (1.82 eV, $E_0^{1,2}$) being also doubly-degenerate.

Both bright and dark excitons are strongly bound, displaying EBE of 0.93 eV and 0.66 eV, for $E_0^{1,2}$ and $E_0^{4,5}$. The EBE are computed considering the difference between the excitation energy of the exciton and the average energy of the involved electron-hole transitions, as shown in the lower panel of Fig. 5.6. Interestingly, the EBE of the lowest bright exciton $E_0^{4,5}$ satisfies the scaling law EBE $\sim \frac{1}{4} E_{IP-GW}$, found valid for 2D single-layered systems. [228, 229].

In order to analyze the spatial extension of the main excitons, we plot their excitonic wavefunction, by showing the electron spatial distribution for a fixed hole position. The upper panel of Fig. 5.6 displays the excitonic wavefunction for the lowest ($E_0^{1,2}$) and the brightest ($E_0^{4,5}$) direct excitons, with the hole placed on a N site. Both excitons show a 3-fold rotational plus a reflection symmetry with respect to the axis in the armchair direction. Interestingly, these excitons are localized on benzene rings, avoiding the N atoms. We observe that the dark excitons (lower energy) are strongly localized around the hole, while the active ones (higher energy) are more delocalized. We can explain the different spatial localization in terms of the single particle transitions that contribute to the excitations, as represented in the lower panels of Fig. 5.6. The first excitons $E_0^{1,2}$ are built from electron-hole transitions belonging to a larger region of the Brillouin zone with respect to $E_0^{4,5}$, resulting in a larger confinement in real space. Similarly to the fundamental gap, the optical gap of C_3N is also smaller than the ones calculated for g-C_3N_4 and C_2N (by about $\sim$2 eV and $\sim$1 eV [224], respectively, by considering the first bright excitons), which is consistent with a picture where the presence of saturated pores in each layer of the structure induces wavefunction localization and quantum confinement.

5.3 Indirect excitons

Besides the optical absorption limit, our understanding of electron-hole excitations in C_3N is further enhanced by inspecting the excitonic spectrum over a wider range of transferred momenta $\mathbf{q} = \mathbf{k}_{\text{elec}} - \mathbf{k}_{\text{hole}}$, providing us with the exciton dispersion in momentum space. Indeed, the excitonic dispersion was recently proposed [218] as a powerful tool to distinguish excitons of different character in low-dimensional

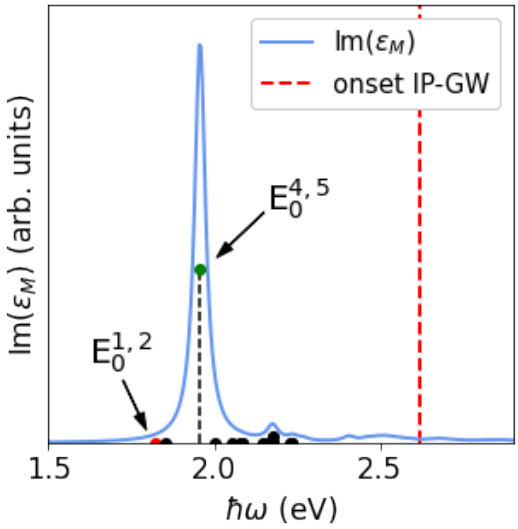

Figure 5.5: Calculated $\mathrm{Im}(\epsilon_M)$ in the optical limit ($\mathbf{q} \to 0$), in arbitrary units (arb. units). A Lorentzian broadening of 0.02 eV has been included. The dots indicate the amplitude of each excitonic state in the BSE solution. The vertical dashed red line represents the onset of the single quasiparticle continuum (minimum direct gap in the GW solution, 2.62 eV).

systems, going beyond the mere evaluation of the EBE. The solution of the BSE for finite $\mathbf{q}$ then allows us to fully characterize the C_3N excitations accessible by means of momentum-resolved electron energy loss spectroscopy or non-resonant inelastic X-ray scattering. Figure 5.7 shows the loss function calculated for different transferred momenta $\mathbf{q}$ along the $\Gamma - M$ path. To compare spectra at different momentum, we multiplied the loss function by a q^2 factor. While making the plot more readable, this factor is also experimentally motivated by the form of the NRIXS cross section, as discussed in the theory section.

We observe that the low-energy peak goes down in energy for $\mathbf{q}$ moving away from Γ, as expected for an indirect gap system. This indicates the presence of a dispersive excitonic band reaching a minimum of $\sim$0.8 eV at $\mathbf{q} = M$ in correspondence of the indirect gap.

To complement the information provided by the loss spectra, in Fig. 5.8a we present the calculated $\mathbf{q}$-resolved exciton band structure. A color map is added to indicate the (generalized) amplitude/strength of each excitonic state, actually offering richer information complementary to the loss spectrum. The lowest degenerate exciton $E_0^{1,2}$ at Γ splits into two excitonic bands that we call $E_{\mathbf{q}}^1$ and $E_{\mathbf{q}}^2$. For both $\Gamma - M$ and $\Gamma - K$ directions, we observe that the lowest excitons present quadratic and almost linear dispersions in the neighborhood of the Γ point, as also found for other 2D systems [217, 230, 218]. Nevertheless, at variance with what reported in the work of Qiu *et al.* [217] for the direct gap MoS_2

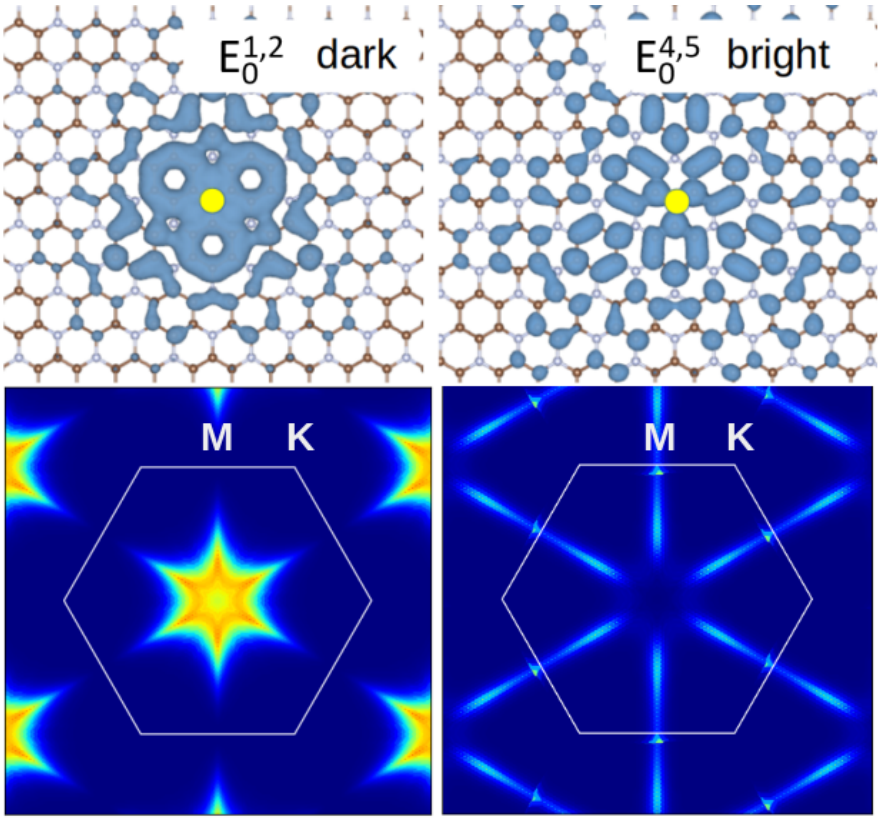

Figure 5.6: Upper panels: excitonic probability distribution for the dark $E_0^{1,2}$ and the bright (1.96 eV, $E_0^{4,5}$) excitons at vanishing $\mathbf{q}$. The blue contours represent the probability of finding the electron (hole) when the hole (electron) is fixed on a N atom (yellow circle). Lower panels: distribution of the electron-hole transitions in the BZ for the corresponding excitons of the upper panels.

monolayer, here we find a lower band with quasi-linear dependence on $|\mathbf{q}|$ and an upper band with a clear parabolic dispersion, both with a negative slope and concavity. Such a behavior is due to the indirect nature of the gap, and we note that –at difference with other 2D materials such as MoS_2 and phosphorene [219]– in the case of C_3N we do not observe a non-analytical dispersion for the lowest bands. This is related to the fact that the $E_0^{1,2}$ excitons are dark, making the exchange contribution to the dispersion negligible. Moreover, the observed downward quasi-linear behavior can be seen to be connected to the independent-particle contribution to the excitonic Hamiltonian, as shown in Section 5.3.1.

Moreover, the $\Gamma - M$ direction is of special interest, since it corresponds to $\mathbf{q}$-vector involved in the indirect band gap: the most relevant excitonic transitions occur in that zone, and the decrease of excitation energies going from Γ to M reflects the indirect gap of C_3N. From Fig. 5.8a we observe that the lowest exciton ($E_{\mathbf{q}}^1$) is inactive, with an energy minimum of 0.8 eV at $\mathbf{q} = M$. For this momentum,

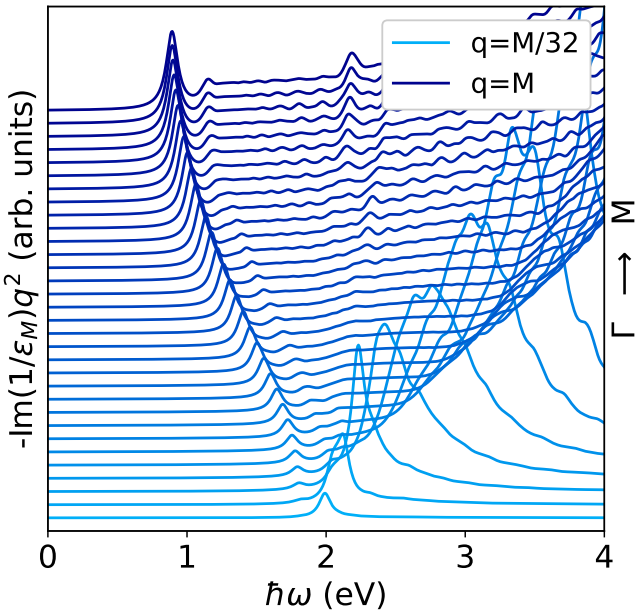

Figure 5.7: Loss function for different values of the transferred momentum along the direction Γ-M , starting from the lowest $\mathbf{q}$ = M/32 (light blue), to the highest $\mathbf{q}$ = M (dark blue). Following Cudazzo *et al.* [218], we multiplied all spectra by the corresponding $\mathbf{q}^2$. This is needed in order to enhance higher momentum spectra and physically motivated by the form of the NRIXS cross section (as shown in Eq. 2.30).

the immediately higher-energy exciton (0.9 eV, $E^2_{\mathbf{q}}$) is active. Concerning the Γ-K path, we observe a minimum near $K/2$ that corresponds to an inactive state of energy ∼1.3 eV. We find that EBE range from 0.6 eV to 0.93 eV for the lowest excitonic band in the Γ-M direction ($E^{1,2}_0$-$E^1_{\mathbf{q}}$). As we move out of the long-wavelength regime and choose given directions of the center-of-mass momentum $\mathbf{q}$, we expect some symmetries in the excitonic wavefunctions, like the 3-fold rotational invariance observed in the plots of Fig. 5.6, to break. Figure 5.8b shows the square modulus of exciton wavefunctions ($E^1_{\mathbf{q}}$ and $E^2_{\mathbf{q}}$) at $\mathbf{q}$=M, corresponding to minima in the band structure of Fig. 5.8a. As before, the hole is placed on a nitrogen atom. The 3-fold rotational symmetry is no longer present, and only the reflection invariance with respect to the armchair direction is maintained. Both $E^1_{\mathbf{q}}$ and $E^2_{\mathbf{q}}$ excitons are delocalized along the zig-zag direction. For the inactive excitons the symmetry axis lies on a nodal plane, where the probability amplitude of finding electrons vanishes. The spatial delocalization increases with $\mathbf{q}$ and is higher for the indirect active exciton $E^2_{\mathbf{q}}$, as happens for the bright excitons in the optical limit case. The behavior of the excitonic wavefunctionc of C_3N is very similar to that observed in hBN by Sponza *et al.* [230]. This is because, along

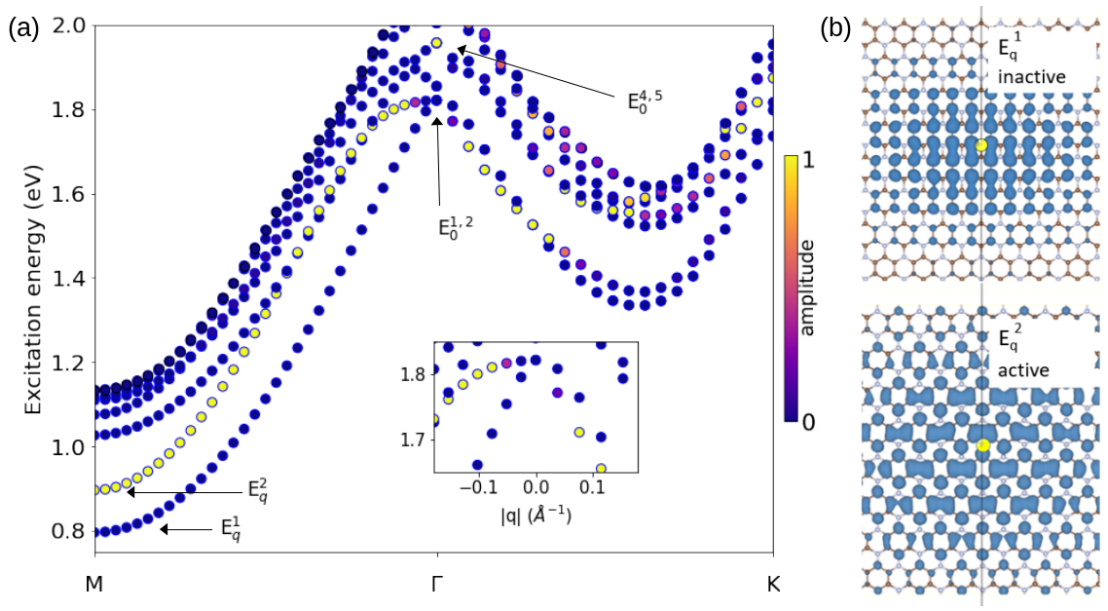

Figure 5.8: (a) Momentum-resolved exciton band structure for the lowest seven excitons. Excitonic amplitudes are normalized with respect to the brightest exciton among all the bands for each momenta from dark violet to yellow (active exciton). Inset: focus on the region near the q=0 for the two lowest excitonic bands. (b) Exciton probability distribution for $E^1_{\mathbf{q}}$ (top) and $E^2_{\mathbf{q}}$ (bottom), at $\mathbf{q} = M$. The vertical solid line denotes the symmetry plane perpendicular to the figure and the hole position is indicated in yellow near the center of the figures.

the armchair direction, both systems present the same reflection symmetry that characterizes the localization of excitons.

5.3.1 Independent particle effects in the excitonic band structure

As shown in the previous Section, close to Γ the first two bands in the excitonic band structure have negative slope and concavity. Moreover, the lowest one has a quasi-linear dependence on $|\mathbf{q}|$. The comparison between the full BSE solution at finite $\mathbf{q}$ close to Γ with the average of the independent particle (IP) transition energies, as done in Fig. 5.9, shows that these two peculiar features of the excitonic band structure are inherited from the IP contribution to the Hamiltonian.

Formally, we consider the BSE excitonic Hamiltonian, together with its eigenvectors represented on the transition basis, and separate out its finite-$\mathbf{q}$ contributions, as follows:

$$H^{\text{exc}}(\mathbf{q})|\lambda,\mathbf{q}\rangle = E^{\lambda}(\mathbf{q})|\lambda,\mathbf{q}\rangle, \tag{5.1}$$

$$|\lambda,\mathbf{q}\rangle = \sum_{vc\mathbf{k}} A^{\lambda}_{vc\mathbf{k}}(\mathbf{q})|vc\mathbf{k},\mathbf{q}\rangle, \tag{5.2}$$

where

$$\begin{aligned} H^{\text{exc}}(\mathbf{q}) &= H^{\text{IP}}(\mathbf{q}) + K_x(\mathbf{q}) + K_d(\mathbf{q}) \\ &= H^{\text{exc}}(0) + \Delta H^{\text{IP}}(\mathbf{q}) + \Delta K_x(\mathbf{q}) + \Delta K_d(\mathbf{q}). \end{aligned} \tag{5.3}$$

Then, the average independent particle contribution, $\langle\text{IP}\rangle$, plotted in Fig. 5.9 is computed as the expectation value of the diagonal IP term of the BSE excitonic Hamiltonian on the eigenvectors obtained diagonalizing the whole Hamiltonian at each $\mathbf{q}$, namely $\langle\text{IP}\rangle_\lambda = \langle\lambda,\mathbf{q}|H^{\text{IP}}(\mathbf{q})|\lambda,\mathbf{q}\rangle$. In practice, these IP energies are evaluated as the weighted energies of all the transitions concurring in the formation of the given exciton as:

$$\langle\text{IP}\rangle_\lambda = \sum_{cv\mathbf{k}} |A^{\lambda}_{vc\mathbf{k}}(\mathbf{q})|^2 \, (E^{\text{qp}}_{c,\mathbf{k}} - E^{\text{qp}}_{v,\mathbf{k}-\mathbf{q}}). \tag{5.4}$$

Moreover, the $\langle\text{IP}\rangle$ and BSE points in the plot are also aligned at $\mathbf{q} = 0$ by a shift ΔBSE_0 (equal to -0.93 eV, i.e. the EBE of the lowest exciton at Γ). This amounts to consider the whole BSE Hamiltonian at $\mathbf{q} = 0$, while neglecting the $\mathbf{q}$-dependence of $\Delta K_{x,d}$ at finite $\mathbf{q}$, i.e.

$$\langle\text{IP}\rangle_\lambda + \Delta\text{BSE}_0 = \langle\lambda,\mathbf{q}|H^{\text{exc}}(0) + \Delta H^{\text{IP}}(\mathbf{q})|\lambda,\mathbf{q}\rangle. \tag{5.5}$$

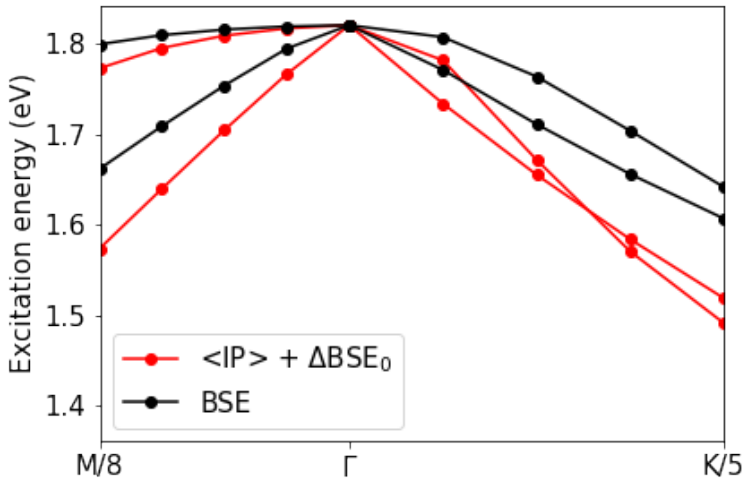

Figure 5.9: Comparison between independent particle (IP) transition energies (red) and proper excitonic energies (black) for the two lowest excitonic bands. The IP energies are shifted in order to match the excitonic energies at the Γ point. We can observe that the negative concavity and the linearity of the lowest excitonic bands are effects already included in the IP dispersion. $\langle \text{IP} \rangle$ and BSE points are aligned at $\mathbf{q} = 0$ by including a shift ΔBSE_0=-0.93 eV.

5.4 Conclusions

In this chapter we have studied the electronic and optical properties of single-layer C_3N by using ab initio methods based on DFT and many-body schemes. In particular, we have computed the 2D band structure of C_3N within the GW approximation, revealing an indirect quasi-particle band-gap of 1.42 eV (top of the valence band located at M, bottom of the conduction band at Γ), with direct gaps at Γ and M of 2.96 and 2.67 eV, respectively. The GW corrections to quasi-particle energies were also discussed in view of the orbital symmetry and localization.

Neutral excitations, as those sampled by optical absorption ($\mathbf{q} = 0$) and electron energy loss spectroscopy (finite $\mathbf{q}$), are computed using the Bethe Salpeter equation. One of the main results of the work comes from the calculation of the full excitonic dispersion of C_3N in $\mathbf{q}$-space, giving access to indirect exciton energies and intensities. These excitons play an important role in phonon-assisted photoluminescence [231, 232], and they can be efficiently exploited for chemical sensing [233]. Interestingly, while the excitonic dispersion shows a parabolic behavior at M, corresponding to the indirect band gap, at Γ we observe a degenerate doublet which splits into a parabolic and a quasi-linear dispersing bands, as for other 2D materials. A peculiarity of C_3N, connected with its indirect gap as well as with the dark nature of the excitons involved, is that the quasi-linear band has

downward convexity, at variance with MoS_2 or hBN and the quasi-linear dispersion of the lower excitonic band, comes from its independent-particle contribution. Finally, this work represents a solid starting point to consider the role of excitonic effects of C_3N in more specific cases, e.g. in describing exciton-phonon scattering or the spectroscopy of in-plane adsorbates/defects.

Chapter 6

Band gap opening and dielectric response in double-side highly hydrogenated free-standing graphene

The manipulation of material properties is tremendously attractive to materials scientists as a rich playground for both fundamental science and technological developments. In this respect, graphene [5, 6] is among the most extensively studied materials of the last decades. Despite its widely-recognized, intriguing properties [7, 8] are promising for a variety of applications (from sensing to energy storage [9, 10, 11]), many others are hindered by its gapless semi-metallic band structure of pristine graphene. Several efforts have been done in the past to overcome this issue and open a band gap in various ways, among them: chemical modifications, functionalization and doping [234, 235, 236, 237, 238]. Here, we focus on the hydrogenation of mono- and bi-layer graphene, which leads to a band gap opening whose magnitude depends on the H chemisorption configuration and on its effective surface-ratio storage [239, 240]. Moreover, stable hydrogen harvesting is crucial in hydrogen-based fuel cells as promising solutions for efficient and clean delivery of electricity [241].

Fully hydrogenated graphene, the so-called *graphane*, is characterized sp^3 bonds between carbon and hydrogen atoms. So far, this ideal system has not been yet realized experimentally, as the maximum H uptake approach an upper limit of $\sim$36% in terms of H/C ratio, and depends on the hydrogenation techniques as well as the graphene quality [242, 243, 244, 245, 246, 247, 248, 249, 250, 251, 252, 253]. Other limiting factors for a large and clean hydrogenation can be oxygen contamination, the influence of the substrate, and the presence of defects/edges in graphene flakes (either pre-existing or induced by the hydrogenation itself). In the following, we present a computational characterization of electronic and optical properties of various ideal configurations of hydrogenated graphene by means of

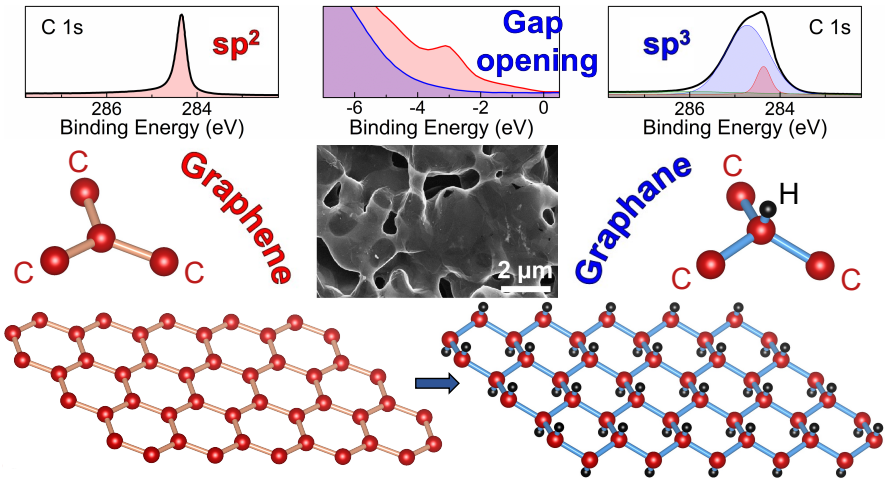

Figure 6.1: The top panels represent the photoemission spectromicroscopy for UHV-clean NPG (left), hydrogenated sample (right) and valence band (center, for both the two cases of left and right top panels). We observe the presence of distorted sp^3 bounds appearing with the hydrogenation and corresponding to a band gap opening. The panel located at the center of this figure shows a Scanning electron microscopy (SEM) imaging zoomed at a mesoscopic level ($10 \times 10\ \mu m^2$), unveiling the porous structure of NPG.

GW and BSE methods. Our results corroborate an experimental characterization performed by the groups led by Prof. Maria Grazia Betti and Prof. Carlo Mariani at the Sapienza University in Roma, and by Prof. Roberto Biagi and Prof. Valentina De Renzi at the University of Modena and Reggio Emilia. The experimental samples are constituted by the so-called nano-porous graphene (NPG), i.e., a compact, bi-continuous interconnected 3D arrangement of high-quality graphene veils, composed by one to a few weakly interacting layers [254, 255]. was synthesized by using a nano-porous Ni template via chemical vapor deposition (CVD). Subsequently, the as-grown NPG acquires the three-dimensional morphology of the substrate and is subsequently exfoliated by chemical dissolution of the Ni template. In this way, it was possible to obtain a high-quality, nearly defect-free, and free-standing graphane prototype. The hydrogenation (deuteration) process happened in ultra-high-vacuum (UHV) conditions, by exposure of the sample to atomic H produced by H_2 cracking into a capillary source locally heated at 2100 °C. For more details on the sample preparation we redirect to Ref. 73.

In particular, my contribution concerned the calculation of quasiparticle band structures and density of states (DoS) which corroborate spectromicroscopy photoemission measurements on the NPG samples and allow us to address the hydrogenation configurations among the ideal ones proposed, confirming the achievement of an unprecedentedly high H uptake in NPG, around ∼90%, as schematically shown in Fig. 6.1. For the first time an almost complete saturation in fully

free-standing graphene of the available C sites with hydrogen is obtained.

Moreover, I performed a computational characterization of the optical properties of some of the candidate structures (within the BSE method), to support the experimental investigation of the dielectric response of deuterated-NPG (D-NPG) by means of high-resolution electron energy loss spectroscopy (HREELS). The use of the deuterium isotope of hydrogen unequivocally identifies the D-C contribution in the vibrational spectra even at low coverage, neglecting any H contaminant effect. Electron correlation effects lead to a renormalized bandgap and large exciton binding energy. Understanding the changes in the optical properties and electron-hole interaction from semi metallic graphene towards hydrogenated/deuterated graphene with large gap, is crucial for both fundamental knowledge of 2D materials and for emerging applications of graphene/graphane in electronic and optoelectronic devices.

Theoretical results, together with the experimental ones, are collected and exposed in two works. The first part, on electronic properties of hydrogenated graphene, is published on Nano Letters (2022) in Ref. 73: "**Gap opening in double-sided highly hydrogenated free-standing graphene**", from Maria Grazia Betti, Ernesto Placidi, Chiara Izzo, Elena Blundo, Antonio Polimeni, Marco Sbroscia, Jośe Avila, Pavel Dudin, Kailong Hu, Yoshikazu Ito, Deborah Prezzi, **Miki Bonacci**, Elisa Molinari, and Carlo Mariani. The final part about the optical characterization is part of the following preprint: "**Dielectric response and excitations of free-standing graphane**", from Maria Grazia Betti, Dario Marchiani, Elena Blundo, Marta De Luca, Antonio Polimeni, Riccardo Frisenda, Carlo Mariani, Samuel Jeong, Yoshikazu Ito, Andrea Tonelli, Nicola Cavani, Roberto Biagi, Valentina De Renzi, Peter N. O. Gillespie, **Miki Bonacci**, Elisa Molinari, and Deborah Prezzi (2022).

6.1 Quasiparticle electronic properties

As mentioned above, our experimental collaborators were able to obtain, in the NPG sample, an unprecedented hydrogen uptake of $\sim 90\%$, which is in line with a chemisorption model for graphane with almost each C sp^3 being bound, never achieved experimentally before in fully free-standing low-defect graphene [73]. The next step was to correlate the opening of a band gap in H–NPG with the transition from $sp^2 \rightarrow sp^3$ due to the C–H bonding. This was done by performing spatial resolved photoemission spectroscopy on a partially hydrogenated sample ($\sim 50\%$) in order to distinguish the valence and core level spectral shapes for regions of different levels of hydrogenation. Results are exposed in Fig. 6.2, where in panel (a) and (d) are shown the spatially resolved intensity of the sp^2/sp^3 (cross/star) character and the intensity of the 2p–π peak, respectively. Panel (b) and (c) represent the schematics of the core-level XPS spectra for the two levels of hydrogenation, respectively low and high. The 2p–π peak is associated with the

graphene band structure and corresponds to the regions where the sp^2 character is dominant. This can also be observed for the spectral density of states (DoS), shown panel (e): in the case of sp^2 character (red line) we definitely see the 2p–π peak, whereas in the sp^3 dominant region the peak is almost quenched. Indeed, at

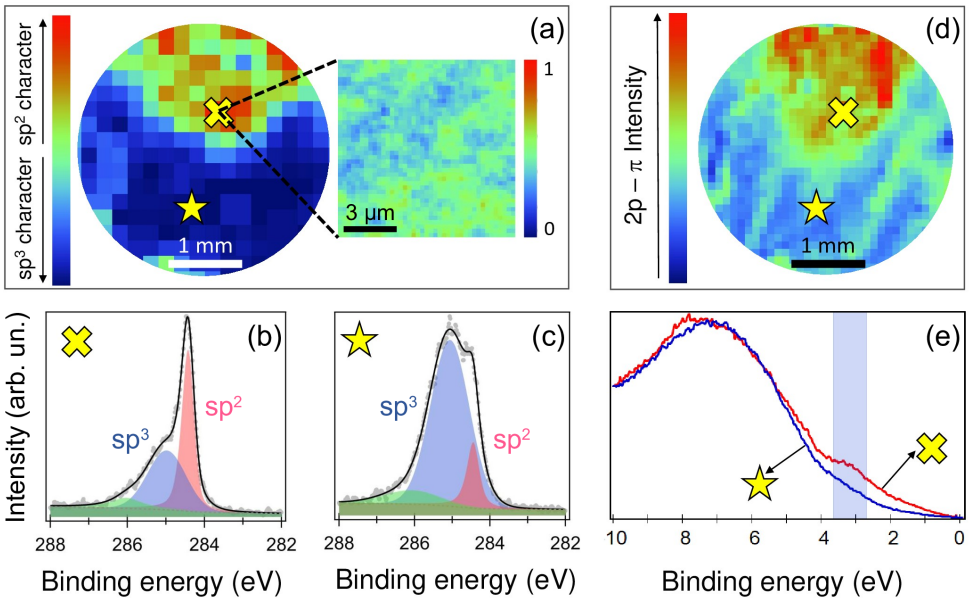

Figure 6.2: (a) sp^2 C 1s intensity map, quantified as the ratio $I_{sp^2}/(I_{sp^2} + I_{sp^3})$, after background subtraction; the blow-up represents the same ratio in a $10 \times 10\,\mu m^2$ area; The spectra taken in the sp^2-rich and in sp^3-rich regions (labeled by a cross and a star, respectively) are shown in panels (b) and (c), respectively. (d) Valence band intensity map corresponding to the 2p-π intensity. The ratio was calculated as in panel (a); the intensity was found by integrating in the energy range indicated by the shadowed vertical ribbon in panel (e), which displays the VB spectrum for sp^2-rich (cross) and sp^3-rich (star) regions.

H saturation coverage ($\sim 90\%$), the quenching of the DoS below the Fermi level E_F suggests a transition from semimetal to a semiconducting state, as clearly observed in Fig. 6.4a. From the experimental results, the valence band maximum (VBM) can be extrapolated to be located at about 3.50±0.25 eV below E_F. The correlation between the emergence of C–H sp^3 bonding and the position of the VBM unambiguously ascribes the gap opening to the distortion of the bond to sp^3 [1].

The theoretical support to corroborate these experimental results, and address the band-gap opening to a given degree of H chemisorption, is provided by means of ab-initio computational characterization of the spectral DoS for some hydro-

[1]Despite this, the assignment of the hydrogen adsorption sites, as well as the fundamental band gap size, cannot be unambiguously identified from the photoemission experiment only.

genated graphene configurations. We performed both DFT and GW simulations, in order to first assess the stability of the structures and provide preliminary information on electronic properties (by means of DFT), and then to obtain the accurate quasiparticle band structures and DoS, by performing GW calculations, to directly compare with experimental spectral DoS. As shown in Fig. 6.3a, we investigated single- (1side) and double-side (2side) hydrogenation of the single- (H-Gr) and bi-layer (H-bGr) graphene. In fact, in addition to the ideal *graphane* configuration (Fig. 6.3a-3), where each C atom of single-layer graphene is bound to H forming an alternately up and down sp^3 distorted structure (also called *chair* or meta), we also considered the case of monolayer graphene saturated on one side only, i.e. the so-called *graphone* [256]. For the latter, we investigated both the *chair-like* (Fig. 6.3a-2), also denoted as triangular, T, or meta) and *boat-like* (Fig. 6.3a-1, also denoted as rectangular, R, or para/ortho) structures, the latter being the most stable one for single-side hydrogenated free-standing graphene.

As displayed in Fig. 6.3a(4-6), we also considered the two-side hydrogenation of graphene bi-layers with different registry, which aim at mimicking the various local structures of a turbostratic arrangement, as recognised by an atomic-scale analysis of the NPG microscopic structure [254]. The 2-side hydrogenation of the bi-layer graphene is found to foster the formation of C puckering and interlayer bonding, as also found in the studies on the stability and realization of diamanes, i.e. 2D diamond-like thin films, as summarized in a recent review [257].

For each of the above described systems, the atomic positions within the cell were fully relaxed until forces were less than 5×10^{-4} a.u. A vacuum region larger than 15 Å in the non-periodic direction was introduced to prevent interaction between periodic images. The kinetic energy cutoff for the wave functions was set to 80 Ry; the Brillouin zone was sampled by using a $14 \times 14 \times 1$ ($8 \times 8 \times 1$) **k**-points grid for the primitive (2×2) cell, respectively, according to Monkhorst-Pack algorithm. The optimized in-plane lattice parameters, $a = b$, are reported in 6.1, together with the C–C bond lengths, l_{CC}, as well as the energy gap $E_{g,PBE}$. Fig. 6.3b displays the DFT-PBE DoS for the configurations described above and reported in panel (a). An additional curve, representing the average of all the 2-side hydrogenated configurations (solid black line), is also reported in panel (b), to mimic the results for turbostratic few-layer samples and ease the comparison with the experimental VB spectra (inset, dashed cyan and solid thick black lines). While the comparison clearly highlights the well-known limitations of the DFT-PBE theory for a quantitative description of the electronic properties [2], the overall shape is in agreement with experimental findings. The theory curve is however much more detailed if compared to the featureless curve of H–NPG presented in the inset. This is because we only apply an homogeneous broadening of 140 meV to build our DoS, while experimental spectra contain information on the the real spectral amplitude, which is energy- and **k**-dependent [258].

To overcome some of the above-mentioned limitations of DFT, the quasiparticle band structure and DoS for selected geometries were computed within the *GW*

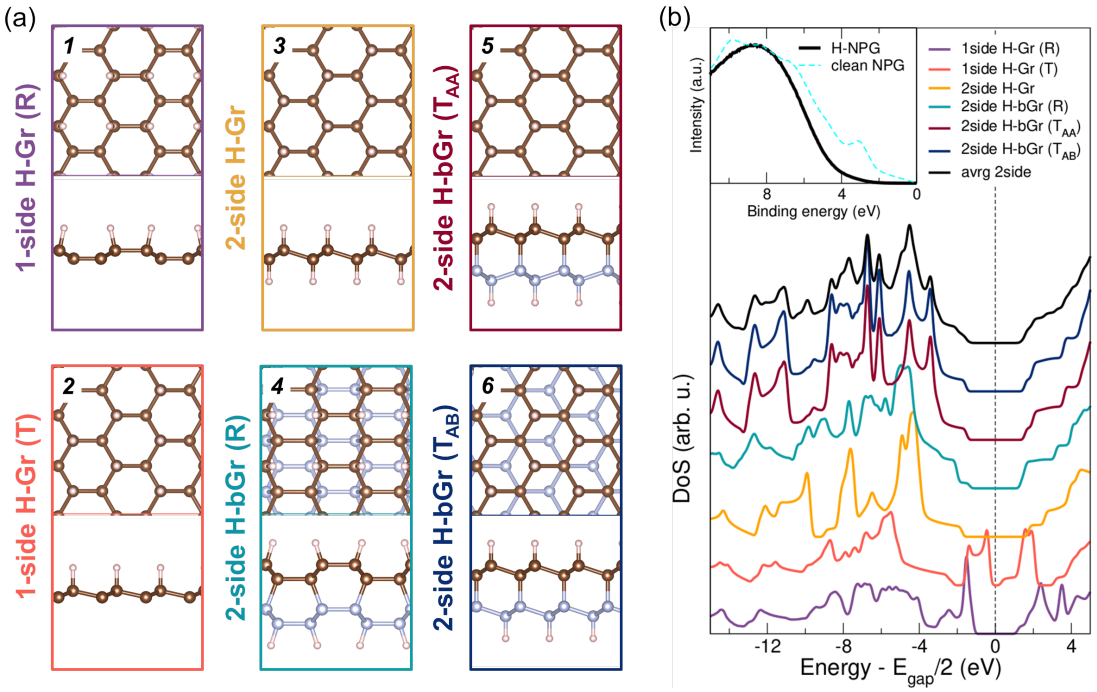

Figure 6.3: (a) Ball-and-stick models (top and side views) for different hydrogenated graphene structures (1-6). C (H) is represented by brown (white) spheres. For the bi-layer structures (4-6), the bottom C layer is represented in light blue, in order to make the figures clearer. (b) DFT-PBE DoS for the configurations reported in (a). An additional curve, representing the average of all the 2-side hydrogenated configurations (labeled as "avrg 2side", solid black line), is also reported in the main panel, to ease the comparison with the experimental VB spectra for clean (inset, dashed cyan) and totally hydrogenated NPG (inset, solid thick black line), taken with HeI$_\alpha$ (21.218 eV) photon energy.

Table 6.1: Calculated structural and electronic properties of the different H-Gr configurations displayed in Fig. 6.1. Except for the 2side H-Gr, all systems are computed in a 2×2 supercell.

System	a (Å)	l_{CC} (Å)	$E_{g,PBE}$ (eV)	E_{g,G_0W_0} (eV)
1side H-Gr (T)	5.063	1.50	0.65	3.18
1side H-Gr (R)	5.019	1.36; 1.50; 1.57	2.46.	5.60
2side H-Gr	2.537	1.54	3.49	6.15
2side H-bGr (R)	4.960	1.61; 1.56; 1.53; 1.57	2.69	4.70
2side H-bGr (T_{AA})	5.043	1.54; 1.58	2.90	-
2side H-bGr (T_{AB})	5.057	1.54; 1.56	3.10	5.10

approximation within the YAMBO code [64, 65]. A slab truncation scheme [115] for the Coulomb potential was adopted to avoid spurious interactions between replica. The Brillouin zone was sampled by $16 \times 16 \times 1$ **k**-points for the primitive cell. We used a random integration scheme for the calculation of the screened Coulomb interaction [159], ensuring convergence of the quasiparticle gap with such low density **k**-points meshes. The sum-over-states in the calculation of polarization function and Green function have been truncated both at N_b=800 bands. The kinetic energy cutoff to represent the response functions corresponds to G_{cut}=30 Ry. The above parameters were chosen by considering a convergence threshold below 15 meV on the fundamental gaps, by employing the automated `aiida-yambo` based workflow [39, 40, 155, 63] described in Chapter 3. The energy gap values E_{g,G_0W_0} computed according to the G_0W_0 approximation are reported in Fig. 6.4 and Table 6.1.

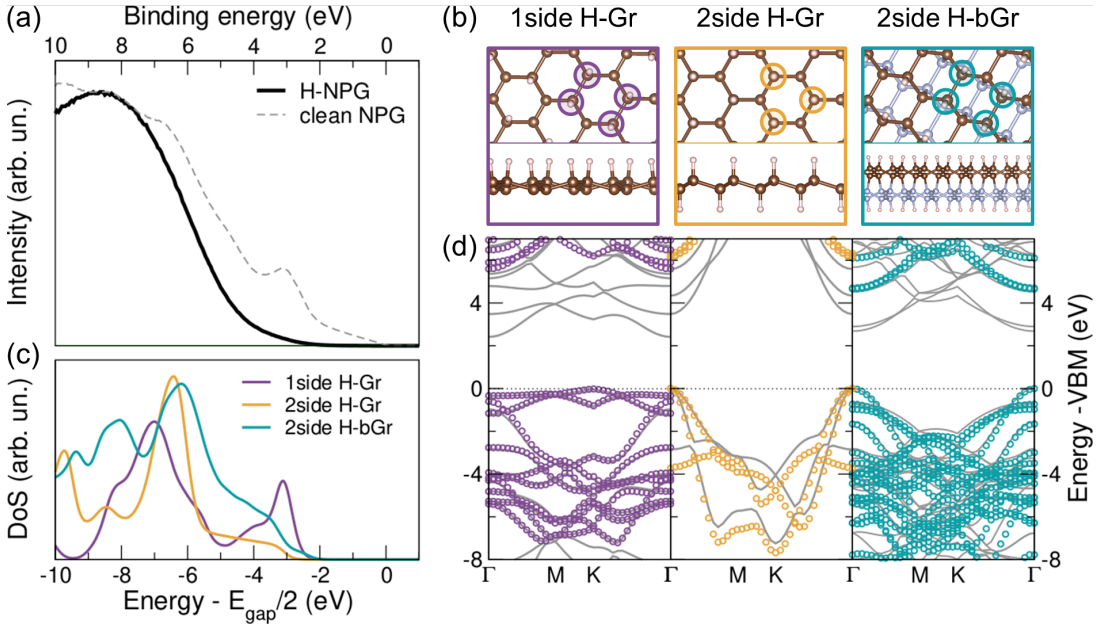

Figure 6.4: (a) Experimental VB spectra for clean (dashed) and totally hydrogenated NPG (solid line), taken with HeI_α (21.218 eV) photon energy. (b) Three model structures of 1-side and 2-side hydrogenated single- and bi-layer graphene (top and side views). The colored circles in the top view highlight the H sites in the hexagon. (c) Simulated quasi-particle density of states (DoS) in the *GW* approximation for the models in (b); zero energy set at midgap; a homogeneous broadening of 140 meV is applied. (d) Simulated DFT (solid gray lines) and *GW* (open circles) band structures for the corresponding models in (b); zero energy set at the VBM.

Fig. 6.4 shows the quasiparticle DoS (c) and band structures (d) of a few selected cases. We find in all cases that the computed quasiparticle band gap for

the free-standing hydrogenated sheets exceeds 3 eV (see Table 6.1). The single-side hydrogenation leads to the appearance of an indirect gap of 5.6 eV. For the double-side hydrogenation, we predict a direct gap of 4.7 eV for the H-bGr and 6.1 eV for H-Gr, the largest of the series, in line with previous calculations [240]. For a more direct comparison with experiments, in Fig. 6.4c we plot the DoS of the three systems, setting the Fermi level to the midgap, a reasonable assumption given the high experimental quality (negligible contaminations/defects) of this hydrogenated sample [2]. Irrespective of the exact position of the VBM onset, the single-side H-Gr system noticeably presents a structured DoS at the VBM, originating from the 2p-π orbitals of the unsaturated side, that is totally absent in the experimentally achieved saturated phase of Fig. 6.4a (solid thick line). On the contrary, the double-side single- and bi-layer hydrogenated graphene is characterized by a step-like DoS at the VBM, typical of 2D semiconductors [259], without any 2p-π contribution, in excellent agreement with the experimental data. Most of the spectral weight is indeed arising from the sp^3 hybrid orbitals, lying in the energy region below -6 eV. This compares well in terms of energies and overall shape with the experimental spectrum (Fig. 6.4a, solid thick line), taking into account the coexistence of single layer and bi-layer graphene [254, 255] in our NPG samples (see also Figure S1b). Overall, we can conclude that the calculated band structure and quasiparticle DoS unequivocally allow us to establish the achievement of double-side hydrogenated single and bi-layers graphene configurations.

6.2 Optical properties of deuterated graphene

In the previous section we provided quasiparticle band structure and DoS for some candidate structures of hydrogenated graphene, in order to support experimental results on H–NPG. We addressed the main hydrogenation process as the double-side one, by directly comparing GW–DoS and experimental photoemission spectral density. However, an experimental estimation of the fundamental gap cannot be obtained, as we only have information on the VBM, at variance with theoretical results where the band gap can be explicitly estimated through GW band structure. While comprehensive spectroscopy studies have focused on hydrogenated on-substrate graphene so far [260], here for the first time quasiparticle and optical band gaps — as predicted for different hydrogen chemisorption configurations [239, 261, 240] — are determined experimentally on fully free-standing and unsupported graphene.

In this chapter we compute optical properties, within the *GW*-BSE scheme, on a few selected candidate structures of hydrogenated graphene. By doing so, we

[2] While not having information on the position of the conduction band bottom from experiments, we though observe that the pristine NPG is undoped, with the Dirac point at the Fermi level. We can thus expect a similar behavior for the H-NPG sample, which supports the assumption of the Fermi level lying approximately at midgap.

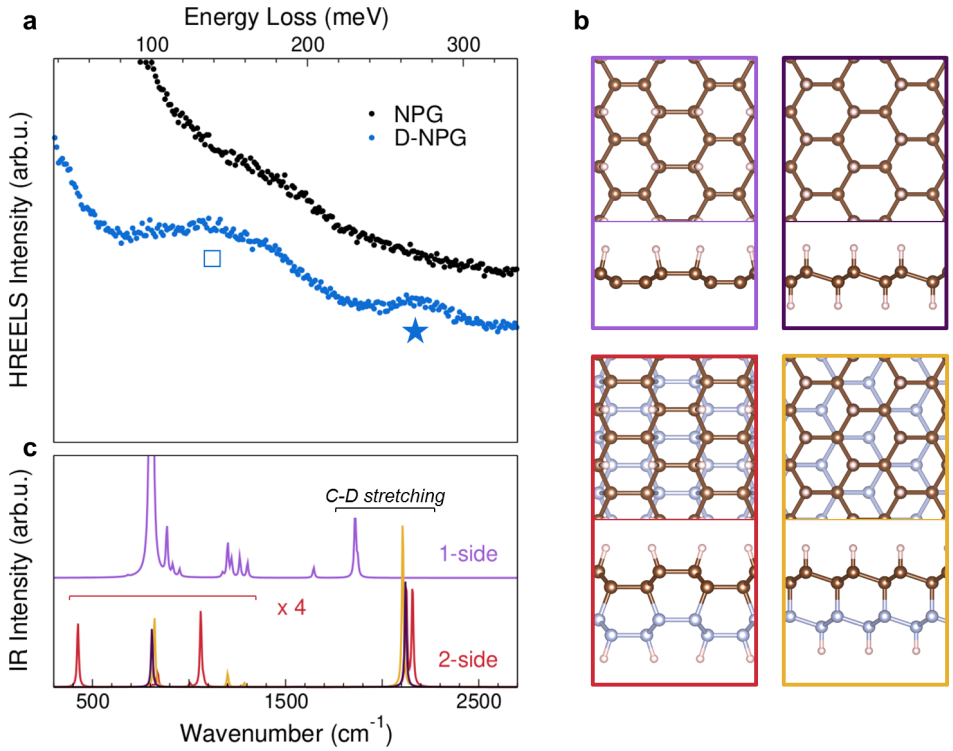

Figure 6.5: (a) HREEL vibrational spectra of NPG (black dots) and D-NPG (blue dots). The NPG spectrum has been upshifted for clarity (complete, unshifted spectra are reported in Supplementary Information). (b) Ball-and-stick models of 1-side (light violet, top left) and 2-side (dark violet, top right) single-layer D-Gr, as well as boat (red, bottom left) and chair (orange, bottom right) conformers of 2-side bi-layer D-Gr. (c) Simulated IR spectra for the structures in (b), displayed with the same color code. The energy range displayed on the x axis is the same as in panel (a), but in different units.

corroborate experimental assessment of the dielectric response of deuterated NPG (D–NPG) as obtained within high resolution electron energy loss spectroscopy (HREELS) [3], which provide information on both vibrational (structural) and dielectric properties of the sample. The use of deuterium for the chemisorption process allows us to definitely distinguish the adsorbed deuterium, with respect to other H contaminants, in view of the isotopic shift imparted to the vibrational features, as detected by HREELS. Fig. 6.6b shows the fundamental gap in the G_0W_0 approximation for all the double-side deuterated systems considered. We neglect the single-side deuteration, which was ruled out by the direct comparison between theoretical (DFT) and experimental (HREELS) vibrational analysis

[3]The HREELS experiments were performed at Modena and Reggio Emilia University in Modena, in the SESAMO laboratory by the group of Prof. Roberto Biagi and Prof. Valentina De Renzi.

(briefly shown in Fig. 6.5, where we can identify the peaks of the 2-side in the theoretical IR spectra of panel (c) with the experimental ones of D–NPG, shown in panel (a)). Depending on the specific configuration, the gap E_g ranges between 4.7 and 6.1 eV, with a VB maximum located at -E_g/2 (i.e. -2.35 and -3.05 eV respectively) if we consider E_F lying at midgap in the absence of doping, as discussed in the previous section (and in Ref. 73). Taking into account that experimental NPG samples are constituted by single and bi-layer graphene in a turbostratic arrangement, the calculated range of *GW* VB maximum values compares well with the experimental findings. BSE eigenvalues are converged up to 10 meV, using a **k**-point mesh of 34 × 34 × 1 in addition to the computational setup already explained in the previous section.

Fig. 6.6d shows the optical absorption spectra for the same configurations, which is characterized by a step-like shape (shaded area), typical of 2D semiconductors, with prominent individual excitonic peaks lying below the onset of the continuum. The optical gap ranges from 4 (yellow curve) to 4.66 eV (violet curve), to be compared with the experimental onset of about 2.8 eV. The discrepancy is probably related to the fact that we are here considering the optical response of ideal systems in vacuum with perfect registry. The real material comprises instead single- and few-layer regions with misoriented (turbostratic) stacking, which can give rise to quantitatively different excitations, including optically inactive ones (see below) that may become relevant when probing the sample at finite momentum. The exciton binding energy (EBE) of the lowest lying excitation with respect to the continuum is predicted to exceed 1 eV, irrespective of the specific free-standing configuration computed here, as can be seen in Fig. 6.6d by comparing the excitation energy of the first exciton, $E_{exc,1}$ with the *GW* gap (exemplified in panel f for 2-side D-Gr, violet curve, where the EBE_1 amounts to 1.44 eV). This holds true also for the boat conformer of 2-side D-2LGr (red curve), for which the first bright exciton corresponds to the 19th excitation, while the first excitation lies at about 3.6 eV, with $EBE_1 = 1.1$ eV. Such a large value results from both the enhanced e-h interaction in reduced dimensions and the weak screening of few-atom-thick free-standing systems in vacuum, as previously found for other low-dimensional materials [218].

To better understand the nature of the excitations, we analyse the excitonic wavefunctions, which are inspected by fixing the hole position in the centre of the C–C bond, where the valence states are located, and by plotting the electron probability density. For both mono and bi-layer deuterated Gr, as shown in Fig. 6.7, we find that the lowest lying excitons have charge transfer character, with the hole localized on the C–C bond and the electron having mixed C–H localization and free-electron-like character, as already shown for single-layer graphane [240]. This again demonstrates that the optical properties of the system are robust irrespective of the actual configuration considered (e.g. single- or bi-layer).

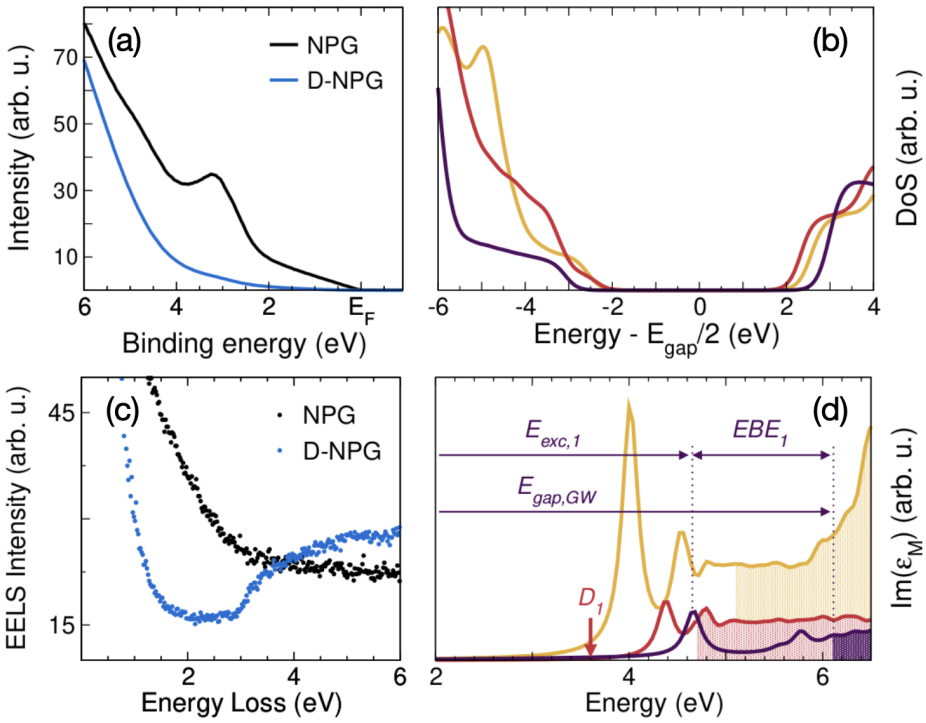

Figure 6.6: (a) Experimental VB spectra for clean NPG (black curve) and deuterated NPG (blue curve). (b) Simulated G_0W_0 DoS for the models in 6.5b (same color code); zero energy set at midgap; a homogeneous broadening of 140 meV is applied. (c) HREEL spectra of pristine NPG (black dots) and deuterated NPG (blue dots). (d) Calculated Im(ϵ_M) in the optical limit (q $\rightarrow$ 0), for the models in 6.5b (same color code). The binding energy of the nth exciton (EBE_n) can be read as the difference between the GW gap $E_{gap,GW}$ and the corresponding excitation energy $E_{exc,n}$, here exemplified for the first exciton of the 2-side D-Gr (violet curve). A Lorentzian broadening of 100 meV has been included. The continuum region is indicated as coloured shaded area.

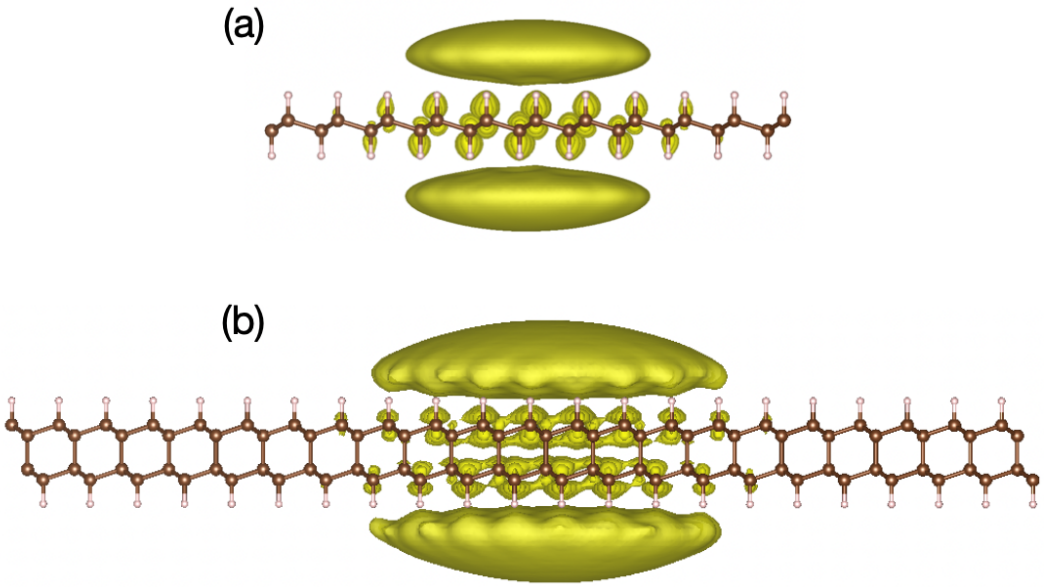

Figure 6.7: Electron probability distribution for the lowest excitons in mono (top) and bi-layer (bottom) configurations. The hole is fixed on a C–C bond. Electrons show mixed C–H localization and free-electron-like character.

6.3 Conclusions

We performed successful computational characterization of different configurations of hydrogenated graphene, and corroborated the experimental results to assess the candidate configurations composing the NPG samples. Strong electron electron interaction effects are identified, resulting in large quasiparticle corrections and the opening of an insulating quasiparticle gap. Besides, large exciton binding energies are computed ($\sim$ 1eV), leading to an optical gap exceeding 4 eV irrespective of the specific configuration, as resulting from GW and BSE simulations. Predicted spectral GW-DoS, band structure and (BSE-enabled) excitonic effects support the realization of double-side, fully-hydrogenated single- and bi-layer structures, thus confirming this as a successful strategy to realize a thermodynamically stable prototype of graphane. Most interestingly, both single layer and bi-layer double side hydrogenated graphene unveil a direct band gap opening, which makes this prototype of semiconducting graphane a promising platform for optoelectronics applications.

Chapter 7

Discovering novel 2D excitonic insulators

In this Chapter I present results on computational screening on a set of 2D materials, proposed to the discovery of novel excitonic insulators. Calculations are still running, as the project started only a few months before the writing of this Thesis, and here only preliminary results are shown. Despite that, they are very promising, and I'm planning to conclude the study in the next future.

More than fifty years ago, hypothesis about the spontaneous Bose condensation of excitons in matter, i.e. without external optical excitation, were done [77, 262, 263]. This new theorized phase shows formal analogies with the superconductor ground state [78], albeit the nature of the order is different [264], and it may exhibit effects like macroscopic quantum coherence and exotic low-energy excitations [79, 80, 81, 82]. Firstly, Mott [265] made the hypothesis that in semimetals, under specific conditions, there can be a formation of non-conducting and strongly interacting bound electron-hole pairs, with a consequent opening of a small band gap. This corresponds to an instability of the ground state of the system with respect to the formation of a Bose condensate of excitons. Additional considerations were done by Knox [266] for semiconductors [1]. He suggested that this crystal instability may occur when the excitonic binding energy (referred as EBE or E_B throughout this work) is larger than the transport energy gap E_g. In this case, the energy required for the formation of an exciton, namely $E_{exc} = E_g - E_B$, is negative. The new ground state, containing these spontaneously formed excitons, presents lower symmetry as for instance the formation of charge density waves (CDW) and eventually structure anomalies with respect to the normal ground state. These two were just the initial ideas that led to speculations and theoret-

[1] He specifically targeted indirect band gap semiconductors, but the same theoretical approach can be used for the direct case.

ical insights [75, 263, 77, 76, 267] that in materials with zero or small band gap this new phase of matter, called the excitonic insulating phase, may be induced (below a critical temperature T_c or above a critical pressure P_c).
Narrow gap low-dimensional materials or bulk semimetals/semiconductors under pressure are promising candidates for the excitonic insulator (EI) realization because of the reduced electronic screening and enhanced Coulomb interactions. A possible strategy to theoretically predict such phase is a combination of ab-initio methods (Many-Body Perturbation Theory), to find the instability $E_g - E_B < 0$, and effective mean field theories with model Hamiltonians to get insight into the excitonic ground state. This approach was successfully used in the past for several systems, e.g. armchair carbon nanotubes [268]. Other examples are T′ MoS_2 [269] (a quantum spin Hall insulator, QSHI) and Bulk MoS_2 under pressure [270], that have been theoretically predicted to develop a purely electronic ferroelectricity associated to the charge density wave driven by the excitonic order. Experimental evidences of the EI phase is rather complex to be found as there are not universal (i.e. not system-independent) fingerprints to guide experimental groups. For example, in Ta_2NiSe_5 an optical gap is found below T_c comparable with the E_B [271], and the temperature-dependent superfluid plasma frequency of the excitonic condensation has been determined from measured optical data [272]. Anyway, in this system, as in $TiSe_2$, besides the excitonic instability a singularity in the phonon density of states indicates that also structural instabilities contribute to the opening of tha gap [273, 274, 275, 276]. The ideal EI transition is purely electronic, with only small lattice distortions [262, 277]. Very recently, two independent researches showed experimental evidence of the realization of the EI in WTe_2 monolayers [278, 279] and other systems as stacked WTe_2 has been shown to present unexpected but interesting properties that might be inquire the EI phase, namely ferroelectricity [280] and gate-induced superconductivity [281, 282] in close proximity to the insulating phase. In this context, theoretical study are of paramount importance in explaining observed experimental features that could be associated to the EI transition as for instance bulk MoS_2, where unexpected fingerprint in Raman spectra where observed experimentally [283, 284, 285, 286, 287] and then clarified by theoretical considerations [270] suggesting the realization of the EI above a critical pressure. Moreover, theoretical predictions can be of great relevance in proposing materials that are good candidates for the EI realization.

In this work we perform an high-throughput study based on MBPT [3, 4, 2] on recently discovered 2D materials (by computational exfoliation) [12] to find candidates showing excitonic instability. MBPT is the state-of-the-art approach to study excited states of materials and is able to correctly capture the electron-electron and electron-hole interactions providing accurate estimation of the electronic gap and electron-hole binding energies from which it is possible to individuate excitonic instabilities.

7.1 A DFT-based preliminary screening

The systems object of this study are contained in the Material Cloud 2D materials database (MC2D) [13]. The database contains N>2000 two-dimensional systems discovered by computational exfoliation [12] of experimentally known bulk crystal structures taken from different available databases: COD [288], ICSD [289] and MPDS [290]. We considered previous relaxed structure as contained in the MC2D, together with the associated KS-DFT band structure to understand the character of the system (metal, semimetal, semiconductor) and extract preliminary information to reduce the number of systems to be studied by means of computationally demanding GW/BSE simulations. A first estimation of the E_B can be provided, at the DFT level, using a simple 2D hydrogenic excitonic model, which requires to know only the exciton effective mass $\mu_{exc} = \mu_e + \mu_h$ and the static polarizability α, both already computed [2] and stored in the database. The model was derived by Thygesen and co-workers [291, 292], and expresses the 2D-E_B as:

$$E_B^{2D} = \frac{8\mu_{exc}}{(1+\sqrt{1+32\pi\alpha\mu_{exc}})^2} \tag{7.1}$$

This preliminary analysis was done by Davide Campi and resulted in the identification of 35 candidates over N>2000 input systems with $E_B^{2D} \sim E_g$. The candidates are shown in Table 7.1, ordered for increasing exfoliation binding energy BE_{exf}. With a B$E_{exf} < 60$ meV/$\mathring{A}^2$, ∼70% of the materials considered here are *easily exfoliable*. We considered metals the systems with $E_g^{DFT} < -200$ meV, namely the As_2Ir_2, As_2Rh_2 and Ir_2P_2. Indeed, as shown in Fig. 7.1 for the Ir_2P_2, this is indeed a metallic band structure. We decided to exclude these 3 systems from our set as metallic systems are not ideal candidates as we are looking for semimetals or small band gap semiconductors. The remaining systems are 13 semimetals (-200 meV $< E_g^{DFT} < 20$ meV), and 19 semiconductors.

Around ∼50% of these candidates are very large systems, with large supercell volumes (V> 750$\mathring{A}^3$) and more than 100 electrons per unit cells. This is shown in Fig. 7.2, where we plotted histograms for the frequency distribution of the number of electrons N_{e^-} and the cell volume V as reported in Table 7.1. Moreover, ∼40% of systems are semimetals: for these cases the effect of the Spin-Orbit Coupling (SOC), that can eventually open a small gap, has been included. In presence of spin orbit coupling, GW and BSE calculation are solved in a spinorial basis which almost double the required computational cost with respect the cases it can be neglected.

[2] At the DFT level

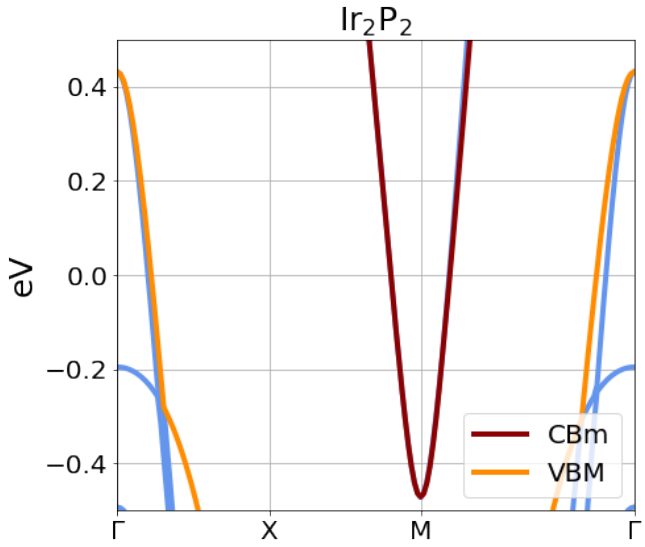

Figure 7.1: Band structure computed at the DFT level for Ir_2P_2. The orange band represents the top of the valence region (VBM), whereas the red one is the bottom of the conduction bands (CBm). These are obtained considering a priori the number of electrons in the unit cell and populating bands. The Fermi level is set to zero. Ir_2P_2 is a metallic system and should be excluded by our study. The other two systems, As_2Ir_2 and As_2Rh_2, present an almost identical band structure (see Appendix I for further details).

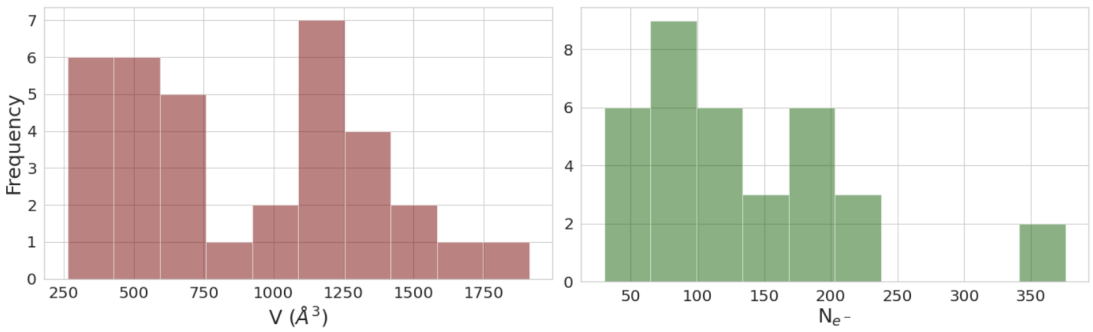

Figure 7.2: Histograms for the distribution of the candidate systems with respect to the cell volume V (left) and the number of electrons in the unit cell (right). We observe that ∼50% of the materials have V> 750$Å^3$ and N_{e^-} >100.

index	**System**	BE_{exf} (meV/Å^2)	V (Å^3)	N_{e^-}	$E_g^{DFT,bands}$ (meV)	$E_{g,coarse}^{GW}$ (meV)	$E_{g,coarse}^{GW,\Gamma-\Gamma}$ (meV)
1	Li_4S_4	7.5	700	36	-65	-157	2061
2	$Fe_2O_{12}Si_4$	8.2	592	120	52	73	132
3	$Ga_2I_2Y_2$	13.4	428	82	-149	-153	1332
4	$I_2N_2Ti_2$	14.6	362	68	20	2008	-1470
5	Hf_2Te_{10}	16.5	1247	212	-20	403	603
6	$Te_{10}Zr_2$	16.7	1259	184	61	94	336
7	$FeNO_8S_2$	18.1	471	81	71	-82	-172
8	CdK_4P_2	19.3	902	66	-154	-981	1558
9	$Fe_3O_{12}Si_4$	19.9	587	136	-32	–	–
10	$Pd_6Ta_4Te_{10}$	23.5	1698	376	-7	1274	1311
11	$Ir_2Ta_2Te_8$	25.8	1151	216	-26	11	11
12	$Rh_2Ta_2Te_8$	26.4	1134	216	33	248	130
13	Mo_4S_8	26.8	674	104	29	-158	-13
14	$Ir_2Nb_2Te_8$	27.1	1153	188	-8	60	-133
15	$Cl_6Cu_2H_8Li_2O_4$	29.5	1278	118	143	2183	2260
16	$O_2S_4Sb_2Y_2$	31.1	492	88	94	75	4119
17	In_2S_4Zn	36.0	392	70	0	247	247
18	$Bi_4Br_2In_2Se_8$	37.8	1913	148	101	–	–
19	$Cl_4K_4O_8V_2$	38.4	1216	112	18	-120	-57
20	$Cl_4K_4O_8$	38.4	1445	112	47	415	431
21	$Cu_2Se_6Tl_2Zr_2$	41.2	1058	124	129	972	972
22	$Cu_2Te_6Ti_2Tl_2$	43.9	1182	184	57	704	709
23	$Cu_4Te_6Ti_2$	44.0	1101	196	1	–	–
24	$Cu_2Sb_2Se_4$	52.2	669	92	200	357	357
25	$Cu_6K_2Te_4$	52.6	947	196	144	1004	1004
26	$AsCuLi_2$	62.7	334	30	-1	136	223
27	Na_2O_6Pt	68.3	492	72	80	515	670
28	As_2Ir_2	72.1	279	44	-1097	–	–
29	$Cu_2Na_2S_4Zr$	73.1	662	92	173	1320	1320
30	$Ag_4K_2Se_8Ta_2$	75.1	1519	196	10	774	865
31	As_2Rh_2	77.1	275	44	-982	–	–
32	$I_6Rb_2Sn_2$	83.4	1355	148	29	1168	1264
33	Ir_2P_2	85.8	262	44	-903	–	–
34	FKO_2Se	116.0	617	34	53	501	1445
35	$Ni_6Ta_4Te_{10}$	–	1317	376	48	-72	-84

Table 7.1: Candidate systems from the DFT-based screening (performed by Davide Campi), ordered for increasing exfoliation binding energy BE_{exf} (as computed using DF2-C09 vdW functional in Ref. [12]). For BE_{exf} <60 meV/Å^2, a system can be considered *easily exfoliable*. This is the case for ∼70% of them. The next three columns indicate the volume of the supercell V, the number of electrons per unit cell N_{e^-}, the KS-DFT band gap as obtained from bands computed on the high-symmetry **k**-path with QUANTUM ESPRESSO. The last two columns concern the minimum and the direct $\Gamma-\Gamma$ band gaps as computed with YAMBO using the coarse **k**-mesh, as described in Section 7.2. The "–" sign indicates that the related data is not yet available to be presented.

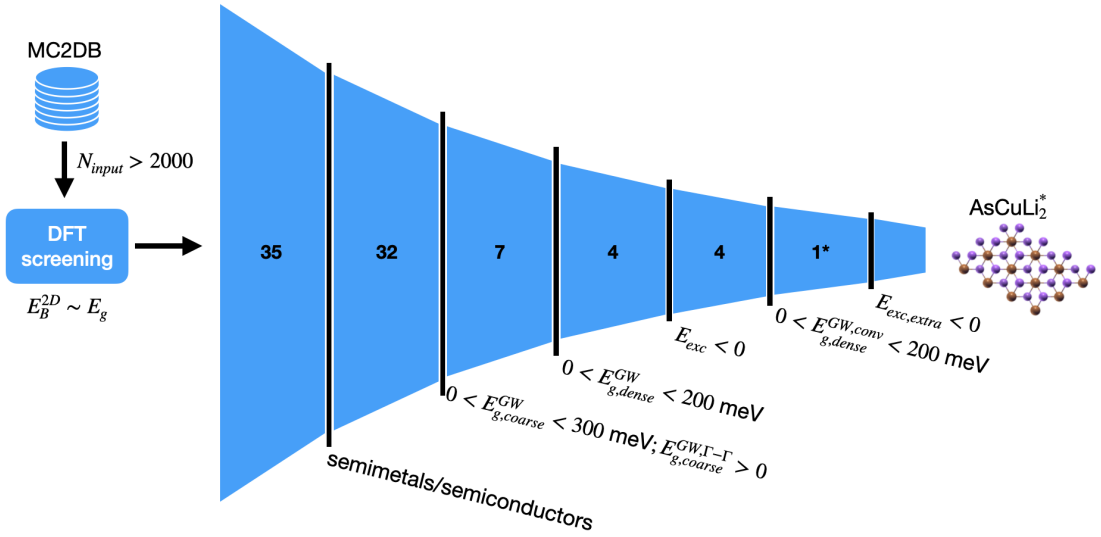

Figure 7.3: Screening funnel. After the first DFT screening, we performed the triple step GW+BSE, to further exclude systems. Then, proper GW convergence and BSE extrapolation is performed. Only for $AsCuLi_2$ we have the BSE extrapolated results. For each step of the funnel, we applied the filter indicated by the lower text in the figure. The superscript * indicates that we are still running simulations, so we only have preliminary results.

7.2 MBPT screening protocol

The large size of the systems object of this study represents a real computational challenge for GW and BSE simulations: Results have to be converged with respect to several interdependent quantities like the empty state summations and PW expansions (see Chapter 3 for more details), considering that each single calculation is computationally heavier than the corresponding DFT step of at least one order of magnitude. These limitations prevent us from proceeding directly with brute force GW and BSE convergence studies for each of the 31 systems. For this reason we designed the following screening protocol, also depicted in Fig. 7.3. The first two steps are the ones already mentioned: the DFT screening and the exclusion of metallic systems from the set under scrutiny. Then we start by performing, for each system, two GW calculations with moderate converged parameters using two different **k**-point meshes, chosen in such a way to include the **k**-points that detects the band gap (as obtained from the KS-DFT bands) with increasing precision:

1. a coarse mesh calculation, i.e. with **k**-point density ρ_k [3] such that $0.125 \leq \rho_k \leq 0.07$ $\mathring{A}^{-1}$;

2. a denser mesh calculation: $0.07 < \rho_k \leq 0.02$ $\mathring{A}^{-1}$.

[3]Expressed as the maximum distance between adjacent points along a reciprocal axis.

An additional criterion for the mesh choice is the number of crystal symmetries characteristic of a system: for N_{symm} <6 symmetries, we used the lowest mesh in the range of the available ρ_k, despite the explicit inclusion of the band gap in the mesh. The denser mesh is very stringent and, as we are using a recently developed **k**-point convergence accelerator (RIM-W [159]), we consider this mesh as safely converged. A further increment of such a mesh will make the calculations to converge the other parameter unfeasible. If the system is a semimetal at the DFT level, or even after the GW simulations, the same calculation is performed again with SOC to observe a possible gap opening. Otherwise, the system is excluded from the ones delivered to the next step of the study. For the two GW steps we filtered only systems with band gap 0< E_g^{GW} <300 meV and 0< E_g^{GW} <200 meV, respectively. These upper limits are reasonable as we are looking for very small band gap semiconductors and we do not expect consistent variations larger than 200 meV with respect to the final converged result.

Next, a BSE single calculation [4] using the denser GW mesh, in order to understand if the energy of the first exciton E_{exc} is already negative for the semi-converged value of the parameters. We expect the value of the excitation energy to lower in modulus, by approaching convergence, but to not change sign.

The most computational effort consists in the GW convergences [5] for the systems showing negative eigenvalue for the first excitons. This is done at fixed **k**-mesh density. The convergence is imposed on the gap E_g^{GW} and the relative absolute convergence threshold is between 10 and 30%, depending on the size of the system and of the band gap. Here, gaps are very small: even a 30% of convergence is near the state-of-the-art GW precision ($\sim$ 10, 20 meV). The usual constraint for the GW gap, i.e. 0< E_g^{GW} <200 meV, is applied at the end of the convergence.

Then, a final BSE extrapolation of the exciton eigenvalue is done considering calculations performed with different **k**-meshes, starting from the GW one and lowering the density ρ_k. The extrapolation is performed using the expression $E = A/(N_k)^{\alpha} + b$, where N_k is the number of k-points in the irreducible Brillouin Zone (iBZ).

[4] The quasiparticles needed are computed with the `YamboWorkflow` provided in the AIIDA-YAMBO plugin and then used in the BSE. For further details see Chapter 3. In this way we can track the real GW gap (not the one inherited from DFT) and understand at what transfer momentum **q** solve the BSE. Now this task is automated, so we are able to run BSE@GW, a non-trivial task, automatically from scratch.

[5] The parameters to be converged are FFTGvecs, Empty states summations and PW cutoff for the screening matrix. FFTGvecs is the number of G-vectors or energy cut off for expanding the wavefunctions/FFT transforms.

7.3 Results

Ground state charge densities and KS-DFT eigenvalues and eigenfunctions are computed by means of Density Functional Theory within the QUANTUM ESPRESSO package [116, 117], implementing plane-wave basis set and pseudopotential approach. The GGA-PBE [98] approximations was used to describe the KS-DFT exchange-correlation functional, by means of optimized norm-conserving Vanderbilt (ONCV) SG15 [110, 111] pseudopotentials. GW and BSE simulations are performed within the Yambo code [64, 65]. The dielectric screening matrix is described by using the Godby-Needs plasmon pole approximation [53] (GNPPA). Slab truncation of the Coulomb potential [115] is used to exclude interactions between supercells along the non-periodic direction (z-axis), and the Random Integration Method [158] (RIM) was used to fix divergences of the Coulomb interaction and to accelerate convergence with respect to the BZ sampling. We adopted the already mentioned stochastic integration of the screened potential (RIM-W method) [159], which allows to have a GW-converged results using Monkhorst-Pack **k**-points grid just slightly denser than the DFT one.

All simulations are performed within the AIIDA-YAMBO plugin [63, 155, 156], based on the AiiDA high-throughput oriented infrastructure [39, 40]. Specifically, we used the implemented workflows, namely `YamboWorkflow` and `YamboConvergence`, to automate the single DFT+GW (BSE) calculations and full convergence studies, respectively. In this way, each single step in the funnel of Fig. 7.3 is computed entirely without human intervention. Analysis of the results is performed by hand, as careful attention has to be paid at the decisional step.

7.3.1 Triple-step MBPT screening

This first screening is composed of three steps, in the sense that we perform two GW and one BSE calculations to preliminary decide if a system has to be further investigated (i.e., converged) or not. The two GW calculations are performed with semi-converged parameters and two different **k**-points meshes, both chosen in such a way to contain the **k**-point of the gap with a certain degree of precision. The results on the first GW calculations, the one with the coarse **k**-point mesh, are shown in the last two columns of Table 7.1. In particular, we note that there are some negative values of $E^{GW}_{g,coarse}$ and $E^{GW,\Gamma-\Gamma}_{g,coarse}$, meaning that we are facing a metallic behavior or a resolution of the band inversion (BI), respectively. This is the case of the $I_2N_2Ti_2$, studied by Marrazzo et al. [24] by means of DFT+MBPT. As shown in Fig. 7.4, the KS-DFT band structure shows a (distorted, due to anisotropy) Dirac cone near the Γ point. When the GW correction is applied, the order of the bands between the Γ and the Dirac cone is inverted due to a positive correction of the valence band and a negative one for the conduction band. This gives a resolution of the BI, here for $I_2N_2Ti_2$ evaluated to be $E^{GW,\Gamma-\Gamma}_{g,coarse} = -1.47$ eV. Both metallic and BI systems are discarded at this level of the study. Excluding

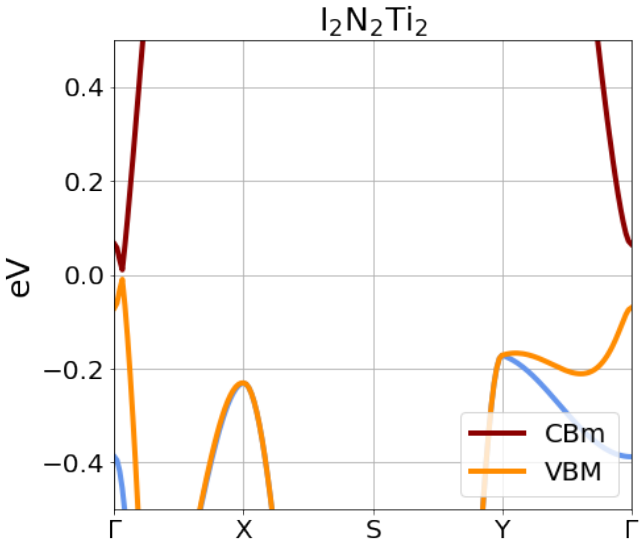

Figure 7.4: KS-DFT band structure of $I_2N_2Ti_2$, showing the band inversion which, once applied the GW correction, gives $E_{g,coarse}^{GW,\Gamma-\Gamma} = -1.47$ eV.

also the other systems with $0< E_{g,coarse}^{GW} <300$ meV, the next step, concerning the GW simulation with the denser **k**-grid, considered only 7 systems. In particular, in this case we computed several quasiparticle corrections in order to inspect the GW band gap of a given system: indeed, the KS-DFT and GW gap can be located at different **k**-points, so an estimation of the GW gap a priori from DFT results can be erroneous. The quasiparticle corrections are computed automatically within the `YamboWorkflow` by imposing a maximum distance of 150 meV for the KS-DFT bands with respect to the middle of the gap region.

As shown in Table 7.2, only 4 out of these 7 materials are predicted to have a $0< E_{g,dense}^{GW} <200$ meV, and so are then further investigated with respect to the BSE eigenvalues E_{exc}. Moreover, plotting the quasiparticle corrections with respect to the corresponding DFT eigenvalues determines the possibility to use or not a scissor&stretching operator to skip the calculation of the quasiparticle bands at the BSE step and approximate with a linear correction the DFT ones. We found that only for $O_2S_4Sb_2Y_2$ this approximation can be done without loss of significant accuracy around the band gap region, as shown in Fig. 7.5 (plots for the other systems are shown in Appendix J).

Among these resulting 4 materials, the $AsCuLi_2$ is the only one with $BE_{exf} >60$ meV/$\mathring{A}^2$, i.e. only potentially exfoliable. Together with $O_2S_4Sb_2Y_2$ (easily exfoliable), there are no previous experimental studies to be compared with. The last two candidate materials, $Rh_2Ta_2Te_8$ and $Ir_2Ta_2Te_8$, are easily exfoliable systems which were already studied in the past as component of layered van der Waals topological metals [293]. In particular the monolayer $Ir_2Ta_2Te_8$ has been predicted

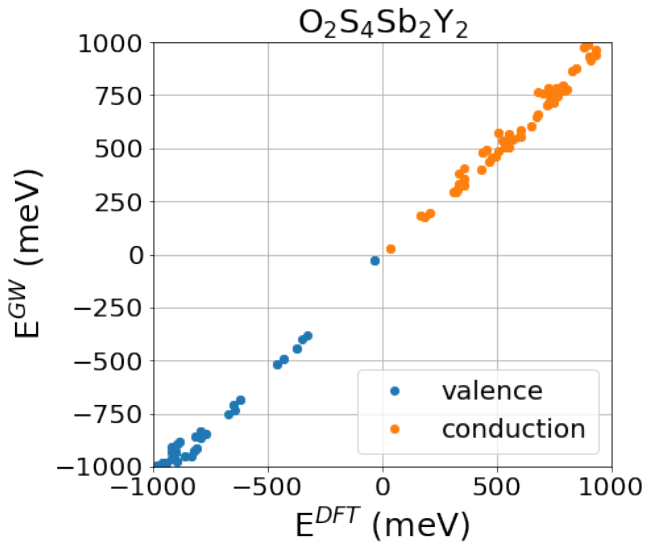

Figure 7.5: GW quasiparticle eigenvalues vs the corresponding DFT results for $O_2S_4Sb_2Y_2$. We observe that in this case a scissor&stretching correction can be a good approximation to correct DFT eigenvalues.

to be a QSHI [294] and the bulk geometry was experimentally characterized to be isostructural to $Rh_2Ta_2Te_8$ (as well as the excluded $Ir_2Nb_2Te_8$) [295, 296]. This is indeed suggested also from the similarities in the KS-DFT bands structures shown in Appendix I. Results for the BSE calculations show for 3 of the systems a negative first excitonic eigenvalue as reported in Table 7.2. BSE calculations on $Rh_2Ta_2Te_8$ are currently ongoing and we decided anyway to also consider it as a candidate for the GW convergence step by virtue of its small value of $E^{GW}_{g,dense}$ and of the similarities with the other candidate $Ir_2Ta_2Te_8$.

7.3.2 GW convergence

This is the most expensive step of the study. Up to now, we performed full GW convergence only for $AsCuLi_2$ and $Rh_2Ta_2Te_8$ [293]. For $O_2S_4Sb_2Y_2$ and $Ir_2Ta_2Te_8$, we have not yet converged results. For $AsCuLi_2$, we obtained a GW band gap of 185 meV, converged up to its 10%, and the final parameters are (FFT-Gvecs, Bands, PW cutoff) = (77 Ry, 1400, 10 Ry). This system was also shown to be a QSHI [24]. For $Rh_2Ta_2Te_8$, easily exfoliable (BE_{exf}=26.4 meV/$\AA^2$), we obtained a GW band gap of 98 meV, converged up to its 25%, and the parameters are (FFTGvecs, Bands, PW cutoff) = (36 Ry, 400, 8 Ry). Here we underline that this band gap is computed for the same **k**-point mesh of the DFT band gap; the difference can arise due to the fact that GW and DFT minimal gaps can be located in different points of the BZ. A better estimation of the gap will be provided after the calculation of quasiparticles over a larger set of k points needed for the

index	**System**	BE_{exf} (meV/Å^2)	$E^{GW}_{g,coarse}$ (meV)	$E^{GW}_{g,dense}$ (meV)	E_{exc} (meV)	$E^{GW,conv}_{g,dense}$ (meV)	SOC	**Candidate**
26	$AsCuLi_2$ [289]	62.7	140	94	-240	185	True	True
16	$O_2S_4Sb_2Y_2$ [290]	31.1	76	52	-365	–	False	True
12	$Rh_2Ta_2Te_8$ [293]	26.4	250	67	–	98	False	True
11	$Ir_2Ta_2Te_8$ [294, 293]	25.8	11	6	-432	–	True	True
14	$Ir_2Nb_2Te_8$ [295, 296]	27.1	60	-155	–	–	True	False
17	In_2S_4Zn [297]	36.0	250	-360	–	–	True	False
6	$Te_{10}Zr_2$ [298, 299]	16.7	94	-225	–	–	False	False

Table 7.2: Summary of the triple step screening. In order, we have the exfoliation Binding Energy BE_{exf}. We consider easily exfoliable materials with a BE_{exf} <60 meV/Å^2. Then, we indicated the GW gap for the coarse mesh $E^{GW}_{g,coarse}$, for the denser one $E^{GW}_{g,dense}$, the eigenvalues for the first exciton E_{exc}, the SOC activated or not and if the system can be considered for GW convergence. We see that the first four systems are candidates to be further investigated. Even if E_{exc} for $Rh_2Ta_2Te_8$ is not yet computed, the value of the $E^{GW}_{g,dense}$ suggests that it can be a possible candidate for the excitonic insulating phase. The last three systems show a strong band inversion, so we decided to not continue the investigation on them. Please note that the GW and BSE quantities shown here are not yet fully converged.

BSE step.

7.3.3 BSE extrapolation

BSE extrapolation has been done firstly on the smallest system of the set, the $AsCuLi_2$. The calculations are performed for a set of four **k**-point meshes: 20×20×1, 26×26×1, 34×34×1 and 40×40×1. Results, shown in Fig. 7.6, are very promising. The extrapolation of the results is done for both the GW band gap and BSE excitation energy with an inverse power law with respect to the number of **k**-points in the iBZ, N_k: $E = A/(N_k)^{\frac{7}{2}} + b$. This was the best power law to perform the fit, in terms of mean squared error. Optimal power laws can be found with more points (i.e. additional **k**-meshes). We performed the extrapolation considering only the largest three meshes (as the mesh (20×20×1) is clearly out of convergence and can be excluded from the fit. From Fig. 7.6 we see that the GW band gap is very well converged ($\sim$ 1 meV), and the first BSE eigenvalue is still out of convergence even for a 40×40×1 mesh (the highest one in the plot) of $\sim$ 20 meV. More calculations have to be included in the extrapolation to have a more accurate extrapolation, but anyway it seems that the exciton energy remains negative, with an extrapolated value of -151 meV. The resulting extrapolated excitonic binding energy is estimated to be $E_{B,extra} = 316$ meV.

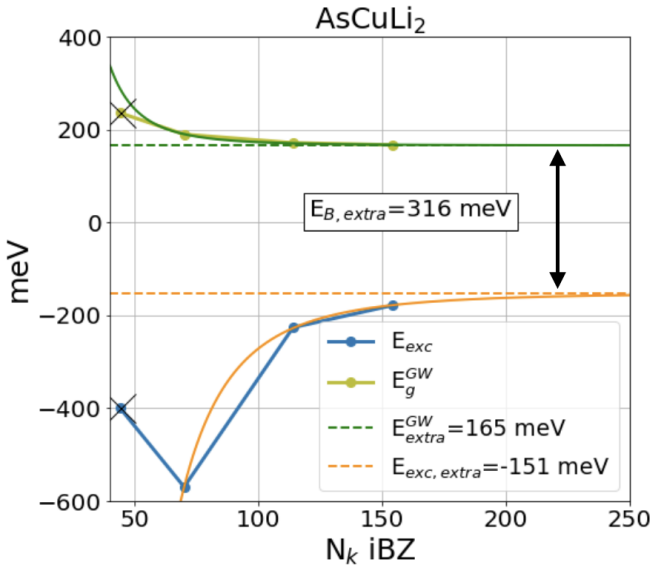

Figure 7.6: First results on $AsCuLi_2$, for GW gap and BSE first eigenvalue. The extrapolation is done using an inverse power law with respect to the number of **k**-points in the iBZ, N_k: $E = A/(N_k)^{\frac{7}{2}} + b$. The black X in the plot represent points not used in the fitting procedure, as too much out of convergence. The resulting extrapolated excitonic binding energy is $E_{B,extra} = 316$ meV.

7.4 Computational details of the simulations

As anticipated above, MBPT calculations on the selected structures are extremely cumbersome due to the large size of the systems and are at the verge of the possibilities of modern machines. Such calculations were possible thanks to the use of a large partition of the CPU partition of the LUMI machine [300], where the access was granted in the framework of a fruitful collaboration with the THEOS-MARVEL group of Prof. Nicola Marzari at EPFL in Lausanne. GW and BSE simulations are done using from 80 up to 200 nodes (128 cores/node, 256 GB of maximum RAM memory per node) with massive usage of the OPENMP (shared memory) parallelism: the average number of CPUs per single MPI (distributed memory) task was between 16 and 128, due to memory reason.

The effective human time and the computational time spent to run the simulations performed in this work (254 runs, excluding the final BSE extrapolations as still ongoing) are shown in Fig 7.7. On the left panel, we observe that the total time to run all the simulations (the cumulant curve) is >200 hours. Considering the cumulant per system, i.e. the cumulant of all the set divided by the number of systems, we can prove that the real global time required to run all the study (each single step of the screening) was 50 hours, i.e. ∼2 days. The right panel shows the core-hours timing for the calculations: to run the full set, we spent ∼2.5

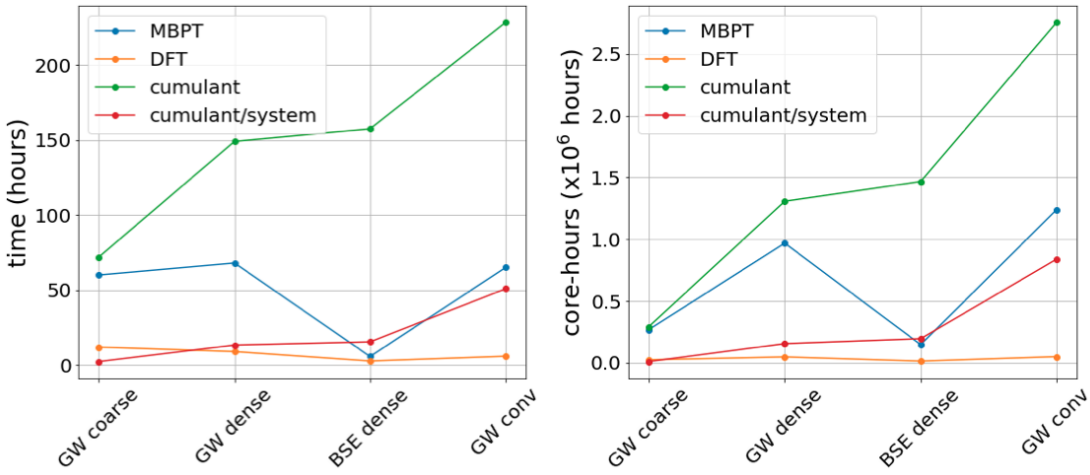

Figure 7.7: Timings for the 254 simulations of the MBPT steps of this work, excluded the BSE extrapolations. Left: effective human time needed to run the simulations. The cumulant per system, i.e. the cumulant for all systems (green curve) divided by their number, shows that the full set required only 50 hours. Right: computational time, in terms of core-hours. The work was performed in ∼2 running days consuming ∼2.5 million core-hours. We underline that all the curves, except the cumulant per system, concern the simulations for all the systems.

million core-hours (in less than two full-running days).

As expected, the DFT simulations represent only a very small fraction of the human (computational) time spent.

7.5 Conclusions and future plan

From these first calculations, $AsCuLi_2$ seems promising to be an excitonic insulator (EI) candidate, as it shows a negative extrapolated BSE eigenvalue (-151 meV). Moreover, this system is also a topological insulator (TI) [24], so it can be interesting to study the interplay between TI phase and EI one (if any), as in the 1T′ MoS_2 case [269].

To conclude the work presented in this Chapter, the following steps will be performed in the next future:

1. complete the study on $AsCuLi_2$ by adding more data for the BSE extrapolation;
2. perform the BSE extrapolation for the $Rh_2Ta_2Te_8$;
3. complete GW convergences for $O_2S_4Sb_2Y_2$ and $Ir_2Ta_2Te_8$ and then compute the BSE extrapolations.

Then, this successful protocol for the discovery of novel excitonic insulator can be applied also to other databases of 2D materials, like the C2DB [14].

Conclusions

In this Thesis I developed advanced and complex workflows to perform MBPT simulations in an automated and HT fashion, requiring the least possible human intervention and encoding ad-hoc algorithms. The most relevant tasks accomplished by these workflows are efficient GW (BSE) convergence and automatic GW band structure interpolation. I specifically designed the workflows to deal with complex chain of interlinked calculations, interfacing different codes (YAMBO, QUANTUM ESPRESSO, WANNIER90), and to perform error handling with respect to several common problems. Moreover, I tackled the issue of interdependence between selected crucial parameters as implemented in YAMBO, fundamental in order to perform accurate convergence studies of MBPT quantities. I also implemented GPU-oriented optimizations in YAMBO, targeting the stringent memory requirements that characterize the study of low-dimensional systems. These developments are fully available, as contained in open source codes (`aiida-yambo` plugin, YAMBO).

I firstly exploited the power of these workflows by computing the quasiparticle ionization potential and electron affinity of the molecules belonging to the GW100 dataset, within the Godby-Needs plasmon pole model, not yet provided among the approximations used in the past for the study of this dataset.

Concerning two-dimensional systems, I obtained the momentum-resolved excitonic dispersion of the carbon-nitride C_3N, showing also that the quasi-linear downward convexity of the excitonic band structure comes from the indirect nature of the fundamental band gap, as a result of the strong independent-particle contribution. Still focusing on carbon-based systems, I corroborated experimental results on hydrogenated nano-porous graphene by computational characterization of the electronic and optical properties for several hydrogenated graphene configurations. My calculations helped in the determination of the candidate structures composing the experimental samples, and provided useful insights for what concerns the character of the involved excitons. I successfully designed and applied a screening protocol to a subset of recently discovered (by computational exfoliation) two-dimensional materials. As a result, I found four materials that are expected to be unstable with respect to exciton formation in their ground state, a prerequisite to the realization of the excitonic insulating phase. Further analysis is still in progress but the preliminary results are very promising.

The results contained in the present Thesis clearly show the power of these newly developed workflows for the automated study of excited states properties of materials, paving the way for real high-throughput studies by means of Many-Body Perturbation Theory. Thanks to these developments and within the next-generation of pre-exascale and exascale supercomputers, these simulations may become extensively and routinely performed by the materials science community in the next future.

List of publications and works in preparation

- **Miki Bonacci**, Matteo Zanfrognini, Elisa Molinari, Alice Ruini, Marilia J. Caldas, Andrea Ferretti, and Daniele Varsano. "*Excitonic effects in graphene-like C_3N*". Phys. Rev. Materials, 6:034009, Mar 2022;

- Maria Grazia Betti, Ernesto Placidi, Chiara Izzo, Elena Blundo, Antonio Polimeni, Marco Sbroscia, Jose Avila, Pavel Dudin, Kailong Hu, Yoshikazu Ito, Deborah Prezzi, **Miki Bonacci**, Elisa Molinari, and Carlo Mariani. "*Gap opening in double-sided highly hydrogenated free-standing graphene*". Nano Letters, 22(7):2971–2977, 04 2022;

- **Miki Bonacci**, Junfeng Qiao, Nicola Spallanzani, Giovanni Pizzi, Antimo Marrazzo, Deborah Prezzi, Elisa Molinari, Daniele Varsano, and Andrea Ferretti, "*Automated Many-Body Perturbation Theory*", *preprint*;

- Matteo Zanfrognini, Nicola Spallanzani, **Miki Bonacci**, Elisa Molinari, Alice Ruini, Marilia J. Caldas, Andrea Ferretti, and Daniele Varsano. "*Effect of uniaxial strain on the excitonic properties of monolayer C_3N*", *preprint*;

- Maria Grazia Betti, Dario Marchiani, Elena Blundo, Marta De Luca, Antonio Polimeni, Riccardo Frisenda, Carlo Mariani, Samuel Jeong, Yoshikazu Ito, Andrea Tonelli, Nicola Cavani, Roberto Biagi, Valentina De Renzi, Peter N. O. Gillespie, **Miki Bonacci**, Elisa Molinari, and Deborah Prezzi, "*Dielectric response and excitations of free-standing graphane*", *preprint*;

- **Miki Bonacci** et al., "*Benchmarking the GW100 dataset with the Yambo code by means of G_0W_0 approximation*", *in preparation*;

- **Miki Bonacci** et al., "*Computational screening of novel 2D excitonic insulators*", *in preparation.*

Appendices

Appendix A

Second quantization

In order to greatly simplify the discussion of many identical interacting particles, we rely on the second quantized form of the Hamiltonian (or, more generally, of operators). This approach considers physical systems in a quantum-basis $|N\rangle = |n_1, ..., n_\infty\rangle$ that describes the number of particles n_i occupying a given state i in a complete set of single-particle states. One advantage of second quantization is that now the quantum-mechanical operators incorporate the statistics of Fermionic (Bosonic) states, and avoid to treat directly the many-body wavefunction that otherwise should be written as antisymmetrized (symmetrized) products of single-particle wavefunctions. Let's focus on fermionic systems: we define the creation and annihilation operator $\hat{a}_i^\dagger$ and $\hat{a}_i$, which create and destroy a particle if acting on a given fermionic state $|i\rangle$. They modify the number of particles belonging to that state, and satisfy the anticommutation relations $\{\hat{a}_i,\hat{a}_j^\dagger\} = \delta_{ij}$, $\{\hat{a}_i,\hat{a}_j\} = 0$. These anticommutation rules reproduce the correct statistics of Fermions.
It is convenient to define the so-called creation and annihilation *field operators*, that are simply a linear combination of the $\hat{a}_i^\dagger$ and $\hat{a}_i$ ones:

$$\begin{aligned} \Psi^\dagger(\mathbf{r}) &= \sum_i \psi_i^\dagger(\mathbf{r})\hat{a}_i^\dagger \\ \Psi(\mathbf{r}) &= \sum_i \psi_i(\mathbf{r})\hat{a}_i \end{aligned} \tag{A.1}$$

the coefficient of the expansion are the single-particle states $\psi_k(\mathbf{r})$, and the sum is over the set of single-particle quantum numbers i. Therefore, the expression of one- and two-body operators in terms of these field operators is, respectively:

$$\begin{aligned} \hat{T} &= \int d\mathbf{r}\Psi^\dagger(\mathbf{r})T(\mathbf{r})\Psi(\mathbf{r}) \\ \hat{V} &= \frac{1}{2}\int d\mathbf{r}d\mathbf{r}'\Psi^\dagger(\mathbf{r})\Psi^\dagger(\mathbf{r}')V(\mathbf{r},\mathbf{r}')\Psi(\mathbf{r}')\Psi(\mathbf{r}). \end{aligned} \tag{A.2}$$

Let $|N_0\rangle$ be the *true many-body ground state*[1] of the fermionic system composed of N identical particles, written in the Heisenberg picture. This is solution of the time-independent *interacting* Schroedinger equation $\hat{H}\,|N_0\rangle = E_0\,|N_0\rangle$, and the time evolution of field operators is described as follows:

$$\Psi(\mathbf{r},t) = e^{i\hat{H}}\Psi(\mathbf{r})e^{-i\hat{H}t}. \tag{A.3}$$

Finally, we can also express the charge density of a fermionic system in terms of the field operators as:

$$\rho(\mathbf{r},t) = \Psi^{\dagger}(\mathbf{r},t)\Psi(\mathbf{r},t). \tag{A.4}$$

[1] We assume also $|N_0\rangle$ to be normalized, i.e. $\langle N_0|N_0\rangle = 1$.

Appendix B

Maxwell's equations and dielectric properties of solids

The vast majority of the studies performed throughout this thesis concern the interaction of radiation with matter. The theoretical treatment of dielectric and optical properties of solids is based on Maxwell's equations and their solution for time-varying electric (magnetic) fields. In the presence of a medium, the action of electric and magnetic fields substantially creates effects like electric dipoles, magnetic moments, polarization charges and induced currents. We can decompose the total charge density of a system in two contributions:

$$\rho_{total} = \rho_{ext} + \rho_{pol} \tag{B.1}$$

where ρ_{ext} the external charge density to the medium, responsible of the external electric field, and ρ_{pol} is the consequently induced polarized charge density, described in terms of the polarization vector $\mathbf{P}$:

$$\rho_{pol} = -\nabla \cdot \mathbf{P} \tag{B.2}$$

Considering no external current [1] $\mathbf{J}_{ext} = 0$, the total current density is:

$$\begin{aligned} \mathbf{J}_{total} &= \mathbf{J}_{cond} + \mathbf{J}_{bound} \\ &= \sigma_1 \mathbf{E} + \left(\frac{\partial \mathbf{P}}{\partial t} + \nabla \times \mathbf{M} \right) \end{aligned} \tag{B.3}$$

where σ_1 is the conductivity of the material and $\mathbf{M}$ is the magnetization vector. From these definitions, we further define the displacement vector $\mathbf{D}$ and the magnetic field strength $\mathbf{H}$ as:

$$\begin{aligned} \mathbf{D} &= \epsilon_1 \mathbf{E} = (1 + 4\pi\chi_e)\mathbf{E} = \mathbf{E} + 4\pi\mathbf{P} \\ \mathbf{H} &= \frac{\mathbf{B}}{\mu_1} = \frac{\mathbf{B}}{(1 + 4\pi\chi_m)} = \mathbf{B} - 4\pi\mathbf{M}, \end{aligned} \tag{B.4}$$

[1] Related with the external charge density by the continuity equation: $\partial\rho_{ext}/\partial t + \nabla \cdot \mathbf{J}_{ext} = 0$

where ϵ_1, χ_e, χ_m are the dielectric constant, the electric and magnetic susceptibility, respectively. After these definitions, we can give the expression of Maxwell's equations in presence of a medium [301]:

$$\begin{aligned} \nabla \times \mathbf{E} + \frac{1}{c}\frac{\partial \mathbf{B}}{\partial t} &= 0 \\ \nabla \cdot \mathbf{B} &= 0 \\ \nabla \times \mathbf{H} - \frac{1}{c}\frac{\partial \mathbf{D}}{\partial t} &= \frac{4\pi}{c}\mathbf{J}_{cond} \\ \nabla \cdot \mathbf{D} &= 4\pi\rho_{ext} \end{aligned} \tag{B.5}$$

Considering an harmonic time dependence of the fields $\mathbf{F} = [\mathbf{D},\mathbf{E}]$, namely $\frac{\partial \mathbf{F}}{\partial t} = -i\omega\mathbf{F}$, it is possible to define the complex dielectric function as

$$\hat{\epsilon} = \epsilon_1 + i\epsilon_2 = \epsilon_1 + i\frac{4\pi\sigma_1}{\omega} = \epsilon_M(\omega). \tag{B.6}$$

The same extension to the complex field can be done for the conductivity: $\hat{\sigma} = \sigma_1 + i\sigma_2$. The solution of Maxwell's equations lead to the following dispersion relation between the complex wavevector $\mathbf{q}$ and the frequency ω:

$$\mathbf{q} = \frac{\omega}{c}\left[\epsilon_1\mu_1 + i\frac{4\pi\mu_1\sigma_1}{\omega}\right]^{1/2}\mathbf{n}_\mathbf{q} \tag{B.7}$$

where $\mathbf{n}_\mathbf{q} = \frac{\mathbf{q}}{|\mathbf{q}|}$. It is possible to define, as new response function, the complex refractive index $\hat{N}$ as:

$$\hat{N} = n + ik = \left[\epsilon_1\mu_1 + i\frac{4\pi\mu_1\sigma_1}{\omega}\right]^{1/2} \tag{B.8}$$

B.1 Absorption coefficient and Loss function

Considering an harmonic electromagnetic wave and the complex form of the wavevector, as we are inside a medium, we obtain the following for the magnitude [2] of the associated electric field:

$$\mathbf{E}(\mathbf{r},t) = \mathbf{E}_0 e^{i\omega\left(\frac{n}{c}\mathbf{n}_\mathbf{q}\cdot\mathbf{r}-t\right)}e^{-\frac{\omega k}{c}\mathbf{n}_\mathbf{q}\cdot\mathbf{r}}, \tag{B.9}$$

where we see that the imaginary part of $\mathbf{q}$ takes into account an attenuation effect due to the energy absorption of the medium. By virtue of the Lambert-Beer's law:

$$\alpha = -\frac{1}{I}\frac{dI}{dr} \tag{B.10}$$

[2] The associated intensity $I(\mathbf{r})$ is proportional to its modulus square.

we can define the absorption coefficient α as:

$$\alpha = -\frac{2k\omega}{c} = \frac{4\pi k}{\lambda}. \tag{B.11}$$

So, $\alpha \propto \sigma_1$ (or equivalently to ϵ_2): highly conducting materials attenuate radiation strongly. The absorption spectrum of a given materials is then computed as:

$$\mathrm{Abs}(\omega) = \epsilon_2(\omega) = \mathrm{Im}\epsilon_M(\omega). \tag{B.12}$$

Considering an external electron moving inside the solid, it will lose energy as measured in electron energy loss (EELS) experiments. This moving charge produces a field $\mathbf{D}$, and the associated rate of electronic energy density absorbed per unit volume is given by:

$$\mathrm{Re}\left(\mathbf{E}\cdot\frac{\partial\mathbf{D}}{\partial t}\right) = \mathrm{Re}\left(\frac{\mathbf{D}}{\hat{\epsilon}}\cdot\frac{\partial\mathbf{D}}{\partial t}\right) = \omega\mathrm{Im}\left(\frac{1}{\hat{\epsilon}(\omega)}\right)|D|^2, \tag{B.13}$$

which clearly allows us to define the Loss function, as considered throughout this work, as:

$$\mathrm{L}(\omega) = -\mathrm{Im}\left(\frac{1}{\epsilon_M(\omega)}\right) \tag{B.14}$$

B.2 Macroscopic and microscopic connection

It is possible to connect the macroscopic dielectric function, and all the associated quantities (like absorption and loss spectra), with the macroscopic description of the materials, i.e. the description of the single electronic states and the associated properties like the energy $\epsilon_{n,\mathbf{k}}$ and the occupation factors $f(\epsilon_{n,\mathbf{k}})$. Indeed, following Ref. 301 in spite of a semiclassical independent single-particle approach, and for the response to a transverse electromagnetic field, we can define the imaginary part of the macroscopic dielectric function as:

$$\begin{aligned}\epsilon_2(\mathbf{q},\omega) = \frac{4\pi^2}{\Omega}\frac{e^2}{\omega^2 m^2}\sum_{\mathbf{k}}\sum_{l,l'} f(\epsilon_{l,\mathbf{k}})[\delta(\epsilon_{l,\mathbf{k}} - \epsilon_{l',\mathbf{k}-\mathbf{q}} - \hbar\omega) - \\ - \delta(\epsilon_{l',\mathbf{k}+\mathbf{q}} - \epsilon_{l,\mathbf{k}} - \hbar\omega)] \times |\left\langle l', \mathbf{k}+\mathbf{q}\right| \mathbf{p} \left|l, \mathbf{k}\right\rangle|^2\end{aligned} \tag{B.15}$$

where we see that indeed ϵ_2 is built on the sum of single particle transitions between states of energy $\epsilon_{n,\mathbf{k}}$ and occupations $f(\epsilon_{n,\mathbf{k}})$, obtainable from the microscopic information of the solid.

Appendix C

Additional numerical aspects within the Yambo Code

In this chapter we present technical details and approximations as implemented in the YAMBO Code, and used throughout this work.

C.1 Godby-Needs Plasmon Pole Approximation and beyond

We already pointed out as in computing the dynamical screening W, the standard method to computed the dielectric function is to apply the so-called plasmon pole model [134, 52, 53], in which all the spectral weight is concentrated in a single pole:

$$\begin{aligned} \text{Re } \epsilon^{-1}_{\mathbf{GG'}}(\mathbf{q},\omega) &= 1 - \frac{A_{\mathbf{GG'}}(\mathbf{q})\tilde{\omega}^2_{\mathbf{GG'}}(\mathbf{q})}{\omega^2 - \tilde{\omega}^2_{\mathbf{GG'}}(\mathbf{q})} \\ \text{Im } \epsilon^{-1}_{\mathbf{GG'}}(\mathbf{q},\omega) &= A_{\mathbf{GG'}}(\mathbf{q}) \times [\delta(\omega - \tilde{\omega}_{\mathbf{GG'}}(\mathbf{q})) - \delta(\omega + \tilde{\omega}_{\mathbf{GG'}}(\mathbf{q})] \end{aligned} \tag{C.1}$$

where the matrices $A_{\mathbf{GG'}}(\mathbf{q})$ and $\tilde{\omega}^2_{\mathbf{GG'}}(\mathbf{q})$ are the parameters of the model. Among the flavours of PPA [134], YAMBO implements the Godby-Needs PPA (GN-PPA) [53], which imposes the condition that the model should exactly fit the ϵ^{-1} function at zero frequency, i.e. $\omega = 0$, and at an imaginary frequency $\omega = iE_{PPA}$, given the plasmon frequency E_{PPA} (by default at 1 Ha in Yambo, but tunable from input). In this way the integral on frequencies in Eq. 2.57 can be done analytically, yielding the result:

$$\Sigma^c_{n\mathbf{k}}(\omega) = \frac{1}{N_q \Omega} \sum_{\mathbf{GG'q}} g^{n\mathbf{k}}_{\mathbf{GG'}} W^c_{\mathbf{GG'}}(\mathbf{q}) \tag{C.2}$$

Where $W^c(\mathbf{q})$ is the static correlation part of the screening potential, and $g^{n\mathbf{k}}$ is the frequency dependent part:

$$g^{n\mathbf{k}}_{\mathbf{GG'}} = \frac{1}{2}\sum_m \frac{-\rho_{nm}(\mathbf{k},\mathbf{q},\mathbf{G})\tilde{\omega}_{\mathbf{GG'}}(\mathbf{q})\rho^*_{nm}(\mathbf{k},\mathbf{q},\mathbf{G'})}{\omega + [\tilde{\omega}_{\mathbf{GG'}}(\mathbf{q}) - i\eta]\mathrm{sgn}(\nu - \epsilon^{KS}_{m\mathbf{k-q}}) - \epsilon^{KS}_{m\mathbf{k-q}}}. \tag{C.3}$$

If one wants to get rid of a model function for the dielectric function, has to rely on Full-Frequency(FF) methods [51], where the integration is performed numerically: a more sophisticated description of the dielectric function can be achieved, useful in cases where the PPA fails. In Yambo, the FF integral is performed on the real-axis, as explained in Ref. 65. However, as computational effort is considerably heavier, we should always try to rely on PPA as a first approximation. All the results in this work are obtained using GN-PPA. Last, but not least, intermediate possibilities between PPA and FF methods are possible, like Pade expansions of the dielectric matrix [200] or a recently developed multipole approximation, implemented in Yambo. [54].

C.2 Random integration methods

Most of the quantities considered in the GW implementation in the YAMBO code require an integration over q, where q belongs to the BZ. This integral is then substituted by a summation over a suitable grid of points:

$$\int_{BZ} \frac{d\mathbf{k}}{(2\pi)^3} \rightarrow \frac{1}{N_{\mathbf{k}}\Omega}\sum_{\mathbf{k}}. \tag{C.4}$$

For example, the exchange part of the Self-Energy becomes:

$$\Sigma^x_{n\mathbf{k}} \approx -\frac{(2\pi)^3}{N_q\Omega}\sum_{m,\mathbf{q}}\sum_{\mathbf{G}} |\rho_{nm}(\mathbf{k},\mathbf{q},\mathbf{G})|^2 f_{m,\mathbf{k-q}} v(\mathbf{q}+\mathbf{G}) \tag{C.5}$$

this approximation can be written assuming that Σ^x is a smooth function of $\mathbf{q}$. This is in general not true for the Coulomb interaction $v(\mathbf{q}+\mathbf{G})$, that diverges for vanishing momentum. If in a three-dimensional system this divergence is removed [115], for a low-dimensional system it is a very critical issue. To treat with this problem, YAMBO implements the Random Integration Method (RIM) [158], which rewrites the HF self-energy, Eq. C.5 as:

$$\Sigma^x_{n\mathbf{k}} \approx -\frac{(2\pi)^3}{N_q\Omega}\sum_{m,\mathbf{q}}\sum_{\mathbf{G}} |\rho_{nm}(\mathbf{k},\mathbf{q},\mathbf{G})|^2 f_{m,\mathbf{k-q}} \int_{R_\Gamma} \frac{d\mathbf{q'}}{(2\pi)^3} v(\mathbf{q}+\mathbf{q'}+\mathbf{G}) \tag{C.6}$$

where the integral is evaluated in a region R_Γ around Γ is performed using a Monte Carlo technique. In this way, the divergence at $\mathbf{q} = \Gamma$ is cured and moreover,

an acceleration on the convergence of the **k**-point sampling is obtained for the exchange of self-energy. Combining this method with a stochastic integration technique for the static screening, as done by Guandalini et al. in Ref. 159 for 2D semiconductor and implemented in the YAMBO code, it is possible to obtain very accurate GW results with a **k**-mesh grid only slightly larger than the one used to compute the DFT starting point. We pictorially named this method "RIM-W".

C.3 The supercell approach within MBPT

When we deal with a low-dimensional system in a PW basis, a supercell with a large amount of vacuum along the non-periodic direction has to be taken into account. This is done in order to avoid spurious interaction between the fictitious supercell replica along the direction where the periodicity is not wanted to be physically true. The vacuum space then requires a large number of **G** vectors in the PW expansion to be accurately described. If in DFT these "vacuum layer" can be safely retained to be not so large (for 2D, usually $R_z = 15\mathring{A}$), when we consider excited state properties, these length can be very large, making very soon the calculations not feasible from the computational point of view. This is due to the correlation part of the self-energy [115]. A solution, implemented in Yambo, is the so-called *Truncation* of the Coulomb potential [115]. Within this method, the Coulomb potential is truncated near the boundaries of the supercell non-periodic edges in real space. This allows the use of a supercell with a moderate (usually similar to the DFT case) vacuum layer. Several types of truncation are proposed in Ref. 115, for a given dimensionality of the system. We proposed here the two schemes used in this work, the *spherical* and the *slab* cutoff. For 0D systems, like molecules the first method truncates the potential at the edges of a sphere of radius R [302]:

$$\tilde{v}^{0D}(G) = \frac{4\pi}{G^2}[1 - \cos(GR)] \tag{C.7}$$

We can indeed observe that also the divergence for $\mathbf{q}\to 0$ is analytically curated in this case. For 2D systems instead, placed in a supercell of lenght L along the non periodic direction, the slab cutoff lead to the following form for the Coulomb potential:

$$v_{\mathbf{G}}(\mathbf{q}) = \frac{4\pi}{|\mathbf{q}+\mathbf{G}|^2}\left[1 - e^{-|\mathbf{q}_\parallel+\mathbf{G}_\parallel|L/2}\cos[(q_z+G_z)L/2]\right], \tag{C.8}$$

which still is divergent for $\mathbf{q}\to 0$. In this case the divergence can be cured numerically through the RIM method explained in Sec. C.2.

Appendix D

Maximally-localized Wannier functions

Maximally-localized Wannier functions (MLWFs) are an optimized (local) basis set that can be profitably used to describe advanced properties of materials which require very dense Brillouin zone integration like, e.g., interpolated band structure, shift currents [303], gyrotropic effects [304] and superconductivity [305]. They can be efficiently used to build tight-binding models and then bridge the atomic and the mesoscopic scales, i.e. from the microscopic description of materials to functional nano-devices [306, 307]. Here, we give a review the basic theory the method relies on. More details can be found in several works and reviews [308, 309, 310, 311].

D.1 Basic theory

Considering a Bloch state $|\psi_{n\mathbf{k}}\rangle$, satisfying the Bloch theorem $\psi_{n\mathbf{k}}(\mathbf{r}) = u_{n\mathbf{k}}(\mathbf{r})e^{i\mathbf{k}\cdot\mathbf{r}}$ ($u_{n\mathbf{k}}(\mathbf{r})$ being a periodic function of with the same periodicity of the lattice), the Wannier function corresponding band n can be computed via a unitary transformation

$$|w_{n\mathbf{R}}\rangle = V \int_{BZ} \frac{d\mathbf{k}}{(2\pi)^3} e^{-i\mathbf{k}\cdot\mathbf{R}} |\psi_{n\mathbf{k}}\rangle \tag{D.1}$$

where V is the volume of the unit cell, and $\mathbf{R}$ is a Bravais lattice vector. This transformation is known as Wannier transform [312]. Bands that are well separated from the others in terms of energy gaps, are said to be *isolated*. Generalizing the theory for a single band, it is possible to describe the bundle of *isolated* electronic states in terms of wavefunctions related to Bloch states via two unitary transformations:

$$|w_{n\mathbf{R}}\rangle = V \int_{BZ} \frac{d\mathbf{k}}{(2\pi)^3} e^{-i\mathbf{k}\cdot\mathbf{R}} \sum_{m=1}^{J} |\psi_{n\mathbf{k}}\rangle U_{mn\mathbf{k}} \tag{D.2}$$

where $U_{\mathbf{k}}$ are unitary matrices mixing Bloch states, and J is the subset of the isolated bands. Up to now, we have not imposed any condition on the wavefunctions $|w_{n\mathbf{R}}\rangle$. To obtain MLWFs it is necessary to impose the minimization on the sum of the quadratic spread of the wavefunctions about their centers with respect to a reference $\mathbf{R}$ (for example $\mathbf{R}$=$\mathbf{0}$). This quantity is called the *spread functional*:

$$\Omega = \sum_{n=1}^{J} \left[\langle w_{n\mathbf{0}} | \, \mathbf{r} \cdot \mathbf{r} \, | w_{n\mathbf{0}} \rangle - | \langle w_{n\mathbf{0}} | \, \mathbf{r} \, | w_{n\mathbf{0}} \rangle |^2 \right]. \tag{D.3}$$

The spread functional can be seen as composed [308, 311] of a gauge-invariant term Ω_I:

$$\Omega_I = \sum_{n=1}^{J} \left[\langle w_{n\mathbf{0}} | \, \mathbf{r} \cdot \mathbf{r} \, | w_{n\mathbf{0}} \rangle - \sum_{m\mathbf{R}} | \langle w_{n\mathbf{0}} | \, \mathbf{r} \, | w_{m\mathbf{R}} \rangle |^2 \right], \tag{D.4}$$

and a gauge-dependent part Ω_D:

$$\Omega_D = \sum_{n=1}^{J} \sum_{m\mathbf{R}\neq n\mathbf{0}}^{J} | \langle w_{n\mathbf{0}} | \, \mathbf{r} \, | w_{m\mathbf{R}} \rangle |^2. \tag{D.5}$$

This last part of the spread functional, Ω_D, is the only one that changes under $U_{\mathbf{k}}$ action, and so it is the quantity that has to be minimized in order to obtain maximally localized Wannier functions. By making reference to Bloch wavefunctions, Eqs. D.4 and D.5 can be re-written as [311, 313]:

$$\Omega_I = \frac{1}{N_{\mathbf{k}}} \sum_{\mathbf{k},\mathbf{b}} w_b \sum_{m=1}^{J} \left[1 - \sum_{n=1}^{J} |\mathrm{M}_{mn\mathbf{kb}}|^2 \right] \tag{D.6}$$

and

$$\Omega_D = \frac{1}{N_{\mathbf{k}}} \sum_{\mathbf{k},\mathbf{b}} w_b \left[\sum_{n=1}^{J} (-\mathrm{Im}(\ln \mathrm{M}_{mn\mathbf{kb}}) - \mathbf{b} \cdot \langle w_{n\mathbf{0}} | \, \mathbf{r} \, | w_{n\mathbf{0}} \rangle)^2 + \sum_{m\neq n} |\mathrm{M}_{mn\mathbf{kb}}|^2 \right], \tag{D.7}$$

where $\mathbf{b}$ connects a $\mathbf{k}$ point and its neighbour $\mathbf{k}$+$\mathbf{b}$, w_b are the associated weights to the finite difference representation of the gradient operator in $\mathbf{k}$-space and $\mathrm{M}_{mn\mathbf{kb}}$ are defined as:

$$\mathrm{M}_{mn\mathbf{kb}} = \langle u_{m\mathbf{k}} | u_{n\mathbf{k}+\mathbf{b}} \rangle \, . \tag{D.8}$$

If bands are not well isolated, but hybridize with other bands which do not belong to the energy range of interest, these bands are called *entangled*. In this very common case, the number of bands in a given energy window is not fixed, so the subset of target wavefunction $J_{\mathbf{k}}$ (now $\mathbf{k}$-dependent) can be different with respect to the desired subset J. These requires the so-called disentanglement procedure [309] that is composed of two steps:

- select the smoothest possible subspace by applying unitary transformation to the $J_{\mathbf{k}}$ states;
- perform the minimization of Ω_D as for the isolated bands case.

The smoothness of the subspace is minimized by minimizing the gauge invariant spread Ω_I [309]. However, this disentanglement procedure is strongly dependent on the initial trial wavefunctions belonging to the J subset, and is often guided by chemical intuition. A recent method, the selected columns of the density matrix (SCDM) algorithm [314, 315], has been proposed to avoid the need of this initial guess and produce automatically already well localized candidate wavefunctions to obtain MLWFs. Recently, this approach was successfully used in a high-throughput study on solids [149]. SCDM is parameter-free for an isolated set of bands, and in the case of entangled bands requires only two parameters together with the choice of the target dimensionality for the disentangled subspace (i.e., the number of MLWFs required).

D.2 Band structure interpolation

Once MLWFs have been obtained, the energy band structure can be interpolated without major additional computational cost at arbitrary **k**-points in the BZ [309, 310]. The interpolation is performed by means of Slater-Koster interpolation scheme [316, 317]. Considering the rotated Bloch states $|\psi^{rot}_{n\mathbf{k}}\rangle$, obtained by the action of the unitary matrix $U_{\mathbf{k}}$ (determined from the minimization of Ω_D), their corresponding Hamiltonian is computed from the starting (unrotated) one as:

$$H^{rot}(\mathbf{k}) = U^{\dagger}_{\mathbf{k}} \tilde{H}(\mathbf{k}) U_{\mathbf{k}} \tag{D.9}$$

with $\tilde{H}_{mn}(\mathbf{k}) = \tilde{\epsilon}_{m\mathbf{k}}\delta_{mn}$. Then, $H^{rot}(\mathbf{k})$ is Fourier transformed in real space into N Bravais lattice vectors $\mathbf{R}$ belonging to a Wigner-Seitz supercell centered in $\mathbf{R}$=0, and eventually Fourier transformed back to an arbitrary $\mathbf{k}$':

$$H^{rot}_{mn}(\mathbf{k}') = \sum_{\mathbf{R}} e^{i\mathbf{k}'\cdot\mathbf{R}} H_{mn}(\mathbf{R}). \tag{D.10}$$

Appendix E

Provenance graphs for `aiida-yambo` workflows

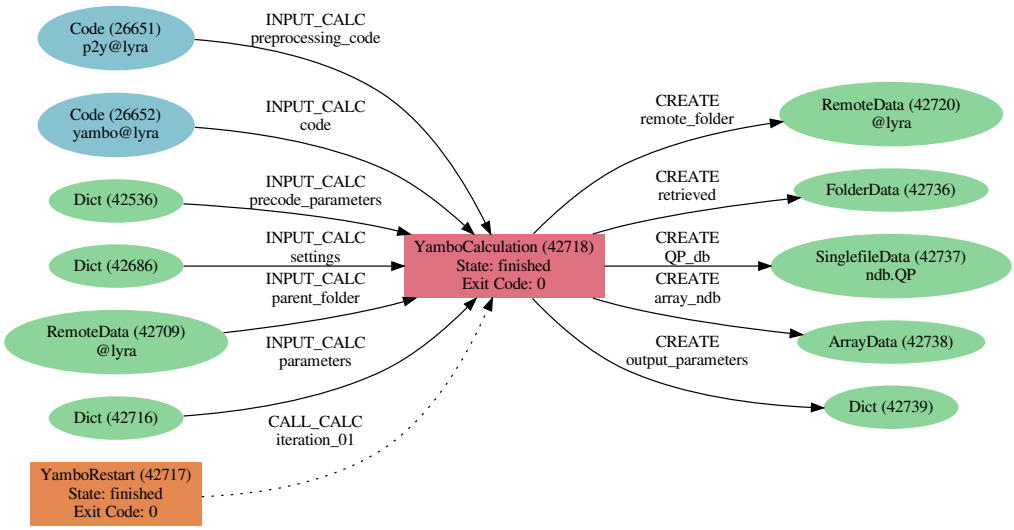

Figure E.1: **Example of provenance graph for `YamboCalculation`.** A set of inputs are provided to the calculation instance, and outputs are collected and generated after the actual `yambo` calculation, managed by the `YamboCalculation` calcjob. We can observe that actually, this `YamboCalculation` was called by a `YamboRestart` workflow.

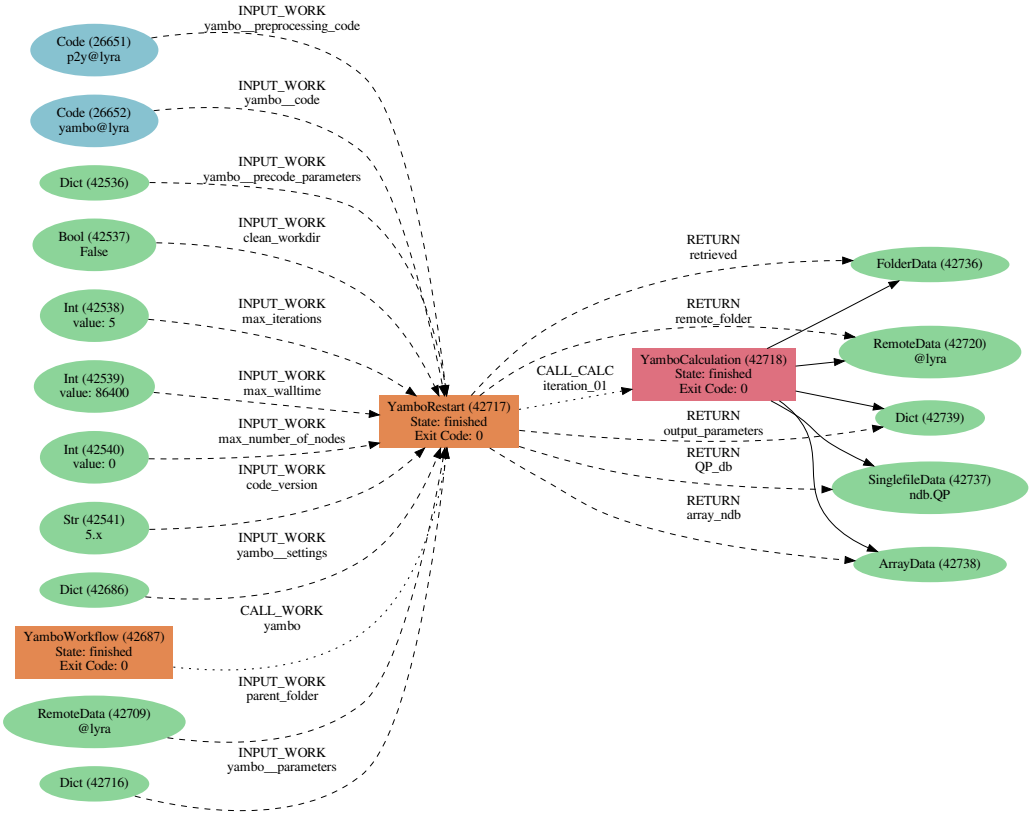

Figure E.2: **Example of provenance graph for** `YamboRestart`.

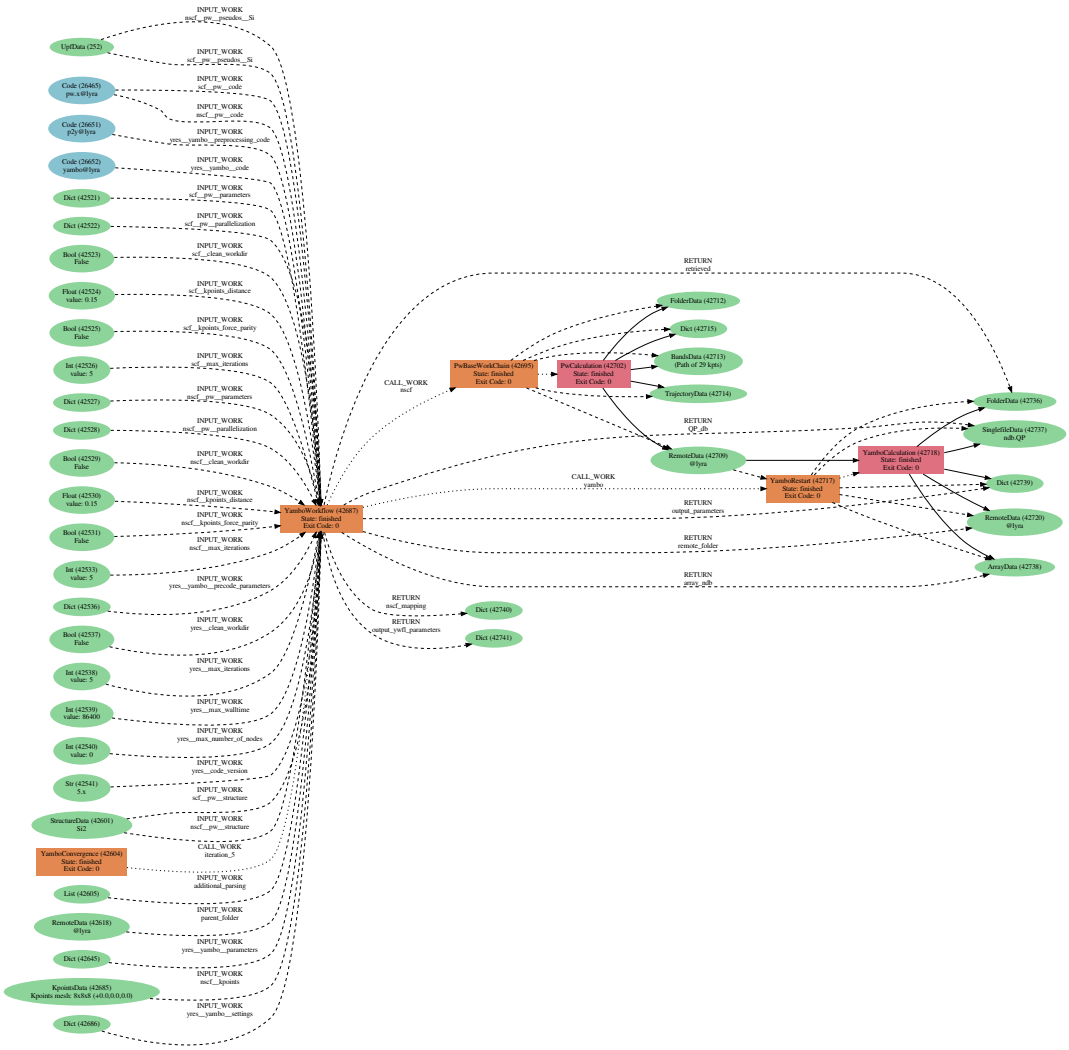

Figure E.3: **Example of provenance graph for `YamboWorkflow`.**

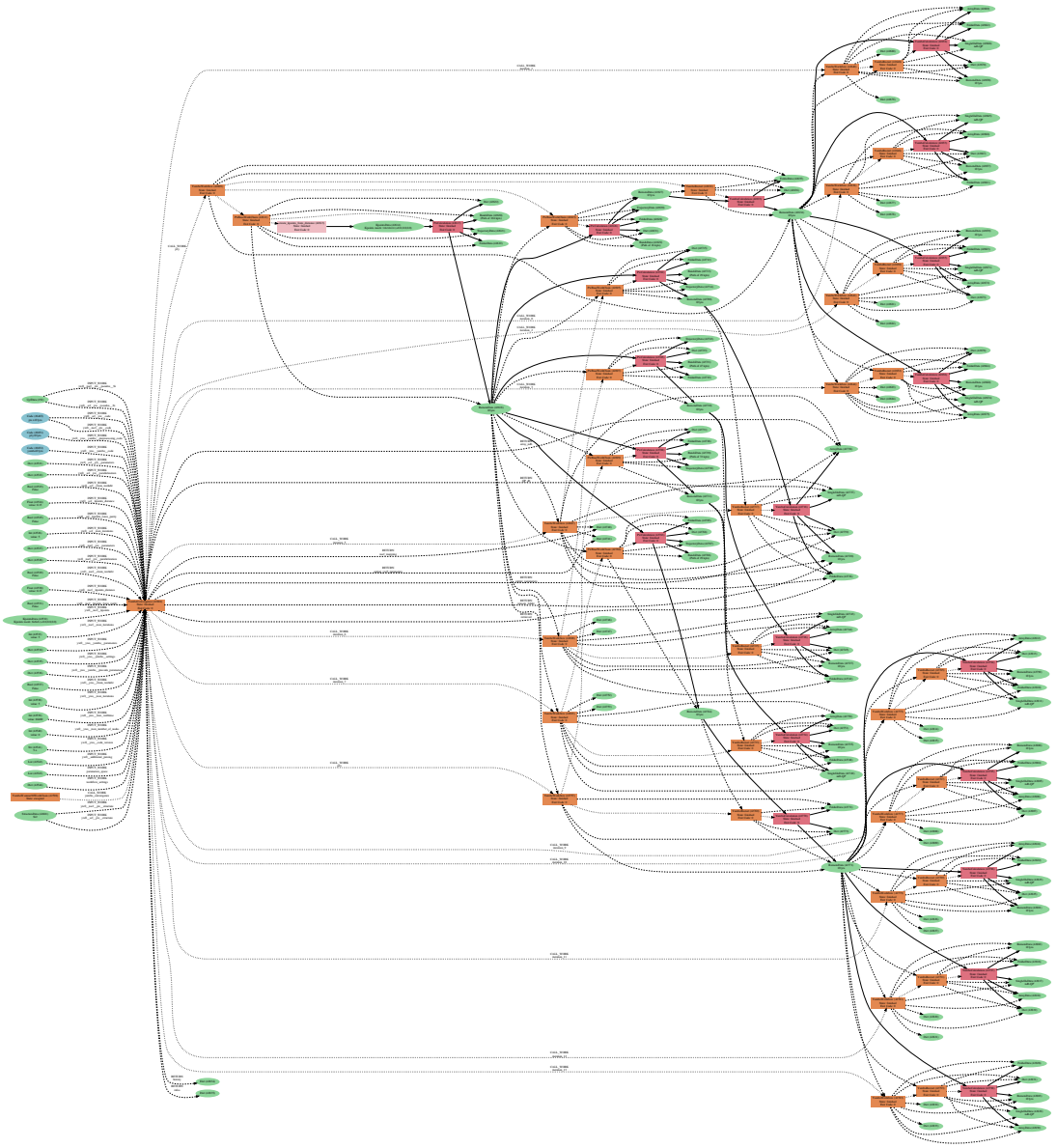

Figure E.4: **Example of provenance graph for** `YamboConvergence`. Provided the inputs (the first column of boxes from the left), the `YamboConvergence` calls a series of `YamboWorkflows` to perform the needed runs of `PwCalculation` and `YamboCalculation`, represented by the red boxes. Outputs are then generated and analysed by the workflow.

Appendix F

Convergence plots for all the systems studied in Chapter 3

In the following, we show the plots produced during the convergence studies of the systems analyzed in Section VI of the main text. We converged the $\Gamma - \Gamma$ band gap with respect to the two coupled parameters N_b and G_{cut} and the **k**-point grid as well, except for TiO_2 and ZnO. For diamond, we also converged the FFTGvecs parameter, responsible for the Fast-Fourier-Transform (FFT) grids.

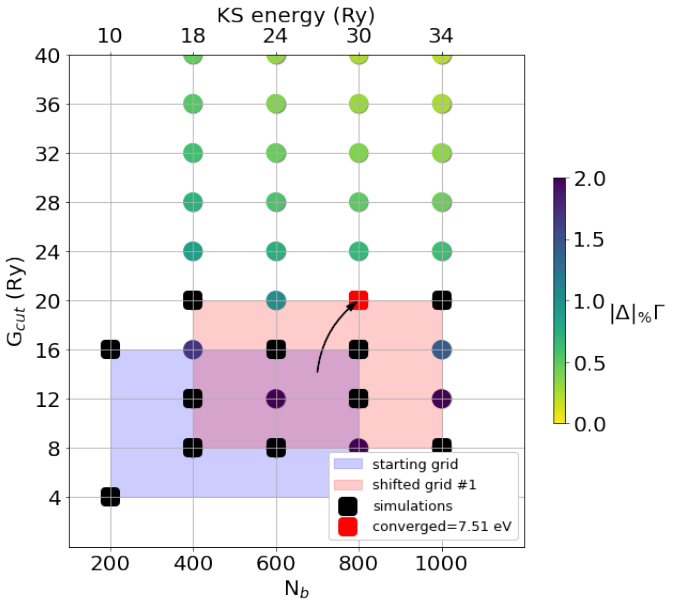

Figure F.1: Convergence of N_b and G_{cut} for bulk hBN.

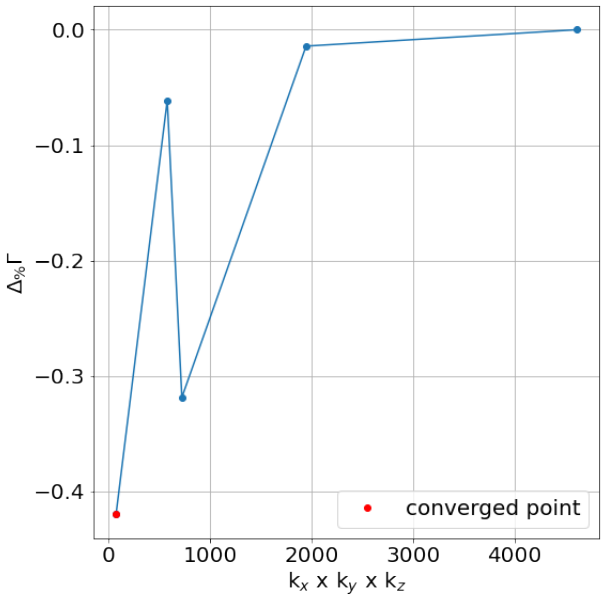

Figure F.2: Convergence of N_b and G_{cut} for monolayer hBN.

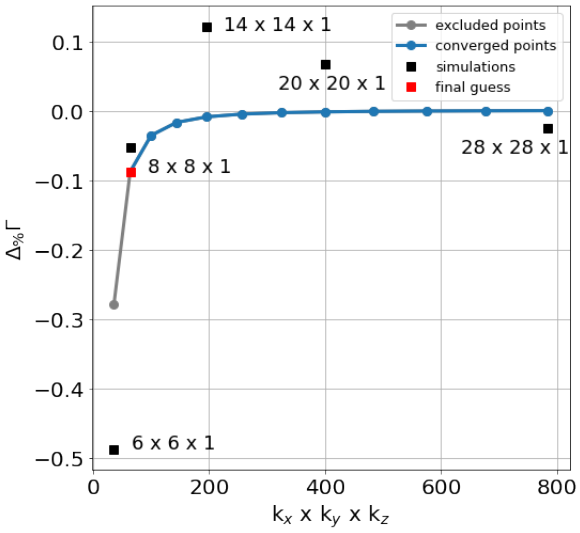

Figure F.3: **k**-mesh convergence for monolayer hBN.

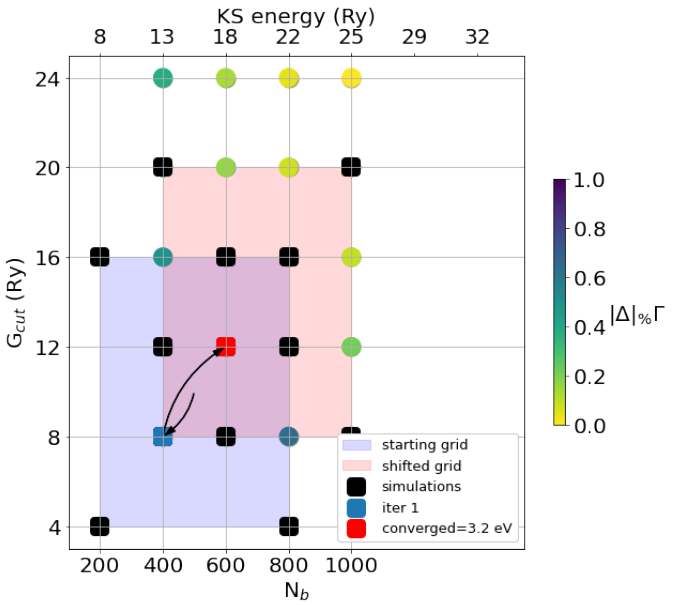

Figure F.4: Convergence of N_b and G_{cut} for Rutile TiO_2.

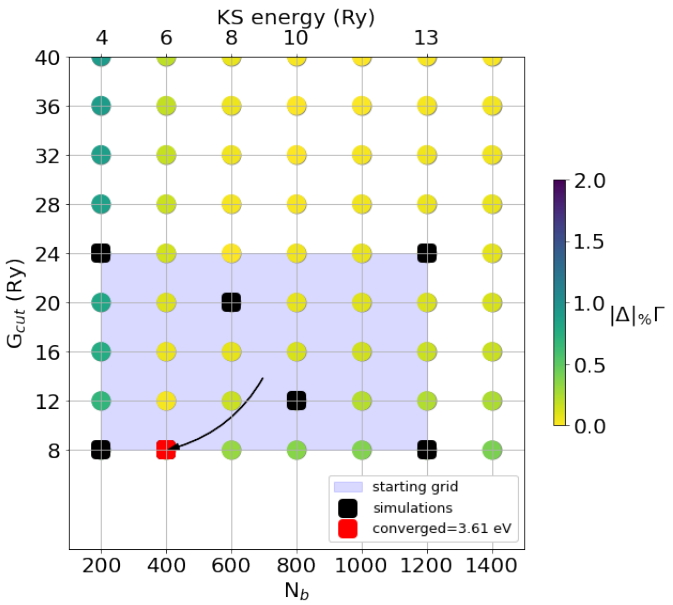

Figure F.5: Convergence of N_b and G_{cut} for monolayer MoS_2.

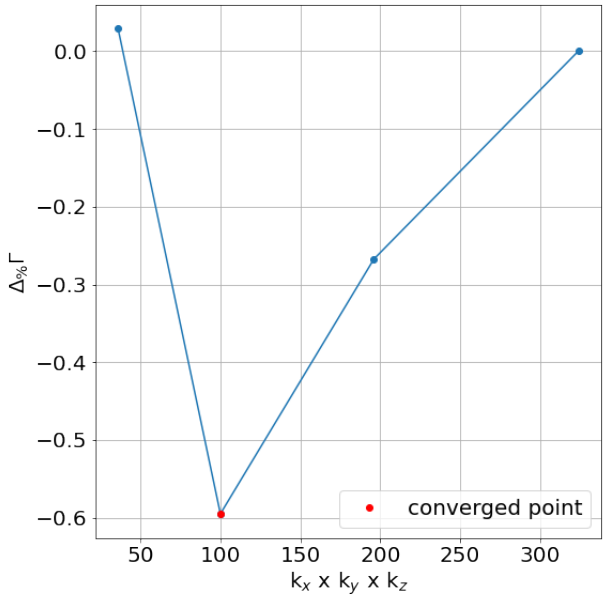

Figure F.6: **k**-mesh convergence for monolayer MoS_2.

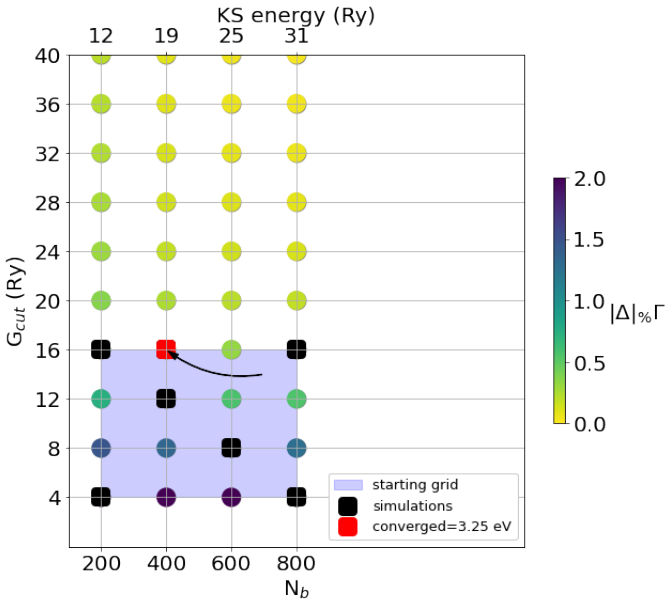

Figure F.7: Convergence of N_b and G_{cut} for silicon.

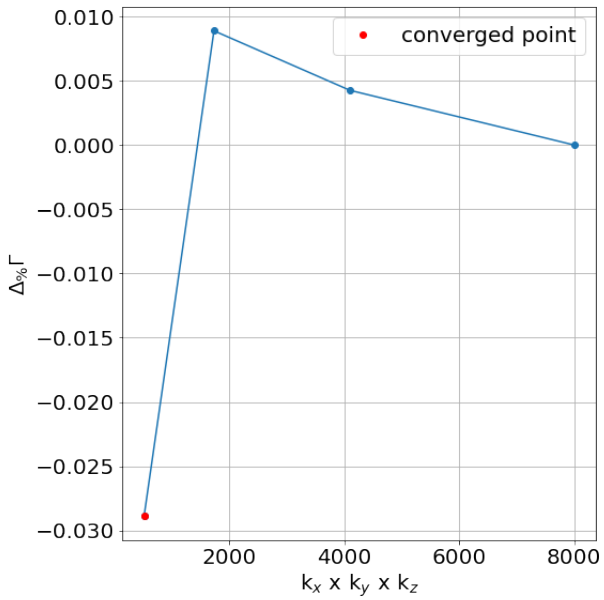

Figure F.8: **k**-mesh convergence for silicon.

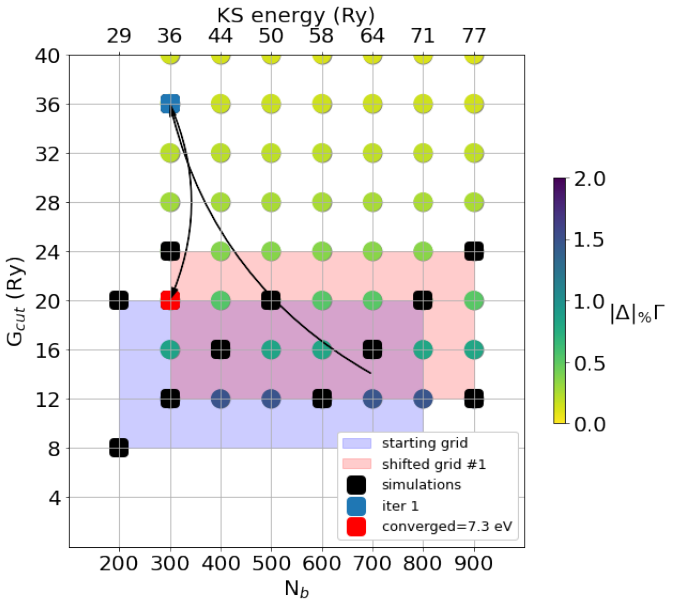

Figure F.9: Convergence of N_b and G_{cut} for diamond.

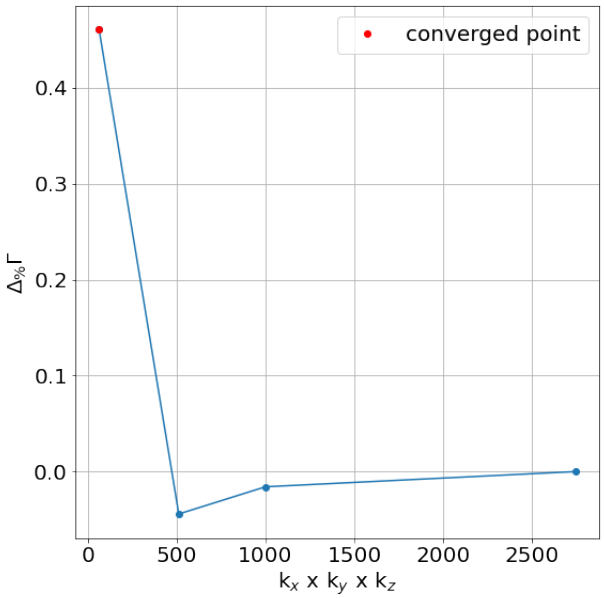

Figure F.10: **k**-mesh convergence for diamond.

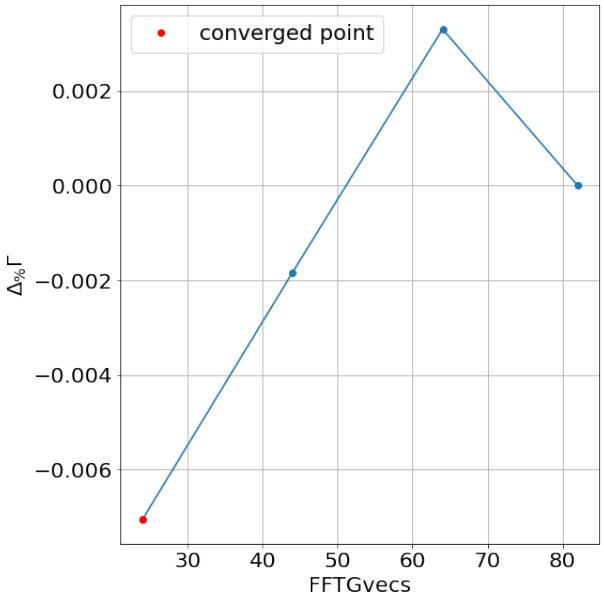

Figure F.11: FFT convergence for diamond.

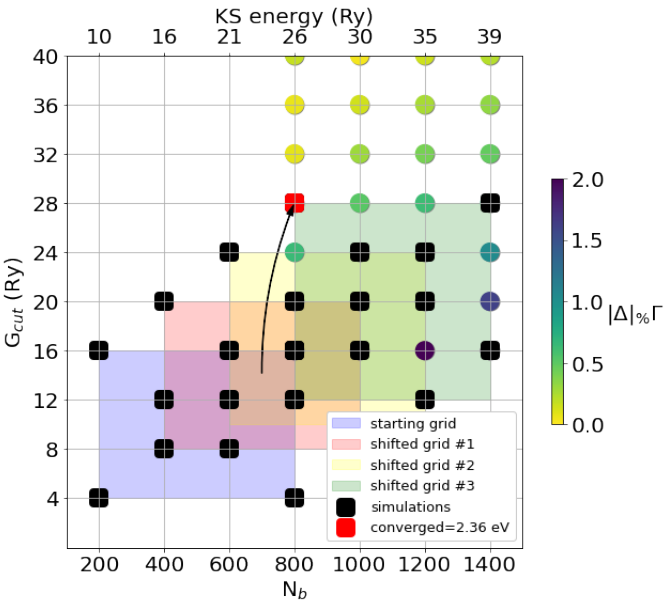

Figure F.12: Convergence of N_b and G_{cut} for ZnO.

Appendix G

Old implemented algorithm in the `aiida-yambo` plugin

The procedure explained in the following describes the simplest convergence algorithm, and was the one implemented in the first version of the `aiida-yambo` plugin [65], working with the AiiDA 0.x version [35]. It performs univariate convergences on each parameter serially (i.e. one at the time) and cyclic way (i.e. it converges multiple times the same parameter). This cyclic approach is necessary due to the interdependency of the parameters: when a parameter is converged, often the other one is out of convergence (in other terms, the Hessian of the function describing the space is not diagonal, or at least its out-of-diagonal elements are not negligible for the tested region of the parameters space). Each parameter convergence consists in the following: N calculations are performed each time increasing the parameter of a user-defined δ (and starting from a user-defined value), where N is the user-defined number of steps for each iteration. Then, the results are compared with respect to the last one (considered the most converged): if enough calculations (i.e. more than a given convergence window, usually three) are converged, we consider the parameter converged and we continue to convergence the next one. If not, we perform other N calculations increasing the same parameter. This is performed up to a maximum number of iterations M. When N$*$iter>M, the workflow exits in *Failed* state. Several calculations are needed, and we do not make any prediction on the space: saddle points can trap the algorithm, and we are limited only to the simulations carried out explicitly. Indeed, this algorithm is highly inefficient - working, but inefficient - especially for interdependent parameters:

- As the Hessian is usually not diagonal, we require a lot of calculation to converge all parameters, and so the convergence is slow;

- We may be stuck in local flat regions (not minima or maxima), as we are checking only the discrepancy with the last calculation; This follows in the

need of strict convergence thresholds: risk to reach very high value of the parameters; this can be also caused by poor choice of the starting parameters, the δ incremental step and the convergence thresholds (see Fig.G.1).

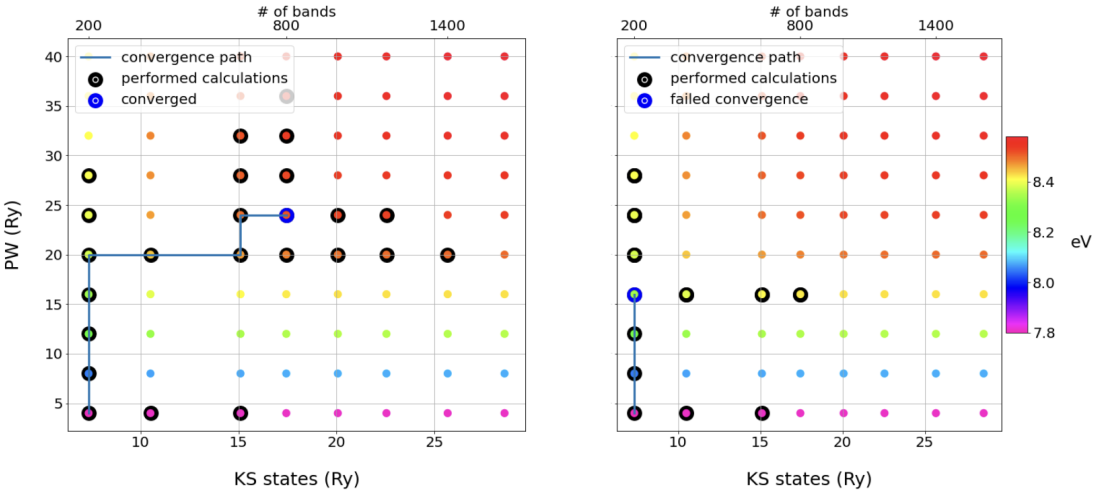

Figure G.1: Old implemented algorithm for the $\Gamma - \Gamma$ gap of 2D hBN and the number of empty states (N_b in above plots, here indicated as # of bands) and PW cutoff (the G_{cut} parameter). Left panel: we imposed a convergence threshold of 0.03 eV, and we reached convergence ($\sim$8.5) after 25 calculations, doubled with respect to the 13 calculations needed with the new algorithm (see Fig.F.2). Right: poor choice of the convergence threshold = 0.1 eV give a wrong converged result of $\sim$8.2 eV, anyway not consistent with the final 8.5 obtained before.

This method is suitable for the convergence of independent parameters (so no need of cycling procedures) that we know how to converge. For example, the **k**-point mesh is very efficient, as we know that it is not dependent on the other parameters and we usually change the mesh in a smart way.

Appendix H

Details on Wannierization at the GW level and restart from DFT Wannierization

Figure H.1 shows a detailed flowchart of the Wannierization workflow for GW band structure. The left column of Fig. H.1 is essentially the same as Fig. 3.5 in the main text. The right column shows further details of Wannierization. Firstly, a `Wannier90Calculation` is launched to generate the `nnkp` file for the subsequent `YppRestart`, which performs the `ypp` calculation for writing the quasiparticle correction in the `eig` file format for WANNIER90. Then, a `Wannier90BandsWorkChain` is launched for Wannier interpolated bands at DFT level. Next, a `Gw2wannier90Calculation` sorts the new eigenenergies in ascending order, and rewrites relevant files. Finally, a `Wannier90BaseWorkChain` is launched to obtain the Wannier interpolated bands at G0W0 level.

Some special cares need to be taken at the step of incorporating the GW correction to the WANNIER90 inputs, i.e., the initial projection matrices $A_{mn\boldsymbol{k}}$, the overlap matrices $M_{mn\boldsymbol{kb}}$, the eigenvalues $\epsilon_{n\boldsymbol{k}}$, and the Bloch wavefunctions $|u_{n\boldsymbol{k}}\rangle$, where the $\boldsymbol{b}$ is the $\boldsymbol{b}$ vectors connecting neighboring **k**-points[150]. Since the GW correction might change the order of eigenvalues, and the Wannierization disentanglement process requires the eigenvalues to be sorted in ascending order, we need to sort the GW corrected eigenenergies and rewrite the $A_{mn\boldsymbol{k}}$, $M_{mn\boldsymbol{kb}}$, and $|u_{n\boldsymbol{k}}\rangle$ files accordingly. Then the Wannierization and interpolation proceed as usual. Another option is reusing the unitary transformation matrices $U_{mn\boldsymbol{k}}$ from the Wannierization at DFT level. Since G0W0 only corrects energies, while the wavefunctions are left unchanged, it is expected that the orbital characters of the wavefunctions are unchanged, thus the disentanglement process should still choose the same set of orbitals, i.e., the previous $U_{mn\boldsymbol{k}}$ should work as well for the G0W0 corrections. Therefore, we can also reuse the $U_{mn\boldsymbol{k}}$ for the Wannier interpolation of G0W0 eigenenergies thus skipping the second disentanglement step. The Wannier interpolation is the inverse Fourier transform of the Hamiltonian on the **k**-point

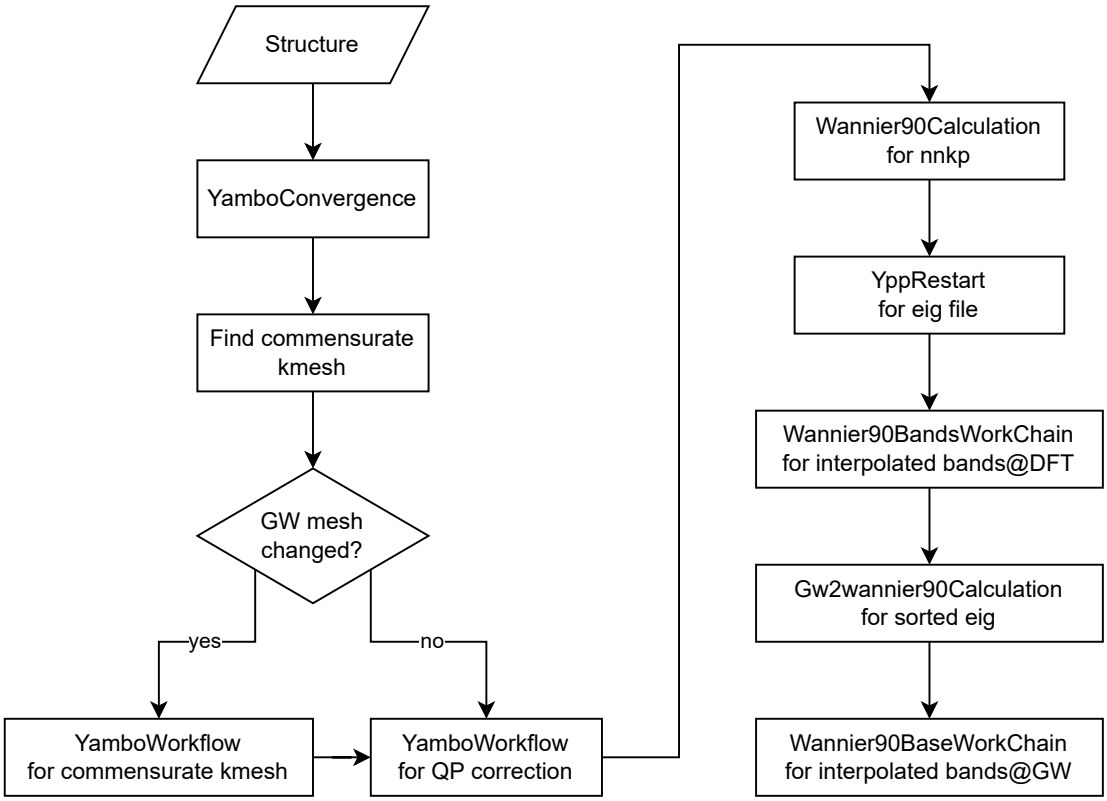

Figure H.1: Detailed flowchart of the `YamboWannier90WorkChain` for automated GW convergence and Wannier interpolated GW band structure. The workflow performs the YAMBO convergence, searching of commensurate **k**-point mesh between YAMBO and WANNIER90, and running the Yambo quasiparticle calculation. The quasiparticle correction is provided and the final steps of the flow comprise the Wannierization and the band interpolations at DFT level and GW level.

path for the band structure, the order of eigenenergies is irrelevant, thus the $A_{mn\boldsymbol{k}}$, $M_{mn\boldsymbol{kb}}$, and $|u_{n\boldsymbol{k}}\rangle$ can be left intact. This can speed up large-scale calculations where the file size of these matrices are large, since usually the disk read/write speed is the slowest part of the calculations. Moreover, reusing the $U_{mn\boldsymbol{k}}$ means it will reach the same minimum as the Wannierization at DFT level, thus the Wannier interpolation accuracy of GW eigenenergies should be similar to that at DFT level.

Appendix I

KS-DFT bands for the systems studied in Chapter 7

In the following, we show the KS-DFT band structures for all the systems studied in Chapter 7, as stored in the MC2DB [13, 12] and used to perform the DFT screening as well as the first estimation of the fundamental band gap.

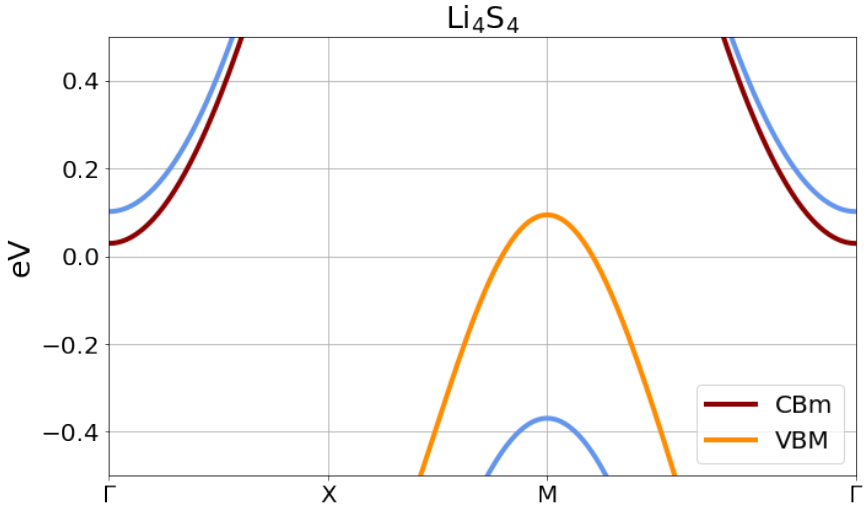

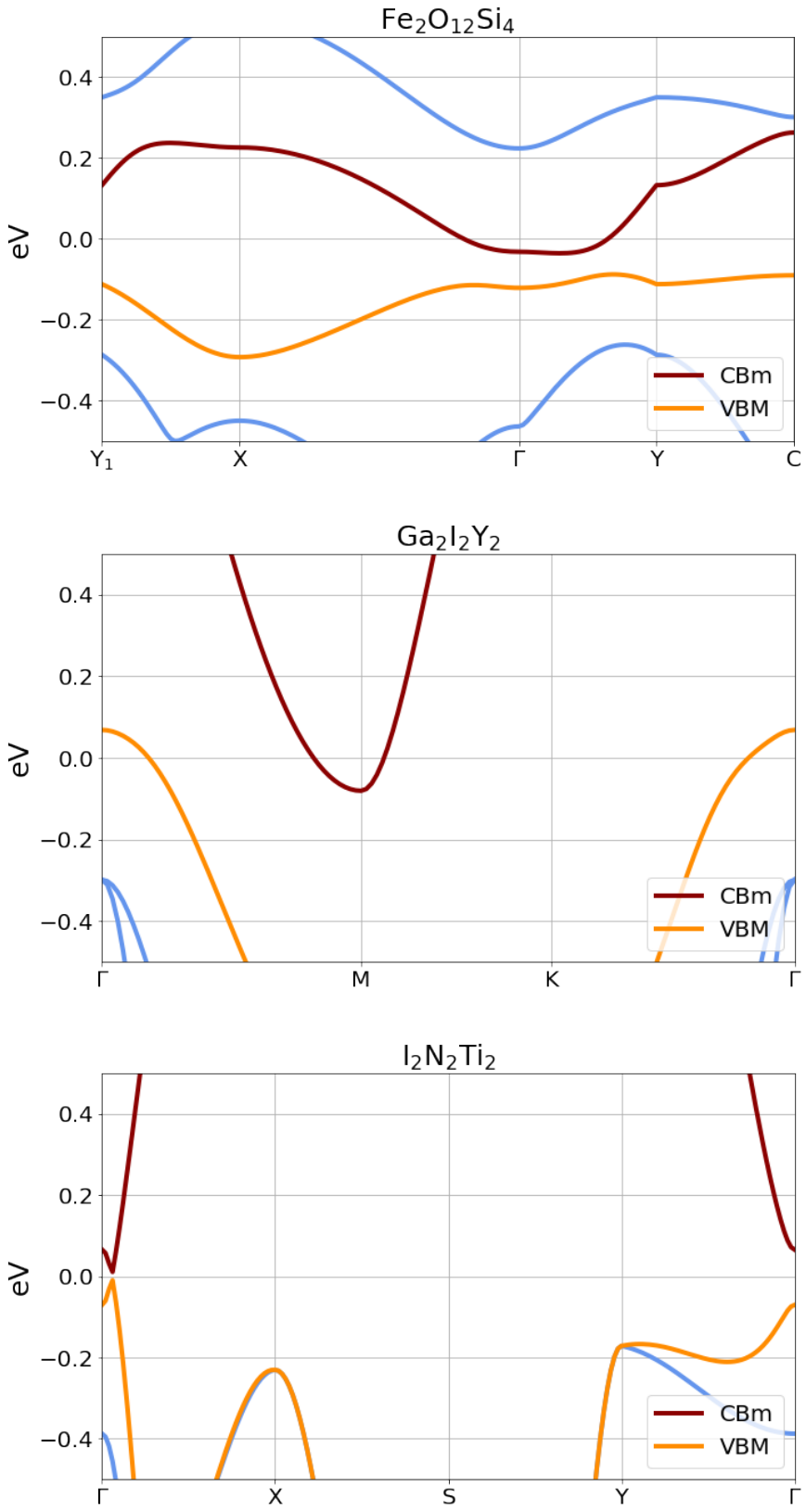
$Fe_2O_{12}Si_4$
eV
0.4
0.2
0.0
−0.2
−0.4
CBm
VBM
Y_1
X
Γ
Y
C
$Ga_2I_2Y_2$
eV
0.4
0.2
0.0
−0.2
−0.4
CBm
VBM
Γ
M
K
Γ
$I_2N_2Ti_2$
eV
0.4
0.2
0.0
−0.2
−0.4
CBm
VBM
Γ
X
S
Y
Γ

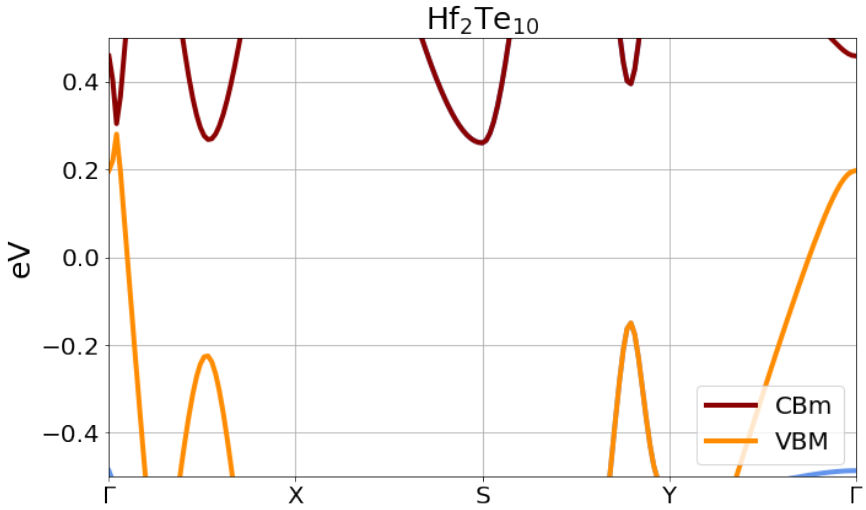
Hf_2Te_{10}
eV
0.4
0.2
0.0
−0.2
−0.4
Γ
X
S
Y
Γ
CBm
VBM

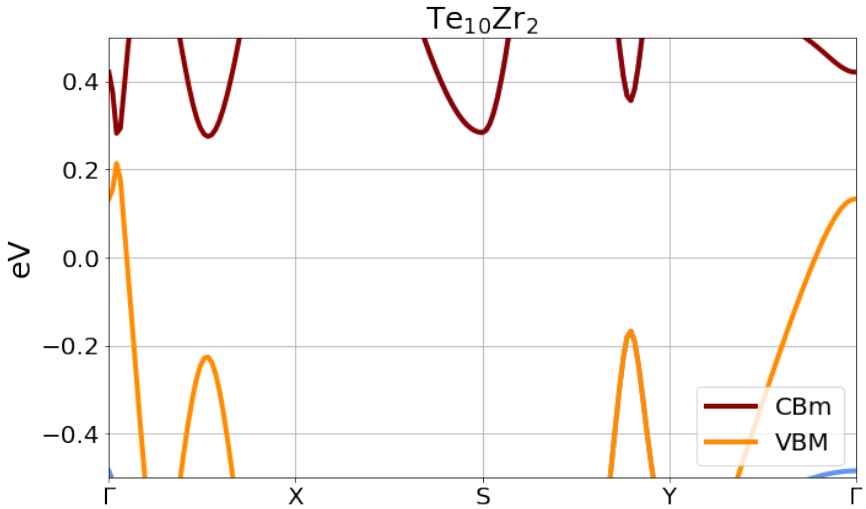
$Te_{10}Zr_2$
eV
0.4
0.2
0.0
−0.2
−0.4
Γ
X
S
Y
Γ
CBm
VBM

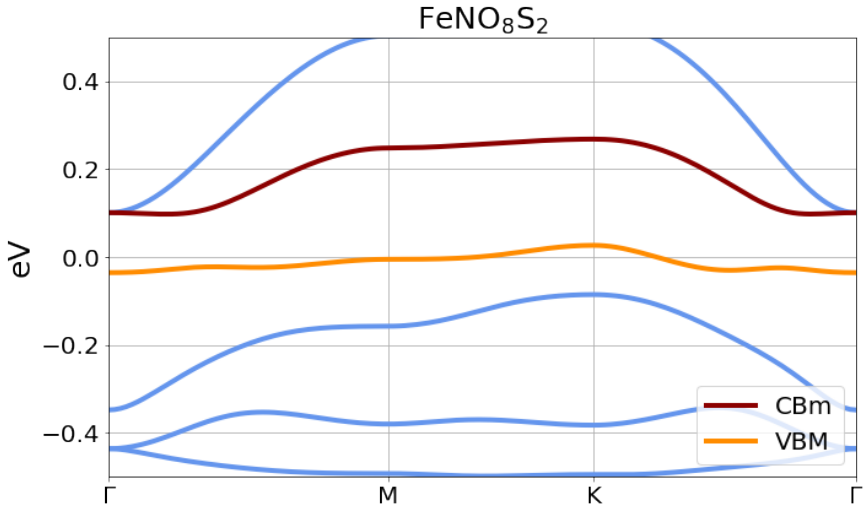
$FeNO_8S_2$
eV
0.4
0.2
0.0
−0.2
−0.4
Γ
M
K
Γ
CBm
VBM

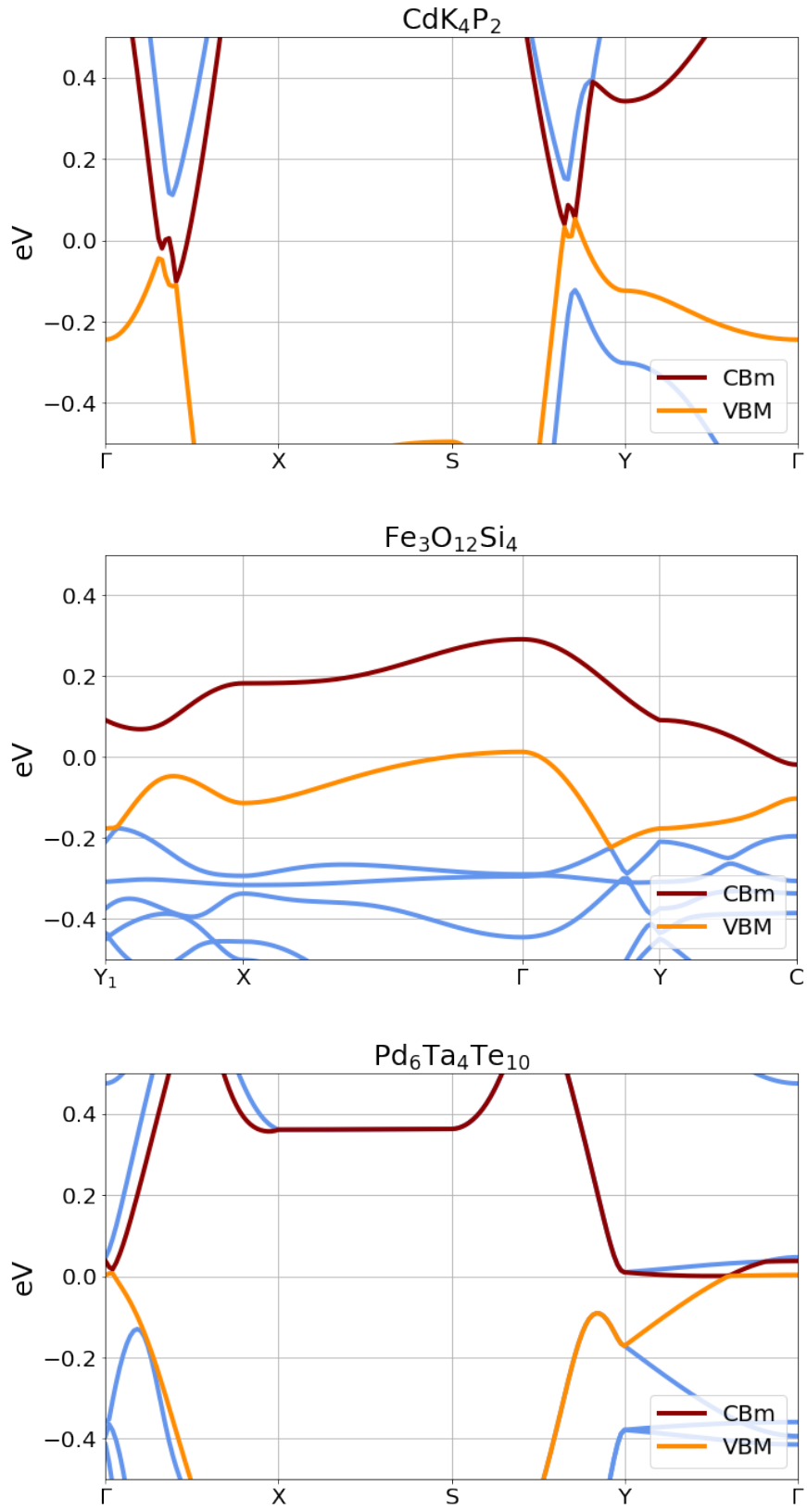
CdK4P2
0.4
0.2
0.0
−0.2
−0.4
eV
CBm
VBM
Γ
X
S
Y
Γ
Fe3O12Si4
0.4
0.2
0.0
−0.2
−0.4
eV
CBm
VBM
Y1
X
Γ
Y
C
Pd6Ta4Te10
0.4
0.2
0.0
−0.2
−0.4
eV
CBm
VBM
Γ
X
S
Y
Γ

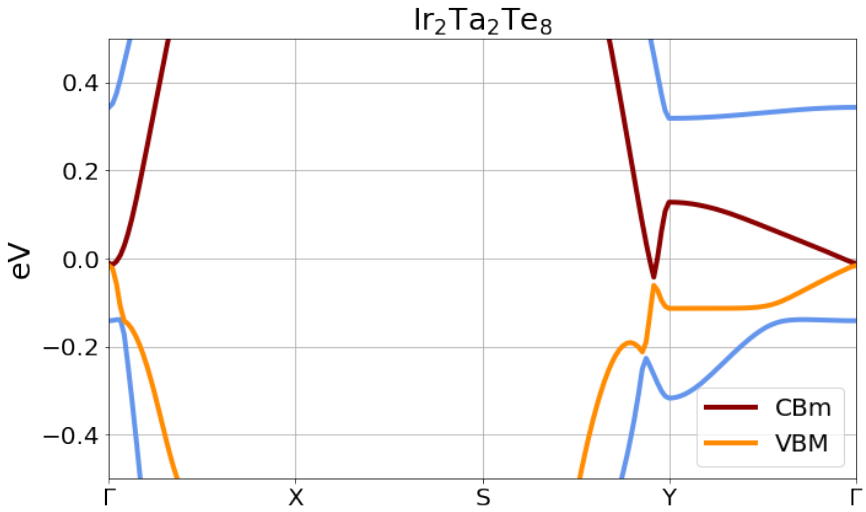
$Ir_2Ta_2Te_8$
0.4
0.2
0.0
−0.2
−0.4
eV
CBm
VBM
Γ
X
S
Y
Γ

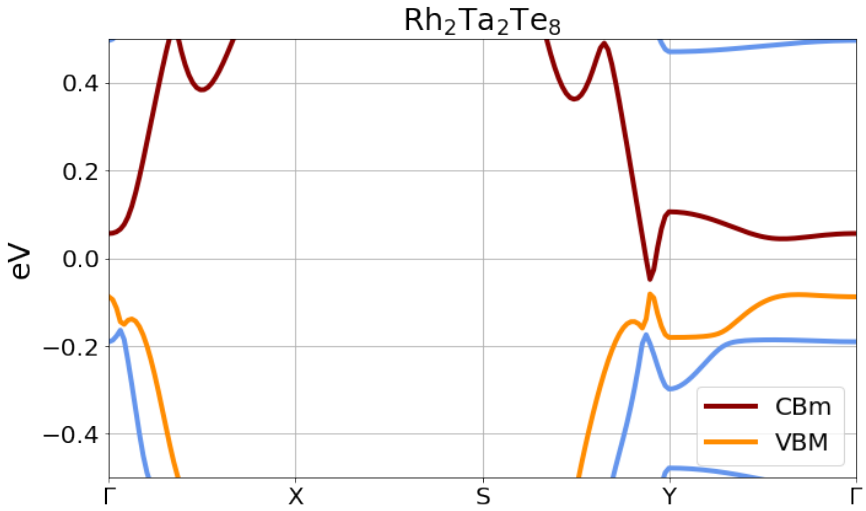
$Rh_2Ta_2Te_8$
0.4
0.2
0.0
−0.2
−0.4
eV
CBm
VBM
Γ
X
S
Y
Γ

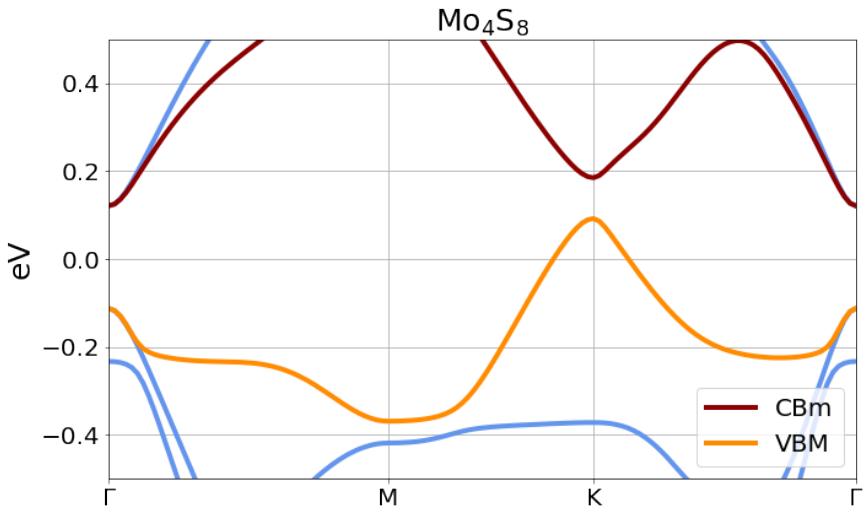
Mo_4S_8
0.4
0.2
0.0
−0.2
−0.4
eV
CBm
VBM
Γ
M
K
Γ

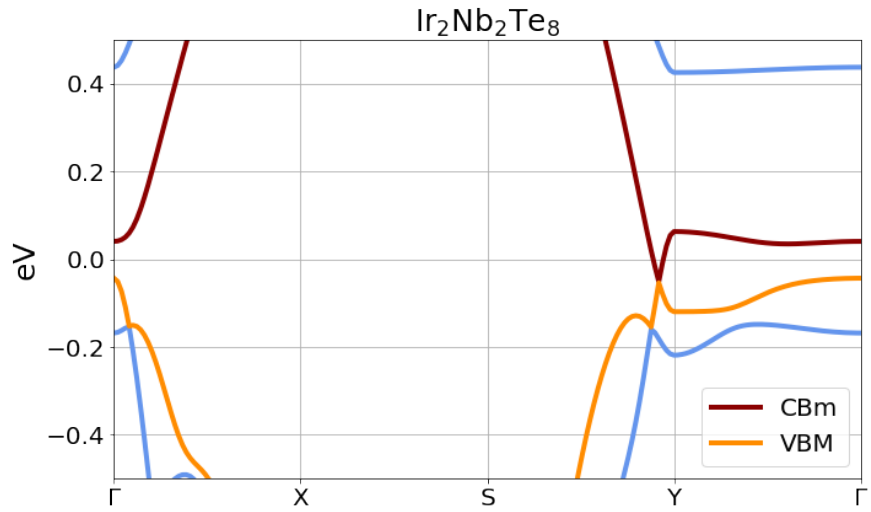
$Ir_2Nb_2Te_8$
eV
0.4
0.2
0.0
−0.2
−0.4
Γ
X
S
Y
Γ
CBm
VBM

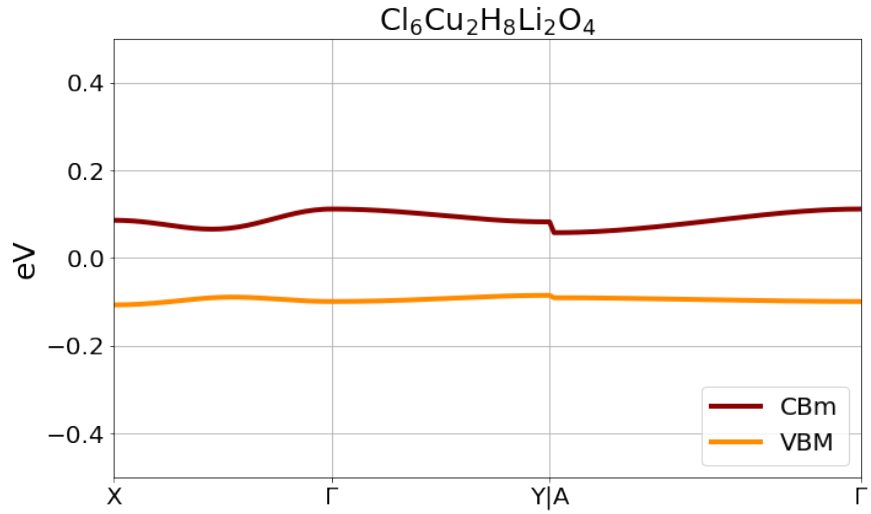
$Cl_6Cu_2H_8Li_2O_4$
eV
0.4
0.2
0.0
−0.2
−0.4
X
Γ
Y|A
Γ
CBm
VBM

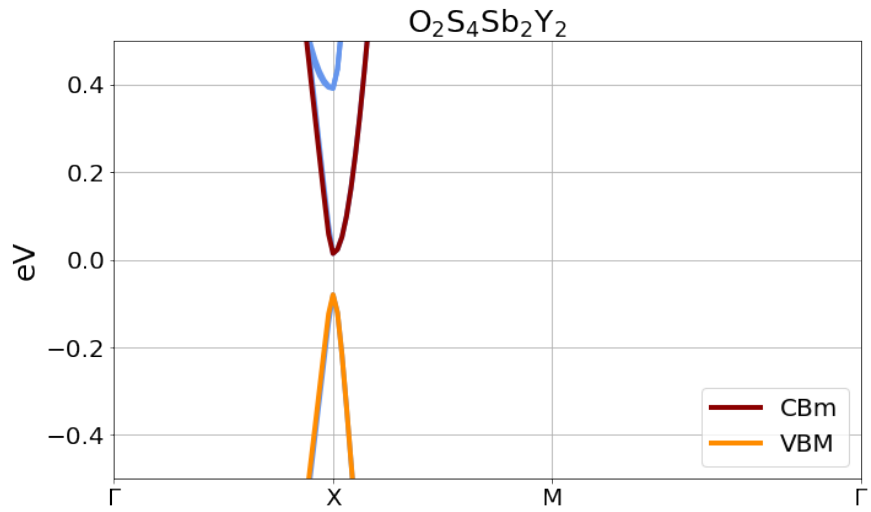
$O_2S_4Sb_2Y_2$
eV
0.4
0.2
0.0
−0.2
−0.4
Γ
X
M
Γ
CBm
VBM

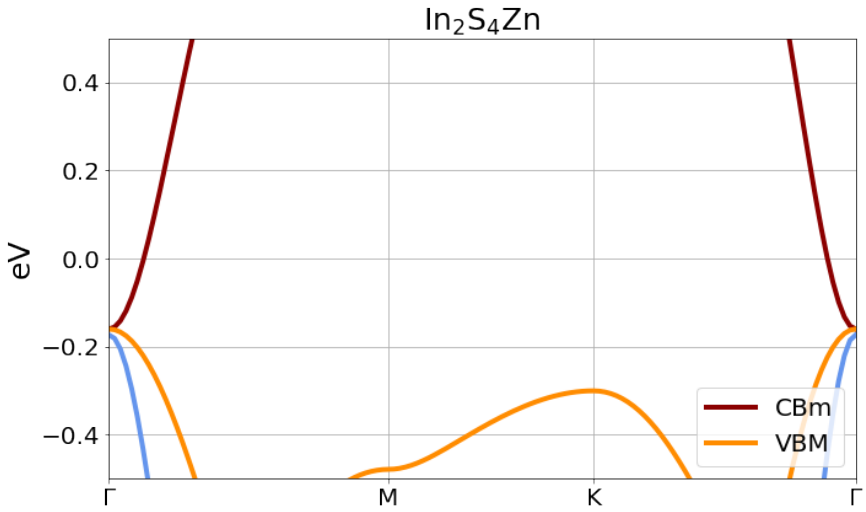
In_2S_4Zn
0.4
0.2
0.0
−0.2
−0.4
eV
CBm
VBM
Γ
M
K
Γ

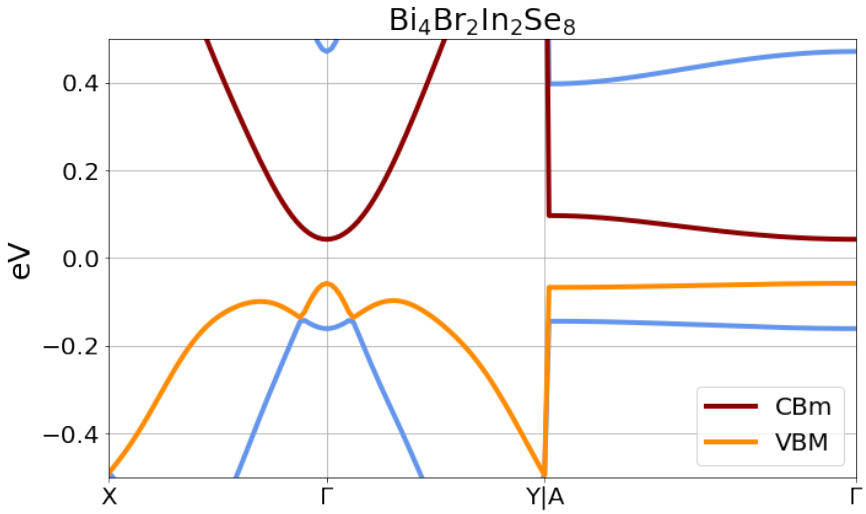
$Bi_4Br_2In_2Se_8$
0.4
0.2
0.0
−0.2
−0.4
eV
CBm
VBM
X
Γ
Y|A
Γ

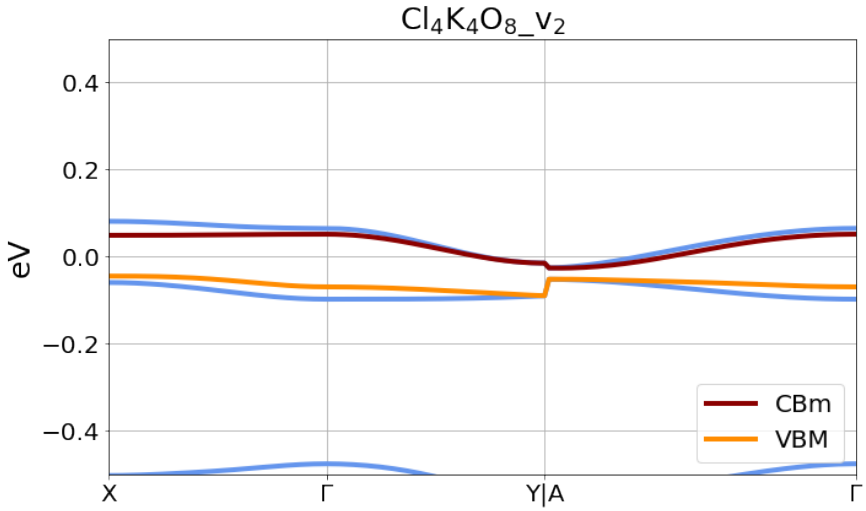
$Cl_4K_4O_8\_v_2$
0.4
0.2
0.0
−0.2
−0.4
eV
CBm
VBM
X
Γ
Y|A
Γ

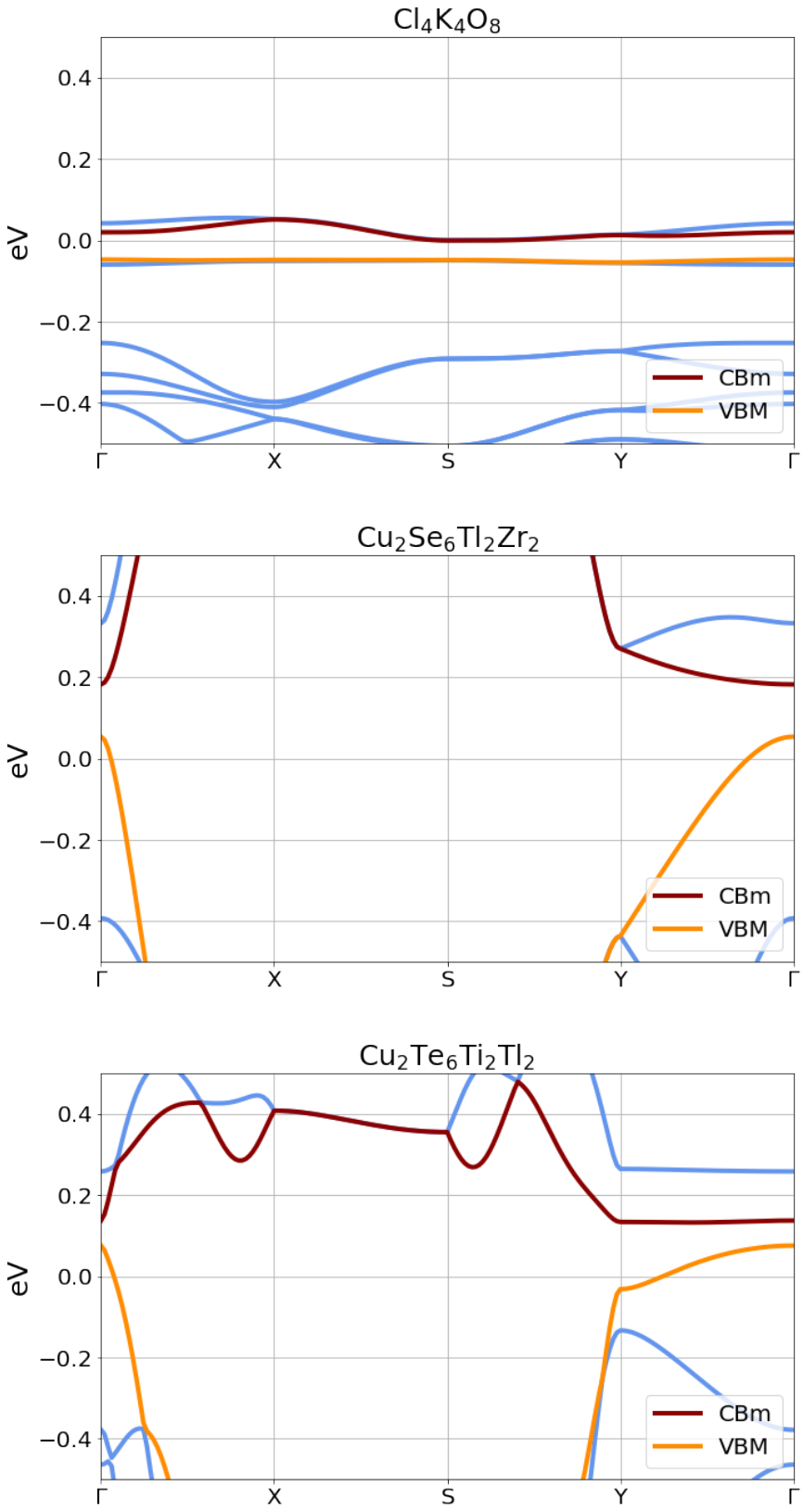
$Cl_4K_4O_8$
0.4
0.2
0.0
−0.2
−0.4
eV
CBm
VBM
Γ
X
S
Y
Γ
$Cu_2Se_6Tl_2Zr_2$
0.4
0.2
0.0
−0.2
−0.4
eV
CBm
VBM
Γ
X
S
Y
Γ
$Cu_2Te_6Ti_2Tl_2$
0.4
0.2
0.0
−0.2
−0.4
eV
CBm
VBM
Γ
X
S
Y
Γ

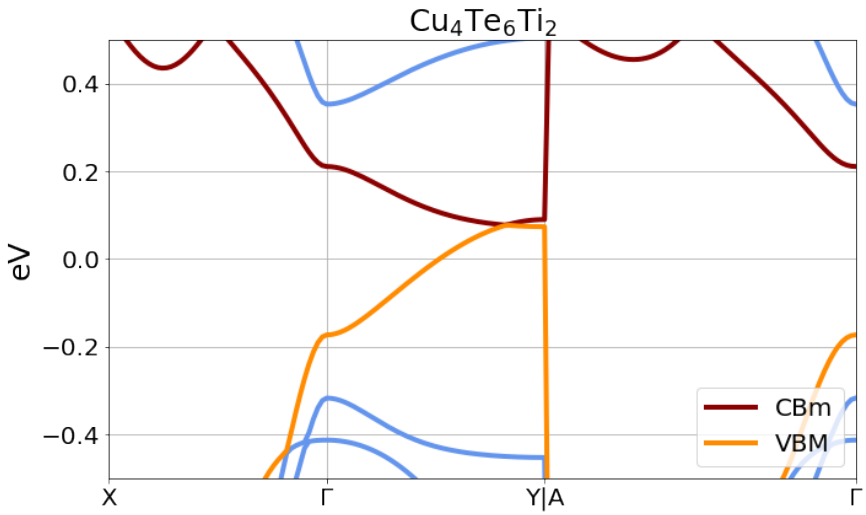
$Cu_4Te_6Ti_2$
eV
0.4
0.2
0.0
−0.2
−0.4
X
Γ
Y|A
Γ
CBm
VBM

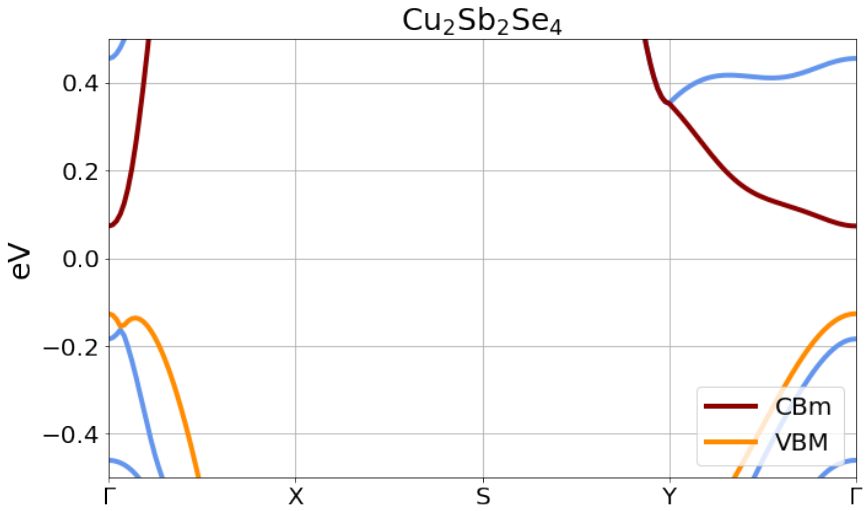
$Cu_2Sb_2Se_4$
eV
0.4
0.2
0.0
−0.2
−0.4
Γ
X
S
Y
Γ
CBm
VBM

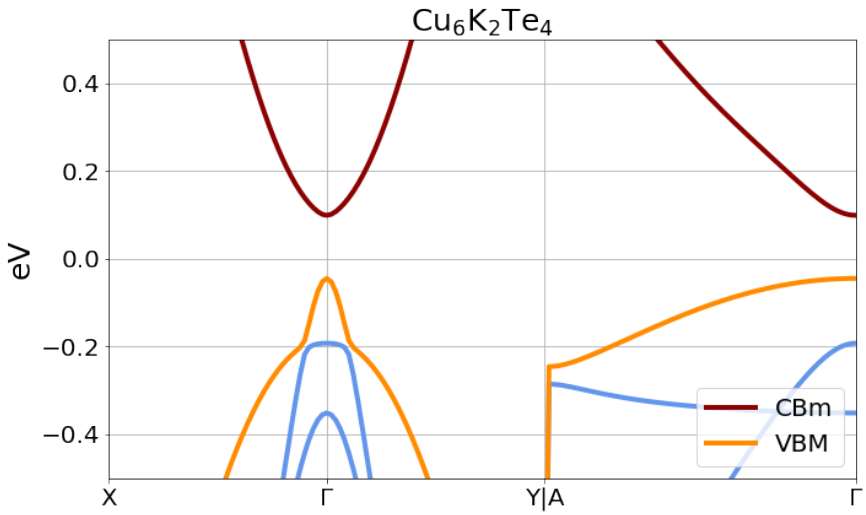
$Cu_6K_2Te_4$
eV
0.4
0.2
0.0
−0.2
−0.4
X
Γ
Y|A
Γ
CBm
VBM

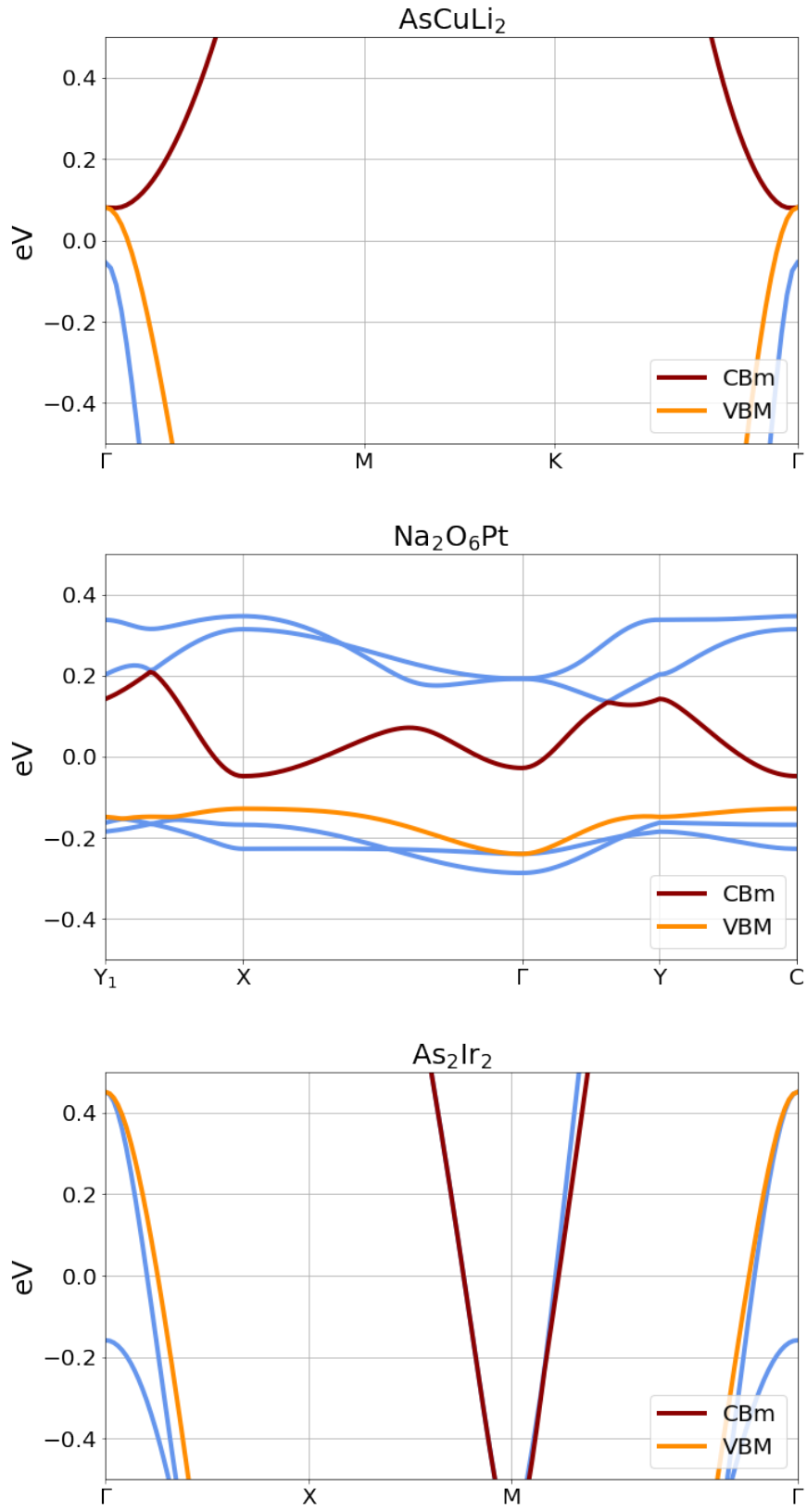
AsCuLi2
0.4
0.2
0.0
−0.2
−0.4
eV
CBm
VBM
Γ
M
K
Γ
Na2O6Pt
0.4
0.2
0.0
−0.2
−0.4
eV
CBm
VBM
Y1
X
Γ
Y
C
As2Ir2
0.4
0.2
0.0
−0.2
−0.4
eV
CBm
VBM
Γ
X
M
Γ

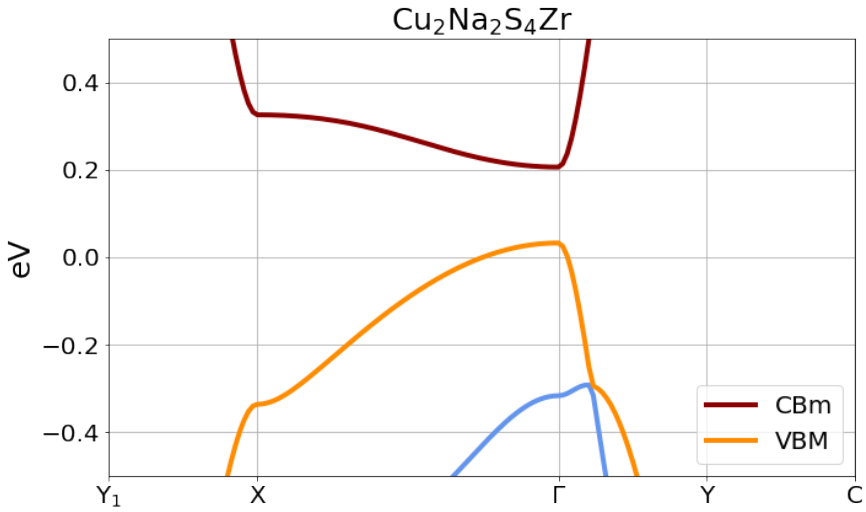
$Cu_2Na_2S_4Zr$
0.4
0.2
0.0
−0.2
−0.4
eV
CBm
VBM
Y_1
X
Γ
Y
C

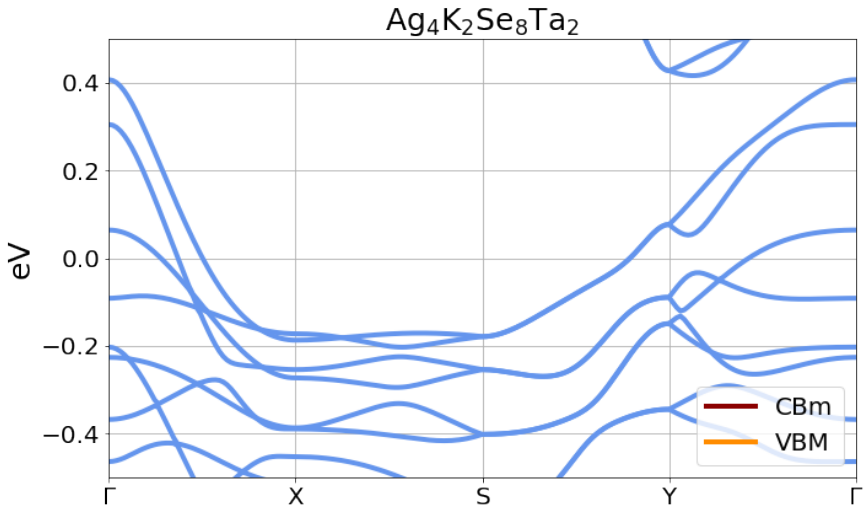
$Ag_4K_2Se_8Ta_2$
0.4
0.2
0.0
−0.2
−0.4
eV
CBm
VBM
Γ
X
S
Y
Γ

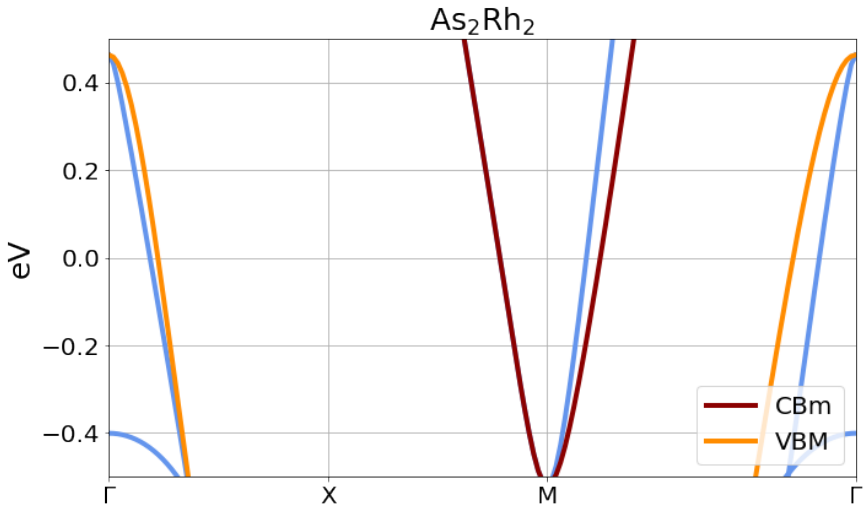
As_2Rh_2
0.4
0.2
0.0
−0.2
−0.4
eV
CBm
VBM
Γ
X
M
Γ

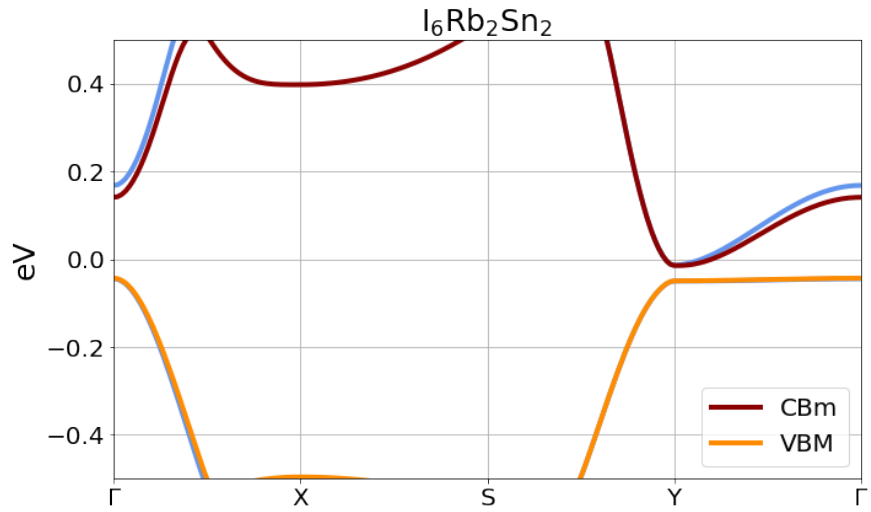
$I_6Rb_2Sn_2$
0.4
0.2
0.0
−0.2
−0.4
eV
CBm
VBM
Γ
X
S
Y
Γ

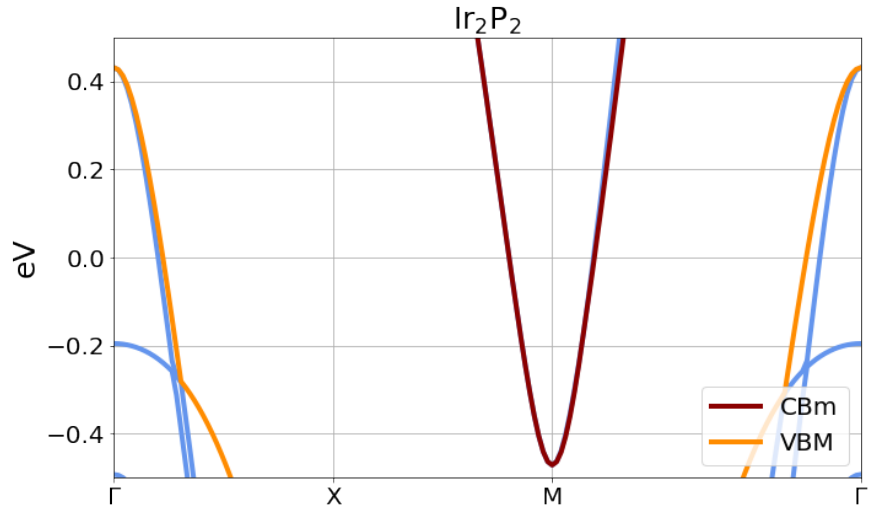
Ir_2P_2
0.4
0.2
0.0
−0.2
−0.4
eV
CBm
VBM
Γ
X
M
Γ

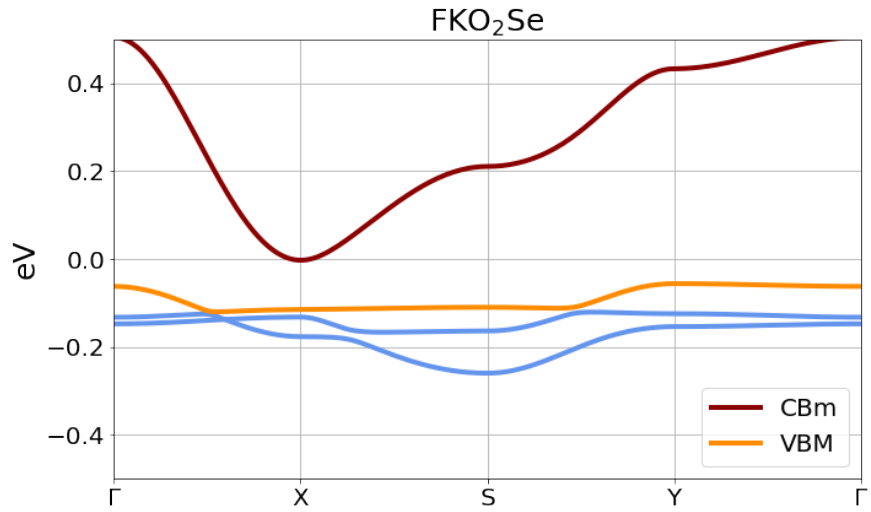
FKO_2Se
0.4
0.2
0.0
−0.2
−0.4
eV
CBm
VBM
Γ
X
S
Y
Γ

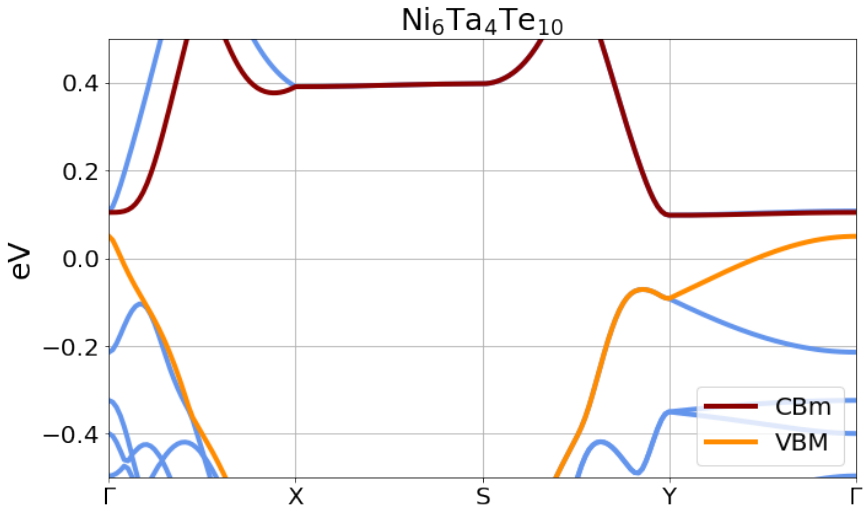
Ni6Ta4Te10
0.4
0.2
0.0
−0.2
−0.4
eV
Γ
X
S
Y
Γ
CBm
VBM

Appendix J

Plots of GW corrections vs DFT eigenvalues for candidate systems studied in Chapter 7

In the following, we show the GW corrections with respect to the corresponding DFT eigenvalues of the 7 systems resulted candidates after the first GW single calculation (the one with the coarse mesh). Here the quasiparticles are computed with the dense mesh to determine easily the real quasiparticle gap and understand if a linear correction of the DFT bands is reliable to reproduce the GW ones.

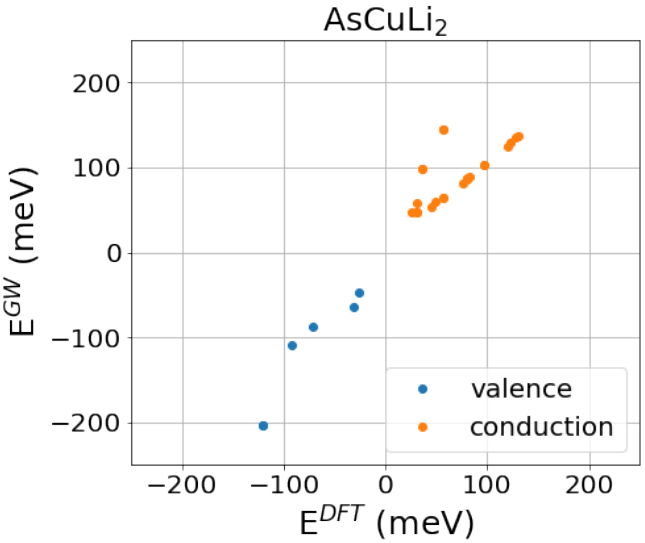

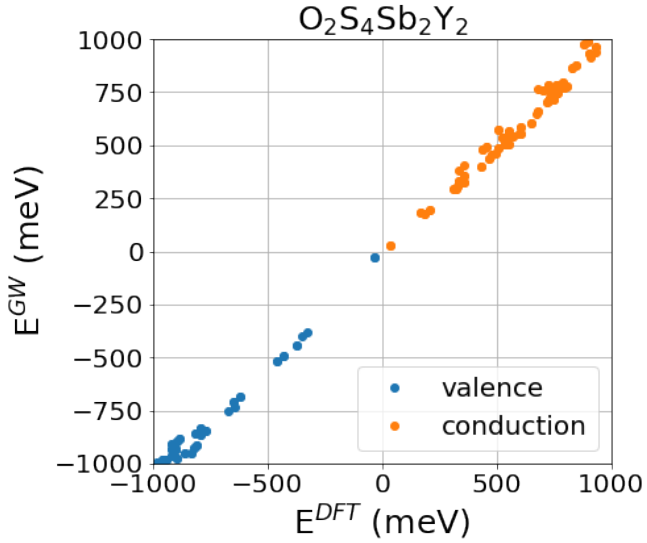
$O_2S_4Sb_2Y_2$
1000
750
500
250
0
−250
−500
−750
−1000
−1000
−500
0
500
1000
E^{GW} (meV)
E^{DFT} (meV)
valence
conduction

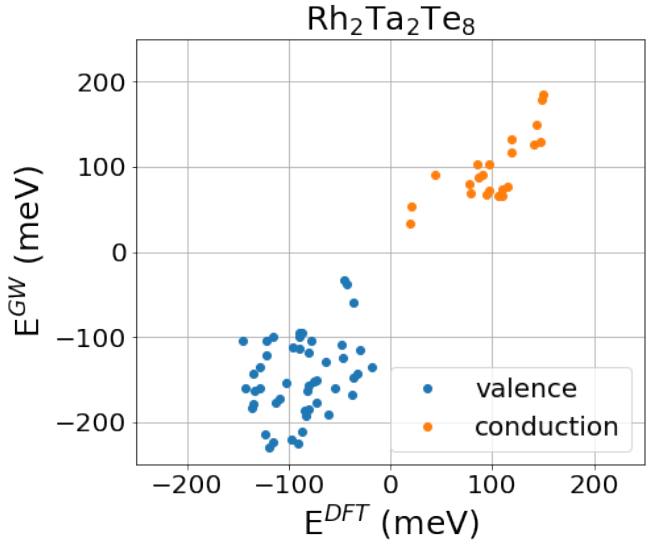
$Rh_2Ta_2Te_8$
200
100
0
−100
−200
−200
−100
0
100
200
E^{GW} (meV)
E^{DFT} (meV)
valence
conduction

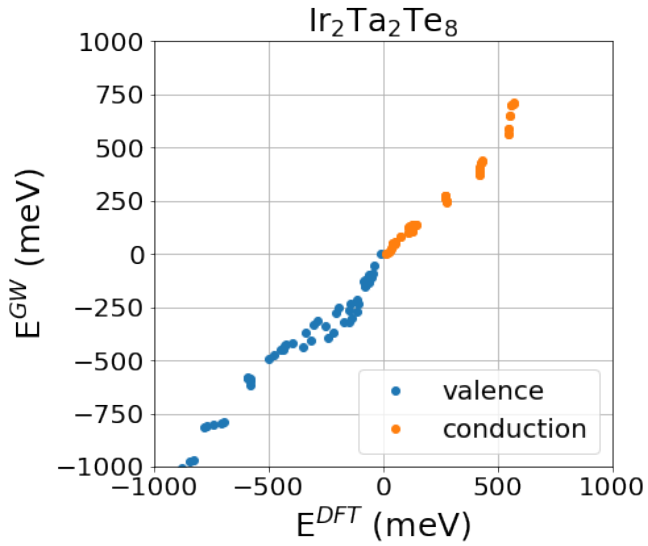
$Ir_2Ta_2Te_8$
1000
750
500
250
0
−250
−500
−750
−1000
−1000
−500
0
500
1000
E^{GW} (meV)
E^{DFT} (meV)
valence
conduction

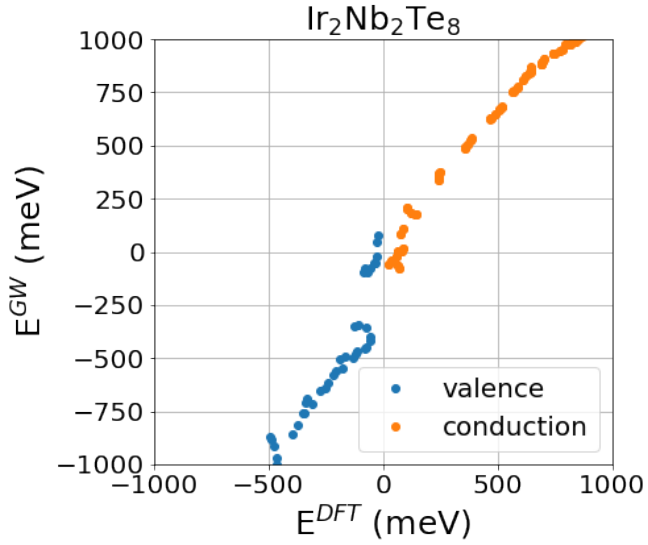
$Ir_2Nb_2Te_8$
1000
750
500
250
0
−250
−500
−750
−1000
−1000
−500
0
500
1000
E^{GW} (meV)
E^{DFT} (meV)
valence
conduction

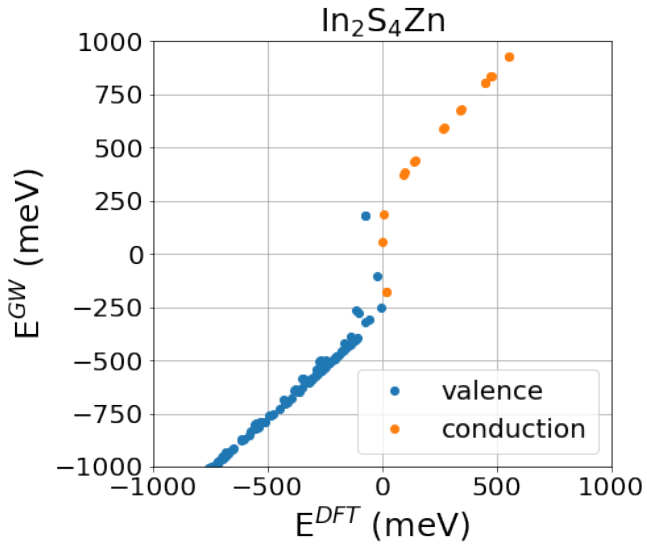
In2S4Zn
1000
750
500
250
0
−250
−500
−750
−1000
−1000
−500
0
500
1000
E^GW (meV)
E^DFT (meV)
valence
conduction

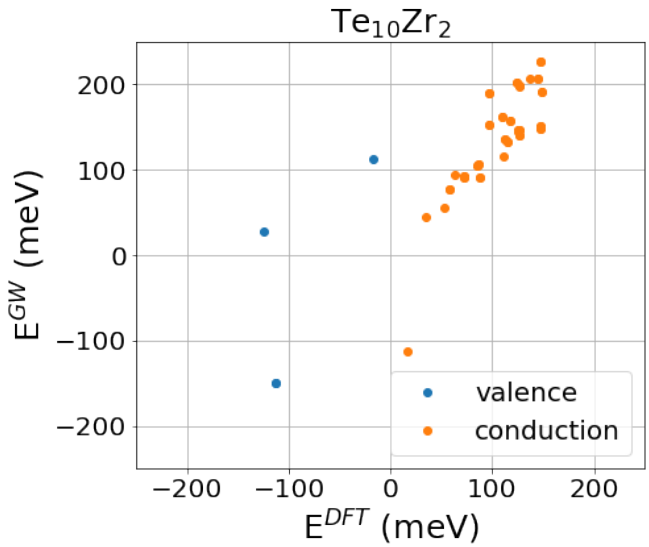
Te10Zr2
200
100
0
−100
−200
−200
−100
0
100
200
E^GW (meV)
E^DFT (meV)
valence
conduction

Bibliography

[1] Lars Hedin. New Method for Calculating the One-Particle Green's Function with Application to the Electron-Gas Problem. Phys. Rev., 139:796–823, August 1965.

[2] Giovanni Onida, Lucia Reining, and Angel Rubio. Electronic excitations: density-functional versus many-body Green's-function approaches. Rev. Mod. Phys., 74(2):601–659, June 2002.

[3] G Strinati, HJ Mattausch, and W Hanke. Dynamical aspects of correlation corrections in a covalent crystal. Physical Review B, 25(4):2867, 1982.

[4] G Strinati. Application of the green's functions method to the study of the optical properties of semiconductors. La Rivista del Nuovo Cimento (1978-1999), 11(12):1–86, 1988.

[5] K. S. Novoselov, A. K. Geim, S. V. Morozov, D. Jiang, Y. Zhang, S. V. Dubonos, I. V. Grigorieva, and A. A. Firsov. Electric field effect in atomically thin carbon films. Science, 306(5696):666–669, 2004.

[6] K. S. Novoselov, A. K. Geim, S. V. Morozov, D. Jiang, M. I. Katsnelson, I. V. Grigorieva, S. V. Dubonos, and A. A. Firsov. Two-dimensional gas of massless Dirac fermions in graphene. Nature, 438(7065):197–200, November 2005.

[7] A E Galashev and O R Rakhmanova. Mechanical and thermal stability of graphene and graphene-based materials. Physics-Uspekhi, 57(10):970–989, October 2014.

[8] Yung-Chang Lin, Chuanhong Jin, Jung-Chi Lee, Shou-Feng Jen, Kazu Suenaga, and Po-Wen Chiu. Clean transfer of graphene for isolation and suspension. ACS Nano, 5(3):2362–2368, 2011.

[9] Saptarshi Das, Joshua A. Robinson, Madan Dubey, Humberto Terrones, and Mauricio Terrones. Beyond graphene: Progress in novel two-dimensional materials and van der waals solids. Ann. Rev. Mater. Res., 45(1):1–27, 2015.

[10] Sang Jin Kim, Kyoungjun Choi, Bora Lee, Yuna Kim, and Byung Hee Hong. Materials for flexible, stretchable electronics: Graphene and 2d materials. Ann. Rev. Mater. Res., 45(1):63–84, 2015.

[11] Rui Zhang and Rebecca Cheung. Mechanical properties and applications of two-dimensional materials. In Pramoda Kumar Nayak, editor, Two-dimensional Materials, chapter 10. IntechOpen, Rijeka, 2016.

[12] Nicolas Mounet, Marco Gibertini, Philippe Schwaller, Davide Campi, Andrius Merkys, Antimo Marrazzo, Thibault Sohier, Ivano Eligio Castelli, Andrea Cepellotti, Giovanni Pizzi, and et al. Two-dimensional materials from high-throughput computational exfoliation of experimentally known compounds. Nature Nanotechnology, 13(3):246–252, Feb 2018.

[13] Nicolas Mounet, Marco Gibertini, Philippe Schwaller, Davide Campi, Andrius Merkys, Antimo Marrazzo, Thibault Sohier, Ivano Eligio Castelli, Andrea Cepellotti, and Giovanni Pizzi. Two-dimensional materials from high-throughput computational exfoliation of experimentally known compounds. Materials Cloud Archive, 2020.158(3), 2020.

[14] Sten Haastrup, Mikkel Strange, Mohnish Pandey, Thorsten Deilmann, Per S Schmidt, Nicki F Hinsche, Morten N Gjerding, Daniele Torelli, Peter M Larsen, Anders C Riis-Jensen, Jakob Gath, Karsten W Jacobsen, Jens Jørgen Mortensen, Thomas Olsen, and Kristian S Thygesen. The Computational 2D Materials Database: high-throughput modeling and discovery of atomically thin crystals. 2D Materials, 5(4):042002, September 2018.

[15] Qing Hua Wang, Kourosh Kalantar-Zadeh, Andras Kis, Jonathan N Coleman, and Michael S Strano. Electronics and optoelectronics of two-dimensional transition metal dichalcogenides. Nature Nanotech., 7(11):699–712, 2012.

[16] Han Liu, Adam T. Neal, Zhen Zhu, Zhe Luo, Xianfan Xu, David Tománek, and Peide D. Ye. Phosphorene: An unexplored 2d semiconductor with a high hole mobility. ACS Nano, 8(4):4033–4041, 2014.

[17] C. R. Dean, A. F. Young, I. Meric, C. Lee, L. Wang, S. Sorgenfrei, K. Watanabe, T. Taniguchi, P. Kim, K. L. Shepard, and et al. Boron nitride substrates for high-quality graphene electronics. Nature Nanotech., 5(10):722–726, Oct 2010.

[18] Stefano Curtarolo, Gus L. W. Hart, Marco Buongiorno Nardelli, Natalio Mingo, Stefano Sanvito, and Ohad Levy. The high-throughput highway to computational materials design. Nature Materials, 12(3):191–201, March 2013.

[19] Kenneth S. Vecchio, Olivia F. Dippo, Kevin R. Kaufmann, and Xiao Liu. High-throughput rapid experimental alloy development (HT-READ). Acta Materialia, 221:117352, December 2021.

[20] Shulin Luo, Tianshu Li, Xinjiang Wang, Muhammad Faizan, and Lijun Zhang. High-throughput computational materials screening and discovery of optoelectronic semiconductors. WIREs Computational Molecular Science, 11(1), January 2021.

[21] Michael Ashton, Joshua Paul, Susan B. Sinnott, and Richard G. Hennig. Topology-Scaling Identification of Layered Solids and Stable Exfoliated 2D Materials. Physical Review Letters, 118(10):106101, March 2017.

[22] Gowoon Cheon, Karel-Alexander N. Duerloo, Austin D. Sendek, Chase Porter, Yuan Chen, and Evan J. Reed. Data Mining for New Two- and One-Dimensional Weakly Bonded Solids and Lattice-Commensurate Heterostructures. Nano Letters, 17(3):1915–1923, March 2017.

[23] Kamal Choudhary, Irina Kalish, Ryan Beams, and Francesca Tavazza. High-throughput identification and characterization of two-dimensional materials using density functional theory. Scientific Reports, 7(1):5179, 2017.

[24] Antimo Marrazzo, Marco Gibertini, Davide Campi, Nicolas Mounet, and Nicola Marzari. Relative Abundance of Z2 Topological Order in Exfoliable Two-Dimensional Insulators. Nano Letters, 19(12):8431–8440, December 2019.

[25] Scott Kirklin, Bryce Meredig, and Chris Wolverton. High-Throughput Computational Screening of New Li-Ion Battery Anode Materials. Advanced Energy Materials, 3(2):252–262, February 2013.

[26] Zihe Zhang, Xu Zhang, Xudong Zhao, Sai Yao, An Chen, and Zhen Zhou. Computational Screening of Layered Materials for Multivalent Ion Batteries. ACS Omega, 4(4):7822–7828, April 2019.

[27] Wei Chen, Jan-Hendrik Pöhls, Geoffroy Hautier, Danny Broberg, Saurabh Bajaj, Umut Aydemir, Zachary M. Gibbs, Hong Zhu, Mark Asta, G. Jeffrey Snyder, Bryce Meredig, Mary Anne White, Kristin Persson, and Anubhav Jain. Understanding thermoelectric properties from high-throughput calculations: trends, insights, and comparisons with experiment. Journal of Materials Chemistry C, 4(20):4414–4426, 2016.

[28] Sandip Bhattacharya and Georg K. H. Madsen. High-throughput exploration of alloying as design strategy for thermoelectrics. Physical Review B, 92(8):085205, August 2015.

[29] Ivano E. Castelli, Thomas Olsen, Soumendu Datta, David D. Landis, Søren Dahl, Kristian S. Thygesen, and Karsten W. Jacobsen. Computational screening of perovskite metal oxides for optimal solar light capture. Energy Environ. Sci., 5(2):5814–5819, 2012.

[30] Liping Yu and Alex Zunger. Identification of Potential Photovoltaic Absorbers Based on First-Principles Spectroscopic Screening of Materials. Physical Review Letters, 108(6):068701, February 2012.

[31] Korina Kuhar, Mohnish Pandey, Kristian S. Thygesen, and Karsten W. Jacobsen. High-Throughput Computational Assessment of Previously Synthesized Semiconductors for Photovoltaic and Photoelectrochemical Devices. ACS Energy Letters, 3(2):436–446, February 2018.

[32] Sergio Maffioletti and Riccardo Murri. GC3Pie: A Python framework for high-throughput computing. In Proceedings of EGI Community Forum 2012 / EMI Second Technical Conference — PoS(EGICF12-EMITC2), page 143, Munich, Germany, December 2012. Sissa Medialab.

[33] Stefano Curtarolo, Wahyu Setyawan, Gus L.W. Hart, Michal Jahnatek, Roman V. Chepulskii, Richard H. Taylor, Shidong Wang, Junkai Xue, Kesong Yang, Ohad Levy, Michael J. Mehl, Harold T. Stokes, Denis O. Demchenko, and Dane Morgan. AFLOW: An automatic framework for high-throughput materials discovery. Computational Materials Science, 58:218–226, June 2012.

[34] Anubhav Jain, Shyue Ping Ong, Wei Chen, Bharat Medasani, Xiaohui Qu, Michael Kocher, Miriam Brafman, Guido Petretto, Gian-Marco Rignanese, Geoffroy Hautier, Daniel Gunter, and Kristin A. Persson. FireWorks: a dynamic workflow system designed for high-throughput applications. Concurrency and Computation: Practice and Experience, 27(17):5037–5059, December 2015.

[35] Giovanni Pizzi, Andrea Cepellotti, Riccardo Sabatini, Nicola Marzari, and Boris Kozinsky. Aiida: automated interactive infrastructure and database for computational science. Comput. Mater. Sci., 111:218 – 230, 2016.

[36] Ask Hjorth Larsen, Jens Jørgen Mortensen, Jakob Blomqvist, Ivano E Castelli, Rune Christensen, Marcin Dułak, Jesper Friis, Michael N Groves, Bjørk Hammer, Cory Hargus, Eric D Hermes, Paul C Jennings, Peter Bjerre Jensen, James Kermode, John R Kitchin, Esben Leonhard Kolsbjerg, Joseph Kubal, Kristen Kaasbjerg, Steen Lysgaard, Jón Bergmann Maronsson, Tristan Maxson, Thomas Olsen, Lars Pastewka, Andrew Peterson, Carsten Rostgaard, Jakob Schiøtz, Ole Schütt, Mikkel Strange, Kristian S Thygesen, Tejs Vegge, Lasse Vilhelmsen, Michael Walter, Zhenhua Zeng,

and Karsten W Jacobsen. The atomic simulation environment—a Python library for working with atoms. Journal of Physics: Condensed Matter, 29(27):273002, July 2017.

[37] Kiran Mathew, Joseph H. Montoya, Alireza Faghaninia, Shyam Dwarakanath, Muratahan Aykol, Hanmei Tang, Iek-heng Chu, Tess Smidt, Brandon Bocklund, Matthew Horton, John Dagdelen, Brandon Wood, Zi-Kui Liu, Jeffrey Neaton, Shyue Ping Ong, Kristin Persson, and Anubhav Jain. Atomate: A high-level interface to generate, execute, and analyze computational materials science workflows. Computational Materials Science, 139:140–152, November 2017.

[38] Jens Mortensen, Morten Gjerding, and Kristian Thygesen. MyQueue: Task and workflow scheduling system. Journal of Open Source Software, 5(45):1844, January 2020.

[39] Sebastiaan P. Huber, Spyros Zoupanos, Martin Uhrin, Leopold Talirz, Leonid Kahle, Rico Häuselmann, Dominik Gresch, Tiziano Müller, Aliaksandr V. Yakutovich, Casper W. Andersen, Francisco F. Ramirez, Carl S. Adorf, Fernando Gargiulo, Snehal Kumbhar, Elsa Passaro, Conrad Johnston, Andrius Merkys, Andrea Cepellotti, Nicolas Mounet, Nicola Marzari, Boris Kozinsky, and Giovanni Pizzi. AiiDA 1.0, a scalable computational infrastructure for automated reproducible workflows and data provenance. Sci. Data, 7(1):300, December 2020.

[40] Martin Uhrin, Sebastiaan P. Huber, Jusong Yu, Nicola Marzari, and Giovanni Pizzi. Workflows in AiiDA: Engineering a high-throughput, event-based engine for robust and modular computational workflows. Comp. Mat. Sci., 187:110086, February 2021.

[41] Qimin Yan, Jie Yu, Santosh K. Suram, Lan Zhou, Aniketa Shinde, Paul F. Newhouse, Wei Chen, Guo Li, Kristin A. Persson, John M. Gregoire, and Jeffrey B. Neaton. Solar fuels photoanode materials discovery by integrating high-throughput theory and experiment. Proceedings of the National Academy of Sciences, 114(12):3040–3043, March 2017.

[42] Fengnian Xia, Thomas Mueller, Yu-ming Lin, Alberto Valdes-Garcia, and Phaedon Avouris. Ultrafast graphene photodetector. Nature Nanotechnology, 4(12):839–843, December 2009.

[43] Won-Yong Lee, Seunghyun Ha, Hyunjae Lee, Jin-Hyuk Bae, Bongho Jang, Hyuk-Jun Kwon, Yeonghun Yun, Sangwook Lee, and Jaewon Jang. High-Detectivity Flexible Near-Infrared Photodetector Based on Chalcogenide Ag $_2$ Se Nanoparticles. Advanced Optical Materials, 7(22):1900812, November 2019.

[44] P.G. Eliseev. Optical strength of semiconductor laser materials. Progress in Quantum Electronics, 20(1):1–82, January 1996.

[45] Stephen Derenzo, Gregory Bizarri, Ramesh Borade, Edith Bourret-Courchesne, Rostyslav Boutchko, Andrew Canning, Anurag Chaudhry, Yetta Eagleman, Gautam Gundiah, Stephen Hanrahan, Martin Janecek, and Marvin Weber. New scintillators discovered by high-throughput screening. Nuclear Instruments and Methods in Physics Research Section A: Accelerators, Spectrometers, Detectors and Associated Equipment, 652(1):247–250, October 2011.

[46] Kurt Lejaeghere, Gustav Bihlmayer, Torbjörn Björkman, Peter Blaha, Stefan Blügel, Volker Blum, Damien Caliste, Ivano E. Castelli, Stewart J. Clark, Andrea Dal Corso, Stefano de Gironcoli, Thierry Deutsch, John Kay Dewhurst, Igor Di Marco, Claudia Draxl, Marcin Dułak, Olle Eriksson, José A. Flores-Livas, Kevin F. Garrity, Luigi Genovese, Paolo Giannozzi, Matteo Giantomassi, Stefan Goedecker, Xavier Gonze, Oscar Grånäs, E. K. U. Gross, Andris Gulans, François Gygi, D. R. Hamann, Phil J. Hasnip, N. A. W. Holzwarth, Diana Iuşan, Dominik B. Jochym, François Jollet, Daniel Jones, Georg Kresse, Klaus Koepernik, Emine Küçükbenli, Yaroslav O. Kvashnin, Inka L. M. Locht, Sven Lubeck, Martijn Marsman, Nicola Marzari, Ulrike Nitzsche, Lars Nordström, Taisuke Ozaki, Lorenzo Paulatto, Chris J. Pickard, Ward Poelmans, Matt I. J. Probert, Keith Refson, Manuel Richter, Gian-Marco Rignanese, Santanu Saha, Matthias Scheffler, Martin Schlipf, Karlheinz Schwarz, Sangeeta Sharma, Francesca Tavazza, Patrik Thunström, Alexandre Tkatchenko, Marc Torrent, David Vanderbilt, Michiel J. van Setten, Veronique Van Speybroeck, John M. Wills, Jonathan R. Yates, Guo-Xu Zhang, and Stefaan Cottenier. Reproducibility in density functional theory calculations of solids. Science, 351(6280):aad3000, March 2016.

[47] Gianluca Prandini, Antimo Marrazzo, Ivano E. Castelli, Nicolas Mounet, and Nicola Marzari. Precision and efficiency in solid-state pseudopotential calculations. npj Computational Materials, 4(1):72, 2018.

[48] Tonatiuh Rangel, Mauro Del Ben, Daniele Varsano, Gabriel Antonius, Fabien Bruneval, Felipe H. da Jornada, Michiel J. van Setten, Okan K. Orhan, David D. O'Regan, Andrew Canning, Andrea Ferretti, Andrea Marini, Gian-Marco Rignanese, Jack Deslippe, Steven G. Louie, and Jeffrey B. Neaton. Reproducibility in G 0 W 0 calculations for solids. Computer Physics Communications, 255:107242, October 2020.

[49] M. J. van Setten, F. Weigend, and F. Evers. The GW -Method for Quantum Chemistry Applications: Theory and Implementation. Journal of Chemical Theory and Computation, 9(1):232–246, January 2013.

[50] Martin M. Rieger, L. Steinbeck, I.D. White, H.N. Rojas, and R.W. Godby. The GW space-time method for the self-energy of large systems. Computer Physics Communications, 117(3):211–228, March 1999.

[51] Fang Liu, Lin Lin, Derek Vigil-Fowler, Johannes Lischner, Alexander F. Kemper, Sahar Sharifzadeh, Felipe H. da Jornada, Jack Deslippe, Chao Yang, Jeffrey B. Neaton, and Steven G. Louie. Numerical integration for ab initio many-electron self energy calculations within the GW approximation. Journal of Computational Physics, 286:1–13, April 2015.

[52] Mark S. Hybertsen and Steven G. Louie. Electron correlation in semiconductors and insulators: Band gaps and quasiparticle energies. Phys. Rev. B, 34:5390–5413, Oct 1986.

[53] R. W. Godby and R. J. Needs. Metal-insulator transition in Kohn-Sham theory and quasiparticle theory. Phys. Rev. Lett., 62(10):1169–1172, March 1989.

[54] Dario A. Leon, Claudia Cardoso, Tommaso Chiarotti, Daniele Varsano, Elisa Molinari, and Andrea Ferretti. Frequency dependence in G W made simple using a multipole approximation. Physical Review B, 104(11):115157, September 2021.

[55] Lucia Reining, Giovanni Onida, and R. W. Godby. Elimination of unoccupied-state summations in ab initio self-energy calculations for large supercells. Phys. Rev. B, 56:R4301–R4304, Aug 1997.

[56] Hugh F. Wilson, Deyu Lu, Fran çois Gygi, and Giulia Galli. Iterative calculations of dielectric eigenvalue spectra. Phys. Rev. B, 79:245106, Jun 2009.

[57] Feliciano Giustino, Marvin L. Cohen, and Steven G. Louie. Gw method with the self-consistent sternheimer equation. Phys. Rev. B, 81:115105, Mar 2010.

[58] P. Umari, Geoffrey Stenuit, and Stefano Baroni. GW quasiparticle spectra from occupied states only. Physical Review B, 81(11):115104, March 2010.

[59] Marco Govoni and Giulia Galli. Large Scale GW Calculations. Journal of Chemical Theory and Computation, 11(6):2680–2696, June 2015.

[60] Jiří Klimeš, Merzuk Kaltak, and Georg Kresse. Predictive G W calculations using plane waves and pseudopotentials. Physical Review B, 90(7):075125, August 2014.

[61] C. Rostgaard, K. W. Jacobsen, and K. S. Thygesen. Fully self-consistent GW calculations for molecules. Physical Review B, 81(8):085103, February 2010.

[62] Fabien Bruneval and Miguel A. L. Marques. Benchmarking the Starting Points of the GW Approximation for Molecules. Journal of Chemical Theory and Computation, 9(1):324–329, January 2013.

[63] Bonacci, Miki and Qiao, Junfeng and Spallanzani, Nicola and Pizzi, Giovanni and Marrazzo, Antimo and Prezzi, Deborah and Molinari, Elisa and Varsano, Daniele and Ferretti, Andrea. Automated Many-Body Perturbation Theory, preprint (2022).

[64] Andrea Marini, Conor Hogan, Myrta Grüning, and Daniele Varsano. yambo: An ab initio tool for excited state calculations. Comput. Phys. Commun., 180:1392–1403, Aug 2009.

[65] D Sangalli, A Ferretti, H Miranda, C Attaccalite, I Marri, E Cannuccia, P Melo, M Marsili, F Paleari, A Marrazzo, G Prandini, P Bonfà, M O Atambo, F Affinito, M Palummo, A Molina-Sánchez, C Hogan, M Grüning, D Varsano, and A Marini. Many-body perturbation theory calculations using the yambo code. J. Phys.: Condens. Matter, 31(32):325902, may 2019.

[66] Michiel J. van Setten, Fabio Caruso, Sahar Sharifzadeh, Xinguo Ren, Matthias Scheffler, Fang Liu, Johannes Lischner, Lin Lin, Jack R. Deslippe, Steven G. Louie, Chao Yang, Florian Weigend, Jeffrey B. Neaton, Ferdinand Evers, and Patrick Rinke. Gw100: Benchmarking g0w0 for molecular systems. Journal of Chemical Theory and Computation, 11(12):5665–5687, 2015.

[67] Javeed Mahmood, Eun Kwang Lee, Minbok Jung, Dongbin Shin, Hyun-Jung Choi, Jeong-Min Seo, Sun-Min Jung, Dongwook Kim, Feng Li, Myoung Soo Lah, Noejung Park, Hyung-Joon Shin, Joon Hak Oh, and Jong-Beom Baek. Two-dimensional polyaniline (c3n) from carbonized organic single crystals in solid state. Proc. Natl. Ac. Sci., 113(27):7414–7419, 2016.

[68] Li-Bin Shi, Yan-Yan Zhang, Xiaoming Xiu, and Hai-Kuan Dong. Structural characteristics and strain behaviors of two-dimensional c_3n: First principles calculations. Carbon, 134:103–111, 03 2018.

[69] Dandan Wang, Yu Bao, Tongshun Wu, Shiyu Gan, Dongxue Han, and Li Niu. First-principles study of the role of strain and hydrogenation on c3n. Carbon, 134:22 – 28, 2018.

[70] Bohayra Mortazavi. Ultra high stiffness and thermal conductivity of graphene like c3n. Carbon, 118:25 – 34, 2017.

[71] Y. Gao, H. Wang, M. Sun, Y. Ding, L. Zhang, and Q. Li. First-principles study of intrinsic phononic thermal transport in monolayer C_3N. Phys. E: Low-Dimens. Syst. Nanostructures, 99:194–201, May 2018.

[72] Miki Bonacci, Matteo Zanfrognini, Elisa Molinari, Alice Ruini, Marilia J. Caldas, Andrea Ferretti, and Daniele Varsano. Excitonic effects in graphene-like c_3N. Phys. Rev. Materials, 6:034009, Mar 2022.

[73] Maria Grazia Betti, Ernesto Placidi, Chiara Izzo, Elena Blundo, Antonio Polimeni, Marco Sbroscia, José Avila, Pavel Dudin, Kailong Hu, Yoshikazu Ito, Deborah Prezzi, Miki Bonacci, Elisa Molinari, and Carlo Mariani. Gap opening in double-sided highly hydrogenated free-standing graphene. Nano Letters, 22(7):2971–2977, 04 2022.

[74] Maria Grazia Betti, Dario Marchiani, Elena Blundo, Marta De Luca, Antonio Polimeni, Riccardo Frisenda, Carlo Mariani, Samuel Jeong, Yoshikazu Ito, Andrea Tonelli, Nicola Cavani, Roberto Biagi, Valentina De Renzi, Peter N. O. Gillespie, Miki Bonacci, Elisa Molinari, and Deborah Prezzi. Dielectric response and excitations of free-standing graphane, 2022. preprint.

[75] Jacques Des Cloizeaux. Exciton instability and crystallographic anomalies in semiconductors. Journal of Physics and Chemistry of Solids, 26(2):259–266, February 1965.

[76] D. Sherrington and W. Kohn. Speculations about Grey Tin. Reviews of Modern Physics, 40(4):767–769, October 1968.

[77] D. Jérome, T. M. Rice, and W. Kohn. Excitonic insulator. Phys. Rev., 158:462–475, Jun 1967.

[78] J. Bardeen, L. N. Cooper, and J. R. Schrieffer. Theory of Superconductivity. Physical Review, 108(5):1175–1204, December 1957.

[79] B.I. Halperin and T.M. Rice. The excitonic state at the semiconductor-semimetal transition**a summary of thin paper was presented at the meeting of the american physical society, at toronto, canada, june 1967. volume 21 of Solid State Physics, pages 115–192. Academic Press, 1968.

[80] T. Portengen, Th. Östreich, and L. J. Sham. Theory of electronic ferroelectricity. Phys. Rev. B, 54:17452–17463, Dec 1996.

[81] J. P. Eisenstein and A. H. MacDonald. Bose–einstein condensation of excitons in bilayer electron systems. Nature, 432(7018):691–694, 2004.

[82] M. Rontani, L. J. Sham, "Coherent exciton transport in semiconductors" in *Novel Superfluids* Vol. 2, K. H. Bennemann, J. B. Ketterson, Eds. (International Series of Monographs on Physics, Oxford University Press, Oxford, UK, 2014), vol. 157, pp. 423–474.

[83] M. Born and J. R. Oppenheimer. Zur quantentheorie der molekeln. Ann. Physik, 84(457), 1927.

[84] D. R. Hartree. The Wave Mechanics of an Atom with a Non-Coulomb Central Field. Part I. Theory and Methods. Mathematical Proceedings of the Cambridge Philosophical Society, 24(1):89–110, January 1928.

[85] V. Fock. Näherungsmethode zur Lösung des quantenmechanischen Mehrkörperproblems. Zeitschrift fur Physik, 61(1-2):126–148, January 1930.

[86] W. Kohn. Nobel Lecture: Electronic structure of matter—wave functions and density functionals. Reviews of Modern Physics, 71(5):1253–1266, October 1999.

[87] Richard M. Martin. Electronic structure: basic theory and practical methods. Cambridge University Press, Cambridge, UK ; New York, 2004.

[88] P. Hohenberg and W. Kohn. Inhomogeneous Electron Gas. Physical Review, 136(3B):B864–B871, November 1964.

[89] W. Kohn, in *Highlights of Condensed Matter Theory* (North-Holland, Amsterdam, 1985).

[90] Mel Levy. Electron densities in search of Hamiltonians. Physical Review A, 26(3):1200–1208, September 1982.

[91] E. Lieb, in Physics as Natural Philosophy, edited by A. Shimony and H. Feshbach, MIT Press, Cambridge, MA, 1982, p. 111.

[92] Giuseppe Pastori Parravicini Giuseppe Grosso. Solid State Physics. San Diego, Calif.: Academic Press, 2003.

[93] W. Kohn and L. J. Sham. Self-Consistent Equations Including Exchange and Correlation Effects. Physical Review, 140(4A):A1133–A1138, November 1965.

[94] J. P. Perdew and Alex Zunger. Self-interaction correction to density-functional approximations for many-electron systems. Physical Review B, 23(10):5048–5079, May 1981.

[95] David M Ceperley and Berni J Alder. Ground state of the electron gas by a stochastic method. Physical review letters, 45(7):566, 1980.

[96] A. L. Fetter and J. D. Walecka. Quantum Theory of Many-Particle Systems. McGraw-Hill, New York, 1971.

[97] Axel D. Becke. Perspective: Fifty years of density-functional theory in chemical physics. The Journal of Chemical Physics, 140(18):18A301, May 2014.

[98] John P. Perdew, Kieron Burke, and Matthias Ernzerhof. Generalized gradient approximation made simple. Phys. Rev. Lett., 77:3865–3868, Oct 1996.

[99] Enrico Fermi. Sopra lo Spostamento per Pressione delle Righe Elevate delle Serie Spettrali. Il Nuovo Cimento, 11(3):157–166, March 1934.

[100] James C. Phillips and Leonard Kleinman. New method for calculating wave functions in crystals and molecules. Phys. Rev., 116:287–294, Oct 1959.

[101] Leonard Kleinman and James C. Phillips. Crystal potential and energy bands of semiconductors. iii. self-consistent calculations for silicon. Phys. Rev., 118:1153–1167, Jun 1960.

[102] Carlos Fiolhais, Fernando Nogueira, Miguel A. L. Marques, R. Beig, B. G. Englert, U. Frisch, P. Hänggi, K. Hepp, W. Hillebrandt, D. Imboden, R. L. Jaffe, R. Lipowsky, H. v. Löhneysen, I. Ojima, D. Sornette, S. Theisen, W. Weise, J. Wess, and J. Zittartz, editors. A Primer in Density Functional Theory, volume 620 of Lecture Notes in Physics. Springer Berlin Heidelberg, Berlin, Heidelberg, 2003.

[103] V. Heine and I. Abarenkov. A new method for the electronic structure of metals. The Philosophical Magazine: A Journal of Theoretical Experimental and Applied Physics, 9(99):451–465, 1964.

[104] I. V. Abarenkov and V. Heine. The model potential for positive ions. The Philosophical Magazine: A Journal of Theoretical Experimental and Applied Physics, 12(117):529–537, 1965.

[105] N. W. Ashcroft and David C. Langreth. Compressibility and binding energy of the simple metals. Phys. Rev., 155:682–684, Mar 1967.

[106] W.A. Harrison. Pseudopotentials in the Theory of Metals. Frontiers in Physics : a lecture note and reprint series. W.A. Benjamin, 1966.

[107] William C. Topp and John J. Hopfield. Chemically motivated pseudopotential for sodium. Phys. Rev. B, 7:1295–1303, Feb 1973.

[108] Alex Zunger and Marvin L. Cohen. First-principles nonlocal-pseudopotential approach in the density-functional formalism: Development and application to atoms. Phys. Rev. B, 18:5449–5472, Nov 1978.

[109] D. R. Hamann, M. Schlüter, and C. Chiang. Norm-conserving pseudopotentials. Phys. Rev. Lett., 43:1494–1497, Nov 1979.

[110] D. R. Hamann. Optimized norm-conserving vanderbilt pseudopotentials. Phys. Rev. B, 88:085117, Aug 2013.

[111] Martin Schlipf and François Gygi. Optimization algorithm for the generation of oncv pseudopotentials. Computer Physics Communications, 196:36 – 44, 2015.

[112] M.J. van Setten, M. Giantomassi, E. Bousquet, M.J. Verstraete, D.R. Hamann, X. Gonze, and G.-M. Rignanese. The PseudoDojo: Training and grading a 85 element optimized norm-conserving pseudopotential table. Computer Physics Communications, 226:39–54, May 2018.

[113] Steven G. Louie, Sverre Froyen, and Marvin L. Cohen. Nonlinear ionic pseudopotentials in spin-density-functional calculations. Physical Review B, 26(4):1738–1742, August 1982.

[114] Neil W. Ashcroft and N. David Mermin. Solid state physics. Saunders College Publ., Fort Worth, internat. ed., 21. print edition, 1995.

[115] Carlo A. Rozzi, Daniele Varsano, Andrea Marini, Eberhard K. U. Gross, and Angel Rubio. Exact Coulomb cutoff technique for supercell calculations. Physical Review B, 73(20):205119, May 2006.

[116] Paolo Giannozzi, Stefano Baroni, Nicola Bonini, Matteo Caland ra, Roberto Car, Carlo Cavazzoni, Davide Ceresoli, Guido L. Chiarotti, Matteo Cococcioni, Ismaila Dabo, Andrea Dal Corso, Stefano de Gironcoli, Stefano Fabris, Guido Fratesi, Ralph Gebauer, Uwe Gerstmann, Christos Gougoussis, Anton Kokalj, Michele Lazzeri, Layla Martin-Samos, Nicola Marzari, Francesco Mauri, Riccardo Mazzarello, Stefano Paolini, Alfredo Pasquarello, Lorenzo Paulatto, Carlo Sbraccia, Sandro Scandolo, Gabriele Sclauzero, Ari P. Seitsonen, Alexander Smogunov, Paolo Umari, and Renata M. Wentzcovitch. QUANTUM ESPRESSO: a modular and open-source software project for quantum simulations of materials. J. Phys.: Condens. Matter, 21:395502, Sep 2009.

[117] P. Giannozzi, O. Andreussi, T. Brumme, O. Bunau, M. Buongiorno Nardelli, M. Calandra, R. Car, C. Cavazzoni, D. Ceresoli, M. Cococcioni, N. Colonna, I. Carnimeo, A. Dal Corso, S. de Gironcoli, P. Delugas, Jr. DiStasio, R. A., A. Ferretti, A. Floris, G. Fratesi, G. Fugallo, R. Gebauer, U. Gerstmann, F. Giustino, T. Gorni, J. Jia, M. Kawamura, H. Y. Ko, A. Kokalj, E. Küçükbenli, M. Lazzeri, M. Marsili, N. Marzari, F. Mauri, N. L. Nguyen, H. V. Nguyen, A. Otero-de-la-Roza, L. Paulatto, S. Poncé, D. Rocca,

R. Sabatini, B. Santra, M. Schlipf, A. P. Seitsonen, A. Smogunov, I. Timrov, T. Thonhauser, P. Umari, N. Vast, X. Wu, and S. Baroni. Advanced capabilities for materials modelling with Quantum ESPRESSO. J. Phys.: Condens. Matter, 29:465901, Nov 2017.

[118] John P. Perdew. Density functional theory and the band gap problem. International Journal of Quantum Chemistry, 28(S19):497–523, 1985.

[119] R. W. Godby, M. Schlüter, and L. J. Sham. Self-energy operators and exchange-correlation potentials in semiconductors. Phys. Rev. B, 37:10159–10175, Jun 1988.

[120] L. D. Landau, Sov. Phys. JETP **8**, 70 (1959).

[121] Richard M. Martin, Lucia Reining, and David M. Ceperley. Interacting Electrons: Theory and Computational Approaches. Cambridge University Press, 2016.

[122] F. J. Dyson. The s matrix in quantum electrodynamics. Phys. Rev., 75:1736–1755, Jun 1949.

[123] Stephen L. Adler. Quantum theory of the dielectric constant in real solids. Phys. Rev., 126:413–420, Apr 1962.

[124] Nathan Wiser. Dielectric constant with local field effects included. Phys. Rev., 129:62–69, Jan 1963.

[125] K. Sturm. Dynamic structure factor: An introduction. Zeitschrift für Naturforschung A, 48(1-2):233–242, 1993.

[126] Frédéric Fossard, Lorenzo Sponza, Léonard Schué, Claudio Attaccalite, François Ducastelle, Julien Barjon, and Annick Loiseau. Angle-resolved electron energy loss spectroscopy in hexagonal boron nitride. Phys. Rev. B, 96(11):115304, September 2017.

[127] V. M. Galitskii and A. B. Migdal. Sov. Phys. JETP, 7(7), 1958.

[128] G. C. Wick. The evaluation of the collision matrix. Phys. Rev., 80:268–272, Oct 1950.

[129] R. P. Feynman. Space-time approach to quantum electrodynamics. Phys. Rev., 76:769–789, Sep 1949.

[130] F.W. Byron and R.W. Fuller. Mathematics of Classical and Quantum Physics. Number v. 1-2 in Dover books on physics and chemistry. Dover Publications, 1992.

[131] Stefan Hüfner. Photoelectron Spectroscopy. Advanced Texts in Physics. Springer Berlin Heidelberg, Berlin, Heidelberg, 2003.

[132] Ke Wang, Ben Ecker, and Yongli Gao. Angle-Resolved Photoemission Study on the Band Structure of Organic Single Crystals. Crystals, 10(9):773, September 2020.

[133] Eric L. Shirley. Self-consistent gw and higher-order calculations of electron states in metals. Phys. Rev. B, 54:7758–7764, Sep 1996.

[134] M. Stankovski, G. Antonius, D. Waroquiers, A. Miglio, H. Dixit, K. Sankaran, M. Giantomassi, X. Gonze, M. Côté, and G.-M. Rignanese. G 0 W 0 band gap of ZnO: Effects of plasmon-pole models. Physical Review B, 84(24):241201, December 2011.

[135] M. van Schilfgaarde, Takao Kotani, and S. Faleev. Quasiparticle self-consistent *gw* theory. Phys. Rev. Lett., 96:226402, Jun 2006.

[136] Sergey V. Faleev, Mark van Schilfgaarde, and Takao Kotani. All-electron self-consistent *gw* approximation: Application to si, mno, and nio. Phys. Rev. Lett., 93:126406, Sep 2004.

[137] Raul Laasner. G0w0 band structure of cdwo4. Journal of Physics: Condensed Matter, 26(12):125503, 2014.

[138] E. E. Salpeter and H. A. Bethe. A relativistic equation for bound-state problems. Phys. Rev., 84:1232–1242, Dec 1951.

[139] G. Strinati. Dynamical shift and broadening of core excitons in semiconductors. Phys. Rev. Lett., 49:1519–1522, Nov 1982.

[140] G. Strinati. Effects of dynamical screening on resonances at inner-shell thresholds in semiconductors. Phys. Rev. B, 29:5718–5726, May 1984.

[141] S. Albrecht, Ph.D. thesis, Ecole Polytechnique, France (1999).

[142] I. Tamm. Relativistic interaction of elementary particles. J. Phys. (USSR), 9:449, 1945.

[143] S. M. Dancoff. Non-adiabatic meson theory of nuclear forces. Phys. Rev., 78:382–385, May 1950.

[144] M. J. van Setten, M. Giantomassi, X. Gonze, G.-M. Rignanese, and G. Hautier. Automation methodologies and large-scale validation for G W : Towards high-throughput G W calculations. Physical Review B, 96(15):155207, October 2017.

[145] Asbjørn Rasmussen, Thorsten Deilmann, and Kristian S. Thygesen. Towards fully automated GW band structure calculations: What we can learn from 60.000 self-energy evaluations. npj Computational Materials, 7(1):22, December 2021.

[146] Nicola Marzari, Arash A. Mostofi, Jonathan R. Yates, Ivo Souza, and David Vanderbilt. Maximally localized Wannier functions: Theory and applications. Reviews of Modern Physics, 84(4):1419–1475, October 2012.

[147] Rocío Mercado, Rueih-Sheng Fu, Aliaksandr V. Yakutovich, Leopold Talirz, Maciej Haranczyk, and Berend Smit. In Silico Design of 2D and 3D Covalent Organic Frameworks for Methane Storage Applications. Chemistry of Materials, 30(15):5069–5086, August 2018.

[148] Gianluca Prandini, Antimo Marrazzo, Ivano E. Castelli, Nicolas Mounet, and Nicola Marzari. Precision and efficiency in solid-state pseudopotential calculations. npj Computational Materials, 4(1):72, December 2018.

[149] Valerio Vitale, Giovanni Pizzi, Antimo Marrazzo, Jonathan R. Yates, Nicola Marzari, and Arash A. Mostofi. Automated high-throughput Wannierisation. npj Comput. Mater., 6(1):66, jun 2020.

[150] Giovanni Pizzi, Valerio Vitale, Ryotaro Arita, Stefan Blügel, Frank Freimuth, Guillaume Géranton, Marco Gibertini, Dominik Gresch, Charles Johnson, Takashi Koretsune, Julen Ibañez-Azpiroz, Hyungjun Lee, Jae-Mo Lihm, Daniel Marchand, Antimo Marrazzo, Yuriy Mokrousov, Jamal I Mustafa, Yoshiro Nohara, Yusuke Nomura, Lorenzo Paulatto, Samuel Poncé, Thomas Ponweiser, Junfeng Qiao, Florian Thöle, Stepan S Tsirkin, Małgorzata Wierzbowska, Nicola Marzari, David Vanderbilt, Ivo Souza, Arash A Mostofi, and Jonathan R Yates. Wannier90 as a community code: new features and applications. Journal of Physics: Condensed Matter, 32(16):165902, jan 2020.

[151] Weiwei Gao, Weiyi Xia, Xiang Gao, and Peihong Zhang. Speeding up GW Calculations to Meet the Challenge of Large Scale Quasiparticle Predictions. Scientific Reports, 6(1):36849, December 2016.

[152] Emanuele Maggio, Peitao Liu, Michiel J. van Setten, and Georg Kresse. Gw100: A plane wave perspective for small molecules. Journal of Chemical Theory and Computation, 13(2):635–648, 2017. PMID: 28094981.

[153] Arno Schindlmayr. Analytic evaluation of the electronic self-energy in the G W approximation for two electrons on a sphere. Physical Review B, 87(7):075104, February 2013.

[154] Sebastiaan P. Huber, Emanuele Bosoni, Marnik Bercx, Jens Bröder, Augustin Degomme, Vladimir Dikan, Kristjan Eimre, Espen Flage-Larsen, Alberto Garcia, Luigi Genovese, Dominik Gresch, Conrad Johnston, Guido Petretto, Samuel Poncé, Gian-Marco Rignanese, Christopher J. Sewell, Berend Smit, Vasily Tseplyaev, Martin Uhrin, Daniel Wortmann, Aliaksandr V. Yakutovich, Austin Zadoks, Pezhman Zarabadi-Poor, Bonan Zhu, Nicola Marzari, and Giovanni Pizzi. Common workflows for computing material properties using different quantum engines. npj Computational Materials, 7(1):136, December 2021.

[155] The `aiida-yambo` code is available at https://github.com/yambo-code/aiida-yambo.

[156] The `aiida-yambo` documentation is available at https://aiida-yambo.readthedocs.io/en/master/.

[157] Fabien Bruneval and Xavier Gonze. Accurate G W self-energies in a plane-wave basis using only a few empty states: Towards large systems. Physical Review B, 78(8):085125, August 2008.

[158] Olivia Pulci, Giovanni Onida, Rodolfo Del Sole, and Lucia Reining. *Ab Initio* Calculation of Self-Energy Effects on Optical Properties of GaAs(110). Physical Review Letters, 81(24):5374–5377, December 1998.

[159] Alberto Guandalini, Pino D'Amico, Andrea Ferretti, and Daniele Varsano. Efficient gw calculations in two dimensional materials through a stochastic integration of the screened potential, 2022.

[160] Xin-Zheng Li, Ricardo Gómez-Abal, Hong Jiang, Claudia Ambrosch-Draxl, and Matthias Scheffler. Impact of widely used approximations to the $G_0 W_0$ method: an all-electron perspective. New Journal of Physics, 14(2):023006, February 2012.

[161] Hongliang Shi, Hui Pan, Yong-Wei Zhang, and Boris I. Yakobson. Quasiparticle band structures and optical properties of strained monolayer MoS 2 and WS 2. Physical Review B, 87(15):155304, April 2013.

[162] Falco Hüser, Thomas Olsen, and Kristian S. Thygesen. Quasiparticle GW calculations for solids, molecules, and two-dimensional materials. Physical Review B, 87(23):235132, June 2013.

[163] The `aiida-yambo-wannier90` code is available at https://github.com/aiidaplugins/aiida-yambo-wannier90.

[164] The `aiida-yambo-wannier90` documentation is available at https://aiida-yambo-wannier90.readthedocs.io/en/latest/.

[165] K. Lejaeghere, V. Van Speybroeck, G. Van Oost, and S. Cottenier. Error Estimates for Solid-State Density-Functional Theory Predictions: An Overview by Means of the Ground-State Elemental Crystals. Critical Reviews in Solid State and Materials Sciences, 39(1):1–24, January 2014.

[166] Sergey V. Faleev, Mark van Schilfgaarde, and Takao Kotani. All-electron self-consistent *gw* approximation: Application to si, mno, and nio. Phys. Rev. Lett., 93:126406, Sep 2004.

[167] M. van Schilfgaarde, Takao Kotani, and S. Faleev. Quasiparticle self-consistent *gw* theory. Phys. Rev. Lett., 96:226402, Jun 2006.

[168] M. Shishkin and G. Kresse. Self-consistent *gw* calculations for semiconductors and insulators. Phys. Rev. B, 75:235102, Jun 2007.

[169] Hong Jiang and Peter Blaha. *gw* with linearized augmented plane waves extended by high-energy local orbitals. Phys. Rev. B, 93:115203, Mar 2016.

[170] Jack Deslippe, Georgy Samsonidze, David A. Strubbe, Manish Jain, Marvin L. Cohen, and Steven G. Louie. BerkeleyGW: A massively parallel computer package for the calculation of the quasiparticle and optical properties of materials and nanostructures. Computer Physics Communications, 183(6):1269–1289, June 2012.

[171] Aldo H. Romero, Douglas C. Allan, Bernard Amadon, Gabriel Antonius, Thomas Applencourt, Lucas Baguet, Jordan Bieder, François Bottin, Johann Bouchet, Eric Bousquet, Fabien Bruneval, Guillaume Brunin, Damien Caliste, Michel Côté, Jules Denier, Cyrus Dreyer, Philippe Ghosez, Matteo Giantomassi, Yannick Gillet, Olivier Gingras, Donald R. Hamann, Geoffroy Hautier, François Jollet, Gérald Jomard, Alexandre Martin, Henrique P. C. Miranda, Francesco Naccarato, Guido Petretto, Nicholas A. Pike, Valentin Planes, Sergei Prokhorenko, Tonatiuh Rangel, Fabio Ricci, Gian-Marco Rignanese, Miquel Royo, Massimiliano Stengel, Marc Torrent, Michiel J. van Setten, Benoit Van Troeye, Matthieu J. Verstraete, Julia Wiktor, Josef W. Zwanziger, and Xavier Gonze. Abinit: Overview, and focus on selected capabilities. J. Chem. Phys., 152:124102, 2020.

[172] Carsten Rostgaard, Karsten Wedel Jacobsen, and Kristian Sommer Thygesen. Fully self-consistent gw calculations for molecules. Physical Review B, 81(8):085103, 2010.

[173] Xavier Blase, Claudio Attaccalite, and Valerio Olevano. First-principles gw calculations for fullerenes, porphyrins, phtalocyanine, and other molecules of interest for organic photovoltaic applications. Physical Review B, 83(11):115103, 2011.

[174] Fabien Bruneval and Miguel A. L. Marques. Benchmarking the starting points of the gw approximation for molecules. Journal of Chemical Theory and Computation, 9(1):324–329, 01 2013.

[175] F. Kaplan, M. E. Harding, C. Seiler, F. Weigend, F. Evers, and M. J. van Setten. Quasi-particle self-consistent gw for molecules. Journal of Chemical Theory and Computation, 12(6):2528–2541, 06 2016.

[176] The GW100 repository is available at https://github.com/setten/GW100.

[177] Fabio Caruso, Matthias Dauth, Michiel J. van Setten, and Patrick Rinke. Benchmark of *GW* Approaches for the *GW* 100 Test Set. Journal of Chemical Theory and Computation, 12(10):5076–5087, October 2016.

[178] Marco Govoni and Giulia Galli. Gw100: Comparison of methods and accuracy of results obtained with the west code. Journal of Chemical Theory and Computation, 14(4):1895–1909, 2018. PMID: 29397712.

[179] J.F. Stanton and J. Gauss. A DISCUSSION OF SOME PROBLEMS ASSOCIATED WITH THE QUANTUM MECHANICAL TREATMENT OF OPEN-SHELL MOLECULES. Adv. Chem. Phys., 125(101), 2003.

[180] Bengt Holm and Ulf von Barth. Cancellation Effects in the GW Approximation. Physica Scripta, T109:135, 2004.

[181] Patrick Rinke, Abdallah Qteish, Jörg Neugebauer, Christoph Freysoldt, and Matthias Scheffler. Combining *GW* calculations with exact-exchange density-functional theory: an analysis of valence-band photoemission for compound semiconductors. New Journal of Physics, 7:126–126, May 2005.

[182] Viktor Atalla, Mina Yoon, Fabio Caruso, Patrick Rinke, and Matthias Scheffler. Hybrid density functional theory meets quasiparticle calculations: A consistent electronic structure approach. Physical Review B, 88(16):165122, October 2013.

[183] B. Arnaud and M. Alouani. All-electron projector-augmented-wave GW approximation: Application to the electronic properties of semiconductors. Physical Review B, 62(7):4464–4476, August 2000.

[184] M. Shishkin and G. Kresse. Implementation and performance of the frequency-dependent G W method within the PAW framework. Physical Review B, 74(3):035101, July 2006.

[185] Andrey Kutepov, Kristjan Haule, Sergey Y. Savrasov, and Gabriel Kotliar. Electronic structure of Pu and Am metals by self-consistent relativistic G W method. Physical Review B, 85(15):155129, April 2012.

[186] Takao Kotani and Mark van Schilfgaarde. All-electron GW approximation with the mixed basis expansion based on the full-potential LMTO method. Solid State Communications, 121(9-10):461–465, March 2002.

[187] Florian Weigend and Reinhart Ahlrichs. Balanced basis sets of split valence, triple zeta valence and quadruple zeta valence quality for H to Rn: Design and assessment of accuracy. Physical Chemistry Chemical Physics, 7(18):3297, 2005.

[188] Leonard Kleinman and D. M. Bylander. Efficacious Form for Model Pseudopotentials. Physical Review Letters, 48(20):1425–1428, May 1982.

[189] David Vanderbilt. Soft self-consistent pseudopotentials in a generalized eigenvalue formalism. Physical Review B, 41(11):7892–7895, April 1990.

[190] Andrew M. Rappe, Karin M. Rabe, Efthimios Kaxiras, and J. D. Joannopoulos. Optimized pseudopotentials. Physical Review B, 41(2):1227–1230, January 1990.

[191] Martin Fuchs and Matthias Scheffler. Ab initio pseudopotentials for electronic structure calculations of poly-atomic systems using density-functional theory. Computer Physics Communications, 119(1):67–98, June 1999.

[192] Michael Rohlfing, Peter Krüger, and Johannes Pollmann. Quasiparticle Band Structure of CdS. Physical Review Letters, 75(19):3489–3492, November 1995.

[193] S. Lebègue, B. Arnaud, M. Alouani, and P. E. Bloechl. Implementation of an all-electron GW approximation based on the projector augmented wave method without plasmon pole approximation: Application to Si, SiC, AlAs, InAs, NaH, and KH. Physical Review B, 67(15):155208, April 2003.

[194] David Linton Johnson. Local field effects and the dielectric response matrix of insulators: A model. Physical Review B, 9(10):4475–4484, May 1974.

[195] Sree Ganesh Balasubramani, Guo P. Chen, Sonia Coriani, Michael Diedenhofen, Marius S. Frank, Yannick J. Franzke, Filipp Furche, Robin Grotjahn, Michael E. Harding, Christof Hättig, Arnim Hellweg, Benjamin Helmich-Paris, Christof Holzer, Uwe Huniar, Martin Kaupp, Alireza Marefat Khah, Sarah Karbalaei Khani, Thomas Müller, Fabian Mack, Brian D. Nguyen, Shane M. Parker, Eva Perlt, Dmitrij Rappoport, Kevin Reiter, Saswata Roy, Matthias Rückert, Gunnar Schmitz, Marek Sierka, Enrico Tapavicza, David P. Tew, Christoph van Wüllen, Vamsee K. Voora, Florian Weigend, Artur Wodyński, and Jason M. Yu. TURBOMOLE: Modular program suite for *ab initio* quantum-chemical and condensed-matter simulations. The Journal of Chemical Physics, 152(18):184107, May 2020.

[196] Volker Blum, Ralf Gehrke, Felix Hanke, Paula Havu, Ville Havu, Xinguo Ren, Karsten Reuter, and Matthias Scheffler. Ab initio molecular simulations with numeric atom-centered orbitals. Computer Physics Communications, 180(11):2175–2196, November 2009.

[197] Xinguo Ren, Patrick Rinke, Volker Blum, Jürgen Wieferink, Alexandre Tkatchenko, Andrea Sanfilippo, Karsten Reuter, and Matthias Scheffler. Resolution-of-identity approach to Hartree-Fock, hybrid density functionals, RPA, MP2 and GW with numeric atom-centered orbital basis functions. New Journal of Physics, 14(5):053020, May 2012.

[198] Jack Deslippe, Georgy Samsonidze, Manish Jain, Marvin L. Cohen, and Steven G. Louie. Coulomb-hole summations and energies for G W calculations with limited number of empty orbitals: A modified static remainder approach. Physical Review B, 87(16):165124, April 2013.

[199] G. Kresse and J. Furthmüller. Efficiency of ab-initio total energy calculations for metals and semiconductors using a plane-wave basis set. Computational Materials Science, 6(1):15–50, July 1996.

[200] Merzuk Kaltak, Jiří Klimeš, and Georg Kresse. Low Scaling Algorithms for the Random Phase Approximation: Imaginary Time and Laplace Transformations. Journal of Chemical Theory and Computation, 10(6):2498–2507, June 2014.

[201] Hugh F. Wilson, Deyu Lu, François Gygi, and Giulia Galli. Iterative calculations of dielectric eigenvalue spectra. Physical Review B, 79(24):245106, June 2009.

[202] Glenn J. Martyna and Mark E. Tuckerman. A reciprocal space based method for treating long range interactions in *ab initio* and force-field-based calculations in clusters. The Journal of Chemical Physics, 110(6):2810–2821, February 1999.

[203] Filip A. Rasmussen and Kristian S. Thygesen. Computational 2D Materials Database: Electronic Structure of Transition-Metal Dichalcogenides and Oxides. The Journal of Physical Chemistry C, 119(23):13169–13183, June 2015.

[204] Katharina Krause, Michael E. Harding, and Wim Klopper. Coupled-cluster reference values for the GW27 and GW100 test sets for the assessment of GW methods. Molecular Physics, 113(13-14):1952–1960, July 2015.

[205] Lias, S. G.; Levin, R. D.; Kafafi, S. A. Ion Energetics Data in NIST Chemistry WebBook. *NIST Standard Reference Database Number.*

http://webbook.nist.gov, d.d. September 1, 2012, 69th ed.; National Institute of Standards and Technology: Gaithersburg, MD, 2003.

[206] Johannes Lischner, Sahar Sharifzadeh, Jack Deslippe, Jeffrey B. Neaton, and Steven G. Louie. Effects of self-consistency and plasmon-pole models on G W calculations for closed-shell molecules. Physical Review B, 90(11):115130, September 2014.

[207] David Adekoya, Shangshu Qian, Xingxing Gu, William Wen, Dongsheng Li, Jianmin Ma, and Shanqing Zhang. Dft-guided design and fabrication of carbon-nitride-based materials for energy storage devices: A review. Nano-Micro Letters, 13:13, Oct. 2020.

[208] Yuan Xu and Shang-Peng Gao. Band gap of C3N4 in the GW approximation. Int. J. Hydrogen Energy, 37(15):11072–11080, August 2012.

[209] Amene Naseri, Morasae Samadi, Ali Pourjavadi, Alireza Z. Moshfegh, and Seeram Ramakrishna. Graphitic carbon nitride (g-C $_3$ N $_4$)-based photocatalysts for solar hydrogen generation: recent advances and future development directions. J. Mater. Chem. A, 5(45):23406–23433, 2017.

[210] Siwei Yang, Wei Li, Caichao Ye, Gang Wang, He Tian, Chong Zhu, Peng He, Gu Ding, Xiaoming Xie, Yang Liu, Y Lifshitz, Shuit-Tong Lee, Zhenhui Kang, and Mianheng Jiang. C3n—a 2d crystalline, hole-free, tunable-narrow-bandgap semiconductor with ferromagnetic properties. Adv. Mater., 29:1605625, 02 2017.

[211] Jiantie Xu, Javeed Mahmood, Yuhai Dou, Shixue Dou, Feng Li, Liming Dai, and Jong-Beom Baek. 2d frameworks of c2n and c3n as new anode materials for lithium-ion batteries. Adv. Mater., 29(34):1702007, 2017.

[212] Gen-Cai Guo, Ru-Zhi Wang, Bang-Ming Ming, Changhao Wang, Si-Wei Luo, Ming Zhang, and Hui Yan. C $_3$ N/phosphorene heterostructure: a promising anode material in lithium-ion batteries. J. Mater. Chem. A, 7(5):2106–2113, 2019.

[213] Qin Liu, Bo Xiao, Jian-bo Cheng, Yan-chun Li, Qing-zhong Li, Wen-zuo Li, Xiu-feng Xu, and Xue-fang Yu. Carbon Excess C $_3$ N: A Potential Candidate as Li-Ion Battery Material. ACS Appl. Materials & Interfaces, 10(43):37135–37141, October 2018.

[214] Preeti Bhauriyal, Arup Mahata, and Biswarup Pathak. Graphene-like Carbon–Nitride Monolayer: A Potential Anode Material for Na- and K-Ion Batteries. J. Phys. Chem. C, 122(5):2481–2489, February 2018.

[215] Chunmei Zhang, Yalong Jiao, Tianwei He, Steven Bottle, Thomas Frauenheim, and Aijun Du. Predicting two-dimensional c3b/c3n van der waals p–n heterojunction with strong interlayer electron coupling and enhanced photocurrent. J. Phys. Chem. Lett., 9(4):858–862, 2018.

[216] Jiajun Wang, Xiaoting Li, Ya You, Xintong Yang, Ying Wang, and Qunxiang Li. Interfacial coupling induced direct z-scheme water splitting in metal-free photocatalyst: C3n/g-c3n4 heterojunctions. Nanotechnology, 29(36):365401, jul 2018.

[217] Diana Y. Qiu, Ting Cao, and Steven G. Louie. Nonanalyticity, Valley Quantum Phases, and Lightlike Exciton Dispersion in Monolayer Transition Metal Dichalcogenides: Theory and First-Principles Calculations. Phys. Rev. Lett., 115(17):176801, October 2015.

[218] Pierluigi Cudazzo, Lorenzo Sponza, Christine Giorgetti, Lucia Reining, Francesco Sottile, and Matteo Gatti. Exciton band structure in two-dimensional materials. Phys. Rev. Lett., 116:066803, Feb 2016.

[219] Diana Y Qiu, Galit Cohen, Dana Novichkova, and Sivan Refaely-Abramson. Signatures of dimensionality and symmetry in exciton band structure: Consequences for exciton dynamics and transport. Nano Lett., 21:7644–7650, 2021.

[220] Xiaodong Zhou, Wanxiang Feng, Shan Guan, Botao Fu, Wenyong Su, and Yugui Yao. Computational characterization of monolayer c3n: A two-dimensional nitrogen-graphene crystal. J. Mater. Res., 32(15):2993–3001, 2017.

[221] Yabei Wu, Weiyi Xia, Weiwei Gao, Fanhao Jia, Peihong Zhang, and Wei Ren. Quasiparticle electronic structure of honeycomb c 3 n: from monolayer to bulk. 2D Materials, 6(1):015018, Nov 2018.

[222] Aliaksandr V Krukau, Oleg A Vydrov, Artur F Izmaylov, and Gustavo E Scuseria. Influence of the exchange screening parameter on the performance of screened hybrid functionals. J. Chem. Phys., 125(22):224106, 2006.

[223] Wei Wei and Timo Jacob. Strong excitonic effects in the optical properties of graphitic carbon nitride g -c 3 n 4 from first principles. Phys. Rev. B, 87(8):085202, Feb 2013.

[224] Jiuyu Sun, Ruiqi Zhang, Xingxing Li, and Jinlong Yang. A many-body GW + BSE investigation of electronic and optical properties of C $_2$ N. Appl. Phys. Lett., 109(13):133108, September 2016.

[225] Li Yang, Marvin L. Cohen, and Steven G. Louie. Excitonic Effects in the Optical Spectra of Graphene Nanoribbons. Nano Letters, 7(10):3112–3115, October 2007.

[226] Deborah Prezzi, Daniele Varsano, Alice Ruini, Andrea Marini, and Elisa Molinari. Optical properties of graphene nanoribbons: The role of many-body effects. Phys. Rev. B, 77:041404, Jan 2008.

[227] M. J. van Setten, M. Giantomassi, X. Gonze, G.-M. Rignanese, and G. Hautier. Automation methodologies and large-scale validation for *gw*: Towards high-throughput *gw* calculations. Phys. Rev. B, 96:155207, Oct 2017.

[228] Jin-Ho Choi, Ping Cui, Haiping Lan, and Zhenyu Zhang. Linear scaling of the exciton binding energy versus the band gap of two-dimensional materials. Phys. Rev. Lett., 115:066403, Aug 2015.

[229] Zeyu Jiang, Zhirong Liu, Yuanchang Li, and Wenhui Duan. Scaling universality between band gap and exciton binding energy of two-dimensional semiconductors. Phys. Rev. Lett., 118:266401, Jun 2017.

[230] Lorenzo Sponza, Hakim Amara, Claudio Attaccalite, Sylvain Latil, Thomas Galvani, Fulvio Paleari, Ludger Wirtz, and Fran çois Ducastelle. Direct and indirect excitons in boron nitride polymorphs: A story of atomic configuration and electronic correlation. Phys. Rev. B, 98:125206, Sep 2018.

[231] Léonard Schué, Lorenzo Sponza, Alexandre Plaud, Hakima Bensalah, Kenji Watanabe, Takashi Taniguchi, François Ducastelle, Annick Loiseau, and Julien Barjon. Bright Luminescence from Indirect and Strongly Bound Excitons in h-BN. Phys. Rev. Lett., 122(6):067401, February 2019.

[232] Samuel Brem, August Ekman, Dominik Christiansen, Florian Katsch, Malte Selig, Cedric Robert, Xavier Marie, Bernhard Urbaszek, Andreas Knorr, and Ermin Malic. Phonon-assisted photoluminescence from indirect excitons in monolayers of transition-metal dichalcogenides. Nano Lett., 20(4):2849–2856, Apr 2020.

[233] Maja Feierabend, Gunnar Berghäuser, Andreas Knorr, and Ermin Malic. Proposal for dark exciton based chemical sensors. Nature Commun., 8(1):14776, Apr 2017.

[234] Rod Ruoff. Calling all chemists. Nature Nanotechnology, 3(1):10–11, 2008.

[235] Xinran Wang, Xiaolin Li, Li Zhang, Youngki Yoon, Peter K. Weber, Hailiang Wang, Jing Guo, and Hongjie Dai. N-doping of graphene through electrothermal reactions with ammonia. Science, 324(5928):768–771, 2009.

[236] D. Bouša, M. Pumera, D. Sedmidubský, J. Šturala, J. Luxa, V. Mazánek, and Z. Sofer. Fine tuning of graphene properties by modification with aryl halogens. Nanoscale, 8:1493–1502, 2016.

[237] Chiranjeevi Srinivasa Rao Vusa, Manju Venkatesan, Aneesh K, Sheela Berchmans, and Palaniappan Arumugam. Tactical tuning of the surface and interfacial properties of graphene: A versatile and rational electrochemical approach. Scientific Reports, 7(1):8354, 2017.

[238] Jisoo Park, Young Shik Cho, Sae Jin Sung, Minhoo Byeon, Seung Jae Yang, and Chong Rae Park. Characteristics tuning of graphene-oxide-based-graphene to various end-uses. Energy Storage Materials, 14:8–21, 2018.

[239] Jorge O. Sofo, Ajay S. Chaudhari, and Greg D. Barber. Graphane: A two-dimensional hydrocarbon. Phys. Rev. B, 75:153401, Apr 2007.

[240] Pierluigi Cudazzo, Claudio Attaccalite, Ilya V. Tokatly, and Angel Rubio. Strong charge-transfer excitonic effects and the bose-einstein exciton condensate in graphane. Phys. Rev. Lett., 104:226804, Jun 2010.

[241] Valentina Tozzini and Vittorio Pellegrini. Prospects for hydrogen storage in graphene. Phys. Chem. Chem. Phys., 15:80–89, 2013.

[242] Sunmin Ryu, Melinda Y. Han, Janina Maultzsch, Tony F. Heinz, Philip Kim, Michael L. Steigerwald, and Louis E. Brus. Reversible basal plane hydrogenation of graphene. Nano Letters, 8(12):4597–4602, 2008. PMID: 19053793.

[243] D. C. Elias, R. R. Nair, T. M. G. Mohiuddin, S. V. Morozov, P. Blake, M. P. Halsall, A. C. Ferrari, D. W. Boukhvalov, M. I. Katsnelson, A. K. Geim, and K. S. Novoselov. Control of graphene's properties by reversible hydrogenation: Evidence for graphane. Science, 323(5914):610–613, 2009.

[244] D. Haberer, D. V. Vyalikh, S. Taioli, B. Dora, M. Farjam, J. Fink, D. Marchenko, T. Pichler, K. Ziegler, S. Simonucci, M. S. Dresselhaus, M. Knupfer, B. Buuchner, and A. Gruneis. Tunable band gap in hydrogenated quasi-free-standing graphene. Nano Lett. , 10(9):3360–3366, 2010.

[245] Zhiqiang Luo, Jingzhi Shang, Sanhua Lim, Dehui Li, Qihua Xiong, Zexiang Shen, and et al. Modulating the electronic structures of graphene by controllable hydrogenation. Applied Physics Letters, 97(23):233111, 2010.

[246] James S. Burgess, Bernard R. Matis, Jeremy T. Robinson, Felipe A. Bulat, F. Keith Perkins, Brian H. Houston, and Jeffrey W. Baldwin. Tuning the electronic properties of graphene by hydrogenation in a plasma enhanced chemical vapor deposition reactor. Carbon, 49(13):4420 – 4426, 2011.

[247] Richard Balog, Mie Andersen, Bjarke Jørgensen, Zeljko Sljivancanin, Bjørk Hammer, Alessandro Baraldi, Rosanna Larciprete, Philip Hofmann, Liv Hornekær, and Silvano Lizzit. Controlling hydrogenation of graphene on ir(111). ACS Nano, 7(5):3823–3832, 2013. PMID: 23586740.

[248] Alessio Paris, Nikolay Verbitskiy, Alexei Nefedov, Ying Wang, Alexander Fedorov, Danny Haberer, Martin Oehzelt, Luca Petaccia, Dmitry Usachov, Denis Vyalikh, Hermann Sachdev, Christoph Wöll, Martin Knupfer, Bernd Büchner, Lucia Calliari, Lada Yashina, Stephan Irle, and Alexander Grüneis. Kinetic isotope effect in the hydrogenation and deuteration of graphene. Advanced Functional Materials, 23(13):1628–1635, 2013.

[249] A. Felten, D. McManus, C. Rice, L. Nittler, J.-J. Pireaux, and C. Casiraghi. Insight into hydrogenation of graphene: Effect of hydrogen plasma chemistry. Applied Physics Letters, 105(18):183104, 2014.

[250] Mohammad Panahi, Navid Solati, and Sarp Kaya. Modifying hydrogen binding strength of graphene. Surface Science, 679:24 – 30, 2019.

[251] Mahmoud Mohamed Saad Abdelnabi, Elena Blundo, Maria Grazia Betti, Gianluca Cavoto, Ernesto Placidi, Antonio Polimeni, Alessandro Ruocco, Kailong Hu, Yoshikazu Ito, and Carlo Mariani. Towards free-standing graphane: atomic hydrogen and deuterium bonding to nano-porous graphene. Nanotechnology, 32(3):035707, oct 2020.

[252] Mahmoud Mohamed Saad Abdelnabi, Chiara Izzo, Elena Blundo, Maria Grazia Betti, Marco Sbroscia, Giulia Di Bella, Gianluca Cavoto, Antonio Polimeni, Isabel García-Cortés, Isabel Rucandio, Alejandro Moroño, Kailong Hu, Yoshikazu Ito, and Carlo Mariani. Deuterium adsorption on free-standing graphene. Nanomaterials, 11(1):130, 2021.

[253] Fang Zhao, Yevgeny Raitses, Xiaofang Yang, Andi Tan, and Christopher G. Tully. High hydrogen coverage on graphene via low temperature plasma with applied magnetic field. Carbon, 177:244–251, 2021.

[254] Iolanda Di Bernardo, Giulia Avvisati, Carlo Mariani, Nunzio Motta, Chaoyu Chen, José Avila, Maria Carmen Asensio, Stefano Lupi, Yoshikazu Ito, Mingwei Chen, Takeshi Fujita, and Maria Grazia Betti. Two-dimensional hallmark of highly interconnected three-dimensional nanoporous graphene. ACS Omega, 2(7):3691–3697, 2017.

[255] Iolanda Di Bernardo, Giulia Avvisati, Chaoyu Chen, José Avila, Maria Carmen Asensio, Kailong Hu, Yoshikazu Ito, Peter Hines, Josh Lipton-Duffin, Llew Rintoul, Nunzio Motta, Carlo Mariani, and Maria Grazia Betti. Topology and doping effects in three-dimensional nanoporous graphene. Carbon, 131:258 – 265, 2018.

[256] J. Zhou, Q. Wang, Q. Sun, X. S. Chen, Y. Kawazoe, and P. Jena. Ferromagnetism in semihydrogenated graphene sheet. Nano Letters, 9(11):3867–3870, 2009.

[257] Leonid A. Chernozatonskii, Victor A. Demin, and Dmitry G. Kvashnin. Fully hydrogenated and fluorinated bigraphenes-diamanes: Theoretical and experimental studies. C, 7(1), 2021.

[258] Nicola Marzari, Andrea Ferretti, and Chris Wolverton. Electronic-structure methods for materials design. Nat. Mater., 2(6):736 – 749, 2021.

[259] J. Singh. Physics of Semiconductors and Their Heterostructures. McGraw-Hill, New York, 1992.

[260] Jangyup Son, Soogil Lee, Sang Jin Kim, Byung Cheol Park, Han-Koo Lee, Sanghoon Kim, Jae Hoon Kim, Byung Hee Hong, and Jongill Hong. Hydrogenated monolayer graphene with reversible and tunable wide band gap and its field-effect transistor. Nature Communications, 7(1):13261, 2016.

[261] S. Lebègue, M. Klintenberg, O. Eriksson, and M. I. Katsnelson. Accurate electronic band gap of pure and functionalized graphane from gw calculations. Phys. Rev. B, 79:245117, Jun 2009.

[262] W. Kohn, "Metals and insulators" in *Many-Body Physics*, C. de Witt, R. Balian, Eds. (Gordon & Breach, New York, NY, 1967), pp. 351–411.

[263] L. V. Keldysh and Y. V. Kopaev. Possible instability of the semimetallic state against Coulomb interaction. Sov. Phys. Sol. State, 6(2219), 1965.

[264] C. N. Yang. Concept of Off-Diagonal Long-Range Order and the Quantum Phases of Liquid He and of Superconductors. Reviews of Modern Physics, 34(4):694–704, October 1962.

[265] N. F. Mott. The transition to the metallic state. Philosophical Magazine, 6(62):287–309, February 1961.

[266] R. S. Knox. Solid State Physics. Academic Press Inc., New York, 1963.

[267] B. I. Halperin and T. M. Rice. Possible Anomalies at a Semimetal-Semiconductor Transistion. Reviews of Modern Physics, 40(4):755–766, October 1968.

[268] Daniele Varsano, Sandro Sorella, Davide Sangalli, Matteo Barborini, Stefano Corni, Elisa Molinari, and Massimo Rontani. Carbon nanotubes as excitonic insulators. Nature Commun., 8(1), Nov 2017.

[269] Daniele Varsano, Maurizia Palummo, Elisa Molinari, and Massimo Rontani. A monolayer transition-metal dichalcogenide as a topological excitonic insulator. Nature Nanotechnology, 15(5):367–372, May 2020.

[270] S. Samaneh Ataei, Daniele Varsano, Elisa Molinari, and Massimo Rontani. Evidence of ideal excitonic insulator in bulk MoS $_2$ under pressure. Proceedings of the National Academy of Sciences, 118(13):e2010110118, March 2021.

[271] Y. F. Lu, H. Kono, T. I. Larkin, A. W. Rost, T. Takayama, A. V. Boris, B. Keimer, and H. Takagi. Zero-gap semiconductor to excitonic insulator transition in ta2nise5. Nature Communications, 8(1):14408, 2017.

[272] Yu-Seong Seo, Man Jin Eom, Jun Sung Kim, Chang-Jong Kang, Byung Il Min, and Jungseek Hwang. Temperature-dependent excitonic superfluid plasma frequency evolution in an excitonic insulator, ta2nise5. Scientific Reports, 8(1):11961, 2018.

[273] H. Hedayat, C. J. Sayers, D. Bugini, C. Dallera, D. Wolverson, T. Batten, S. Karbassi, S. Friedemann, G. Cerullo, J. van Wezel, S. R. Clark, E. Carpene, and E. Da Como. Excitonic and lattice contributions to the charge density wave in $1t - TiSe_2$ revealed by a phonon bottleneck. Phys. Rev. Research, 1:023029, Sep 2019.

[274] Jianqiang Sky Zhou, Lorenzo Monacelli, Raffaello Bianco, Ion Errea, Francesco Mauri, and Matteo Calandra. Anharmonicity and doping melt the charge density wave in single-layer tise2. Nano Letters, 20(7):4809–4815, 07 2020.

[275] Akitoshi Nakano, Takumi Hasegawa, Shinya Tamura, Naoyuki Katayama, Satoshi Tsutsui, and Hiroshi Sawa. Antiferroelectric distortion with anomalous phonon softening in the excitonic insulator ta_2nise_5. Phys. Rev. B, 98:045139, Jul 2018.

[276] Jian Yan, Ruichun Xiao, Xuan Luo, Hongyan Lv, Ranran Zhang, Yan Sun, Peng Tong, Wenjian Lu, Wenhai Song, Xuebin Zhu, and Yuping Sun. Strong electron–phonon coupling in the excitonic insulator ta2nise5. Inorganic Chemistry, 58(14):9036–9042, 07 2019.

[277] W. KOHN and D. SHERRINGTON. Two kinds of bosons and bose condensates. Rev. Mod. Phys., 42:1–11, Jan 1970.

[278] Bosong Sun, Wenjin Zhao, Tauno Palomaki, Zaiyao Fei, Elliott Runburg, Paul Malinowski, Xiong Huang, John Cenker, Yong-Tao Cui, Jiun-Haw Chu, et al. Evidence for equilibrium exciton condensation in monolayer wte2. Nature Physics, 18(1):94–99, 2022.

[279] Yanyu Jia, Pengjie Wang, Cheng-Li Chiu, Zhida Song, Guo Yu, Berthold Jäck, Shiming Lei, Sebastian Klemenz, F Alexandre Cevallos, Michael Onyszczak, et al. Evidence for a monolayer excitonic insulator. Nature Physics, 18(1):87–93, 2022.

[280] Zaiyao Fei, Wenjin Zhao, Tauno A. Palomaki, Bosong Sun, Moira K. Miller, Zhiying Zhao, Jiaqiang Yan, Xiaodong Xu, and David H. Cobden. Ferroelectric switching of a two-dimensional metal. Nature, 560(7718):336–339, 2018.

[281] Ebrahim Sajadi, Tauno Palomaki, Zaiyao Fei, Wenjin Zhao, Philip Bement, Christian Olsen, Silvia Luescher, Xiaodong Xu, Joshua A. Folk, and David H. Cobden. Gate-induced superconductivity in a monolayer topological insulator. Science, 362(6417):922–925, 2018.

[282] Valla Fatemi, Sanfeng Wu, Yuan Cao, Landry Bretheau, Quinn D. Gibson, Kenji Watanabe, Takashi Taniguchi, Robert J. Cava, and Pablo Jarillo-Herrero. Electrically tunable low-density superconductivity in a monolayer topological insulator. Science, 362(6417):926–929, 2018.

[283] Zhen-Hua Chi, Xiao-Miao Zhao, Haidong Zhang, Alexander F. Goncharov, Sergey S. Lobanov, Tomoko Kagayama, Masafumi Sakata, and Xiao-Jia Chen. Pressure-induced metallization of molybdenum disulfide. Phys. Rev. Lett., 113:036802, Jul 2014.

[284] Zhenhua Chi, Xuliang Chen, Fei Yen, Feng Peng, Yonghui Zhou, Jinlong Zhu, Yijin Zhang, Xiaodi Liu, Chuanlong Lin, Shengqi Chu, Yanchun Li, Jinggeng Zhao, Tomoko Kagayama, Yanming Ma, and Zhaorong Yang. Superconductivity in pristine $2H_a-\mathrm{mos}_2$ at ultrahigh pressure. Phys. Rev. Lett., 120:037002, Jan 2018.

[285] Zi-Yu Cao, Jia-Wei Hu, Alexander F. Goncharov, and Xiao-Jia Chen. Nontrivial metallic state of mos_2. Phys. Rev. B, 97:214519, Jun 2018.

[286] Nirup Bandaru, Ravhi S. Kumar, Daniel Sneed, Oliver Tschauner, Jason Baker, Daniel Antonio, Sheng-Nian Luo, Thomas Hartmann, Yusheng Zhao, and Rama Venkat. Effect of pressure and temperature on structural stability of mos2. The Journal of Physical Chemistry C, 118(6):3230–3235, 02 2014.

[287] Alexander F. Goncharov, Maxim Bykov, Elena Bykova, Konstantin Glazyrin, Vitali Prakapenka, Zi-Yu Cao, and Xiao-Jia Chen. Structure and stability of $2H_a-\mathrm{Mos}_2$ at high pressure and low temperatures. Phys. Rev. B, 102:064105, Aug 2020.

[288] Antanas Vaitkus, Andrius Merkys, and Saulius Gražulis. Validation of the Crystallography Open Database using the Crystallographic Information Framework. Journal of Applied Crystallography, 54(2):661–672, Apr 2021.

[289] D. Zagorac, H. Müller, S. Ruehl, J. Zagorac, and S. Rehme. Recent developments in the Inorganic Crystal Structure Database: theoretical crystal structure data and related features. Journal of Applied Crystallography, 52(5):918–925, Oct 2019.

[290] The MPDS database is available at: https://mpds.io/#start.

[291] Thomas Olsen, Simone Latini, Filip Rasmussen, and Kristian S. Thygesen. Simple Screened Hydrogen Model of Excitons in Two-Dimensional Materials. Physical Review Letters, 116(5):056401, February 2016.

[292] Kristian Sommer Thygesen. Calculating excitons, plasmons, and quasiparticles in 2D materials and van der Waals heterostructures. 2D Materials, 4(2):022004, June 2017.

[293] G. Shipunov, B. R. Piening, C. Wuttke, T. A. Romanova, A. V. Sadakov, O. A. Sobolevskiy, E. Yu. Guzovsky, A. S. Usoltsev, V. M. Pudalov, D. V. Efremov, S. Subakti, D. Wolf, A. Lubk, B. Büchner, and S. Aswartham. Layered van der Waals Topological Metals of TaTMTe $_4$ (TM = Ir, Rh, Ru) Family. The Journal of Physical Chemistry Letters, 12(28):6730–6735, July 2021.

[294] Peng-Jie Guo, Xiao-Qin Lu, Wei Ji, Kai Liu, and Zhong-Yi Lu. Quantum spin hall effect in monolayer and bilayer tairte$_4$. Phys. Rev. B, 102:041109, Jul 2020.

[295] Arthur Mar, Stephane Jobic, and James A. Ibers. Metal-metal vs tellurium-tellurium bonding in wte2 and its ternary variants tairte4 and nbirte4. Journal of the American Chemical Society, 114(23):8963–8971, 11 1992.

[296] Arthur Mar and James A. Ibers. Synthesis and physical properties of the new layered ternary tellurides mirte4 (m = nb, ta), and the structure of nbirte4. Journal of Solid State Chemistry, 97(2):366–376, 1992.

[297] Tianxi Zhang, Tian Wang, Fanlu Meng, Minquan Yang, and Sibudjing Kawi. Recent advances in znin2s4-based materials towards photocatalytic purification, solar fuel production and organic transformations. J. Mater. Chem. C, 10:5400–5424, 2022.

[298] Nathan D. Lowhorn, Terry M. Tritt, Edward E. Abbott, and J. W. Kolis. Enhancement of the power factor of the transition metal pentatelluride hfte5 by rare-earth doping. Applied Physics Letters, 88(2):022101, 2006.

[299] Davide Grassano, Davide Campi, Antimo Marrazzo, and Nicola Marzari. A complementary screening for quantum spin hall insulators in 2d exfoliable materials, 2022.

[300] https://www.lumi-supercomputer.eu.

[301] Martin Dressel and George Grüner. Electrodynamics of Solids: Optical Properties of Electrons in Matter. Cambridge University Press, 2002.

[302] M. R. Jarvis, I. D. White, R. W. Godby, and M. C. Payne. Supercell technique for total-energy calculations of finite charged and polar systems. Phys. Rev. B, 56:14972–14978, Dec 1997.

[303] Liang Z Tan, Fan Zheng, Steve M Young, Fenggong Wang, Shi Liu, and Andrew M Rappe. Shift current bulk photovoltaic effect in polar materials—hybrid and oxide perovskites and beyond. npj Computational Materials, 2(1):16026, 2016.

[304] Stepan S. Tsirkin, Pablo Aguado Puente, and Ivo Souza. Gyrotropic effects in trigonal tellurium studied from first principles. Phys. Rev. B, 97:035158, Jan 2018.

[305] S. Poncé, E. R. Margine, C. Verdi, and F. Giustino. EPW: Electron-phonon coupling, transport and superconducting properties using maximally localized Wannier functions. Computer Physics Communications, 209:116–133, December 2016.

[306] Arrigo Calzolari, Nicola Marzari, Ivo Souza, and Marco Buongiorno Nardelli. Ab initio transport properties of nanostructures from maximally localized wannier functions. Phys. Rev. B, 69:035108, Jan 2004.

[307] Dominik Gresch, QuanSheng Wu, Georg W. Winkler, Rico Häuselmann, Matthias Troyer, and Alexey A. Soluyanov. Automated construction of symmetrized wannier-like tight-binding models from ab initio calculations. Phys. Rev. Materials, 2:103805, Oct 2018.

[308] Nicola Marzari and David Vanderbilt. Maximally localized generalized wannier functions for composite energy bands. Phys. Rev. B, 56:12847–12865, Nov 1997.

[309] Ivo Souza, Nicola Marzari, and David Vanderbilt. Maximally localized wannier functions for entangled energy bands. Phys. Rev. B, 65:035109, Dec 2001.

[310] Jonathan R. Yates, Xinjie Wang, David Vanderbilt, and Ivo Souza. Spectral and fermi surface properties from wannier interpolation. Phys. Rev. B, 75:195121, May 2007.

[311] Nicola Marzari, Arash A. Mostofi, Jonathan R. Yates, Ivo Souza, and David Vanderbilt. Maximally localized wannier functions: Theory and applications. Rev. Mod. Phys., 84:1419–1475, Oct 2012.

[312] Gregory H. Wannier. The structure of electronic excitation levels in insulating crystals. Phys. Rev., 52:191–197, Aug 1937.

[313] E.I. Blount. Formalisms of band theory. 13:305–373, 1962.

[314] Anil Damle, Lin Lin, and Lexing Ying. Compressed representation of kohn–sham orbitals via selected columns of the density matrix. Journal of Chemical Theory and Computation, 11(4):1463–1469, 04 2015.

[315] Anil Damle and Lin Lin. Disentanglement via entanglement: A unified method for wannier localization. Multiscale Modeling & Simulation, 16(3):1392–1410, 2018.

[316] Helmut Bross. A general interpolation scheme for the one-electron energies of a solid. Zeitschrift für Physik A Hadrons and nuclei, 243(4):311–325, 1971.

[317] B. Sporkmann and H. Bross. Calculation of wannier functions for fcc transition metals by fourier transformation of bloch functions. Phys. Rev. B, 49:10869–10876, Apr 1994.